

Study of the ligand effects on the metal-ligand
bond in some new organometallic complexes using
FT-Raman and -IR spectroscopy, isotopic
substitution and density functional theory
techniques

Dissertation zur Erlangung des
naturwissenschaftlichen Doktorgrades
der Bayerischen Julius-Maximilians-Universität Würzburg

vorgelegt von
Damien Moigno
aus
Redon, Frankreich

Würzburg 2001

Eingereicht am:
bei der Fakultät für Chemie und Pharmazie.

1. Gutachter: -----

2. Gutachter: -----

der Dissertation.

1. Prüfer: -----

2. Prüfer: -----

der mündlichen Prüfung.

Tag der mündlichen Prüfung: -----

Doktorurkunde ausgehändigt am: -----

Contents

Chapter 1. Introduction 11

Chapter 2. Theoretical and Experimental Background

2.1 Vibrational spectroscopy	13
2.1.1 Infrared spectroscopy	14
2.1.2 Raman spectroscopy	14
2.1.2.1 Principle	14
2.1.2.2 Theory	15
2.1.3 FT-Raman spectroscopy	17
2.1.3.1 Why do FT-Raman spectroscopy ?	17
2.1.3.2 Obtaining the interferogram	18
2.1.4 Advantage of the 1064 nm wavelength	20
2.1.5 Experimental	21
2.2 Density Functional Theory	22
2.2.1 Basis Set Effects	25
2.2.1.1 Definition	25
2.2.1.2 Minimal Basis Sets	28
2.2.1.3 Split Valence Basis Sets	28
2.2.1.4 Polarized Basis sets	29
2.2.1.5 Diffuse Functions	29
2.2.1.6 Effective Core Potentials (ECP)	29

Chapter 3. Vibrational spectroscopy studies and DFT calculations on square-planar rhodium(I) complexes

3.1 Vinylidene and carbonyl rhodium(I) complexes <i>trans</i> -[RhX(L)(PiPr ₃) ₂] (L = C=CH ₂ and CO; X = F, Cl, Br, I and C≡CPh) and <i>trans</i> -[RhX(=C=CHPh)(PiPr ₃) ₂] (X = F, Cl, Br, I, CH ₃ and C≡CPh)	31
3.1.1 Experimental and theoretical structures	32
3.1.2 NBO and MO calculations	41
3.1.3 Vibrational Spectroscopy	46
3.1.3.1 Vibrational spectrum of PiPr ₃	46
3.1.3.2 Vibrational spectrum of <i>trans</i> -[RhF(=C=CH ₂)(PiPr ₃) ₂] vs. <i>trans</i> -[RhF(= ¹³ C= ¹³ CH ₂)(PiPr ₃) ₂]	47
3.1.3.3 Vibrational spectrum of <i>trans</i> -[RhX(= ¹³ C= ¹³ CH ₂)(PiPr ₃) ₂] (X = F, Cl, Br, I)	50
3.1.3.4 Vibrational spectrum of <i>trans</i> -[RhX(=C=CHPh)(PiPr ₃) ₂] (X = F, Cl, Br, I, CH ₃ , PhC≡C)	53

3.1.3.5	Vibrational spectrum of <i>trans</i> -[RhX(CO)(PiPr ₃) ₂] (X = F, Cl, Br, I, PhC≡C)	58
3.1.4	Discussion	62
3.2	Ethylene rhodium(I) complex <i>trans</i> -[RhF(C ₂ H ₄)(PiPr ₃) ₂]	66
3.2.1	Experimental and Theoretical structures	66
3.2.2	Vibrational spectroscopy	68
3.2.2.1	Vibrational spectrum of <i>trans</i> -[RhF(C ₂ H ₄)(PiPr ₃) ₂]	68
3.3	Isonitrile rhodium(I) complexes <i>trans</i> -[{RhX(PiPr ₃) ₂ } ₂ {μ-1,3-(CN) ₂ C ₆ H ₄ }] (X = Cl, I)	72
3.3.1	Experimental and theoretical structures	73
3.3.1.1	Theoretical structure of <i>m</i> -diisocyanobenzene 1,3-(CN) ₂ C ₆ H ₄	73
3.3.1.2	Structure of <i>trans</i> -[{RhCl(PiPr ₃) ₂ } ₂ {μ-1,3-(CN) ₂ C ₆ H ₄ }]	74
3.3.2	Vibrational Spectroscopy	77
3.3.2.1	Vibrational spectrum of <i>m</i> -diisocyanobenzene 1,3-(CN) ₂ C ₆ H ₄	77
3.3.2.2	Vibrational spectrum of <i>trans</i> -[{RhX(PiPr ₃) ₂ } ₂ {μ-1,3-(CN) ₂ C ₆ H ₄ }] (X = Cl, I)	81
3.4	Isonitrile rhodium(I) complex <i>trans</i> -[RhX(CNR)(PiPr ₃) ₂] (X = F, Cl, Br, I, Ph-C≡C, R = 2,6-xylyl; X = Cl, R = <i>t</i> Bu)	87
3.4.1	Experimental and theoretical structures	87
3.4.1.1	Theoretical structure of 2,6-xylyl isocyanide	87
3.4.1.2	Structure of <i>trans</i> -[RhX(CNR)(PR' ₃) ₂] (X = F, Cl, Br, I, PhC≡C; R = 2,6-xylyl, <i>t</i> Bu; R' = Me, <i>i</i> Pr)	88
3.4.2	Vibrational Spectroscopy	91
3.4.2.1	Vibrational spectrum of 2,6-xylyl isocyanide	91
3.4.2.2	Vibrational spectrum of <i>trans</i> -[RhX(CN-2,6-xylyl)(PiPr ₃) ₂] (X = F, Cl, Br, I, PhC≡C)	93
3.4.2.3	Vibrational spectrum of <i>trans</i> -[RhCl(CN- <i>t</i> Bu)(PiPr ₃) ₂]	98

Chapter 4. Vibrational spectroscopy studies and DFT calculations on tungsten and molybdenum complexes

4.1	Tungsten complexes <i>mer</i> -[W(CO) ₃ (dmpe)(η ² -S=CR ₂)] (R = H, D)	101
4.1.1	Experimental and theoretical structures	102
4.1.2	MO calculation	104
4.1.3	Vibrational spectroscopy	106
4.1.3.1	Vibrational spectrum of <i>mer</i> -[W(CO) ₃ (dmpe)(η ² -S=CR ₂)] (R = H, D)	106
4.2	Cp(CO) ₂ W=PtBu ₂ and Cp(CO) ₂ $\overline{\text{M-PR}_2\text{-X}}$ (M = Mo, W; R = Me, <i>t</i> Bu, Ph; X = S, Se)	113
4.2.1	Experimental and theoretical structures	114
4.2.1.1	Structure of Cp(CO) ₂ W=PtBu ₂	114
4.2.1.2	Structures of Cp(CO) ₂ $\overline{\text{M-PR}_2\text{-S}}$ (M = Mo, W; R = Ph, Me, <i>t</i> Bu)	115
4.2.1.3	Structures of Cp(CO) ₂ $\overline{\text{M-PR}_2\text{-Se}}$ (M = Mo, W; R = Ph, Me, <i>t</i> Bu)	117
4.2.2	NBO and MO calculations	119
4.2.3	Vibrational spectroscopy	120

4.2.3.1 Vibrational spectrum of $\text{Cp}(\text{CO})_2\text{W}=\text{PtBu}_2$	120
4.2.3.2 Vibrational spectrum of $\text{Cp}(\text{CO})_2\text{M}-\text{PPh}_2-\text{X}$ (M = W, Mo; X = S, Se)	121

Chapter 5. Photodissociation of carbonyl iron silyl complexes
 $\text{CpFe}(\text{CO})_2\text{SiH}_2\text{Me}$ and $\text{CpFe}(\text{CO})_2\text{CH}_2\text{SiH}_3$: A theoretical study

5.1 Introduction	129
5.1.1 Results and discussion	131
5.2.2 Conclusion	141

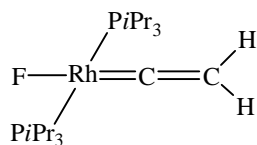
Chapter 6. A theoretical and vibrational analysis of the coordination
behaviour of the $(2\text{-Py})_2\text{P}^-$ and $(2\text{-Py})_2\text{N}^-$ anions

6.1 Introduction	143
6.2 Reactivity	145
6.3 Experimental and theoretical structures	146
6.4 The $(2\text{-Py})_2\text{P}^-$ and $(2\text{-Py})_2\text{N}^-$ anions	153
6.5 Study of the donor-acceptor bond	156
6.6 Vibrational spectroscopy	167
6.7 $[\text{Me}_2\text{Al}\{\text{Py}(\text{Bth})\text{P}\}]$	173
6.7.1 Experimental and theoretical structures	173
6.7.2 NBO analysis and total electron density calculation	175
6.7.3 Vibrational spectroscopy	176

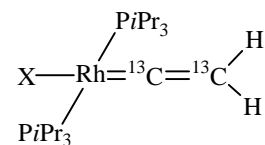
Chapter 7. Summary/Zusammenfassung

References	187
------------	-----

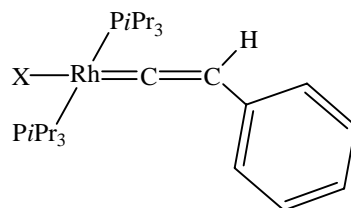
Compounds



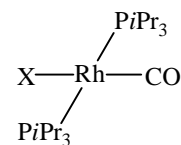
(1)



(2)



(6)



(12)

X = Cl (3)

X = Cl (7)

X = Cl (13)

X = Br (4)

X = Br (8)

X = Br (14)

X = I (5)

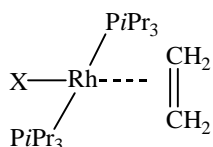
X = I (9)

X = I (15)

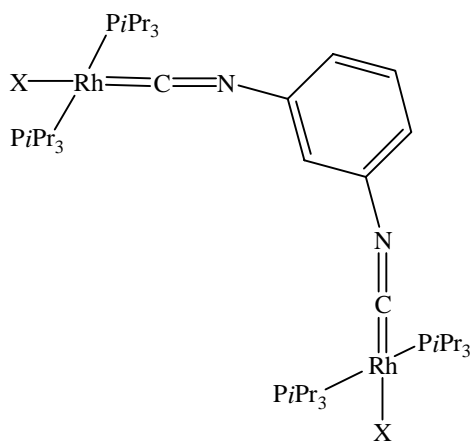
X = CH₃ (10)

X = PhC≡C (16)

X = PhC≡C (11)

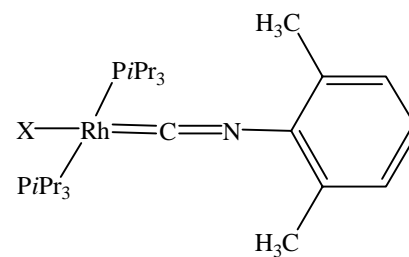


(17)



X = Cl (18)

X = I (19)



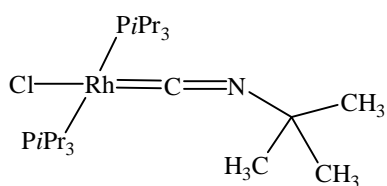
X = F (20)

X = Cl (21)

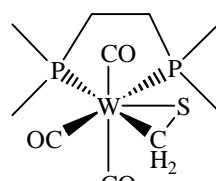
X = Br (22)

X = I (23)

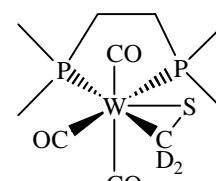
X = PhC≡C (24)



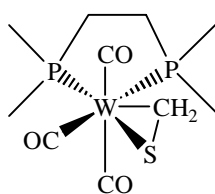
(25)



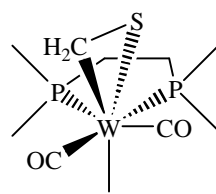
(26)



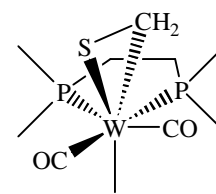
(27)



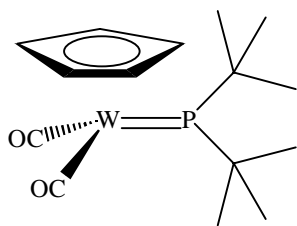
(28)



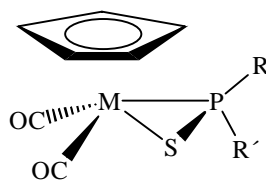
(29)



(30)

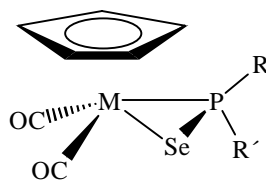


(31)



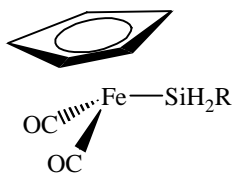
M = Mo; R = R' = Ph (32)

M = W; R = R' = Ph (33)

M = W; R = R' = *t*Bu (34)M = W; R = *t*Bu, R' = Me (35)

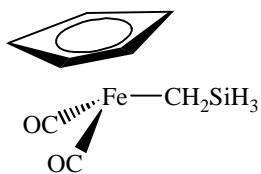
M = Mo; R = R' = Ph (36)

M = W; R = R' = Ph (37)

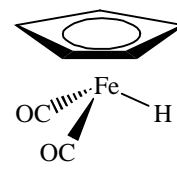
M = W; R = R' = *t*Bu (38)M = W; R = *t*Bu, R' = Me (39)

R = H (40)

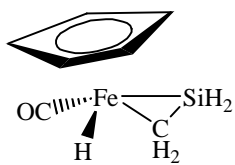
R = Me (41a)



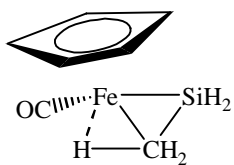
(41b)



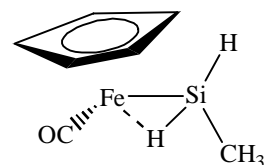
(42)



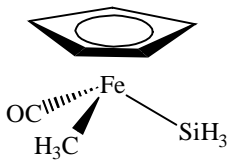
(43b)



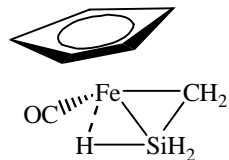
(43c)



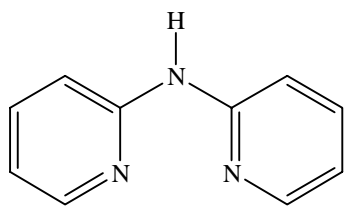
(43a)



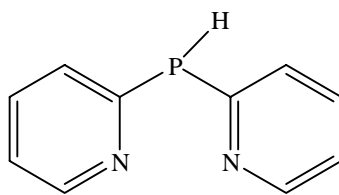
(43e)



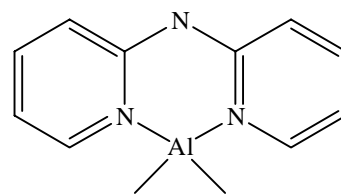
(43d)



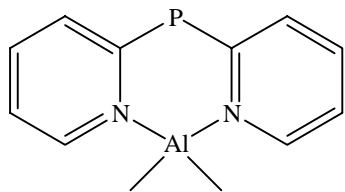
(45)



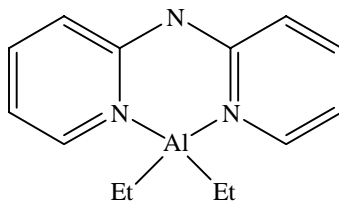
(46)



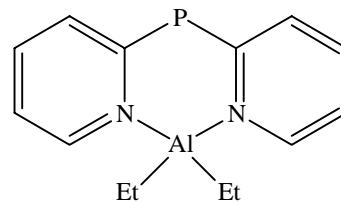
(47)



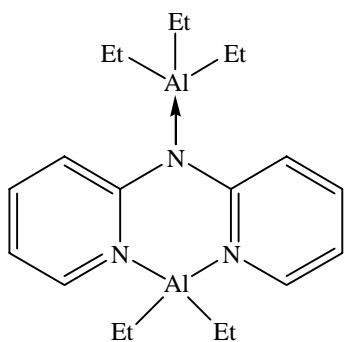
(48)



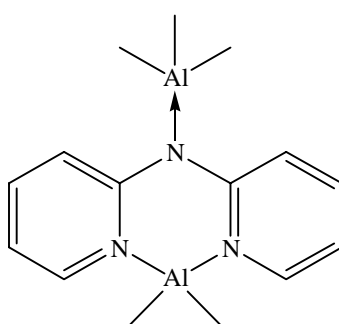
(49)



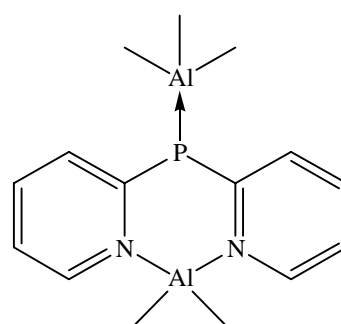
(50)



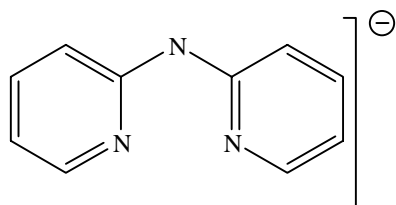
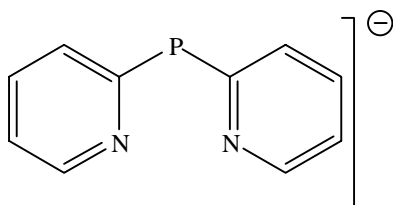
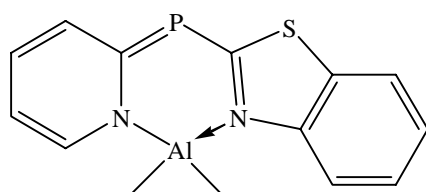
(51)



(52)



(53)

*trans-trans* (54a)*cis-trans* (54b)*cis-cis* (54c)*trans-trans* (55a)*cis-trans* (55b)*cis-cis* (55c)

(56)

Chapter 1

Introduction

In the last twenty years, quantum chemical methods have developed in such successful way, that they are now almost an indispensable complement to experimental studies. One of the central tasks in computational chemistry is the accurate and efficient prediction of molecular geometries, vibrational modes, and energies of chemical reactions. Such predictions are of great value in areas such as synthetic and analytic chemistry, molecular biology, catalysis and materials science.

Today, there is an increasing evidence that density functional Theory (DFT) offers a promising alternative to the Hartree-Fock approach. DFT includes electron correlation in a form that does not lead to the scaling problem of Hartree-Fock based methods. Moreover, calculations which involve transition metal or heavier main group elements are computationally demanding in terms of CPU time, disk space and memory. These demands can be reduced considerably by the description of the inner (or core) electrons using a set of potential functions, i.e. by the use of effective core potentials (ECPs). The success of ECPs in the calculation of geometries and energies of molecules containing transition metal complexes is well documented ^[1-2], and their use in conjunction with density functional theory is also found to be adequate ^[3-5]. Bond lengths of transition-metal compounds can be predicted with an accuracy of ± 5 pm, which is a rather conservative estimate. In most cases the agreement with experimental data is even better ^[6]. Owing to their high reliability, calculated metal-

ligand bond lengths could be even used successfully to question experimental results ^[7]. It is therefore often debatable whether or not it is necessary to employ X-ray diffraction analysis as the method of choice for the detailed structure determination of complex compounds because the structure analysis for large series of compounds is very expensive and limited by the availability of single crystals of the compounds to study.

From the spectroscopic techniques, vibrational (IR and Raman) spectroscopy is probably the most reliable, as the vibrational modes of pure metal-ligand stretching modes are directly related to the strength of the bonds. Nevertheless, the assignment of these bands is not obvious due to their low intensity and to the presence of other bands in the low wavenumber region where they occur. Theoretical calculations, as mentioned above, are therefore, the appropriated tools to obtain a deeper understanding of the vibrational spectra of complicated molecules. Although the use of the high energy laser beam has the advantage of producing relatively strong Raman signals from the considered species it may not be suitable for some organometallic samples with inclusions of higher hydrocarbons or organic impurities due to fluorescence effects: the high energy Ar ion laser beam may induce electronic transitions and in the return of the electron to lower energy levels a light quantum is emitted. These emissions in the range of approximately 400 to 700 nm may cover most of the spectral range of the much weaker Raman signals and thus inhibit the analysis. The problem of fluorescence can be substantially reduced by the use of near IR Raman excitations. The long wavelength/low energy excitation (Nd-YAG laser with 1064 nm) avoids the effects of fluorescence as well as local heating.

In the present work, several metal complexes have been characterized, using Density Functional Theory (DFT) calculations and the FT-IR and -Raman spectroscopy techniques. All of these projects are within the cooperation of the SFB 347 program.

Chapter 2

Theoretical and Experimental Background

2.1 Vibrational spectroscopy

Vibrational spectroscopy is the study of the interaction of the electromagnetic radiation with matter, which gives information about the molecular structure, the vibrational levels and the chemical bonds. Regarding that the molecules consist of electrically charged nuclei and electron, they may interact with the oscillating electric and magnetic fields of the light, absorbing the right amount of energy to promote a transition of one discrete vibrational energy level (ground state) to another more energetic level (excited state).

There are two techniques that are able to measure vibrational transitions: infrared and Raman spectroscopy ^[8-9]. Both methods provide complementary images of molecular vibration, because in these spectroscopic techniques the mechanisms of the interaction of light quanta with molecules are quite different.

2.1.1 Infrared spectroscopy

The absorption in the infrared spectrum occurs when a resonance between the electric vector of the radiation field and the molecular dipole moment takes place. A vibration is infrared active only if the molecular dipole moment is modulated by the normal vibration,

$$\left(\frac{\partial \mu}{\partial q} \right)_0 \neq 0, \quad (1.1)$$

where μ is the molecular dipole moment and q stands for the normal coordinate describing the motion of the atoms during a normal vibration. There are $k = 3N - 6$ normal vibrations of a non-linear molecule with N atoms. These vibrations, may only absorb infrared radiation if they modulate the molecular dipole moment μ_k , (which is a vector with the components μ_x , μ_y and μ_z):

$$\mu_k = \mu_0 + \left(\frac{\partial \mu}{\partial q_k} \right)_0 q_k + \frac{1}{2} \left(\frac{\partial^2 \mu}{\partial q_k^2} \right)_0 q_k^2 + \dots \quad (1.2)$$

with

$$q_k = q_k^0 \cos(2\pi\nu_k t + \varphi_k) \quad (1.3)$$

the k th normal coordinate.

2.1.2 Raman spectroscopy

2.1.2.1 Principle

When light passes through a medium a portion of this light is scattered. Most of the scattered light is elastically scattered and thus without change in wavelength (no change in energy of a photon). This type of scattering is called Rayleigh scattering. If the light is monochromatic and of high intensity as is available in a laser beam then a portion of the light will be scattered inelastically with a shift in wavelength. In 1928, physicist C. V. Raman and his associate Krishnan discovered this effect and latter Raman received the 1930 Nobel prize in physics for this work. The inelastic scattering and the resulting shift in wavelength of the scattered photon is known as the Raman effect (Figure 1).

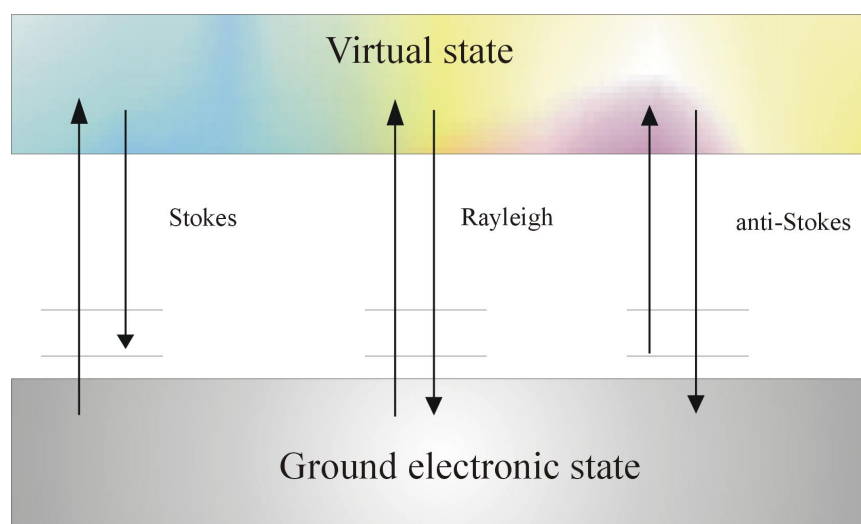


Figure 1. Principle of Raman scattering

The energy of the scattered radiation is less than the incident radiation for the Stokes line and the energy of the scattered radiation is more than the incident radiation for the anti-Stokes line. The energy increase or decrease from the excitation is related to the vibrational energy spacing in the ground electronic state of the molecule and therefore the wavenumber of the Stokes and anti-Stokes lines are a direct measure of the vibrational energies of the molecule. One may notice, that the Stokes and anti-Stokes lines are equally displaced from the Rayleigh line. This occurs because in either case one vibrational quantum of energy is gained or lost. Also, note that the anti-Stokes line is much less intense than the Stokes line. This occurs because only molecules that are vibrationally excited prior to irradiation can give rise to the anti-Stokes line. Hence, in Raman spectroscopy, only the more intense Stokes line is normally measured. With the availability of lasers, Raman spectroscopy has become a more sensitive and useful form of spectroscopy. Raman spectroscopy can provide information that is complementary to infrared spectroscopy but as well has many variants, including resonance Raman spectroscopy, that provide further insights into molecular geometry and electronic structure. Raman spectra are recorded by monitoring the intensity of Raman scattering as a function of wavenumber.

2.1.2.2 Theory

When a molecule is exposed to an electric field, electrons and nuclei are forced to move in opposite directions. A dipole moment is induced which is proportional to the electric field strength and to the molecular polarizability α . A molecular vibration can only be observed in the Raman spectrum if there is a modulation of the molecular polarizability by the vibration,

$$\left(\frac{\partial \alpha}{\partial q}\right)_0 \neq 0. \quad (1.4)$$

The electric field due to the incident radiation is a time-varying quantity of the form

$$E_i = E_0 \cos(2\pi\nu_i t). \quad (1.5)$$

For a vibrating molecule, the polarizability is also a time-varying term that depends on the vibrational frequency of the molecule, ν_{vib}

$$\alpha = \alpha_0 + \alpha_{\text{vib}} \cos(2\pi\nu_{\text{vib}} t). \quad (1.6)$$

Multiplication of these two time-varying terms, E_i and α , gives rise to a cross product term of the form:

$$\frac{\alpha_{\text{vib}} E_0}{2} [\cos 2\pi t(\nu_i + \nu_{\text{vib}}) + \cos 2\pi t(\nu_i - \nu_{\text{vib}})]. \quad (1.7)$$

This cross term in the induced dipole represents light that can be scattered at both higher and lower energy than the Rayleigh (elastic) scattering of the incident radiation. The incremental difference from the frequency of the incident radiation, ν_i , are by the vibrational modes of the molecule, ν_{vib} . These lines are referred to as the "anti-Stokes" and "Stokes" lines, respectively. The ratio of the intensity of the Raman anti-Stokes and Stokes lines is predicted to be

$$\frac{I_{AS}}{I_S} = \frac{(\nu_0 + \nu_{\text{vib}})^4}{(\nu_0 - \nu_{\text{vib}})^4} e^{-h\nu_{\text{vib}}/kT}. \quad (1.8)$$

The Boltzmann exponential factor is the dominant term in equation (1.8), which makes the anti-Stokes features of the spectra much weaker than the corresponding Stokes lines.

Since light scattering depends strongly on polarization, it is important to consider the polarization of the incident light beam and the polarization of the scattered light beam. Some scattered radiation will have the same polarization as the incident beam and is thus considered to have parallel polarization. This can be monitored experimentally by using a polarizer to measure the intensity of scattered light with the same polarization at right angles to the incident beam. The depolarization of the incident beam resulting from scattering can be determined by detecting scattered light (again at right angles) through a polarizer at 90° to the incident polarization vector, \hat{e}_i . The depolarization ratio is the ratio of the intensity of

scattered radiation from a particular spectral feature with measured perpendicular divided by that with parallel polarization.

$$\rho = \frac{I_{\perp}}{I_{\parallel}}. \quad (1.9)$$

The depolarization ratio depends on the symmetry of the vibrational mode which corresponds to the band under investigation. For any nontotally symmetric vibration $\rho = 3/4$ and for totally symmetric modes $\rho < 3/4$.

To summarize: Infrared spectroscopy and Raman spectroscopy are complementary techniques, because the selection rules are different. For example, homonuclear diatomic molecules do not have an infrared absorption spectrum, because they have no dipole moment, but do have a Raman spectrum, because stretching and contraction of the bond changes the interactions between electrons and nuclei, thereby changing the molecular polarizability. For highly symmetric polyatomic molecules possessing a center of inversion (such as benzene) it is observed that bands that are active in the IR spectrum are not active in the Raman spectrum (and vice-versa). In molecules with little or no symmetry, modes are likely to be active in both infrared and Raman spectroscopy.

2.1.3 FT-Raman spectroscopy

2.1.3.1 Why do FT-Raman spectroscopy ?

The Raman spectroscopy has been carried out successfully using dispersive instruments since the 1930s. However, there are a number of advantages to be gained by using Fourier transform rather than dispersive measurements. Both a dispersive Raman spectrometer and a FT-Raman spectrometer consist of four major components: (1) a laser; (2) optics to bring the laser to the sample, collect the scattered light and focus it onto (3) either the entrance slit of the monochromator, or the Jaquinot stop of an interferometer; and (4) a detector (Figure 2).

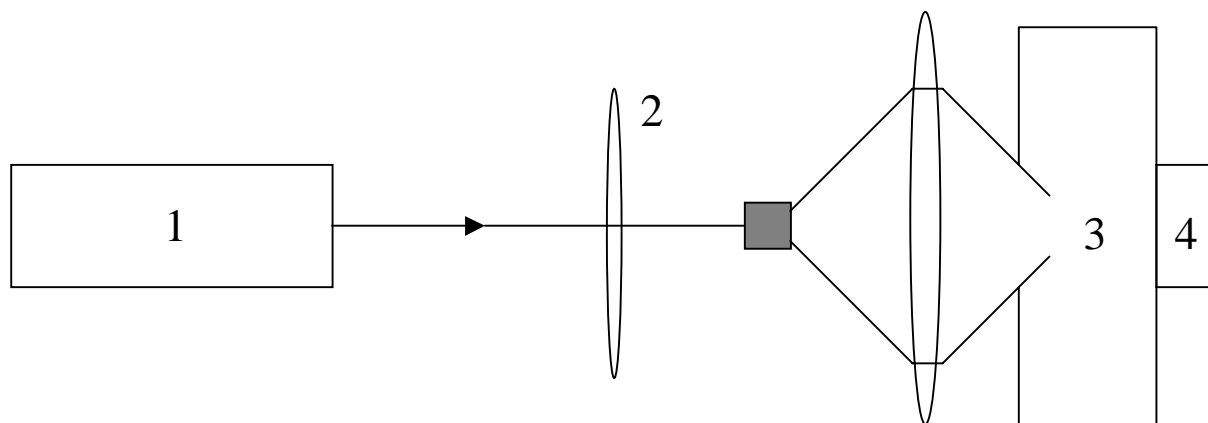


Figure 2. A schematic diagram of a Raman spectrometer.

Two major differences are immediately apparent; firstly, the interferometer does not contain any slits or dispersive elements, thus there is a larger signal reaching the detector; this is known as the throughput advantage.

Secondly, in dispersive instruments that use a single detector, such as a photomultiplier tube, each spectral element is measured separately. So in the time necessary to scan the spectrum, T , with the dispersive instrument, the interferometer has recorded every spectral element for a time T . This may result in a significantly higher signal-to-noise ratio for the same measurement time and is known as the multiplex advantage. Interferometers always display the throughput advantage; whether the multiplex advantage is realized depends on the nature of the dominant noise source in the system; it is present if the noise is independent of the intensity of the signal (detector-noise limited). With currently available detector this is the case in the near-IR region of the spectrum and provides a justification for FT-Raman spectroscopy^[10-11]. However, the practical reason that it is experimentally very straightforward often provides a more powerful motive. One may notice that the noise produced in detectors of infrared radiation is usually of thermal origin. Today, the number of detectors operating at room temperature (Golay cell, thermocouple, pyroelectric detectors) is therefore decreasing and are replaced by cooled detectors.

2.1.3.2 Obtaining the interferogram

The heart of an FT-Raman spectrometer is an interferometer and at present, all commercial FT-systems are based on a Michelson interferometer. In its simplest form, as shown in Figure 3, it consists of a beamsplitter, two mirrors, M1 and M2, and a means of altering the distance between one of the mirrors, M1, and the beamsplitter. To understand how the interferometer works, consider a beam of light incident on the beamsplitter. Assuming a perfect beamsplitter, half of the light is transmitted to mirror M1 and half is

reflected to mirror M2. After reflection at M1 and M2, the two rays are recombined at the beamsplitter; again, half the light is transmitted and half is reflected. The net effect is that half of the light is returned to the source and hence lost, and half reaches the detector. Thus, the theoretical maximum efficiency of an interferometer is 50%. In practice, no beamsplitter is perfect and losses occur every time the light is transmitted or reflected in addition to the reflection losses at the mirrors. All of these factors conspire to reduce the efficiency below 50%.

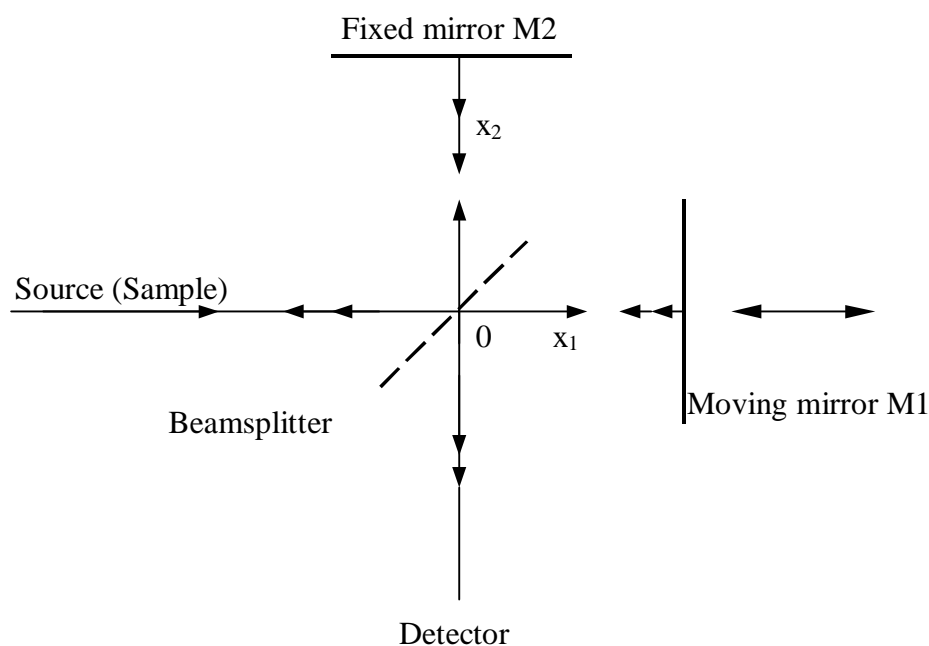


Figure 3. An idealized diagram of a Michelson interferometer.

The fact that every point in the interferogram contains information about every frequency in the spectrum constitutes the basis of the multiplex advantage after Paul Fellgett who first described it ^[12].

The net effect of the Fourier transform is to obtain a wavelength-dispersed spectrum without having to physically disperse the light. The absence of slits or gratings leads to the throughput advantage (or Jacquinot advantage ^[13]) of interferometers over dispersive instruments. Together, the two factors give a major improvement in signal-to-noise ratio (per unit time) over that obtainable from a dispersive instrument under equivalent conditions, i.e. the same laser power at the sample, detector, measurement time, resolution and scattered light collection efficiency. The properties of Fourier transforms are discussed in greater details in the literature ^[14-15].

2.1.4 Advantage of the 1064 nm wavelength

The conventional Raman spectroscopy was for a long time mainly an academic method, which was not available for routine measurement of metal complexes due to the often thermal sensibility and the possible fluorescence of the studied samples. Due to their complementarity, the infrared and Raman spectroscopy are both of great relevance in the analysis of metal complexes. The combination of the Fourier Transform technique with the use of the 1064 nm wavelength is certainly a big improvement in the spectroscopy of organometallic complexes, which are often photosensible. Moreover, excellent spectra can be obtained from even highly coloured materials. Figure 4 shows, that the use of the 1064 nm wavelength allow in main of the case to bypass all fluorescence and thermal deterioration of the measured samples, since most of them have few absorptions bands in the near-infrared region.

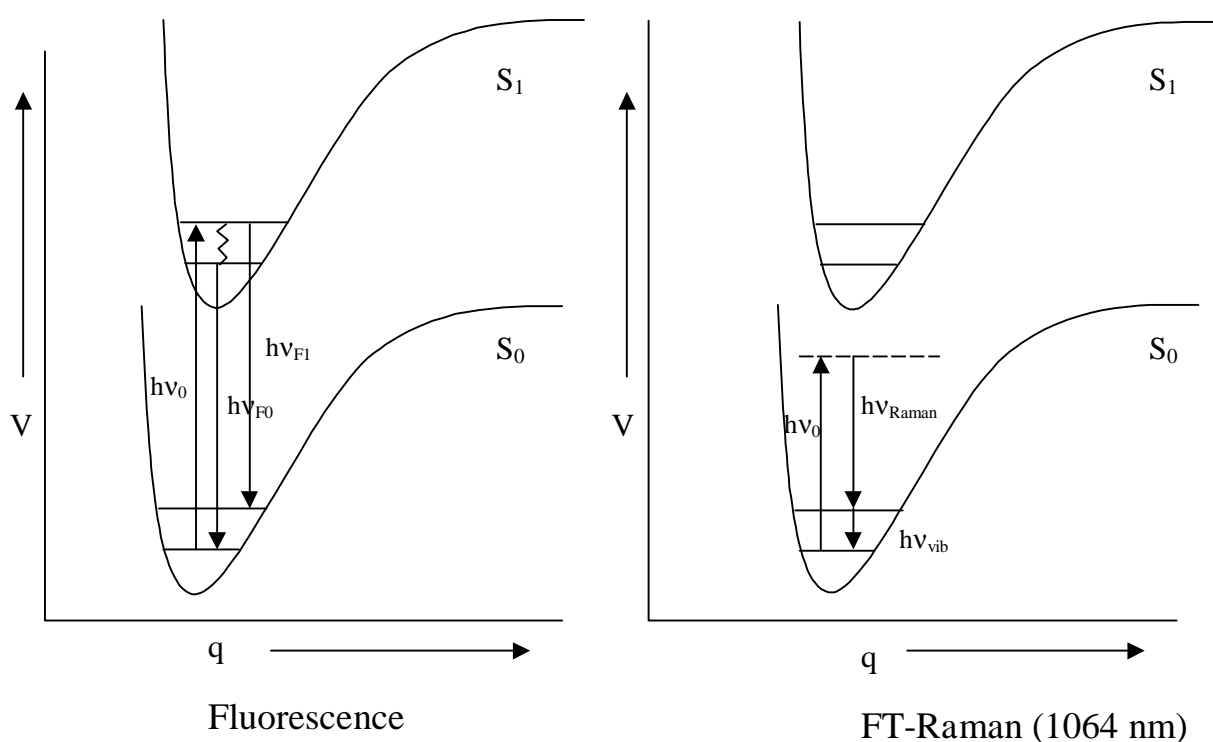


Figure 4. Schematic representation of fluorescence in comparison with the FT-Raman spectroscopy for a laser line excitation at 1064 nm.

2.1.5 Experimental

For the measurements which are reported in this work, a Bruker IFS120 spectrometer equipped with a Raman module FRA 106 was used. Radiation of 1064 nm from a Nd-YAG laser was employed for excitation of solid samples contained in NMR tubes. The back-scattering light, which passed through a Rayleigh filter and a CaF₂-Beamsplitter, was collected on a Ge-diode detector.

The infrared spectra were recorded with a Bruker IFS-25 spectrometer using a nujol suspensions between KBr plates.

UV-visible spectra were recorded using *n*-hexane solutions in a range between 300-700 nm using a Perkin-Elmer UV/VIS/NIR spectrometer Lambda 19.

2.2 Density Functional Theory

The basic notion in Density Functional Theory (DFT) that the energy of an electronic system can be expressed in terms of its density, is almost as old as quantum mechanics and dates back to the early work by Thomas ^[16], Fermi ^[17-18], Dirac ^[19], and Wigner ^[20]. The Hartree-Fock-Slater or X_α method whose origin stem from the solid-state physics, was one of the first DFT-based schemes to be used in studies on systems with more than one atom. The method emerged from the work of J. C. Slater ^[21] who 1951 proposed to represent the exchange-correlation potential by a function which is proportional to the 1/3 power of the electron density. The Thomas-Fermi method and the X_α scheme were at the time of their inceptions considered as useful models based on the notion that the energy of an electronic system can be expressed in terms of its density. A formal proof for this notion was contributed by Hohenberg and Kohn in 1964 ^[22] when they showed that the ground-state energy of an electronic system is uniquely defined by its density, although the exact functional dependence of the energy on density remains unknown. This important theorem has later been extended by Levy ^[23]. Of further importance was the deviation by Kohn ^[24] and Sham of a set of one-electron equations from which, one in principle could obtain the exact electron density and thus the total energy. The main problem in Thomas-Fermi models is that the kinetic energy is represented poorly. The basic idea in the Kohn and Sham (KS) formalism is splitting the kinetic energy functional into two parts, one of which can be calculated exactly, and a small correction term.

Assume for the moment a Hamilton operator of the following form with $0 \leq \lambda \leq 1$.

$$H_\lambda = T + V_{\text{ext}}(\lambda) + \lambda V_{\text{ee}}. \quad (1.18)$$

The V_{ext} operator is equal to V_{ne} for $\lambda=1$, for intermediate λ values, however it is assumed that the external potential $V_{\text{ext}}(\lambda)$ is adjusted so that the same density is obtained for both $\lambda=1$ (the real system) and $\lambda=0$ (a hypothetical system with non-interacting electrons). For the $\lambda=0$ case the exact solution to Schrödinger equation is given as a Slater determinant composed of (molecular) orbitals, ϕ_i , for which the exact kinetic energy functional is given as

$$T_S = \sum_{i=1}^N \langle \phi_i | -\frac{1}{2} \nabla^2 | \phi_i \rangle \quad (1.19)$$

$$\text{with } \rho = \sum_{i=1}^N |\phi_i(r)|^2. \quad (1.20)$$

The key to the Kohn-Sham theory is thus the calculation of the kinetic energy under the assumption of non-interacting electrons (in the same sense as HF orbitals in wave mechanics describe non-interacting electrons) from Eqn (1.19). In reality the electrons are interacting, and Eqn (1.19) does not provide the total kinetic energy. However, just as HF theory provides ~99% of the correct answer, the difference between the exact kinetic energy and that calculated by assuming non-interacting orbitals is small. The remaining kinetic energy is absorbed into an exchange-correlation term, and a general DFT energy expression can be written as

$$E_{\text{DFT}}[\rho] = T_{\text{S}}[\rho] + E_{\text{ne}}[\rho] + J[\rho] + E_{\text{xc}}[\rho]. \quad (1.21)$$

By equating E_{DFT} to the exact energy, this expression may be taken as the definition of E_{xc} , it is the part which remains after subtraction of the non-interacting kinetic energy and the E_{ne} and J potential energy terms.

$$E_{\text{xc}}[\rho] = (T[\rho] - T_{\text{S}}[\rho]) + (E_{\text{ee}}[\rho] - J[\rho]) \quad (1.22)$$

The first parenthesis in Eqn (1.22) may be considered the kinetic correlation energy, while the second contains both exchange and potential correlation energy. One may notice, that the exchange energy E_{x} is by far the largest contributor (> 90 %) to E_{xc} .

The major problem in DFT is deriving suitable formulas for the exchange-correlation term. Assume for the moment that such a functional is available, the problem is then similar to that encountered in wave mechanics HF theory: determine a set of orthogonal orbitals which minimize the energy (the requirement of orthogonal orbitals basically enforces the Pauli principle). Since the $J[\rho]$ (and also $E_{\text{xc}}[\rho]$) functional depends on the total density, a determination of the orbitals involves an iterative sequence. The orbital orthogonality constraint may be enforced by the Lagrange method, again in analogy with the HF method.

$$L[\rho] = E_{\text{DFT}}[\rho] - \sum_{ij}^N \lambda_{ij} [\langle \phi_i | \phi_j \rangle - \delta_{ij}] \quad (1.23)$$

Requiring the variation of L to vanish provides a set of equations involving an effective one-electron operator H_{KS} , similar to the Fock operator.

$$H_{\text{KS}}\phi_i = \sum_j^N \lambda_{ij} \phi_j, \quad (1.24)$$

$$H_{\text{KS}} = -\frac{1}{2}\nabla^2 + V_{\text{eff}}, \quad (1.25)$$

$$V_{\text{eff}}(r) = V_{\text{ne}}(r) + \int \frac{\rho(r')}{|r-r'|} dr' + V_{\text{xc}}(r), \quad (1.26)$$

$$V_{\text{xc}}(r) = \frac{\partial E_{\text{xc}}[\rho]}{\partial \rho(r)}. \quad (1.27)$$

A set of canonical Kohn-Sham (KS) orbitals have been obtained by choosing a unitary transformation which makes the matrix of the Lagrange multiplier diagonal. The resulting pseudo-eigenvalue equations are known as the Kohn-Sham equations.

$$H_{\text{KS}}\phi_i = \varepsilon_i\phi_i \quad (1.28)$$

As a matter of fact, as in the Hartree-Fock (HF) scheme, the KS equation is a pseudo-eigenvalue problem and has to be solved iteratively through a self-consistent field procedure to determine the charge density $\rho(r)$ that corresponds to the lower energy. The self-consistent solution ϕ_i resembles those of the HF equations. Still, one should keep in mind that these orbitals have no physical significance other than in allowing one to constitute the charge density. In spite of the similarity in formal appearance of the HF and KS equations, the latter give in principle the exact solution of the N -electron problem, provided that the correct functional dependence of the exchange-correlation energy E_{XC} with respect to the charge density $\rho(r)$ is available. One may notice, that a wave function for an N -electron system contains $3N$ coordinates, three for each electron (four if spin is included). The electron density is the square of the wave function, integrated over $N-1$ electron coordinates, this only depends on three coordinates, independently of the number of electrons. While the complexity of a wave function increases with the number of electrons, the electron density has the same number of variables, independently of the system size. The „only“ problem is that although it has been proven that each different density yields a different ground-state energy, the functionals connecting these two quantities is not known. And exactly this is the case in DFT: no one knows the correct functional E_{XC} for atoms and molecules. Therefore, approximations have to be made to provide expressions for E_{XC} . In fact, all modern „flavors“ of DFT differ solely in the way the exchange-correlation functional is approximated. The simplest approximation to the exchange-correlation term which is used, is called the Local Density Approximation (LDA). For any small region, the exchange-correlation energy is approximated by that for jellium (jellium is the name given to an homogeneous electron gas) of the same electron density. In other words, the exchange-correlation hole that is modelled is

not the exact one - it is replaced by the hole taken from an electron gas whose density is the same as the local density around the electron. The interesting point about this approximation is that although the exchange-correlation hole may not be represented well in terms of its shape, the overall effective charge is modelled exactly. This means that the attractive potential which the electron feels at its centre is well described. Not only does the LDA approximation work for materials with slowly varying or homogeneous electron densities but in practise demonstrates surprisingly accurate results for a wide range of ionic, covalent and metallic materials. An alternative, slightly more sophisticated approximation is the Generalised Gradient Approximation (GGA) which estimates the contribution of each volume element to the exchange-correlation based upon the magnitude and gradient of the electron density within that element. For more details, it is proposed to look at the following references ^[25-26].

To summarize: The advantage of using DFT calculations is that the Kohn-Sham orbital energies include correlation effects, and thus, orbitals contributions can be directly correlated with total energies. The disadvantage is that the exchange and correlation energy in DFT calculations depend in an unphysical way on the parametrization of the functionals.

2.2.1 Basis Set Effects

2.2.1.1 Definition

A basis set is the mathematical description of the orbitals within a system (which in turn combine to approximate the total electronic wavefunction) used to perform the theoretical calculation. Larger basis sets more accurately approximate the orbitals by imposing fewer restrictions on the locations of the electrons in space. In the true quantum mechanical picture, electrons have a finite probability of existing anywhere in space; this limit corresponds to a infinite basis set expansion.

Historically, the quantum calculations for molecules were performed as LCAO MO, i.e. Linear Combination of Atomic Orbitals-Molecular Orbitals. This means that molecular orbitals are formed as a linear combination of atomic orbitals:

$$\psi_i = \sum_{\mu=1}^n C_{\mu i} \phi_{\mu}, \quad (1.34)$$

where ψ_i is the i -th molecular orbital, $C_{\mu i}$ are the coefficients of linear combination, ϕ_μ is the μ -th atomic orbital, and n is the number of atomic orbitals.

Atomic Orbitals (AO) are solutions of the Hartree-Fock equations for the atom, i.e. wave functions for a single electron in the atom. Anything else is not really an atomic orbital. Some things are similar though, and there is a lot of confusion in the terminology used. Later, the term atomic orbital was replaced by „basis function“ or „contraction,“ when appropriate. Early, the Slater Type Orbitals (STO's) were used as basis functions due to their similarity to atomic orbitals of the hydrogen atom. They are described by the function depending on spherical coordinates:

$$\phi_i(\zeta, n, l, m; r, \theta, \phi) = Nr^{n-1}e^{-\zeta r}Y_{lm}(\theta, \phi), \quad (1.35)$$

where N is a normalization constant, ζ is called „exponent“. The r , θ , and ϕ are spherical coordinates, and Y_{lm} is the angular momentum part (function describing „shape“). The n , l , and m are quantum numbers: principal, angular momentum, and magnetic; respectively.

Slater-type orbitals represent the real situation for the electron density in the valence region and beyond, but are not so good nearer to the nucleus. Many calculations over the years have been carried out with Slater-type orbitals (STOs), particularly for diatomic molecules. However, it soon became clear that there was a practical problem. It is very difficult to evaluate the necessary integrals over these STOs when the orbitals in the integral are centred on three or four different atoms. An immense amount of effort has been put into this problem of integral evaluation over STOs, but still remains a problem. Accurate results are just about possible, but they are very time-consuming. In the 1950s, Frank Boys from Cambridge in the UK, suggested an alternative which has been widely taken up. He pointed out that integrals over Gaussian-type functions which contain the exponential $\exp(-r^2)$, rather than the $\exp(-r)$ of the STOs, are very easy to evaluate. Of course they do not represent the electron density of the real situation as well as the STOs, but the shape of the STO function can be approximated by summing up a number of GTOs with different exponents and coefficients. Even if 4 or 5 GTO's have been used to represent a STO, the integrals will be calculated much faster than if the original STOs had been employed. The GTO (called also cartesian gaussian) is expressed as:

$$g(\alpha, l, m, n; x, y, z) = Ne^{-\alpha r^2} x^l y^m z^n, \quad (1.36)$$

where N is a normalization constant, α is called „exponent“. The x , y , and z are cartesian coordinates. The l , m , and n **are not quantum numbers** but simply integral exponents at cartesian coordinates. $r^2 = x^2 + y^2 + z^2$.

Calling gaussians GTOs is probably a misnomer, since they are not really orbitals. They are simpler functions. In recent literature, they are frequently called gaussian primitives. The main difference is that r^{n-1} , the preexponential factor, is dropped, the r in the exponential function is squared, and angular momentum part is a simple function of cartesian coordinates. The absence of r^{n-1} factor restricts single gaussian primitive to approximating only 1s, 2p, 3d, 4f ... orbitals. It was done for practical reasons, namely, for fast integral calculations. However, combinations of gaussians are able to approximate correct nodal properties of atomic orbitals by taking them with different signs. Following gaussian functions are possible:

$$\begin{aligned}1s &= Ne^{-\alpha r^2} \\2p_x &= Ne^{-\alpha r^2} x \\2p_y &= Ne^{-\alpha r^2} y \\2p_z &= Ne^{-\alpha r^2} z \\3d_{xx} &= Ne^{-\alpha r^2} x^2 \\3d_{xy} &= Ne^{-\alpha r^2} xy \\3d_{xz} &= Ne^{-\alpha r^2} xz \\3d_{yy} &= Ne^{-\alpha r^2} y^2 \\3d_{yz} &= Ne^{-\alpha r^2} yz \\3d_{zz} &= Ne^{-\alpha r^2} z^2 \\4f_{xxx} &= Ne^{-\alpha r^2} x^3 \\4f_{xxy} &= Ne^{-\alpha r^2} x^2y \\&\text{etc.}\end{aligned}$$

Gaussian primitives are usually obtained from quantum calculations on atoms (i.e. Hartree-Fock or Hartree Fock plus some correlated calculations, e.g. CI). Typically, the exponents are varied until the lowest total energy of the atom is achieved (Clementi et al., 1990). In some cases, the exponents are optimized independently. In others, the exponents are related to each other by some equation, and parameters in this equation are optimized (e.g. even-tempered or „geometrical“ and well-tempered basis sets). The primitives so derived describe isolated atoms and cannot accurately describe deformations of atomic orbitals brought by the presence of other atoms in the molecule. Basis sets for molecular calculations are therefore frequently

augmented with other functions (see below). For molecular calculations, these gaussian primitives have to be contracted, i.e., certain linear combinations of them will be used as basis functions. The term contraction means „a linear combination of gaussian primitives to be used as basis function.“ Such a basis function will have its coefficients and exponents fixed. The contractions are sometimes called Contracted Gaussian Type Orbitals (CGTO). The way in which contractions are derived is not easy to summarize. Moreover, it depends upon the intended use for the basis functions. Some basis sets are good for geometry and energies, some are aimed at properties (e.g. polarizability), some are optimized only with Hartree-Fock in mind, and some are tailored for correlated calculations. Finally, some are good for anion and other for cations and neutral molecules. For some calculations, a good representation of the inner (core) orbitals is necessary (e.g. for properties required to analyse NMR spectrum), while other require best possible representation of valence electrons.

2.2.1.2 Minimal Basis Sets

Minimal basis sets contain the minimum number of basis functions needed for each atom, as in these examples:

H: 1s

C: 1s, 2s, 2p_x, 2p_y, 2p_z

Minimal basis sets use fixed-size atomic-type orbitals. The STO-3G basis set is a minimal basis set (although it is not the smallest basis set). It uses three gaussian primitives per basis function, which accounts for the „3G“ in its name. „STO“ stands for „Slater-type orbitals,“ and the STO-3G basis set approximates Slater orbitals with gaussian functions.

2.2.1.3 Split Valence Basis Sets

The first way that a basis set can be made larger is to increase the number of basis functions per atom. Split valence basis sets, such as 3-21G and 6-31G, have two (or more) sizes of basis function for each valence orbital. For example, hydrogen and carbon are represented as:

H: 1s, 1s'

C: 1s, 2s, 2s', 2p_x, 2p_y, 2p_z, 2p_x', 2p_y', 2p_z'

where the primed and unprimed orbitals differ in size. The double zeta basis sets, such as the Dunning-Huzinaga basis set (D95), form all molecular orbitals from linear combinations of two sizes of functions for each atomic orbital.

2.2.1.4 Polarized Basis sets

Split valence basis sets allow orbitals to change size, but not to change shape. Polarized basis sets remove this limitation by adding orbitals with angular momentum beyond what is required for the ground state to the description of each atom.

2.2.1.5 Diffuse Functions

Diffuse functions are large-size versions of s- and p-type functions (as opposed to the standard valence-size functions). They allow orbitals to occupy a larger region of space. Basis set with diffuse functions are important for systems where electrons are relatively far from nucleus: molecules with lone pairs, anions and other systems with significant negative charge, systems in their excited states, system with low ionization potentials, descriptions of absolute acidities, and so on.

2.2.1.6 Effective Core Potentials (ECP) ^[27]

It was known for a long time that core (inner) orbitals are in most cases not affected significantly by changes in chemical bonding. This prompted the development of Effective Core Potential (ECP) or Effective Potentials (EP) approaches, which allow treatment of inner shell electrons as if they were some averaged potential rather than actual particles. ECP's are not orbitals but modifications to a hamiltonian, and as such very efficient computationally. Also, it is very easy to incorporate relativistic effects into ECP ^[28], while all-electron relativistic computations are very expensive. The relativistic effects are very important in describing heavier atoms, and luckily ECP's simplify calculations and at the same time make them more accurate with popular non-relativistic ab initio packages.

Chapter 3

Vibrational spectroscopy studies and DFT calculations on square-planar rhodium(I) complexes

3.1 Vinylidene and carbonyl rhodium(I) complexes $trans-[RhX(L)(PiPr_3)_2]$ ($L = C=CH_2$ and CO ; $X = F, Cl, Br, I$ and $C\equiv CPh$) and $trans-[RhX(=C=CHPh)(PiPr_3)_2]$ ($X = F, Cl, Br, I, CH_3$ and $C\equiv CPh$)

The parent ligands, $C=CH_2$, is not only an isomer of acetylene but also, and perhaps more importantly, isoelectronic to CO and $C\equiv NH$. Since various reports^[29] seem to indicate that vinylidene, carbon monoxide and isonitrile have similar donor-acceptor abilities, we thought it of interest to investigate this similarity by means of Raman and infrared spectroscopy. While the metal-carbon bond vibrational modes have been mainly studied in carbonyl complexes^[30-32], very few studies have been carried out in transition-metal carbene,

carbyne ^[33-42] or isonitrile complexes ^[43-44]. In this context, the $\nu(\text{RhC})$ stretching mode has been characterized using isotopic substitution and DFT calculations. The assignment of the $\nu(\text{MC})$ stretching mode in carbene and carbyne complexes is relevant because it is an easily available source of information about the bonding in these types of compounds. Moreover, this allows us to study the *trans* influence* in a series of square planar vinylidene and carbonyl rhodium(I) complexes. The assignment of the $\nu(\text{RhC})$ stretching mode has been extended to the ethylene and isonitrile complexes, which are discussed in the following parts.

* *The term „trans influence“ has been applied to describe the tendency of a ligand to weaken the bond trans to itself. The trans influence is an equilibrium phenomenon and is to be distinguished from the trans effect, which describes the tendency of a ligand to influence the rate of ligand substitution of a ligand trans to itself.*

The *trans* influence is a well established phenomenon in transition metal chemistry that has received a great deal of both experimental and theoretical study ^[45-52]. It can be detected in many ways. The most obvious is the observation of bond lengths and geometrical distortions in the crystal structure. Similarly, bond weakening/lengthening may be detected by observing the values of vibrational modes and NMR coupling constants ^[45].

The compounds studied are *trans*- $[\text{RhF}(\text{C}=\text{CH}_2)(\text{P}i\text{Pr}_3)_2]$ (**1**), *trans*- $[\text{RhX}(\text{C}=\text{C}^{13}\text{CH}_2)(\text{P}i\text{Pr}_3)_2]$ with X = F (**2**), Cl (**3**), Br (**4**) and I (**5**); *trans*- $[\text{RhX}(\text{C}=\text{CHPh})(\text{P}i\text{Pr}_3)_2]$ with X = F (**6**), Cl (**7**), Br (**8**), I (**9**), CH₃ (**10**) and PhC \equiv C (**11**); and *trans*- $[\text{RhX}(\text{CO})(\text{P}i\text{Pr}_3)_2]$ with X = F (**12**), Cl (**13**), Br (**14**), I (**15**) and PhC \equiv C (**16**). The results have been rationalized with the support of DFT calculations on model compounds where the bulky $\text{P}i\text{Pr}_3$ ligands are replaced by PMe_3 . This project was within the framework of the *SFB 347* and was a cooperation with the work group of Prof. Werner. The investigated compounds were synthesized by Juan Gil-Rubio and Berta Callejas-Gaspar ^[53].

3.1.1 Experimental and theoretical structures

DFT calculations have been carried out for the model compounds *trans*- $[\text{RhX}(\text{L})(\text{PMe}_3)_2]$ (L = C=CH₂; X = F, Cl, Br, I, CH₃ and L = CO; X = F, Cl, Br, I, C \equiv CPh) and *trans*- $[\text{RhX}(\text{C}=\text{CHPh})(\text{PMe}_3)_2]$ (X = F, Cl, CH₃ and C \equiv CPh). The isopropyl groups of the existing complexes have been substituted by methyl groups in order to reduce the computation time. The DFT calculations were performed using Gaussian 98 ^[54] and Becke's 1988 exchange functional ^[55] in combination with the Perdew-Wang 91 gradient-corrected correlation functional (BPW91) ^[56]. The Los Alamos effective core potential plus double zeta

(LANL2DZ)^[57-60] was employed for rhodium, whereas the Dunning/Huzinaga full double zeta basis set with or without polarization and diffuse function (D95, D95+(d) and D95+(3df,2p)) for P, C, H, F, Cl and O atoms (DFT1-3) or 6-31+G(d) for P, C, H, and O, 6-311+G(d) for Br and 3-21G(d) for I (DFT4) was used. In addition, the quasi relativistic energy-adjusted effective core potential (ECP) for the 28 core electrons of rhodium in conjunction with a contracted 6s5p3d basis (311111/22111/411) for the valence orbitals^[61] and the 6-31+G(d) Pople basis set for the other atoms was employed for the calculation of the model compounds *trans*-[RhF(R)(PMe₃)₂] (R = C=CH₂, CO, C₂H₄) and is denoted DFT5.

The methods described above, were applied to a molecular geometry without symmetry restrictions and to a geometry that was restricted to C_{2v} or C_s symmetry. Analytical harmonic vibrational modes have also been calculated for all the structures to confirm that a local minimum on the potential energy surface was found. Using the C_{2v} symmetry, the rotational conformations of the phosphine groups (estimated barrier of rotation < 2.09 kJ/mol) caused difficulties with convergence and the optimization yielded structures with two low imaginary harmonic wavenumbers corresponding to the M-PR₃ rotations which indicated a saddle point. The restriction to C_s symmetry caused also difficulties with convergence of the geometry due to the same reason. After many attempts to circumvent this problem, structures without imaginary harmonic wavenumbers were obtained. One may notice that for both C₁ and C_s symmetries, very similar energies were found (the calculated energies for *trans*-[RhF(=C=CH₂)(PMe₃)₂] using the BPW91/LANL2DZ method (DFT1) were -593.30198 and -593.30101 hartree, respectively). Moreover, one may notice that the C_{2v} symmetry of the rhodium complexes in crystalline state is broken. Due to this, the calculations were performed without symmetry restrictions for all the other model compounds.

The phosphine ligands are slightly bent toward the halogenid atom probably owing to the electrostatic attraction between the negatively charged halogenid and the positively charged phosphorus atoms. A similar bending has been observed in the crystal structure of *trans*-[RhF(CO)(PPh₃)₂]. The computed structures are distorted square-planar with the phosphines in an eclipsed conformation. Theoretical calculations predict a small energy difference between the staggered and eclipsed conformations, (< 2.09 kJ/mol) with the eclipsed conformation more stable, which is likely to be insignificant relative to packing forces in the crystal structure.

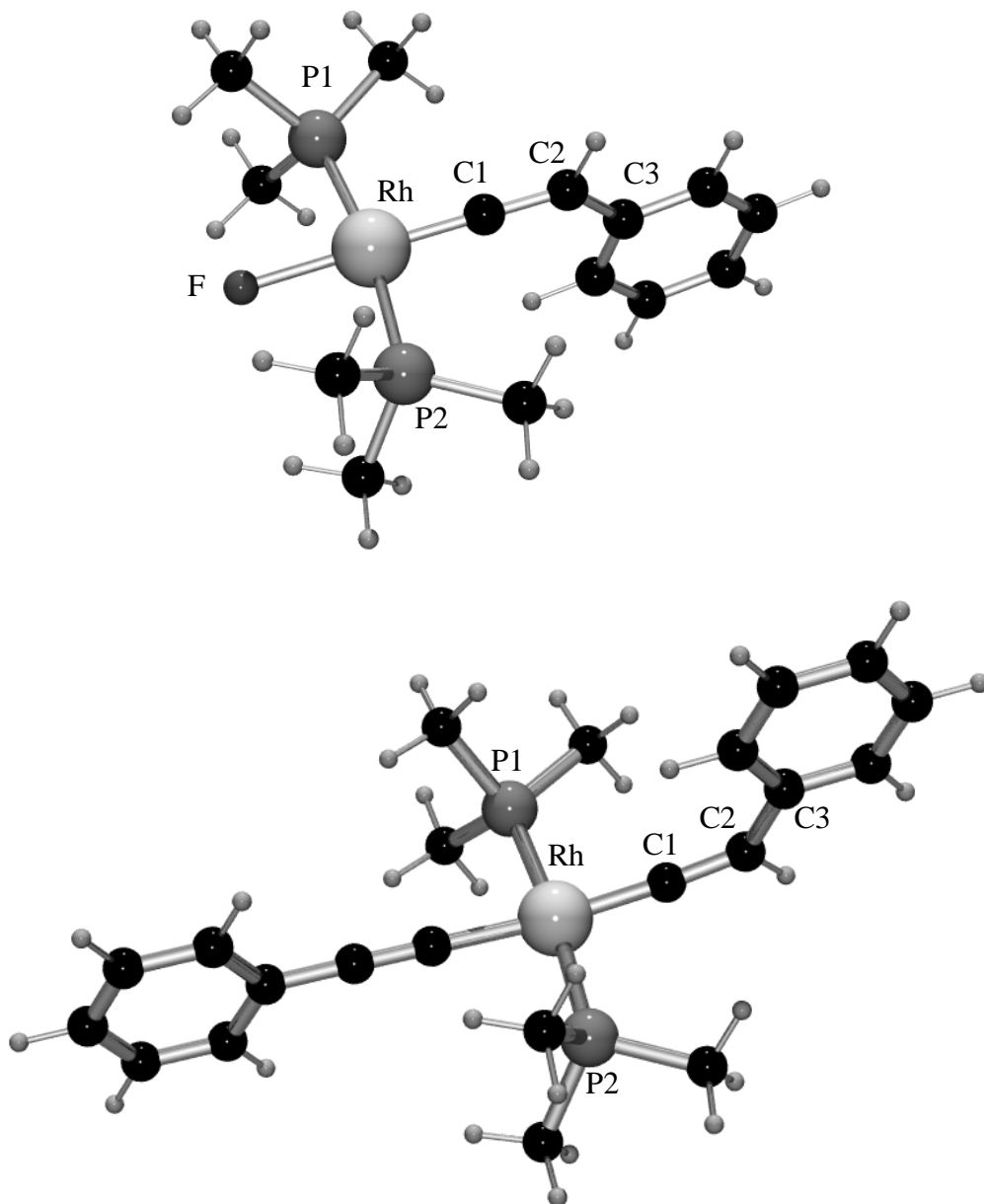


Figure 5. Optimized structures of *trans*-[RhF(=C=CHPh)(PMe₃)₂] and *trans*-[Rh(C≡CPh)(=C=CHPh)(PMe₃)₂] using the BPW91/LANL2DZ (DFT1) method.

Furthermore, the experimental values of the P1-Rh-P2 angle are larger than the computed values for our model compounds. This may be due in part to the staggered conformation of the synthesized complexes and the bulky nature of the *PiPr*₃ and *PPh*₃ ligands. However, the P1-Rh-P2 angle differs significantly from 180° for all computed and theoretical structures.

The structural parameters of the model compounds *trans*-[RhX(=C=CHR)(PMe₃)₂] (X = F, Cl, Br, I, CH₃, PhC≡C; R = H, Ph) and *trans*-[RhX(CO)(PMe₃)₂] (X = F, Cl, Br, I, PhC≡C) which were calculated using the DFT1-5 methods, are summarized in Tables 1-3.

An POV-Ray^[62] draw of the calculated structure of *trans*-[RhX(=C=CHPh)(PMe₃)₂] (X = F, PhC≡C) and *trans*-[RhX(=C=CH₂)(PMe₃)₂] (X = F, CH₃) is shown in Figures 5 and 6.

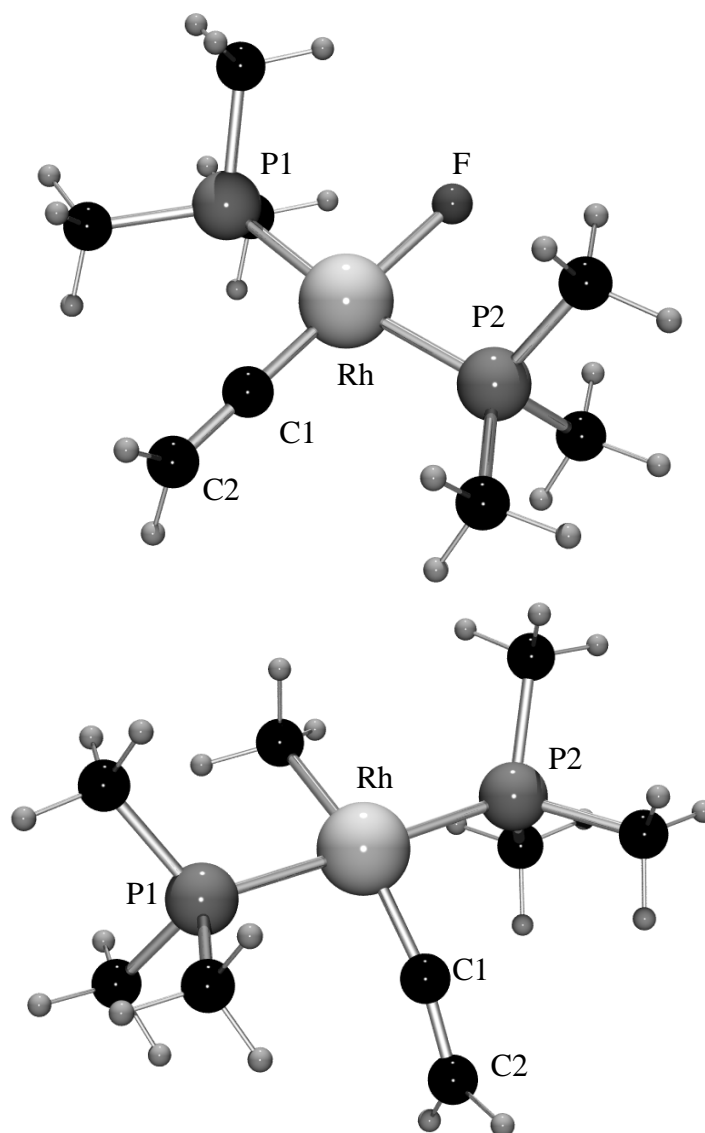


Figure 6. Optimized structures of *trans*-[RhF(=C=CH₂)(PMe₃)₂] and *trans*-[RhMe(=C=CH₂)(PMe₃)₂] using the BPW91/LANL2DZ (DFT1) method.

As expected, the Rh-C1-C2 linkage of the vinylidene halide complexes is almost linear and the plane which contains the vinylidene ligand is perpendicular to the main plane containing the atoms Rh, P1, P2 and X (the dihedral angle between the main planes defined by the atoms [Rh, C1, C2, H1, H2] and [Rh, P1, P2, X] is 90.0°). This structural feature is in agreement with the formation of a π bond between Rh and C1 and confirms the formal analogy between allenes and vinylidene metal complexes. The calculated Rh-F and Rh-P bond distances are similar to the experimental values found in the related fluororhodium complexes *trans*-[RhCl(=C=CHMe)(PiPr₃)₂]^[63] and *trans*-[RhF(CO)(PPh₃)₂]^[64].

Table 1. Selected bond lengths (pm) and angles (degrees) calculated for the model compounds *trans*-[RhX(=C=CH₂)(PMe₃)₂] (X = F, Cl, Br, I, CH₃) together with the experimental values found in *trans*-[RhCl(=C=CHMe)(P*i*Pr₃)₂].

		<i>trans</i> -[RhX(=C=CH ₂)(PMe ₃) ₂]										<i>trans</i> - [RhCl(=C=CHMe)(P <i>i</i> Pr ₃) ₂]			
		X = F		X = Cl		X = Br		X = I		X = CH ₃					
		Bond lengths (pm)													
		DFT1	DFT2	DFT3	DFT5	DFT2	DFT3	DFT4	DFT4	DFT1	DFT4	DFT1	DFT4	DFT5	Exp. ^a
Rh-P1		238.5	234.4	232.1	232.9	235.5	232.9	234.9	235.2	240.6	235.3	238.0	232.6	231.6	234.4(2)
Rh-P2		238.5	234.4	232.1	232.9	235.5	232.9	234.9	235.2	240.6	235.3	238.0	232.6	231.6	234.2(2)
Rh-X		205.5	206.1	204.6	203.9	244.5	242.1	244.2	257.2	278.5	275.7	214.0	214.8	214.3	236.6(2)
Rh-C1		182.0	181.0	180.5	180.4	181.6	181.4	181.7	181.9	182.9	182.4	187.7	186.7	185.9	177.5(6)
C1-C2		134.1	133.3	132.7	133.0	133.1	132.5	132.7	132.7	133.9	132.6	134.9	133.4	133.5	132.0(1)
		Bond angles (°)													
		DFT1	DFT2	DFT3	DFT5	DFT2	DFT3	DFT4	DFT4	DFT1	DFT4	DFT1	DFT4	DFT5	Exp. ^a
X-Rh-Cl		179.4	180.0	179.4	179.4	179.8	179.8	179.9	180.0	180.0	179.9	157.2	155.8	156.0	175.8(2)
P1-Rh-X		84.6	85.2	85.5	85.4	87.35	87.5	87.3	88.1	88.7	88.8	89.3	89.1	89.5	91.9(1)
P1-Rh-Cl		95.4	94.8	94.5	94.6	92.6	92.5	92.7	91.9	91.3	91.2	90.7	90.9	91.0	88.2(2)
P2-Rh-X		84.6	85.2	85.5	85.4	87.35	87.5	87.3	88.1	88.7	88.8	89.3	89.1	89.6	91.2(1)
P2-Rh-Cl		95.4	94.8	94.5	94.6	92.6	92.5	92.7	91.9	91.3	91.2	90.7	90.9	90.9	89.1(2)
Rh-C1-C2		179.6	179.4	179.6	179.6	179.9	179.9	179.9	180.0	180.0	179.9	158.6	157.9	159.0	177.9(6)

^aReference 63.

Table 2. Selected bond lengths (pm) and angles (degrees) calculated for the model compounds *trans*-[RhX(=C=CHPh)(PMe₃)₂] together with the experimental values found in *trans*-[RhCl(=C=CHMe)(P^{*t*}Pr₃)₂].

	<i>trans</i> -[RhX(=C=CHPh)(PMe ₃) ₂]			<i>trans</i> - [RhCl(=C=CHMe)(P ^{<i>t</i>} Pr ₃) ₂]		
	X = F	X = Cl	X = CH ₃	X = PhC≡C ^a		
	Bond lengths (pm)					
	DFT1	DFT2	DFT1	DFT5	DFT1	Exp. ^b
Rh-P1	239.0	234.9	236.0	238.6	239.3	234.4(2)
Rh-P2	239.0	234.9	236.0	238.6	239.3	234.2(2)
Rh-X	205.2	205.3	243.9	213.6	203.5	236.6(2)
Rh-C1	181.3	180.4	181.1	187.1	186.4	177.5(6)
C1-C2	135.1	134.3	134.1	136.0	135.0	132.0(1)
C2-C3	147.8	147.3	147.4	147.9	148.0	
	Bond angles (°)					
	DFT1	DFT2	DFT2	DFT1	DFT1	Exp. ^b
X-Rh-Cl	179.4	179.4	179.7	154.9	171.4	175.8(2)
P1-Rh-X	84.5	85.3	87.6	89.2	87.3	91.9(1)
P1-Rh-Cl	95.5	94.7	92.4	90.9	92.7	88.2(2)
P2-Rh-X	84.5	85.3	87.6	89.3	87.3	91.2(1)
P2-Rh-Cl	95.5	94.7	92.4	91.3	92.7	89.1(2)
Rh-Cl-C2	179.0	179.8	179.1	156.2	174.2	177.9(6)

^ad(C≡C) = 126.0 pm ^bReference 63.

It is striking that the DFT1 method shows a high accuracy for the Rh-F bond lengths which is certainly fortuitous, hence this method fails in the calculation of the Rh-X (X = Cl, Br and I) bond lengths. The computed Rh-C1 distances of the model compounds *trans*-[RhX(=C=CHR)(PMe₃)₂] (X = F, Cl, Br, I; R = H, Ph) and *trans*-[RhF(CO)(PMe₃)₂] are comparable with the Rh-C bond lengths in the fluoro carbonyl rhodium(I) compound *trans*-[RhF(CO)(PPh₃)₂] (179.6(3) pm)^[64] and in *trans*-[RhCl(=C=CHMe)(P*i*Pr₃)₂] (177.5(6) pm)^[63]. Thus, the BPW91 DFT-method with the Los Alamos pseudopotential plus double zeta (LANL2DZ) for rhodium in combination with the Dunning/Huzinaga full double zeta (D95) or the Pople basis sets in combination with polarization and diffuse functions gave the best results for the series of the vinylidene and carbonyl halide complexes.

The agreement between the calculated and the experimental bond distances and bond angles for analogous compounds was quite good (see Tables 1-3). The addition of polarization and diffuse functions to the small basis set LANL2DZ provides in general better structural parameters, particularly for the Rh-P bond lengths (Table 3) and improve significantly the resulting $\nu(\text{CO})$ vibrational modes (Table 10). One may notice that the good agreement of the BPW91/LANL2DZ vibrational modes with the experimental data is most likely due to favorable error cancellation. For the model compounds *trans*-[RhF(=C=CHR)(PMe₃)₂] (R = H, Ph) and *trans*-[RhF(CO)(PMe₃)₂], the Rh-F distances were better reproduced by the DFT1 and DFT3 methods, with values around 205 pm, which are very close to the experimental data found in *trans*-[RhF(CO)(PPh₃)₂] (204.6(2) pm). Unlike, the Rh-C and Rh-P distances were closer to the experimental values when the DFT2, DFT3 or DFT5 methods were used.

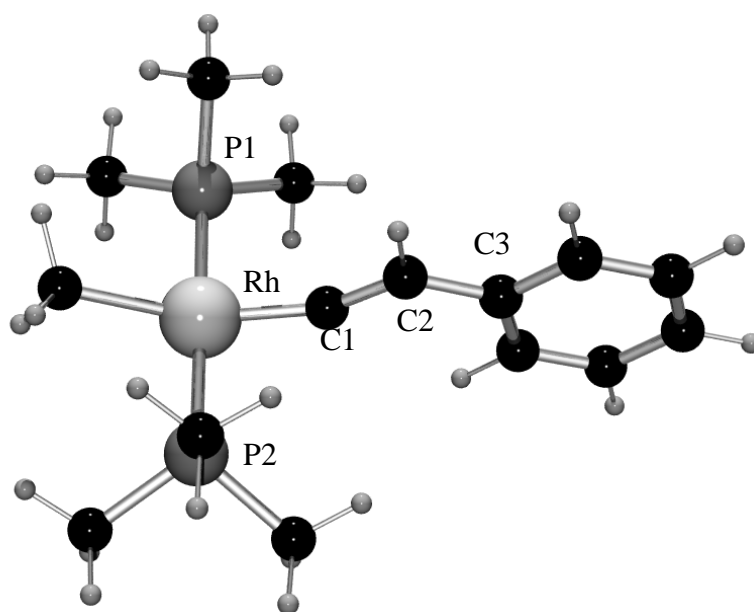


Figure 7. Optimized structure of *trans*-[RhMe(=C=CHPh)(PMe₃)₂] using the DFT2 method.

The calculated structure of *trans*-[Rh(C≡CPh)(=C=CHPh)(PMe₃)₂] (Figure 5; Table 2) with the small basis LANL2DZ (DFT1) was acceptable but for the minimum energy structure of *trans*-[RhMe(=C=CHR)(PMe₃)₂] (R = H or Ph) (Figure 6; Tables 1-2), unexpectedly X-Rh-C1 (157.2°) and Rh-C1-C2 (158.6°) bond angles have been obtained. The freezing of both the X-Rh-C1 (X = CH₃) and Rh-C1-C2 bond angles to 180° leads to a linear structural arrangement with one imaginary harmonic wavenumber corresponding to a C-Rh-C-C bending mode indicating a saddle point. The energy difference between both structures was less than 6 kJ/mol. However, the Rh-C bond lengths, which have been calculated around 214 pm for the model compounds *trans*-[RhMe(=C=CHR)(PMe₃)₂] (R = H, Ph) (Tables 1 and 2), agree very well with the axial Rh-CH₃ bond measured at 210.2(3) pm for the rhodium(III) complex *cis,cis*-[Rh(CH₃)₂(I)(CO)(dmb)]^[66].

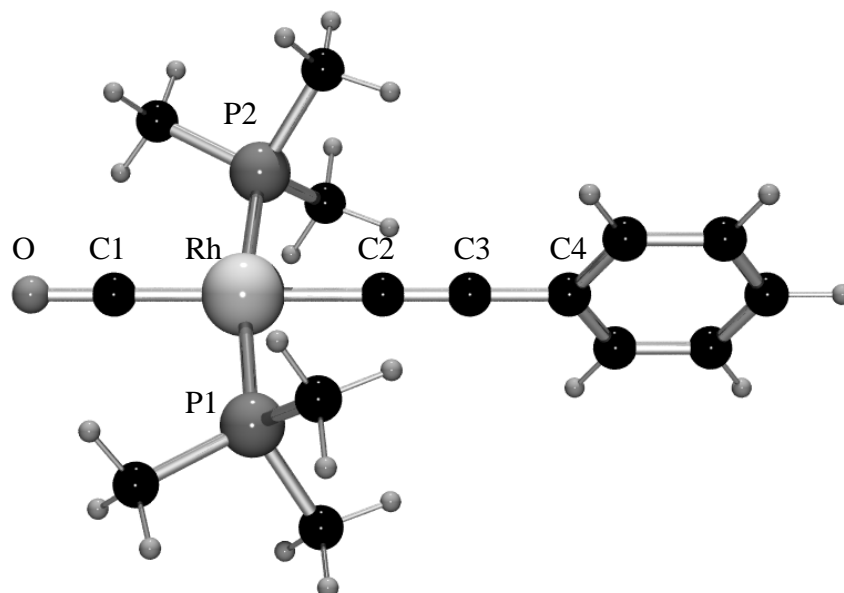


Figure 8. Optimized structure of *trans*-[Rh(C≡CPh)(CO)(PMe₃)₂] using the BPW91/LANL2DZ+(d) (DFT2) method.

The POV-Ray^[62] draw of the calculated structure of *trans*-[Rh(C≡CPh)(CO)(PMe₃)₂] using the BPW91/LANL2DZ+(d) (DFT2) method is depicted in Figure 8 and their structural parameters are presented in Table 3 together with the experimental values measured for *trans*-[Rh(C≡CPh)(CO)(PPh₃)₂]^[65]. The theoretical results agree also very well with the experimental ones, with the exception of the Rh-C2-C3 and C2-C3-C4 angles. Whereas, the calculated values indicated a linear structure for the model compound *trans*-[Rh(C≡CPh)(CO)(PMe₃)₂] (180°), the experimental ones (171.5(6)° and 174.6(8)°, respectively) show for *trans*-[Rh(C≡CPh)(CO)(PPh₃)₂] a slightly distorted structure^[65].

The alkynyl ligand bonded to the rhodium center shows negligible elongation of the C≡C triple bond or shortening of the Rh-C bond, indicating only a small contribution from a vinylidene structure for the ligand ($M=C=C^+-Ph$). One may notice that the computational results indicate that the Rh-C and the C-O bond lengths are coupled as expected: the shorter the Rh-C bond length, the longer the C-O bond distance.

The experimental results for the alkynyl and fluoro complexes are consistent with this trend. It is well-known that the transfer of electrons on to the metal atom is possible via $\pi(p-d)$ interaction for the halogen ligands and that the rhodium atom reduces any increase of electron density via the π -back bonding capacity of the CO ligand. The phenylalkynyl, being a strong σ -donor or a poor π -donor ligand, few of such π -interaction with non-bonding d orbitals of the metal is possible. This reduces the amount of electrons transferred to the anti-bonding π -orbital of the CO *trans* to the ligand. Hence, one would expect a shorter C-O bond length for the phenylalkynyl than for the fluoro complex. Indeed, the C-O bond distance has been determined to be 110.7(8) and 115.1(4) pm for *trans*-[RhX(CO)(PPh₃)₂] with X = C≡CPh and F, respectively (Table 3). The same trend has been observed for the vinylidene complexes.

3.1.2 NBO and MO calculations

The still very popular and widespread Mulliken population analysis^[67] has the disadvantage that the results are unduly sensitive to the basis set and that calculated population can have unphysical negative numbers. It seems that the Mulliken analysis has been replaced by the superior NBO method, which is quite robust toward changing the basis set and which can be used for HF and correlated wave functions as well as for DFT methods. Due to this, the Natural Population Analysis (NPA)^[68] resulting from NBO calculations were performed for the model compounds *trans*-[RhX(=C=CH₂)(PMe₃)₂] (X = F, Cl, Br, I and CH₃) and *trans*-[RhX(CO)(PMe₃)₂] (X = F, Cl, Br and I). The resulting Natural Population Analysis (NPA) gave the partial charges represented in Tables 4 and 5.

The energies of the molecular orbitals for the model compounds *trans*-[RhX(L)(PMe₃)₂] (L = C=CH₂, X = F, Cl, Br, I and Me; L = CO, X = F, Cl, Br, I) were calculated with DFT1 and DFT4. The geometries of the LUMO and HOMO of the vinylidene and carbonyl compounds with X = F are depicted in Figure 9.

The LUMO of the vinylidene complex is a combination of the $p_z(F)$, $d_{xz}(Rh)$ and $p_z(C_2)$ orbitals, the contribution of the $p_z(\beta-C)$ orbital being the most important. For the carbonyl complex, the LUMO is a combination of $p_z(CO)$ and Rh π -orbitals. The HOMO is mainly

composed by the d_z^2 orbital of Rh in both complexes. The shapes of the HOMO and LUMO do not change along the series of compounds involved in the calculation with the exception of the methyl vinylidene complex (see Figure 9).

Table 4. Partial charges (in e) on selected atoms of the model complexes *trans*-[RhX(=C=CH₂)(PMe₃)₂] determined by Natural Population Analysis.

	X	Rh	C_α	C_β	Method
X = F	-0.65	+0.03	+0.04	-0.68	DFT1
	-0.71	+0.01	+0.11	-0.75	DFT4
X = Cl	-0.59	-0.07	+0.05	-0.66	DFT1
	-0.61	-0.10	+0.12	-0.74	DFT4
X = Br	-0.57	-0.09	+0.05	-0.66	DFT1
	-0.55	-0.15	+0.11	-0.74	DFT4
X = I	-0.54	-0.11	+0.04	-0.66	DFT1
	-0.49	-0.15	+0.11	-0.74	DFT4
X = CH₃	-1.02 ^a	-0.06	-0.07	-0.67	DFT1
	-1.03 ^a	-0.09	+0.005	-0.75	DFT4

DFT1: BPW91/LANL2DZ for all atoms. DFT4: LANL2DZ on Rh, 6-311+G(d) on F, Cl, Br, 3-21G(d) on I and 6-31+G(d) on H, P, C.

^a Charge on the carbon atom of the methyl group.

Table 5. Partial charges q on selected atoms of the model complexes *trans*-[RhX(CO)(PMe₃)₂] determined by Natural Population Analysis.^a

	X	Rh	C^b	O
X = F	-0.64	-0.05	+0.42	-0.50
X = Cl	-0.58	-0.19	+0.45	-0.49
X = Br	-0.56	-0.21	+0.45	-0.48
X = I	-0.52	-0.23	+0.44	-0.48

^a BPW91/LANL2DZ for all atoms was used (DFT1).

^b Charge on the carbon atom of the CO ligand.

Similar atomic orbital combinations for the LUMO and HOMO were obtained by Cauletti and coworkers for *trans*-[RhCl(=C=CH₂)(PMe₃)₂] using DV-X α calculations^[69]. However, the calculated MO energies with the DFT1-4 methods (Table 6) are about 1 eV smaller than those using DV-X α . The reason for this difference could be due to the fact that the DV- α calculations were performed without correlation functional in contrast to the exchange and gradient-corrected correlation functional (BPW91) used in this study. The calculated energies with the DFT1 method were higher than those calculated using the DFT2-4 methods, which gave very similar results. However, for the vinylidene complexes the resulting difference $\Delta E(\text{LUMO-HOMO})$ is nearly independent on the method used. For the carbonyl compounds, the calculated differences between the LUMO and the HOMO using DFT1 were 0.2-0.3 eV smaller than those calculated with the DFT2-4 methods. The calculated orbital energies for the phenyl-substituted vinylidenes *trans*-[RhX(=C=CHPh)(PMe₃)₂] were lower than in the related complexes containing the C=CH₂ ligand. The calculated difference $\Delta E(\text{LUMO-HOMO})$ for the model compounds *trans*-[RhX(=C=CH₂)(PMe₃)₂] is in fair agreement with the energies of the lowest-energy absorption of **2-11** in the visible region and decreases also in the order F > Cl > Br > I for **2-5**, and F > CH₃ > Cl > Br > I > C \equiv CPh for **6-11** (Table 6).

For the methyl complex, the LANL2DZ method gave a value $\Delta E(\text{LUMO-HOMO})$ in the minimum energy structure which also agrees with the spectroscopic data, despite the unusual bond angle C-Rh-C of 157.2°. In contrast, the linear structure gives a $\Delta E(\text{LUMO-HOMO})$ of 1.81 eV (DFT1) which differs with the observed trend of the energies of the absorption maxima in the visible region.

For the carbonyl compounds, the calculated energy differences between LUMO-HOMO and the energies of the observed absorption maxima both follow the same trend as in the case of the vinylidene complexes, although the difference between the calculated and the experimental energies is larger. Since the HOMO is mainly located on Rh and the LUMO mainly on the vinylidene or partially on the carbonyl ligand, the corresponding absorptions could be classified as metal-to-ligand charge transfer bands. Also the absorptions in the visible spectra of the related compounds *trans*-[RhX(CY)(PR₃)₂] (Y = O^[70], Y = S^[71]) have been attributed to MLCT transitions.

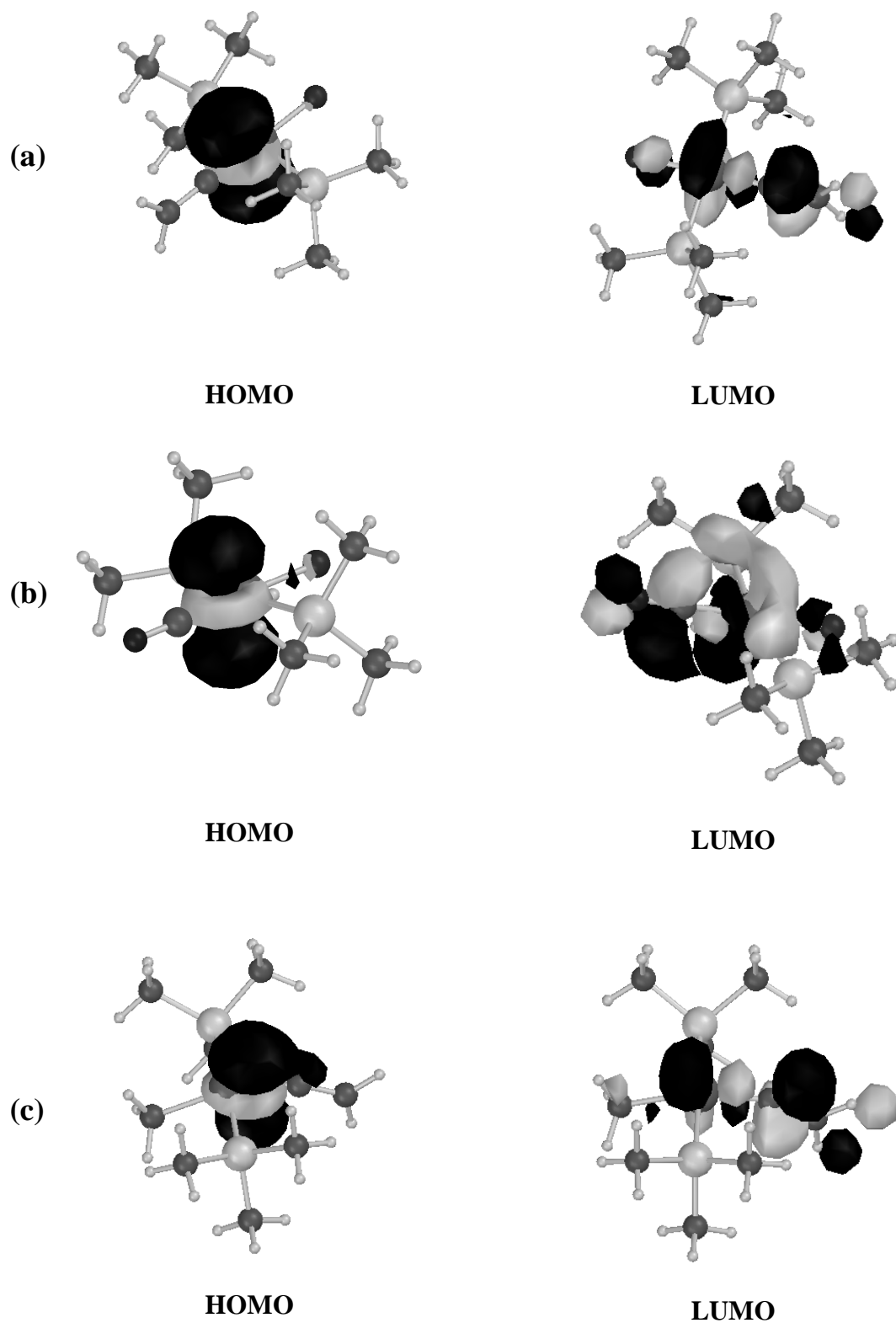


Figure 9. Representation of the calculated LUMO's and HOMO's of *trans*-[RhF(=C=CH₂)(PMe₃)₂] (a), *trans*-[RhF(CO)(PMe₃)₂] (b) and *trans*-[RhMe(=C=CH₂)(PMe₃)₂] (c) (isocontour = 0.04).

Table 6. Energies of the molecular orbitals, orbital energy differences and energies of the lowest energy visible absorption maxima (all in eV) for vinylidene and carbonyl rhodium complexes.

Compound	ethod	E _{LUMO}	E _{HOMO}	E _{LUMO-HOMO}	E _{max} (compound) ^a
<i>trans</i> -[RhF(=C=CH ₂)(PMe ₃) ₂]	DFT1	-1.99	-4.15	2.16	2.37 (2)
	DFT2	-2.23	-4.39	2.16	
	DFT3	-2.21	-4.40	2.19	
	DFT4	-2.25	-4.41	2.16	
<i>trans</i> -[RhF(=C=CHPh)(PMe ₃) ₂]	DFT1	-2.24	-4.26	2.02	2.25 (6)
	DFT2	-2.45	-4.46	2.01	
<i>trans</i> -[RhCl(=C=CH ₂)(PMe ₃) ₂]	DFT1	-2.32	-4.35	2.03	2.20 (3)
	DFT4	-2.51	-4.56	2.05	
<i>trans</i> -[RhCl(=C=CHPh)(PMe ₃) ₂]	DFT2	-2.71	-4.68	1.97	2.12 (7)
<i>trans</i> -[RhBr(=C=CH ₂)(PMe ₃) ₂]	DFT1	-2.41	-4.40	1.99	2.16 (4)
	DFT4	-2.58	-4.59	2.01	
<i>trans</i> -[RhI(=C=CH ₂)(PMe ₃) ₂]	DFT1	-2.47	-4.41	1.94	2.12 (5)
	DFT4	-2.62	-4.60	1.98	
<i>trans</i> -[Rh(CH ₃)(=C=CH ₂)(PMe ₃) ₂]	DFT1	-1.62	-3.77	2.15	2.22 (10)
	DFT4	-1.88	-4.07	2.19	
<i>trans</i> -[Rh(C≡CPh)(=C=CHPh)(PMe ₃) ₂]	DFT1	-2.51	-4.29	1.78	2.03, 2.66(11)
<i>trans</i> -[RhF(CO)(PMe ₃) ₂]	DFT1	-1.24	-4.11	2.87	3.53 (12)
	DFT2	-1.21	-4.30	3.09	
<i>trans</i> -[RhCl(CO)(PMe ₃) ₂]	DFT1	-1.55	-4.33	2.78	3.43 (13)
	DFT2	-1.45	-4.49	3.04	
<i>trans</i> -[RhBr(CO)(PMe ₃) ₂]	DFT1	-1.65	-4.38	2.73	3.41 (14)
	DFT4	-1.51	-4.53	3.02	
<i>trans</i> -[RhI(CO)(PMe ₃) ₂]	DFT1	-1.73	-4.42	2.69	3.35 (15)
	DFT4	-1.55	-4.54	2.99	
<i>trans</i> -[Rh(C≡CPh)(CO)(PMe ₃) ₂]	DFT1	-1.47	-4.09	2.62	
	DFT2	-1.59	-4.27	2.68	

DFT1: BPW91/LANL2DZ. DFT2: BPW91/LANL2DZ on Rh, D95+(d) on the other atoms.

DFT3: BPW91/LANL2DZ on Rh, D95+(3df, 2p) on the other atoms.

DFT4: BPW91/LANL2DZ on Rh, 6-31+G(d) on P, C, H, 6-311+G(d) on F, Cl, Br and 3-21G(d) on I.

DFT5: BPW91/ contracted 6s5p3d basis (311111/22111/411) on Rh, 6-31+G(d) on P, C, H and F.

^a In hexane.

3.1.3 Vibrational Spectroscopy

3.1.3.1 Vibrational spectrum of PiPr_3

In order to identify in the FT-Raman spectra of the rhodium complexes the characteristic vibrational modes of the PiPr_3 ligands, a Raman spectrum of the liquid ligand was measured and assigned (Figure 10).

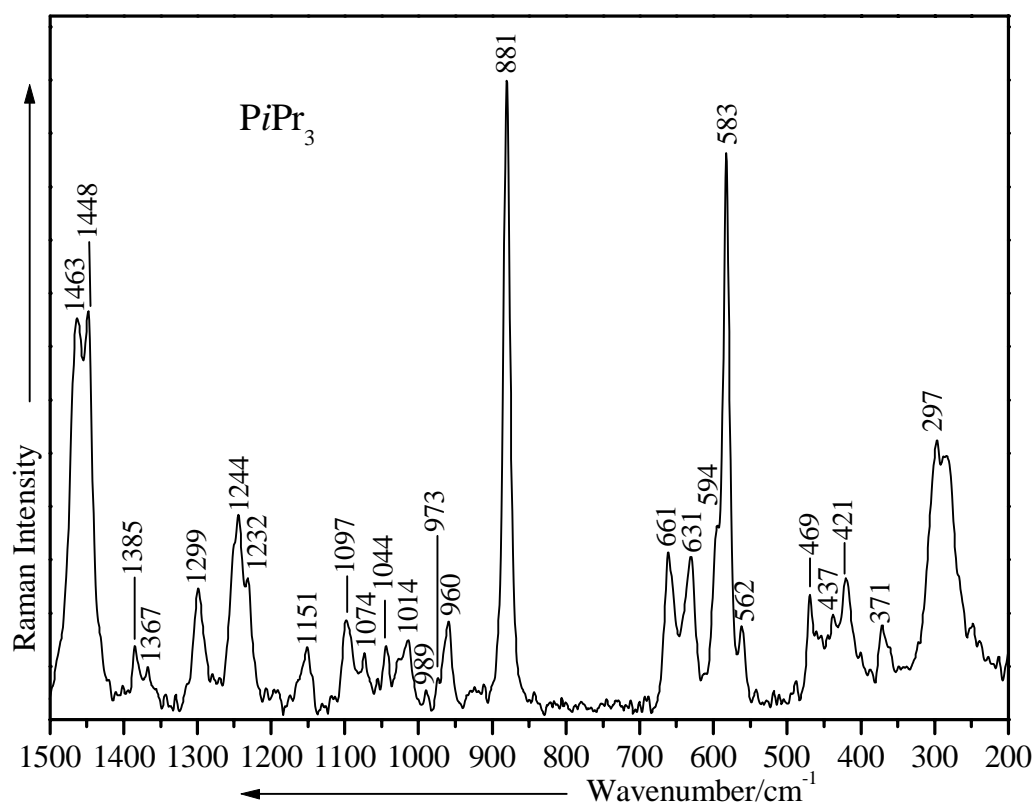


Figure 10. The FT-Raman spectrum of PiPr_3 between 1500 and 200 cm^{-1} .

Extensive vibrational spectroscopic investigations of isopropylhalides reported by Klaboe ^[72] have been used as a tool to assign most of the vibrational modes of the $i\text{Pr}$ groups. In addition, the P-C vibrational modes have been identified and ascribed by comparison with the assignment made by Holmes and co-workers ^[73]. Figure 10 presents the FT-Raman spectrum of triisopropylphosphine in the spectral region between 200 and 1500 cm^{-1} . The $\nu(\text{CH})$ vibrations of PiPr_3 have been located between 2850 and 3000 cm^{-1} ; the $\delta(\text{CH}_3)$ modes lie in the spectral range between 1350 and 1480 cm^{-1} and the rocking modes between 900 and 1160 cm^{-1} . The strong band at 881 cm^{-1} corresponds to the $\nu(\text{CCC})$ vibration. The characteristic $\nu(\text{PC}_3)$ modes are observed in the 500-700 cm^{-1} spectral region, the asymmetric one at higher wavenumbers and the symmetric one as a strongly polarized Raman band at 583 cm^{-1} . The

(CC)-, (CPC)- and (PCC)-deformation modes are present between 200 and 500 cm^{-1} in the FT-Raman spectrum of **1-16**. The $\delta_s(\text{CCC})$ mode appeared around 420 cm^{-1} .

3.1.3.2 Vibrational spectrum of *trans*-[RhF(=C=CH₂)(PiPr₃)₂] (**1**) vs. *trans*-[RhF(=¹³C=¹³CH₂)(PiPr₃)₂] (**2**)

For the assignment of the vibrations of the F-Rh=C=CH₂ skeleton of complex **1** and its ¹³C-analogue **2**, DFT-calculations carried out on the model compound *trans*-[RhF(=C=CH₂)(PMe₃)₂] have been used. The calculated and experimental wavenumbers are displayed in Table 7. The $\nu(\text{C}=\text{C})$ vibration is only IR active for complexes **1** and **2**, giving two close bands which are significantly shifted by ca. 46 cm^{-1} to lower wavenumbers in the ¹³C-containing compound **2** (Figure 11). The in plane $\delta(\text{CH}_2)$ mode was found at 1326 cm^{-1} in the IR spectrum of **1**, which, as expected, is shifted to lower wavenumbers in **2**. In the FT-IR spectrum of **2**, the new band at 1518 cm^{-1} was tentatively assigned to an overtone of the $\omega(\text{CH}_2)$ wagging mode at 759 cm^{-1} (Figure 12). The latter band is shifted by 7 cm^{-1} to lower wavenumbers compared to **1**.

According to the DFT calculation, the $\nu(\text{Rh}=\text{C})$ mode should appear around 571 cm^{-1} . The assignment of the peaks at 574 cm^{-1} and 572 cm^{-1} in the FT-IR (Figure 12) and FT-Raman spectrum (Figure 13) of complex **1**, respectively, was rather complicated due to the presence of the ligand PiPr₃ bands in the same region. Comparing the FT-Raman spectra of **1** and **2** (Figure 13), the band at 572 cm^{-1} could be exactly assigned to the $\nu(\text{RhC})$ mode, since this band was shifted to 559 cm^{-1} for the ¹³C-containing complex **2**. In addition, the wavenumbers corresponding to the $\nu(^{13}\text{C}=\text{C})$, $\nu(\text{Rh}=\text{C})$ and $\nu(\text{RhF})$ stretching modes were calculated using the DFT1 method. The resulting values (1594, 556 and 450 cm^{-1} , respectively) are also in good agreement with the experimental data ($\Delta\nu_{(\text{RhC})\text{calc.}} = 15 \text{ cm}^{-1}$ vs $\Delta\nu_{(\text{RhC})\text{exp.}} = 13 \text{ cm}^{-1}$ and $\Delta\nu_{(\text{C}=\text{C})\text{calc.}} = 62 \text{ cm}^{-1}$ vs $\Delta\nu_{(\text{C}=\text{C})\text{exp.}} = 46 \text{ cm}^{-1}$). The larger difference for the last value can probably be attributed to the higher anharmonicity of this mode or to the coupling with the $\delta(\text{CH}_2)$ mode. Thus, the weak band at 577 cm^{-1} in the FT-Raman spectra of **2** was assigned to the $\nu(\text{PC}_3)$ vibration.

In the FT-IR spectrum of **2** (Figure 12), two bands of medium and weak relative intensity were observed at 574 cm^{-1} and 559 cm^{-1} , respectively. We interpreted this result by postulating that, in contrast with the FT-Raman spectra, in the FT-IR spectra of **1** and **2** the $\nu(\text{PC}_3)$ bands are more intense than the $\nu(\text{Rh}=\text{C})$ bands. Thus, the IR band at 574 cm^{-1} corresponds to the $\nu(\text{PC}_3)$ mode of the phosphine, and should have the same wavenumber for **1** and **2**. In the FT-IR spectrum of **1**, the $\nu(\text{Rh}=\text{C})$ band could be hidden by the $\nu(\text{PC}_3)$ band,

but it is observed at 559 cm^{-1} in the FT-IR spectrum of **2**. The stretching mode $\nu(\text{RhF})$ of **1** was assigned to the strong IR and medium Raman band at 458 cm^{-1} . Visual inspection of the animated vibrational modes showed clearly that the Rh-C and Rh-F stretching vibrations are weakly coupled. This coupling could be responsible for the observed shift by 4 cm^{-1} of the Rh-F stretching band in compound **2**.

In the ^{13}C -substituted compounds, the $\nu(\text{Rh}=\text{C})$ mode gives rise to an intensive peak which is separated from the others, while in *trans*- $[\text{RhX}(\text{C}=\text{CH}_2)(\text{PiPr}_3)_2]$ a band of medium-to-weak intensity, originating from the phosphines, overlaps with the $\nu(\text{Rh}=\text{C})$ mode.

Due to these observations, the series of ^{13}C -labeled complexes *trans*- $[\text{RhX}(\text{C}=\text{CH}_2)(\text{PiPr}_3)_2]$ (**2-5**) is an appropriate system to study the variation of $\nu(\text{Rh}=\text{C})$ as a probe of the electronic influence of the ligand X *trans*-disposed to the Rh=C bond.

Table 7. Selected calculated and experimental vibrational wavenumbers (cm^{-1}) for *trans*- $[\text{RhF}(\text{C}=\text{CH}_2)(\text{PR}_3)_2]$ and *trans*- $[\text{RhF}(\text{C}=\text{CH}_2)(\text{PR}_3)_2]$ complexes together with their tentative assignment.

<i>trans</i> - $[\text{RhF}(\text{C}=\text{CH}_2)(\text{PR}_3)_2]$				<i>trans</i> - $[\text{RhF}(\text{C}=\text{CH}_2)(\text{PR}_3)_2]$			Assignment
Exp.		Calc.		Exp.	Calc.		
(R = <i>i</i> Pr)		(R = Me)		(R = <i>i</i> Pr)	(R = Me)		
R	IR	DFT1	DFT3	R	IR	DFT1	
-	1628s	1656	1654		1582s	1594	$\nu(\text{C}=\text{C})$
-	1326w	1341	1297		1318m	1336	$\delta(\text{CH}_2)$
-	766w	742	717		759m	734	$\omega(\text{CH}_2)$
666mw	636m	624	650	666mw	636m	624	$\nu(\text{PC}_3)$
	620m	622	644		620m	621	$\nu(\text{PC}_3)$
	574ms			577mw	574ms		$\nu(\text{PC}_3)$
572vs	572m	570	571	559s	559m	556	$\nu(\text{RhC})$
		484	491			468	o.o.p. $\delta(\text{RC1C2})$
458m	458s	452	456	454m	454s	450	$\nu(\text{RhF})$
362w		382	384	352shw		374	i.p. $\delta(\text{RhC1C2})$
340w		325	335	341w		322	$\nu(\text{RhP})$
308m		319	312	307m		317	$\nu(\text{RhP})$

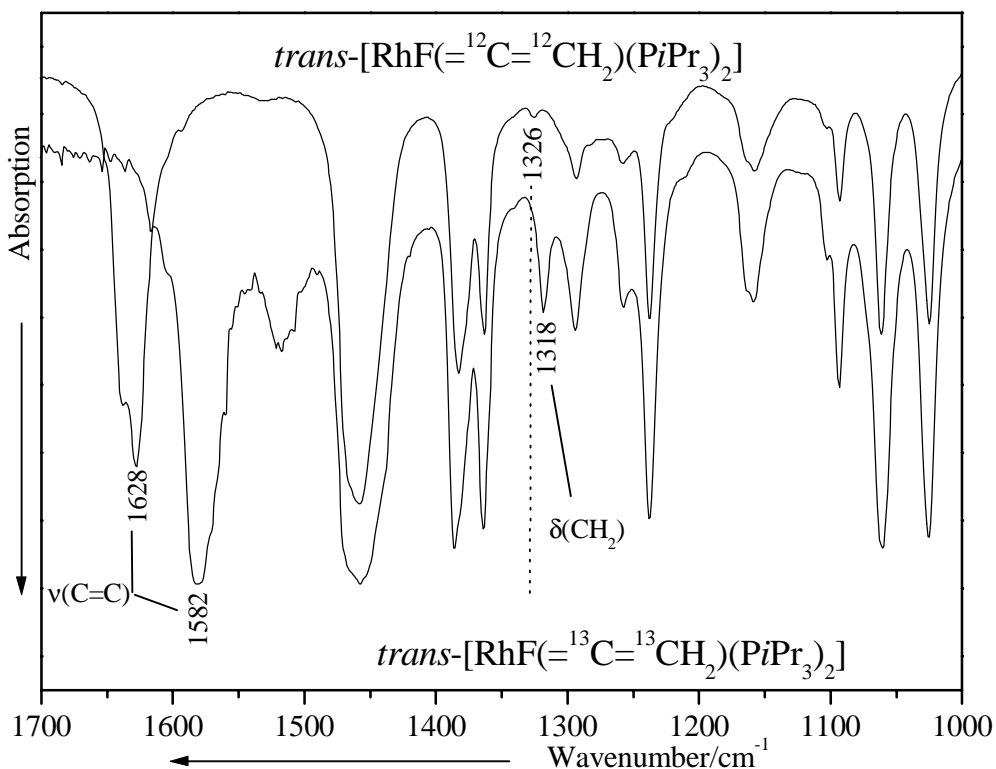


Figure 11. The high-wavenumber region of the FT-IR spectra of $\text{trans-[RhF(=C=CH}_2\text{)(PiPr}_3\text{)}_2\text{]}$ (**1**) and $\text{trans-[RhF(= }^{13}\text{C= }^{13}\text{CH}_2\text{)(PiPr}_3\text{)}_2\text{]}$ (**2**).

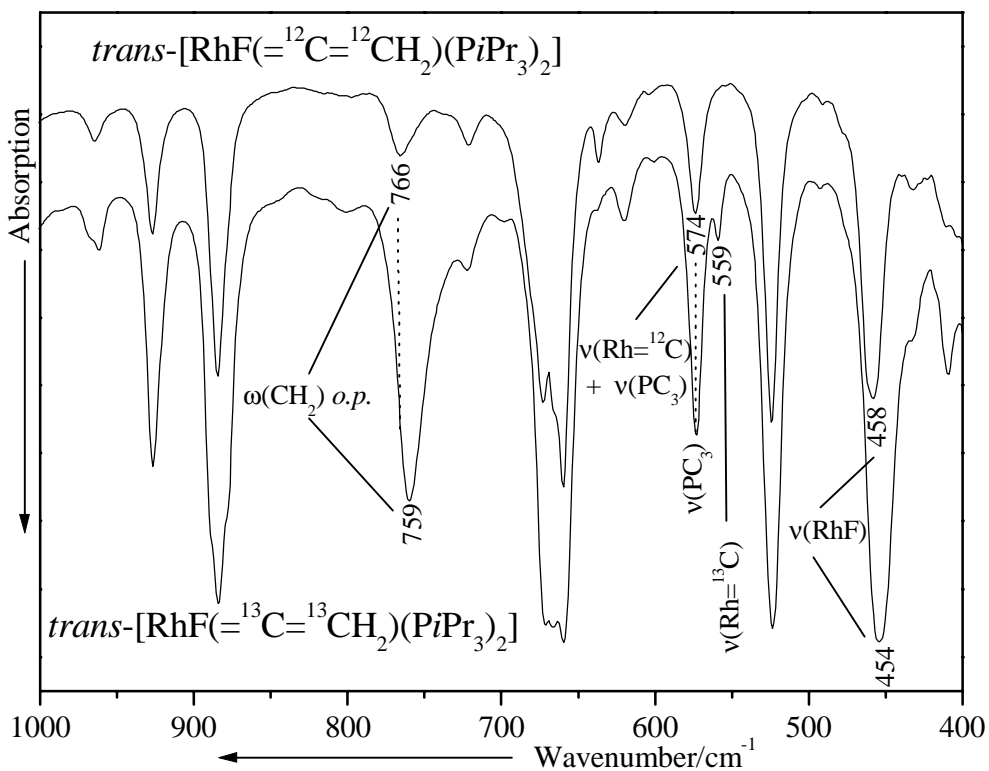


Figure 12. The low-wavenumber region of the FT-IR spectra of $\text{trans-[RhF(=C=CH}_2\text{)(PiPr}_3\text{)}_2\text{]}$ (**1**) and $\text{trans-[RhF(= }^{13}\text{C= }^{13}\text{CH}_2\text{)(PiPr}_3\text{)}_2\text{]}$ (**2**).

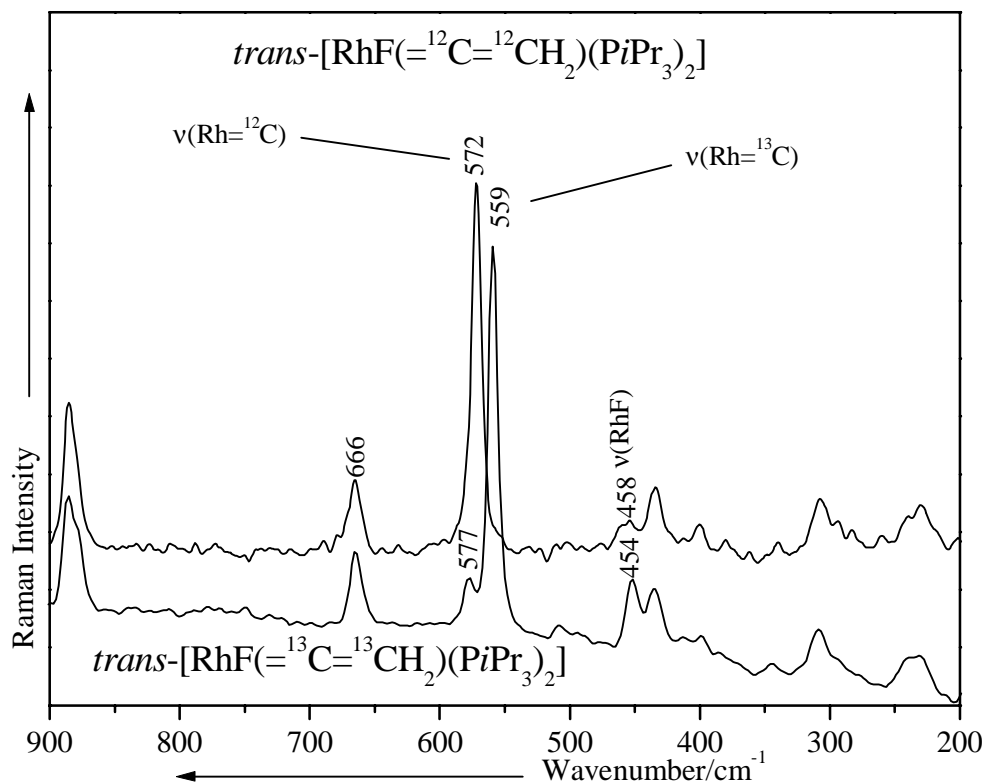


Figure 13. The low-wavenumber region of the FT-Raman spectra of *trans*-[RhF(=C=CH₂)(PiPr₃)₂] (**1**) and *trans*-[RhF(=¹³C=¹³CH₂)(PiPr₃)₂] (**2**).

3.1.3.3 Vibrational spectrum of *trans*-[RhX(=¹³C=¹³CH₂)(PiPr₃)₂] (X = F, Cl, Br, I) (**2-5**)

The low-wavenumber region of the FT-Raman spectra of complexes **2-5** is outlined in Figure 14. The $\nu(\text{Rh}=\text{}^{13}\text{C})$ mode has been assigned to a band in the range between 559 and 540 cm^{-1} on the basis of isotopic substitution and DFT calculations. In the infrared spectra, the corresponding peaks were of very low intensity. The wavenumbers of the metal-carbon stretching modes decrease in the order $\text{F} > \text{Cl} > \text{Br} > \text{I}$. A coupling between the $\nu(\text{Rh}=\text{C})$ and $\nu(\text{RhX})$ modes was observed in the computer-animated vibrational simulation for the model compounds *trans*-[RhX(=C=CH₂)(PMe₃)₂]. This coupling should increase from $\text{X} = \text{I}$ to $\text{X} = \text{F}$ because the $\nu(\text{Rh}=\text{}^{13}\text{C})$ and $\nu(\text{RhX})$ bands are closer to each other (Table 8), the maximum being found for the fluoro complex^[32]. A probe to test the degree of the coupling is the change of the position of the $\nu(\text{RhF})$ band in *trans*-[RhF(=C=CH₂)(PiPr₃)₂] to its ¹³C containing analogue **2**. A great difference would indicate an extensive coupling of the metal-carbon and metal-fluorine stretching vibrations. However, the $\nu(\text{RhF})$ mode is shifted only by 4 cm^{-1} to lower wavenumbers in *trans*-[RhF(=¹³C=¹³CH₂)(PiPr₃)₂] (**2**) compared to *trans*-[RhF(=C=CH₂)(PiPr₃)₂] (**1**) whereas the position of the $\nu(\text{Rh}=\text{C})$ mode is 13 cm^{-1} lower in **2** compared with the non-labeled complex.

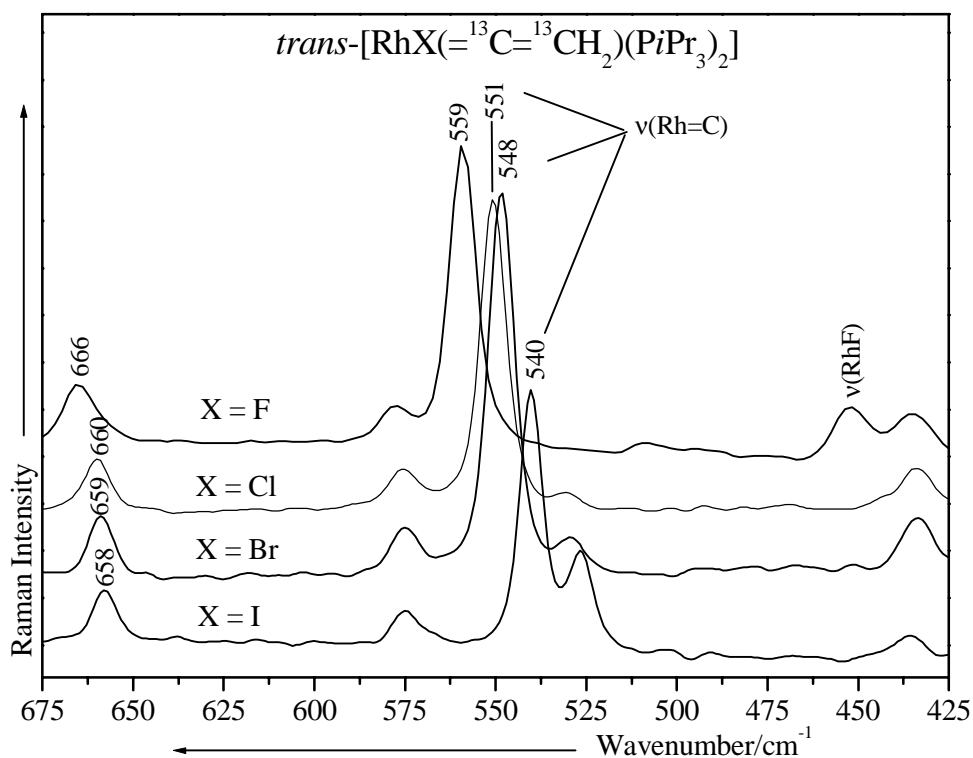


Figure 14. The low-wavenumber region of the FT-Raman spectrum of $trans\text{-}[\text{RhX}(=^{13}\text{C}=\text{}^{13}\text{CH}_2)(\text{PiPr}_3)_2]$ (X = F, Cl, Br, I).

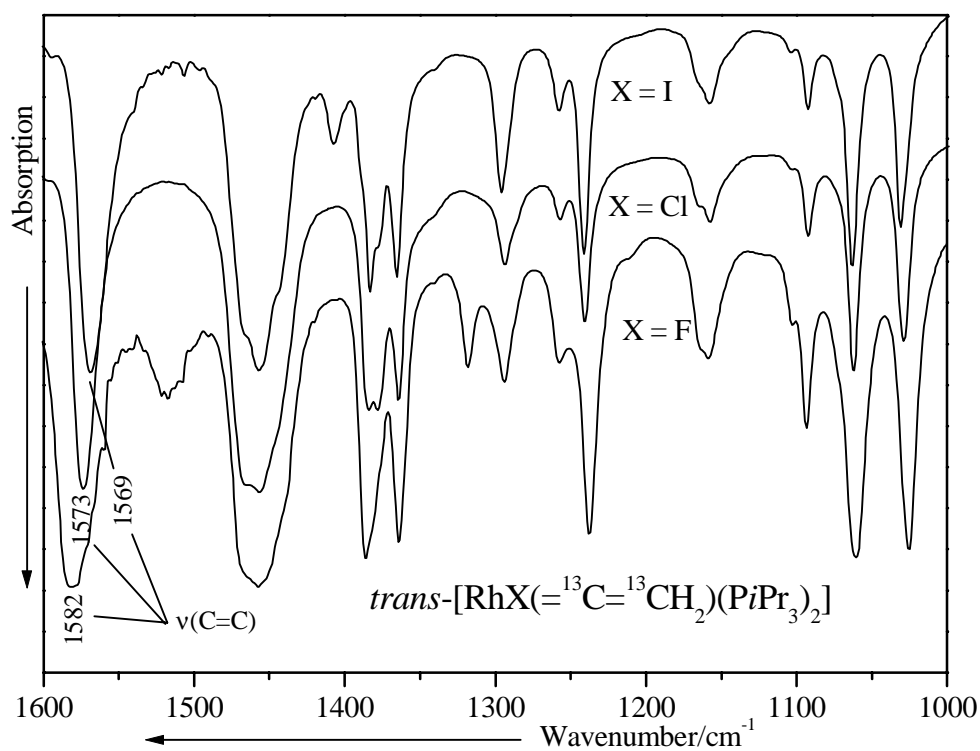


Figure 15. The high-wavenumber region of the FT-IR spectrum of $trans\text{-}[\text{RhX}(=^{13}\text{C}=\text{}^{13}\text{CH}_2)(\text{PiPr}_3)_2]$ (X = F, Cl, I).

Table 8. Calculated and experimental fundamental vibrational modes (cm^{-1}) in vinylidene rhodium complexes.

Compound	Method	$\nu(\text{C}=\text{C})$	$\nu(\text{RhC})$	$\nu(\text{Rh-X})$
<i>trans</i> -[RhF(=C=CH ₂)(PiPr ₃) ₂]	IR	1628s	574m	458s
	R	-	572s	458mw
<i>trans</i> -[RhF(=C=CH ₂)(PMe ₃) ₂]	DFT1	1656	571	451
	DFT2	1655	570	433
	DFT3	1654	571	456
	DFT4	1663	570	438
	DFT5	1659	575	461
<i>trans</i> -[RhF(= ¹³ C= ¹³ CH ₂)(PiPr ₃) ₂]	IR	1582s	559m	454s
	R	-	559s	454m
<i>trans</i> -[RhF(= ¹³ C= ¹³ CH ₂)(PMe ₃) ₂]	DFT1	1594	556	450
<i>trans</i> -[RhCl(= ¹³ C= ¹³ CH ₂)(PiPr ₃) ₂]	IR	1573s	551vw	
	R	-	551s	296shm?
<i>trans</i> -[RhCl(=C=CH ₂)(PMe ₃) ₂]	DFT1	1659	563	282
	DFT2	1657	559	279
	DFT3	1654	554	283
	DFT4	1663	559	281
<i>trans</i> -[RhBr(= ¹³ C= ¹³ CH ₂)(PiPr ₃) ₂]	IR	1572s	548vw	
	R	-	548s	218m?
<i>trans</i> -[RhBr(=C=CH ₂)(PMe ₃) ₂]	DFT1	1659	558	205
	DFT4	1666	555	208, 214
<i>trans</i> -[RhI(= ¹³ C= ¹³ CH ₂)(PiPr ₃) ₂]	IR	1569s	-	
	R	-	540s	134w?
<i>trans</i> -[RhI(=C=CH ₂)(PMe ₃) ₂]	DFT1	1658	553	138
	DFT4	1666	550	146

Although this shift is smaller than the difference in $\nu(\text{Rh}=\text{}^{13}\text{C})$ between compound **2** and compound **3** ($\Delta\nu = 8 \text{ cm}^{-1}$), the effect of the coupling together with the effect of the increasing mass of the metal fragment by going from **2** to **5** provokes some ambiguity in the interpretation of the change of $\nu(\text{Rh}=\text{}^{13}\text{C})$ along the series.

Moreover, the results of the calculations performed (see above) suggest that the order of $\nu(\text{Rh}=\text{}^{13}\text{C})$ reflects the order of the Rh=C bond strengths. The complexes **2**, **3**, **5** display in their FT-IR spectra a band in the range of 1569-1582 cm^{-1} which was not observed in the FT-Raman spectra and is assignable to the vinylidene $\nu(\text{}^{13}\text{C}=\text{}^{13}\text{C})$ vibrational mode (Figure 15).

Furthermore, the medium peak observed at 666 cm^{-1} in the FT-Raman spectrum of **2** can be tentatively ascribed to the $\nu(\text{PC}_3)$ stretching mode and shifts to lower wavenumbers as the $\nu(\text{Rh}=\text{C})$ and the $\nu(\text{C}=\text{C})$ in the order $\text{F} > \text{Cl} > \text{Br} > \text{I}$.

The previous investigation which has been extended to the phenyl-substituted vinylidene complexes **6-11** and to the related carbonyl derivatives **12-16**, is reported in the following parts.

3.1.3.4 Vibrational spectrum of *trans*-[RhX(=C=CHPh)(PiPr₃)₂] (X = F, Cl, Br, I, CH₃, PhC≡C) (**6-11**)

In addition to the $\nu(\text{Rh}=\text{C})$ stretching vibration, two further modes are of great relevance for this investigation. First, the deformation mode $\delta(\text{RhC1C2})$ which is observed in the FT-Raman spectra of the phenyl-substituted vinylidene complexes **6-9** (Figure 16). This mode was predicted by the DFT2 method to be at 472 cm^{-1} for the model compound *trans*-[RhF(=C=CHPh)(PMe₃)₂] and has been assigned to the band of medium intensity at 475 cm^{-1} in the FT-Raman spectrum of **6**.

Second, the C-C_{ring} stretching mode for which a high Raman activity is characteristic. This mode was assigned on the basis of DFT calculations to the strong peaks at 1230 cm^{-1} (X = F; calc. 1231 cm^{-1} , DFT2), 1225 cm^{-1} (X = Cl; calc. 1226 cm^{-1} , DFT2), 1224 cm^{-1} (X = Br), 1220 cm^{-1} (X = I) and 1219 cm^{-1} (X = PhC≡C; calc. 1228 cm^{-1} , DFT1) in the FT-Raman spectra of **6-9** (Figure 17) and **11**, respectively.

The fundamental vibrational modes of the complexes **6** and **7** are reported in Table 9 together with their assignment which is based on DFT calculations using the model complexes *trans*-[RhX(=C=CHPh)(PMe₃)₂] (X = F, Cl) and the DFT1-2 methods.

Two band shifts, in the spectral region between 750 and 850 cm^{-1} , are also observed in Figure 16. One may notice that one of them is decreasing in wavenumbers in the order $\text{F} > \text{Cl} > \text{Br} > \text{I}$, whereas the other one is increasing in the same order. According to the calculations, the band at 825 cm^{-1} (calc. 812 cm^{-1} , DFT2) in the FT-Raman spectrum of compound **6** is assigned to a ring deformation mixed with the deformation vibrations $\delta(\text{RhC1C2})$ and $\delta(\text{CH})_{\text{vinyl}}$ and the other one, which is observed at 763 cm^{-1} (calc. 777 cm^{-1} , DFT2), is assigned to the out-of-plane deformation vibrations $\delta(\text{CH})_{\text{ring}}$ and $\delta(\text{CH})_{\text{vinyl}}$. The decrease in wavenumbers of this mode in the order $\text{I} > \text{Br} > \text{Cl} > \text{F}$ is in agreement with the fact that the phenyl ring is electron richer in the case of compound **6**.

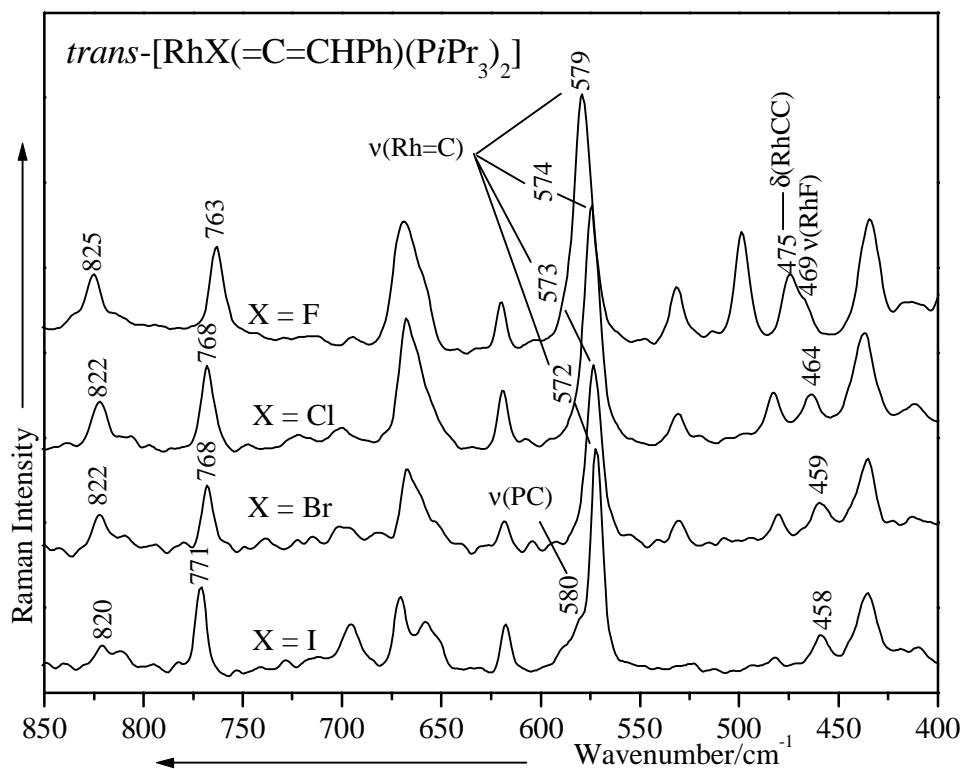


Figure 16. The low-wavenumber region of the FT-Raman spectrum of *trans*-[RhX(=C=CHPh)(PiPr₃)₂] (X = F, Cl, Br, I).

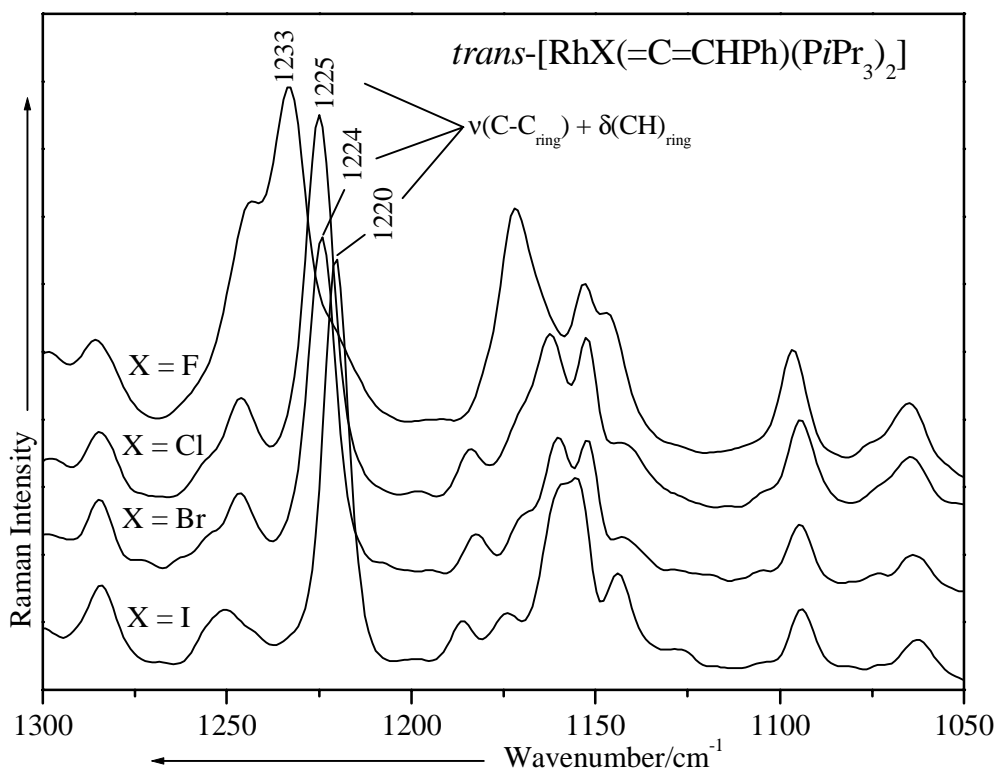


Figure 17. The fingerprint region of the FT-Raman spectrum of *trans*-[RhX(=C=CHPh)(PiPr₃)₂] (X = F, Cl, Br, I).

Table 9. Selected calculated and experimental vibrational wavenumbers (cm^{-1}) for *trans*-[RhX(=C=CHPh)(PMe₃)₂] and *trans*-[RhX(=C=CHPh)(PiPr₃)₂] complexes (X = F, Cl) together with their tentative assignment.

<i>trans</i> -[RhX(C=CHPh)(PR ₃) ₂]						
X = F			X = Cl			Assignment
Exp.	Calc.		Exp.	Calc.		
R	DFT1	DFT2	IR	R	DFT2	
1654sh.m	1652	1649	1649s	1648shm	1652	$\nu(\text{C}=\text{C})_{\text{vinyl}}$
1644m			1641s	1640m		
1624m			1625s	1624m		$\nu(\text{CC})_{\text{ring}} + \delta(\text{CH})_{\text{ring}}$
1596vs	1604	1602	1602m	1602m	1602	
1582m			1594s	1593vs		
1572m	1574	1571	1571m	1574m	1572	
1489m		1477	1490s	1490m	1477	
1474m		1460	1461br.s	1471m	1460	$\delta(\text{CH}_3)_{\text{PiPr}_3}$
1445m	1441	1443	1447s	1445m	1436	$\nu(\text{CC})_{\text{ring}} + \delta(\text{CH})_{\text{ring}}$
1388w	1371	1423	1385s	1388w	1422	$\delta(\text{CH}_3)_{\text{PiPr}_3}$
1369w	1345	1358	1366s	1368w	1358	$\nu(\text{CC})_{\text{ring}} + \delta(\text{CH})_{\text{ring}}$
1332w	1332	1307	1333vw	1334w	1303	$\delta(\text{CH})_{\text{ring}} + \delta(\text{CH})_{\text{vinyl}}$
1298m	1317	1304	1298m	1298m	1308	$\delta(\text{CH}_3)_{\text{PiPr}_3}$
1233s	1241	1231	1225vw	1225s	1226	$\nu(\text{C}-\text{C}_{\text{ring}}) + \delta(\text{CH})_{\text{ring}}$
998vs	985	975	998vw	998vs	976	ring breathing
885m			884s	884m		$\nu(\text{CCC})_{\text{PiPr}_3}$
825w	815	812	821vw	822w	810	$\delta(\text{CCC})_{\text{ring}} + \delta(\text{C1C2Rh}) + \delta(\text{CH})_{\text{vinyl}}$
763m	784	777	767s	768m	770	o.o.p. $\delta(\text{CH})_{\text{ring}} + \delta(\text{CH})_{\text{vinyl}}$
			698s		710	$\nu(\text{PC}_3) + \omega(\text{CH}_3)$
670m	688	670	667s	668m	673	o.o.p. $\delta(\text{CH})_{\text{ring}} + \delta(\text{CH})_{\text{vinyl}}$
			656s		642	$\nu(\text{PC}_3)$
619m	623	645	618w	619m	646	$\nu(\text{PC}_3)$
579m	582	574	574m	574m	570	$\nu(\text{RhC1}) + \text{i.p. } \delta(\text{CCC})_{\text{ring}}$
499m	487	487	482m	482m	485	o.o.p. $\delta(\text{CCC})_{\text{ring}}$
475m	472	473	464w	463m	460	$\delta(\text{RhC1C2})$
469shm	456	439				$\nu(\text{RhF})$

Moreover, it is noteworthy that as for the $\nu(\text{Rh}=\text{C})$, the other modes have also been shifted to lower wavenumbers in the order $\text{F} > \text{Cl} > \text{Br} > \text{I} > \text{PhC}\equiv\text{C}$, which again reflects the *trans* influence of the halide ligand in the rhodium(I) complexes.

One may notice, that the $\text{C}-\text{C}_{\text{ring}}$ stretching mode of the $\text{PhC}\equiv\text{C}$ ligand is expected at 1211 cm^{-1} using DFT1 and is assigned to the medium band at 1206 cm^{-1} . This theoretical shift (17 cm^{-1}) between both $\text{C}-\text{C}_{\text{ring}}$ stretching modes is in good agreement with the experimental one (13 cm^{-1}).

Table 10. Calculated and experimental fundamental vibrational modes (cm^{-1}) for the phenylvinylidene rhodium complexes **10** and **11**.

<i>trans</i> -[Rh(C≡CPh)(=C=CHPh)(PR ₃) ₂]			<i>trans</i> -[Rh(CH ₃)(=C=CHPh)(PR ₃) ₂]			Assignment
Exp. (R = <i>i</i> Pr)		Calc. (R = Me)	Exp. (R = <i>i</i> Pr)		Calc. (R = Me)	
R	IR	DFT1	R	IR	DFT1	
540vs	-	543	452m	452shw	464	$\nu(\text{Rh}-\text{C})$
472m	472w	469	462m	462ms		$\delta(\text{RhCC})$
	480m	489		484m		$\delta(\text{RhCC}) + \text{o.o.p.}$ $\delta(\text{CC})_{\text{ring}}$
511mw	511mw	515				$\delta(\text{CCC}_{\text{ring}})_{\text{phenylethynyl}}$
567s	572shw	571	571m	574shw	573	$\nu(\text{Rh}=\text{C})$
	568ms			557ms		
			592m	592w	604	$\omega(\text{CH}_3)$
788m	788w	784	-	-		$\delta(\text{CCC}) + \nu(\text{RhC})$
1206m	1204m	1211	-	-		$\nu(\text{C}-\text{C}_{\text{ring}})_{\text{phenylethynyl}}$
1219m	-	1228	1220m	-	1226	$\nu(\text{C}-\text{C}_{\text{ring}})_{\text{vinylidene}} +$ $\delta(\text{CH})$
1569m	1569m	1566	1566m	1566m	1570	$\nu(\text{C}=\text{C})_{\text{ring}}$
	1591m	1574		1584s		$\nu(\text{C}=\text{C})$
1594s	1595m	1602	1589s	1590s	1592	$\nu(\text{C}=\text{C})$
	1611	1603	1603wsh	1603m		$\nu(\text{C}=\text{C})$
1635vw	1635m	1642		1633m	1610	$\nu(\text{C}=\text{C})_{\text{vinylidene}}$
2072vs	2072mw	2062	-			$\nu(\text{C}\equiv\text{C})$

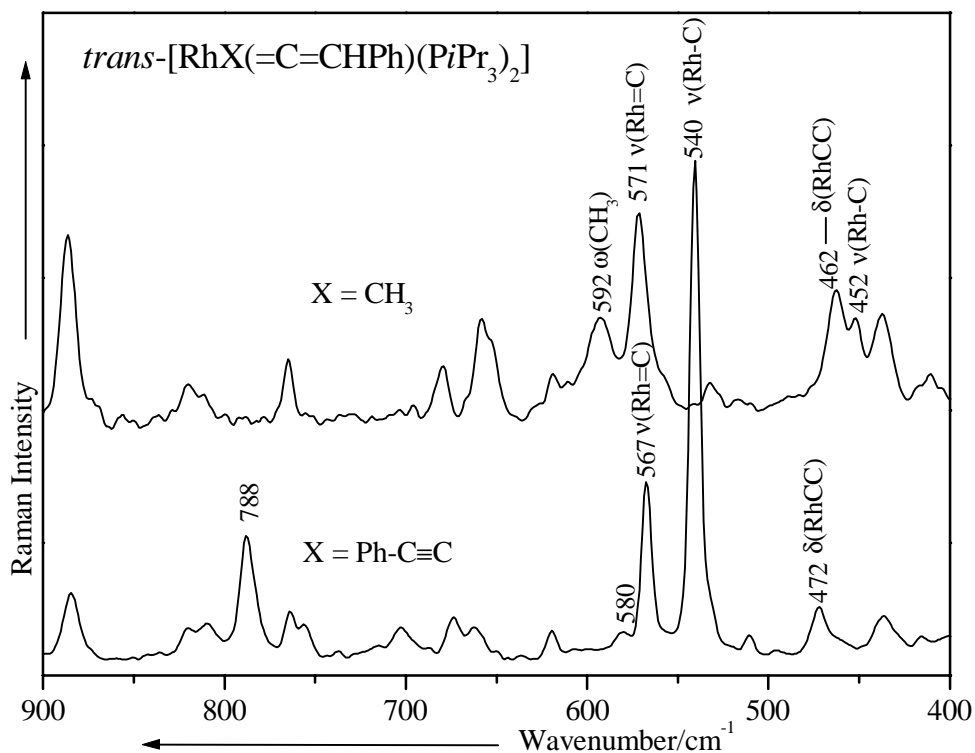


Figure 18. The low-wavenumber region of the FT-Raman spectrum of $\text{trans-[RhX(=C=CHPh)(PiPr}_3)_2]$ ($\text{X} = \text{Me}, \text{C}\equiv\text{CPh}$).

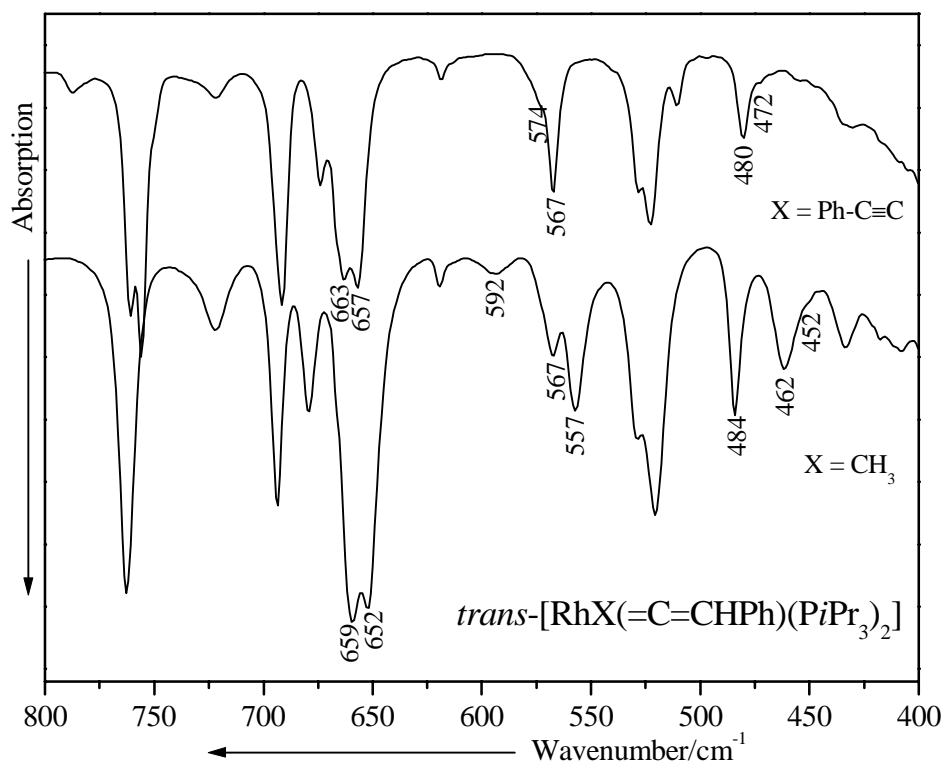


Figure 19. The low-wavenumber region of the FT-IR spectrum of $\text{trans-[RhX(=C=CHPh)(PiPr}_3)_2]$ ($\text{X} = \text{Me}, \text{C}\equiv\text{CPh}$).

For compounds **6-11**, the $\nu(\text{C}=\text{C})$ modes were observed in the range between 1653 and 1633 cm^{-1} and were both active in the Raman and infrared spectra. The corresponding order of X illustrating the *trans* influence is $\text{CH}_3 > \text{PhC}\equiv\text{C} > \text{I} > \text{Br} > \text{Cl} > \text{F}$.

The FT-Raman spectra of compounds **10** and **11** are more complicated in the low wavenumber region (Figure 18). However, the comparison of the FT-IR spectrum of both compounds is very helpful for their assignment (Figure 19). The bands at 571 cm^{-1} for **10** and at 567 cm^{-1} for **11** were assigned to the $\nu(\text{Rh}=\text{C})$ modes. This assignment agrees with the data found for complexes **6-9** and compares well with the calculated vibrational modes for the model compounds *trans*- $[\text{RhMe}(\text{C}=\text{CH}_2)(\text{PMe}_3)_2]$, *trans*- $[\text{RhMe}(\text{C}=\text{CHPh})(\text{PMe}_3)_2]$ and *trans*- $[\text{Rh}(\text{C}\equiv\text{CPh})(\text{C}=\text{CHPh})(\text{PMe}_3)_2]$ (Table 10). The positions of the $\nu(\text{Rh}-\text{C})$ bands were tentatively located at 452 cm^{-1} for **10** and at 540 cm^{-1} for **11**, in agreement with the calculated values of 463 and 542 cm^{-1} , respectively. The $\nu(\text{C}\equiv\text{C})$ mode of compound **11** appeared as a strong peak at 2072 cm^{-1} in the FT-Raman spectrum and as a medium one at 2071 cm^{-1} in the IR spectrum; it is red-shifted by 40 cm^{-1} compared with phenylacetylene (2111 cm^{-1})^[74].

3.1.3.5 Vibrational spectrum of *trans*- $[\text{RhX}(\text{CO})(\text{P}i\text{Pr}_3)_2]$ (X = F, Cl, Br, I, PhC≡C) (12-16)

The metal-carbon multiple bond stretching modes have been studied mainly in carbonyl complexes^[30-32], and for complexes of the type *cis*- $[\text{MX}_2(\text{CO})_2]^-$ (X = Cl, Br) (M = Rh, Ir), Browning et al.^[75] assigned the $\nu(\text{MC})$ stretching mode to the strongest Raman band and the $\delta(\text{MCO})$ to the strongest IR bands in the 400-700 cm^{-1} region. In the related compounds *trans*- $[\text{RhX}(\text{CO})(\text{PMe}_3)_2]$ (X = Cl, Br), the same authors assigned the $\nu(\text{RhC})$ at 550 and 552 cm^{-1} and the $\nu(\text{CO})$ at 1965 and 1961 cm^{-1} for the chloride and bromide substituted complexes, respectively. The FT-Raman spectrum of the carbonyl compound **12-15** exhibited a strong band in the range between 1929 and 1943 cm^{-1} , which was assigned to the $\nu(\text{CO})$ vibration and its wavenumber decreases in the order $\text{I} > \text{Br} > \text{Cl} > \text{F}$ (Figure 20).

In compound **12**, the assignments of the $\nu(\text{RhC})$ and $\nu(\text{RhF})$ vibrational modes at 573 and 465 cm^{-1} , respectively (Table 11), are in good agreement with the calculated wavenumbers for the $\nu(\text{RhC})$ and $\nu(\text{RhF})$ of the model complex *trans*- $[\text{RhF}(\text{CO})(\text{PMe}_3)_2]$ (571 and 451 cm^{-1}). The calculations showed that both $\nu(\text{RhC})$ and $\nu(\text{RhF})$ vibrational modes are weakly coupled as for the vinylidene derivatives. The $\nu(\text{PC}_3)$ band could also overlap with the $\nu(\text{RhC})$ band on the analogy of **1**.

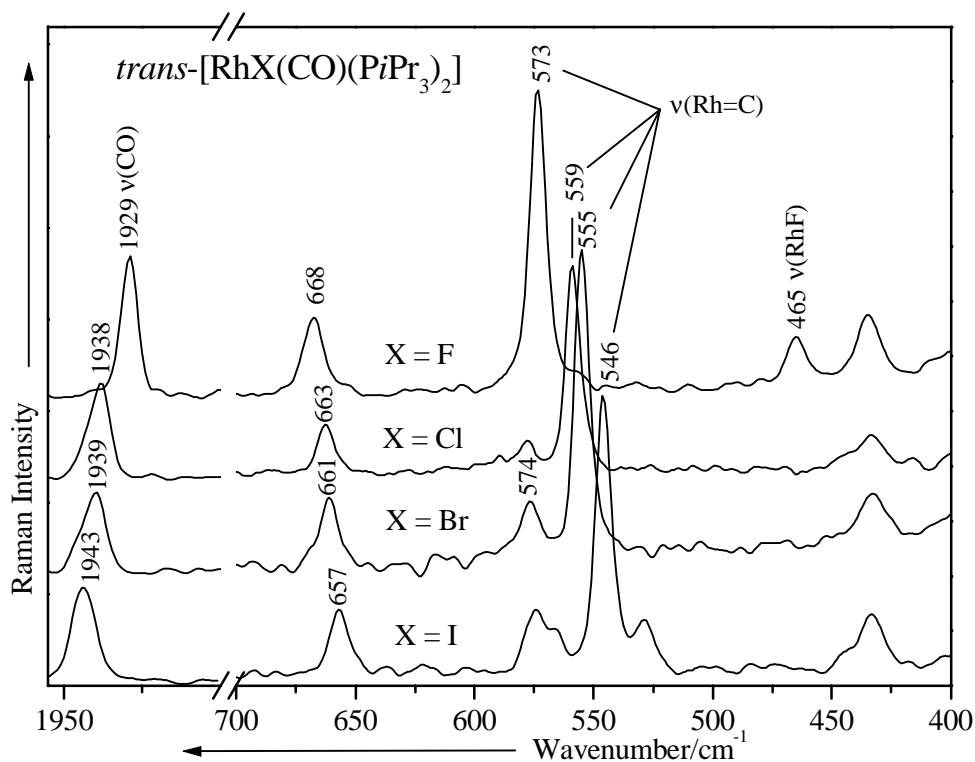


Figure 20. The $\nu(\text{CO})$ and $\nu(\text{RhC})$ wavenumber region of the FT-Raman spectrum of $trans\text{-}[\text{RhX}(\text{CO})(\text{PiPr}_3)_2]$ ($X = \text{F}, \text{Cl}, \text{Br}, \text{I}$).

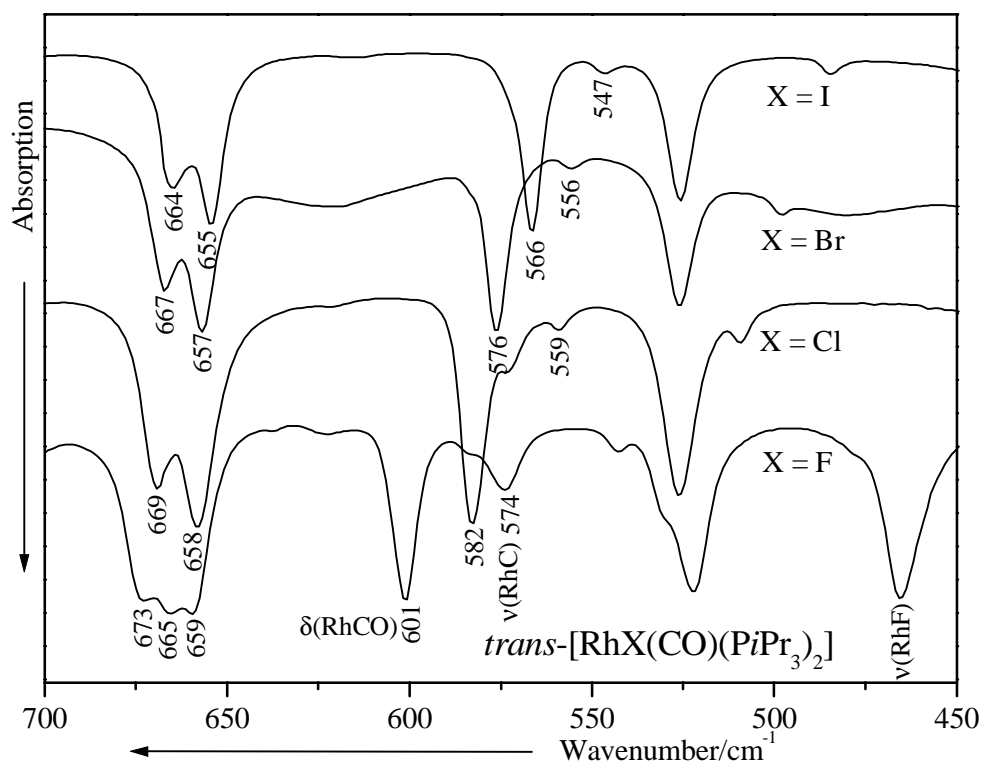


Figure 21. The $\delta(\text{RhCO})$ and $\nu(\text{RhC})$ wavenumber region of the FT-IR spectrum of $trans\text{-}[\text{RhX}(\text{CO})(\text{PiPr}_3)_2]$ ($X = \text{F}, \text{Cl}, \text{Br}, \text{I}$).

Table 11. Calculated and experimental fundamental vibrational modes (cm^{-1}) in carbonyl rhodium complexes.

Compound	Method	$\nu(\text{CO})$	$\nu(\text{RhC})$	$\nu(\text{Rh-X})$
<i>trans</i> -[RhF(CO)(PiPr ₃) ₂]	IR	1934mbr	574m	465vs
	R	1929s	573vs	465s
<i>trans</i> -[RhF(CO)(PMe ₃) ₂]	DFT1	1843	571	450
	DFT2	1952	560	434
	DFT3	1947	563	455
	DFT5	1944	570	460
<i>trans</i> -[RhCl(CO)(PiPr ₃) ₂]	IR	1938mbr	559w	
	R	1938s	559vs	?
<i>trans</i> -[RhCl(CO)(PMe ₃) ₂]	DFT1	1847	561	284
	DFT2	1958	547	283
	DFT3	1954	542	287
<i>trans</i> -[RhBr(CO)(PiPr ₃) ₂]	IR	1941mbr	556w	
	R	1939s	555vs	227m
<i>trans</i> -[RhBr(CO)(PMe ₃) ₂]	DFT1	1847	557	205
	DFT4	1957	542	214, 209
<i>trans</i> -[RhI(CO)(PiPr ₃) ₂]	IR	1944mbr	547w	
	R	1943s	546vs	?
<i>trans</i> -[RhI(CO)(PMe ₃) ₂]	DFT1	1847	551	192, 139
	DFT4	1957	536	194, 147
<i>trans</i> -[Rh(C≡CPh)(CO)(PiPr ₃) ₂]	IR	1948s	503m	-
	R	1940w?	503vs	546m or 534m
<i>trans</i> -[Rh(C≡CPh)(CO)(PMe ₃) ₂]	DFT1	1841	516	547
	DFT2	1958	496	537

$\nu(\text{C}\equiv\text{C})$ 2090 cm^{-1} . Calculated at 2084 cm^{-1} using DFT1-2.

In the FT-Raman spectra of the analogous carbonyl complexes *trans*-[RhX(CO)(PiPr₃)₂], (X = Cl, Br, I) a peak in the range between 559 and 546 cm^{-1} was assigned to the $\nu(\text{RhC})$ mode (Figure 20) on the basis of DFT calculations for the corresponding model compounds (Table 11). The position of the $\nu(\text{RhC})$ mode is dependent on the halide ligand quite similarly as observed for the rhodium-carbon stretching mode of the vinylidene complexes **2-5**. The weak band at 558 cm^{-1} in the FT-Raman spectrum and the very strong band at 601 cm^{-1} in the IR spectrum, which did not appear in the spectra of **1**, can be attributed to the $\delta(\text{RhCO})$ modes. In the infrared spectra of the chloro, bromo and iodo carbonyl compounds, the corresponding

band for the $\delta(\text{RhCO})$ mode is shifted to lower wavenumbers and found at 582, 576 and 566 cm^{-1} , respectively (Figure 21).

In the *trans*- $[\text{RhX}(\text{CO})(\text{PPh}_3)_2]$ compounds, the $\delta(\text{RhCO})$ deformation mode has been assigned at 596, 574, 567 and 558 cm^{-1} for X = F, Cl, Br and I, respectively, ^[76-78] which is in good agreement with our results. Thus, the peak at 601 cm^{-1} of high relative intensity in the IR spectrum of **12**, shows a 19 cm^{-1} red shift in the *trans*- $[\text{RhCl}(\text{CO})(\text{P}i\text{Pr}_3)_2]$ (**13**) complex due to the different Rh-C bond strength of the fluoro and chloro complexes. The influence of the *trans* halogen ligand on the M-C bond strength reflects the shift of the vibrational bending mode too. This is also true for the $\nu(\text{PC}_3)$ modes which are shifted to lower wavenumbers in the order F > Cl > Br > I (Figures 20 and 21).

The vibrational mode $\nu(\text{C}\equiv\text{C})$ of compound **16** has been assigned to the strong and medium band at 2091 cm^{-1} (calc. 2084 cm^{-1} , DFT2) in the FT-Raman and FT-IR spectrum, respectively. This mode has been shifted to lower (20 cm^{-1}) and higher (20 cm^{-1}) wavenumbers compared with the phenylacetylene (2111 cm^{-1}) ^[74] and the corresponding phenylvinylidene compound **11**, respectively. This result is consistent with the C \equiv C bond length which is measured to be at 120.0(1) pm in the complex *trans*- $[\text{Rh}(\text{CO})(\text{C}\equiv\text{CPh})(\text{PPh}_3)_2]$. The $\nu(\text{CO})$ stretching mode appears as a very strong band at 1948 cm^{-1} (calc. 1958 cm^{-1} , DFT2) in the FT-IR spectrum of complex **16**. Only a weak peak at 1940 cm^{-1} can be observed in the FT-Raman spectrum of complex **16**.

One may notice that our result is consistent with the $\nu(\text{CO})$ stretching mode observed at 1968 cm^{-1} in the IR spectrum of *trans*- $[\text{Rh}(\text{CO})(\text{C}\equiv\text{CPh})(\text{PPh}_3)_2]$ ^[65]. Namely, the Rh-PR₃ bond lengths become longer as increasingly σ -donating ligands are used on PR₃. The Rh-X bonds also become longer, but the Rh-CO bonds shorten, with increasingly σ -donating ligands. Consequently, the C-O bond length increases. Of course, these behaviors are consistent with the expectation that increasing the donor ability of PR₃ will enhance the Rh \rightarrow CO back-donation.

It should be noted that the deformation vibration $\delta(\text{RhCO})$ is about 20 cm^{-1} underestimated for the halogen carbonyl complexes **12-15** using DFT1-4. Thus, the calculated $\delta(\text{RhCO})$ modes (559 and 509 cm^{-1}) with DFT1 were tentatively assigned to the band at 583 and 534 cm^{-1} (see Figure 22). The animation of the calculated vibrational modes shows that they are mixed with the deformation vibration $\delta(\text{RhC}\equiv\text{CPh})$. On one hand, the medium peak at 546 cm^{-1} (calc. 537 cm^{-1} , DFT2), which can be only observed in the FT-Raman spectrum of **16**, should be assigned to the $\nu(\text{Rh-C})$ and $\nu(\text{Rh=C})$ stretching modes mixed with a ring bending $\delta(\text{CCC})_{\text{ring}}$. On the other hand, the very strong band in the FT-Raman and medium one in the

FT-IR spectrum at 503 cm^{-1} (calc. 496 cm^{-1} , DFT2), should be attributed to the $\nu(\text{Rh}=\text{C})$ and $\nu(\text{Rh}-\text{C})$ modes too.

As for the vinylidene complex **11**, the $\text{C}-\text{C}_{\text{ring}}$ stretching mode of the $\text{PhC}\equiv\text{C}$ ligand is observed at 1209 cm^{-1} in the FT-Raman spectrum of **16**. It is noteworthy that in comparison with complexes **11** and **16**, the $\nu(\text{C}\equiv\text{C})$ and $\nu(\text{Rh}-\text{C})$ stretching modes decrease in the same order than the $\nu(\text{C}=\text{C})$ and $\nu(\text{Rh}=\text{C})$ modes of the vinylidene complexes. Moreover, the corresponding order of X illustrating the *trans* influence in the carbonyl complexes is also $\text{PhC}\equiv\text{C} > \text{I} > \text{Br} > \text{Cl} > \text{F}$.

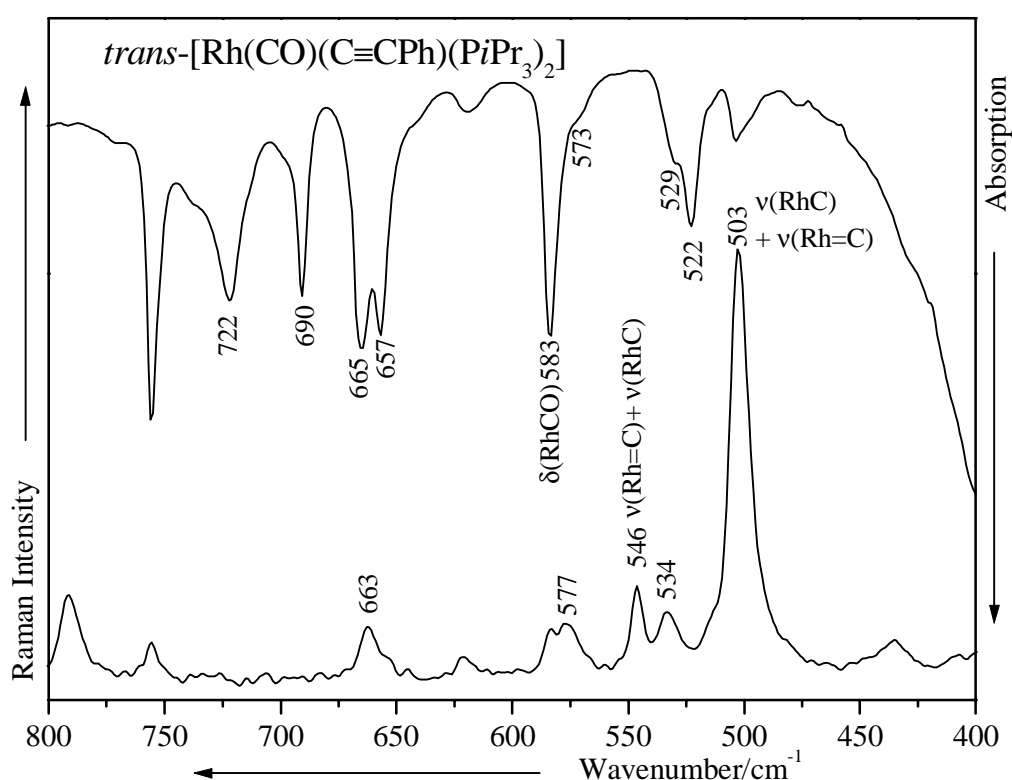


Figure 22. Low wavenumber region of the FT-Raman and FT-IR spectrum of $\text{trans}-[\text{Rh}(\text{CO})(\text{C}\equiv\text{CPh})(\text{PiPr}_3)_2]$.

3.1.4 Discussion

For a diatomic molecule, the vibrational mode is directly related to $(k/m)^{1/2}$, where k is the force constant of the bond and m is the reduced mass. Since the force constant reflects the bond strength, the conclusion is that the stronger the bond, the higher its wavenumber. In polyatomic molecules, the same principle has been generally applied to bands which mainly originate from the stretching of one particular bond.

The coincidence in wavenumber of the $\nu(\text{RhC})$ stretching mode for compounds **2** and **12**, which contain the isoelectronic ligands $\text{C}=\text{CH}_2$ and CO suggests a stronger Rh-C bond strength in the carbonyl complex. Since the complexes **2** and **12** possess the same reduced mass ($^{13}\text{C}=\text{C}^{13}\text{CH}_2$ vs CO), a comparison of the FT-Raman spectra allow for an evaluation of the bonding strength free of any mass effects and therefore only showing effects of electronic nature. Thus, a direct comparison of the $\nu(\text{RhC})$ stretching modes of complex **2** (559 cm^{-1}) and **12** (573 cm^{-1}) allow to point out the difference in the RhC bond strength of the mentioned complexes. Furthermore, the $\nu(\text{RhF})$ stretching mode is also 11 cm^{-1} blue shifted in complex **12**. From this, one can see that the carbonyl ligand is a better π -acceptor and a less effective σ -donor than the vinylidene one.

From the data of the Raman spectra of the vinylidene compounds **2-11** (Tables 8-9, Figures 14, 16 and 18), for different ligands X the following order of the $\nu(\text{Rh}=\text{C})$ and $\nu(\text{Rh}=\text{C})$ wavenumbers has been obtained: $\text{F} > \text{Cl} > \text{Br} > \text{I} > \text{Me} > \text{C}\equiv\text{CPh}$. We have already mentioned that the coupling between the $\nu(\text{Rh}=\text{C})$ and $\nu(\text{RhX})$ modes as well as the mass effect of the heavier halogens also contribute to this sequence. However, the fact that the calculated Rh-C distances increase in the same way as the wavenumber of the $\nu(\text{Rh}=\text{C})$ modes decreases suggests that the observed sequence is mainly due to a variation in the Rh=C bond strengths. This result is consistent with the values obtained from the $J(\text{RhC})$ and $J(\text{C}=\text{C})$ of the complex *trans*- $[\text{RhX}(\text{C}=\text{CHR})(\text{PiPr}_3)_2]$ ^[53]. They increase in the sequence $\text{F} > \text{Cl} > \text{Br} > \text{I}$ for $\text{R} = \text{H}$ and $\text{F} > \text{Cl} > \text{Br} > \text{I} > \text{C}\equiv\text{CPh} > \text{Me}$ for $\text{R} = \text{Ph}$. At the same time, the $J(\text{RhP})$ decrease in the same order, being in good agreement with the red shift of the $\nu(\text{PC})$ stretching mode.

Since for the series of halide complexes, the order of the $\nu(\text{Rh}=\text{C})$ stretching mode is the same for **2-5** as for **6-9**, we assume that the bonding properties of the $\text{C}=\text{CH}_2$ and $\text{C}=\text{CHPh}$ ligands are quite similar indeed. By taking this into consideration, we conclude that on the basis of the vibrational spectra the *trans* influence of the ligands X in compounds **2-11** decreases along the series $\text{C}\equiv\text{CPh} > \text{CH}_3 > \text{I} > \text{Br} > \text{Cl} > \text{F}$.

A slightly exceptional observation is that the wavenumber of the $\nu(\text{Rh}=\text{C})$ mode for compound **6** is 7 cm^{-1} higher than for *trans*- $[\text{RhF}(\text{C}=\text{CH}_2)(\text{PiPr}_3)_2]$. Although this increase might indicate that substitution of H by Ph strengthens the Rh=C bond, it could also originate from the above-mentioned coupling between the $\nu(\text{Rh}=\text{C})$ and an in-plane ring deformation mode. However, the comparison of the FT-Raman spectra of compounds **11** and **16** shows a strongest $\text{C}\equiv\text{C}$ and Rh-C bonds for the carbonyl complex **16**. This shows that the phenyl vinylidene ligand ($\text{C}=\text{CHPh}$) has the strongest *trans* influence and that the order of the π -acceptor ability should rise in the order $\text{C}=\text{CH}_2 < \text{CO} < \text{C}=\text{CHPh}$.

It is interesting to compare the variations of the vibrational data of the vinylidene compounds **2-5** with those of the isoelectronic carbonyls *trans*-[RhX(CO)(PiPr₃)₂], where X = F (**12**), Cl (**13**), Br (**14**) and I (**15**). In the FT-Raman spectra of **12-15** (Figure 20), the $\nu(\text{RhC})$ mode is shifted to lower wavenumbers in the order F > Cl > Br > I, which is the same as found for the analogous vinylidene complexes **2-5** (Figure 14). However, while the $\nu(\text{CO})$ mode of **12-15** is shifted to higher wavenumbers along the sequence F < Cl < Br < I (Figure 19), the $\nu(^{13}\text{C}=\text{C})$ and $\nu(\text{C}=\text{C})$ modes of **2-5** (Figures 14-15) and **6-9** (Figure 16) are shifted to higher wavenumbers in the opposite direction. The observed trend of $\nu(\text{CO})$ for **12-16** is the same as that observed for the triphenylphosphine complexes *trans*-[RhX(CO)(PPh₃)₂] (X = F, Cl, Br, I) [76-78], and has been explained in terms of an increasing π -donor capability of X on going up in group 17.

The surprising situation thus arises that the metal center seems to be more electron-rich if it is bonded to a more electronegative halogen. This supposition has been used to explain the variation of the half-wave reduction potentials and the equilibrium constants for the halide exchange in *trans*-[RhX(CO)(PPh₃)₂] (X = F, Cl, Br, I) [76-78] as well as in related halide complexes of Fe [78], Ru [79], Ir [80] and Pd [81], respectively. With regard to our work, the same clue about a push-pull π -interaction X→Rh→C provides an explanation why we find both for the vinylidene and the carbonyl complexes the highest Rh-C bond strength when fluoride is the *trans*-disposed ligand. Quite remarkably, the calculated atomic charges for the model compounds *trans*-[RhX(L)(PMe₃)₂], where L = C=CH₂ or CO and X = F, Cl, Br and I, are not in agreement with the assumption that the metal center becomes more electron-rich along the sequence F > Cl > Br > I (see Tables 4-5).

Owing to the calculations, the charge of Rh increases from X = I to X = F while the charge on the vinylidene and CO ligands does not vary significantly. In addition, the calculated population of the p(π) orbitals of the halogens is quite similar in the series, suggesting that the shifts of the vibrational modes are not originated by differences in the p(π) donation from the halogen to the metal. In the case of the fluoro complexes, the considerable difference in charge between Rh and F (0.68 for L = C=CH₂ and 0.59 for L = CO), calculated by the DFT1 method, suggests that (i) the Rh-F bond has a strong electrostatic component and (ii) the small and highly negatively charged fluorine atom will cause severe electrostatic repulsions with the electron density at the metal [82]. Thus, the coordination of fluoride has two effects on the Rh-C bond. On one hand, the higher positive charge on the metal leads to an increase of the σ -donation from carbon to rhodium, while on the other hand the repulsion between the p π electrons of the fluoride and the d π electrons of rhodium favors a π -retrodonation from the metal to the empty p π orbitals of the vinylidene ligand. In addition to these two effects, the electrostatic behavior of rhodium may also play a role for the observed variation of the $\nu(\text{CO})$

mode, since it has been shown that the electrostatic influence of a positively charged atom bonded to CO initiates a shift of the CO stretching vibration to lower wavenumbers^[83]. The discussed repulsion between filled orbitals can also be used to explain the variation of the calculated energies of the HOMO's for the model compounds *trans*-[RhX(=C=CH₂)(PMe₃)₂] where X = F, Cl, Br and I (Table 6). The energy of the HOMO decreases along the sequence F > Cl > Br > I, the difference between the fluoro and the chloro complex being the highest. This result agrees with the fact that fluorine as the group 17 element with the smallest radius and the largest negative charge creates the strongest destabilizing repulsion with the electrons of the HOMO which is mainly composed of the d_z² orbital of Rh. Regarding the LUMO's, their energy also decreases along the sequence F > Cl > Br > I (see Table 6). A possible explanation for this trend could be that due to the Rh=C antibonding character of the LUMO's (see Figure 9) these orbitals will be higher in energy if the strength of the Rh=C bond increases. With respect to the analogous model compounds containing CO instead of C=CH₂, the HOMO's are strongly localized on the metal and include only some minor contributions from the CO carbon atom. Although the calculated energies of the HOMO's for the carbonyl and the vinylidene complexes are quite similar (Table 6), the energies of the LUMO's are somewhat higher for L = CO than for L = C=CH₂. This difference causes the observed blue-shift of the absorption maxima in the visible region.

An interesting situation results for the model compound *trans*-[RhMe(=C=CH₂)(PMe₃)₂], where the methyl ligand has no nonbonding electrons which could initiate a repulsion with the d electrons of rhodium. The minimum energy structure calculated by the BPW91/LANL2DZ method for *trans*-[RhMe(=C=CH₂)(PMe₃)₂], reveals a significant distortion from the anticipated linear C-Rh=C=C chain, the theoretical C-Rh-C and Rh-C-C bond angles being 157.2° and 158.6°, respectively. However, the energy of the distorted structure for the vinylidene complex is less than 6 kJ/mol smaller than the energy for the linear arrangement. In this context, it should be noted that in benzene compound **10** rearranges to the π -allyl complex [Rh(η^3 -CH₂CHCHPh)(PiPr₃)₂] by migration of the methyl group to the vinylidene ligand^[84]. Therefore, a coupling of the two C-bonded ligands is possible even without the presence of a supporting Lewis base. Although in this case we should be more cautious regarding the calculated Rh=C bond distance and the value of the assigned $\nu(\text{Rh}=\text{C})$ mode, the calculation suggests that the Rh=C bond is weaker. This can be rationalized by assuming that the electrostatic repulsion, which in the halide complexes pushes the d _{π} orbitals towards the p _{π} orbitals of the carbon, is not present in the methyl compound. The calculated charge of the metal in the methyl rhodium complex lies between that of the fluoro and the chloro derivatives. The NPA analysis reveals that the metal becomes more electron-rich by varying the ligand X along the sequence F < Me < Cl < Br < I. These results can be explained by taking two effects into consideration: First, with the increase of the electronegativity of X the

charge of the metal becomes more positive and the σ -donation from carbon to rhodium becomes stronger. Second, with the increase of the charge on X accompanied by a decrease in size the repulsion between the nonbonding electron pairs of X and the filled d_{π} orbitals of Rh become stronger. The latter effect leads to an increase in π -backbonding from the metal to the empty p_{π} orbital of carbon. For the series of carbonyl compounds *trans*-[RhX(CO)(PiPr₃)₂], where X = F, Cl, Br and I, analogous results have been obtained and confirmed for the model compounds *trans*-[RhX(CO)(PMe₃)₂].

3.2 Ethylene rhodium(I) complex *trans*-[RhF(C₂H₄)(PiPr₃)₂]

It is well-known that ethylene and other olefins form π -complexes with transition metals. The simplest and best-studied complex is the Zeise's salt K[Pt(C₂H₄)Cl₃]H₂O. The complete assignments of the infrared spectra of Zeise's salt and its deuterated analog have been reported in the literature ^[85-88]. In spite of the fact that this kind of complexes have been exhaustively studied, the assignment of the low wavenumber modes have been controversial. The bonding in alkene complexes can be described by two models, the synergistic ligand \rightarrow metal σ -donation and ligand \leftarrow metal π -back-donation of Dewar ^[89], Chatt and Duncanson ^[90], and the model where there are two electronsharing metal-carbon σ -bonds, forming a metallacyclopropane ring. In molecules described by the first model, only one metal-carbon stretching band is expected, while in metallacyclopropane-type compounds two bands, one symmetrical and one antisymmetrical, are expected ^[32, 85, 87].

The following investigation has been devoted to the fluororhodium complex *trans*-[RhF(C₂H₄)(PiPr₃)₂] (**17**), which was synthesized by Juan Gil-Rubio in the work group of Prof. Werner. The complex **17** is the perfect candidate for the completion in our assignment of the $\nu(\text{ML})$ modes. By analogy to the vinylidene and carbonyl complexes, the model compound *trans*-[RhF(C₂H₄)(PMe₃)₂] has been used for the assignment of the vibrational spectra.

3.2.1 Experimental and theoretical structures

The POV-Ray ^[62] draw of the model compound *trans*-[RhF(C₂H₄)(PMe₃)₂] is depicted in Figure 23 and its structural parameters which were calculated using the DFT1-3 and DFT5, are summarized in Table 12 together with the experimental values found for *trans*-[RhF(C₂H₄)(PiPr₃)₂] (**17**) ^[91]. The calculated Rh-F and Rh-P bond distances are similar to the experimental values found in the related fluororhodium complex **17**.

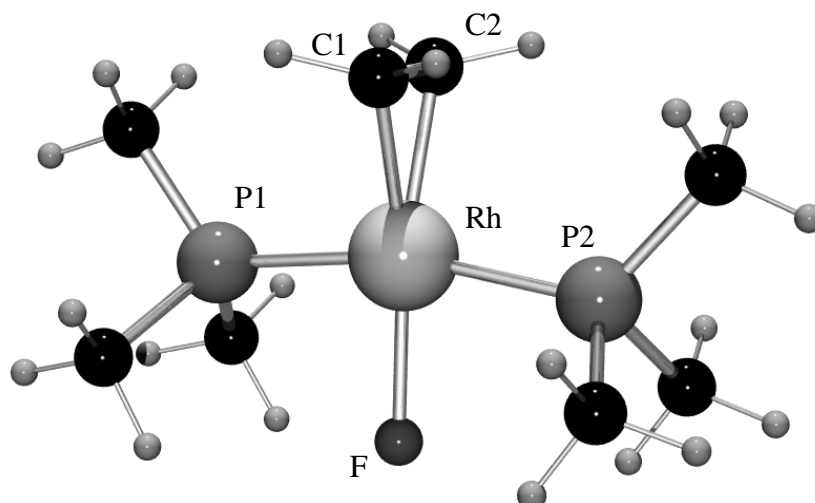


Figure 23. Optimized structure of *trans*-[RhF(C₂H₄)(PMe₃)₂] using BPW91/LANL2DZ (DFT1) method.

The theoretical C1-Rh-C2 angle for all the method agrees very well with the experimental value measured at 38.4° (Table 12). Figure 23 reveals that the ligand sphere around the metal centre is slightly distorted square-planar with moderate bending of the phosphine ligand toward the fluoride. The structure is thus quite similar to that of the carbonyl and vinylidene complexes for which also a non-linear P1-Rh-P2 axis exist. The Rh-F bond length of **17** (206.0(3) pm) (Table 12) is nearly identical to that of the before-mentioned carbonyl compound *trans*-[RhF(CO)(PPh₃)₂] (204.6(2) pm).

One may notice that the calculated geometry for the model compound *trans*-[RhF(C₂H₄)(PMe₃)₂] is in best agreement with the experimental one found for **17** when DFT3 and DFT5 have been used. There is a minor difference between the Rh-C bond lengths of **17** (209.6(5) and 210.3(5) pm) and of the analogous chloro complex *trans*-[RhCl(C₂H₄)(PiPr₃)₂] (211.6(2) and 212.8(2) pm)^[92]. For the model compound *trans*-[RhCl(C₂H₄)(PMe₃)₂] the Rh-C bond lengths have been calculated at 212.2 and 212.9 pm, respectively, which indicate that in the fluoro complex the bond between ethene and the metal is somewhat stronger. A larger difference exists between the C1-C2 distance of the ethene ligand in **17** (138.0(8) pm) and of the chloro counterpart (131.9(4) pm) resulting from a higher degree of back bonding from rhodium to the olefin in **17**. As the electron density on the metal is increased the back donation component is enhanced and the double bond character of the ethene is reduced. This is reflected in a longer (and weaker C-C) bond and a bending back of the substituents on the carbon atoms. As expected, the fluorine halogenid shows a lower *trans* influence than chlorine and permits a stronger push-pull effect to the π*-orbital of ethene.

Table 12. Selected bond lengths (pm) and angles (degrees) of *trans*-[RhF(C₂H₄)(PMe₃)₂] (calculated) and *trans*-[RhF(C₂H₄)(PiPr₃)₂] (experimental).

	<i>trans</i> -[RhF(C ₂ H ₄)(PMe ₃) ₂]				<i>trans</i> -[RhF(C ₂ H ₄)(PiPr ₃) ₂] (17)
	Bond lengths (pm)				
	DFT1	DFT2	DFT3	DFT5	Exp. ^a
Rh-P1	237.4	233.3	230.7	231.5	232.6(2)
Rh-P2	237.4	233.3	230.7	231.5	232.8(2)
Rh-F	206.7	207.2	205.8	204.7	206.0(3)
Rh-C1	213.9	212.1	212.1	211.8	209.6(5)
Rh-C2	214.6	212.4	212.3	212.0	210.3(5)
C1-C2	144.2	143.1	142.5	142.8	138.0(8)
	Bond angles (°)				
	DFT1	DFT2	DFT3	DFT5	Exp. ^a
P1-Rh-P2	164.8	165.8	166.4	166.6	169.5(5)
F-Rh-C1	160.0	159.5	159.7	159.5	160.4(2)
F-Rh-C2	160.6	161.1	161.1	161.1	161.2(2)
P1-Rh-F	82.4	82.9	83.2	83.3	85.7(9)
P2-Rh-F	82.4	82.9	83.2	83.3	84.7(9)
P1-Rh-C1	97.1	96.7	96.4	96.3	93.8(2)
P2-Rh-C1	97.1	96.7	96.4	96.3	93.8(2)
P1-Rh-C2	97.2	96.7	96.4	96.3	95.6(2)
P2-Rh-C2	97.2	96.7	96.4	96.3	94.8(2)
C1-Rh-C2	39.4	39.4	39.2	39.4	38.4(2)

^aReference 91.

3.2.2 Vibrational spectroscopy

3.2.2.1 Vibrational spectrum of *trans*-[RhF(C₂H₄)(PiPr₃)₂] (**17**)

The calculated fundamental modes for the model compound *trans*-[RhF(C₂H₄)(PMe₃)₂] are summarized (Table 13) and depicted (Table 14) together with their tentative assignment and the experimental values which have been measured for compound **17**.

The calculations carried out for the model compound *trans*-[RhF(C₂H₄)(PMe₃)₂] suggested that compound **17** is best described by the second model (see 3.2), since two ν(RhC) modes

were obtained, both weakly coupled with the $\nu(\text{RhF})$ vibration. The calculated wavenumbers were 514 (antisymmetric) and 471 (symmetric) cm^{-1} .

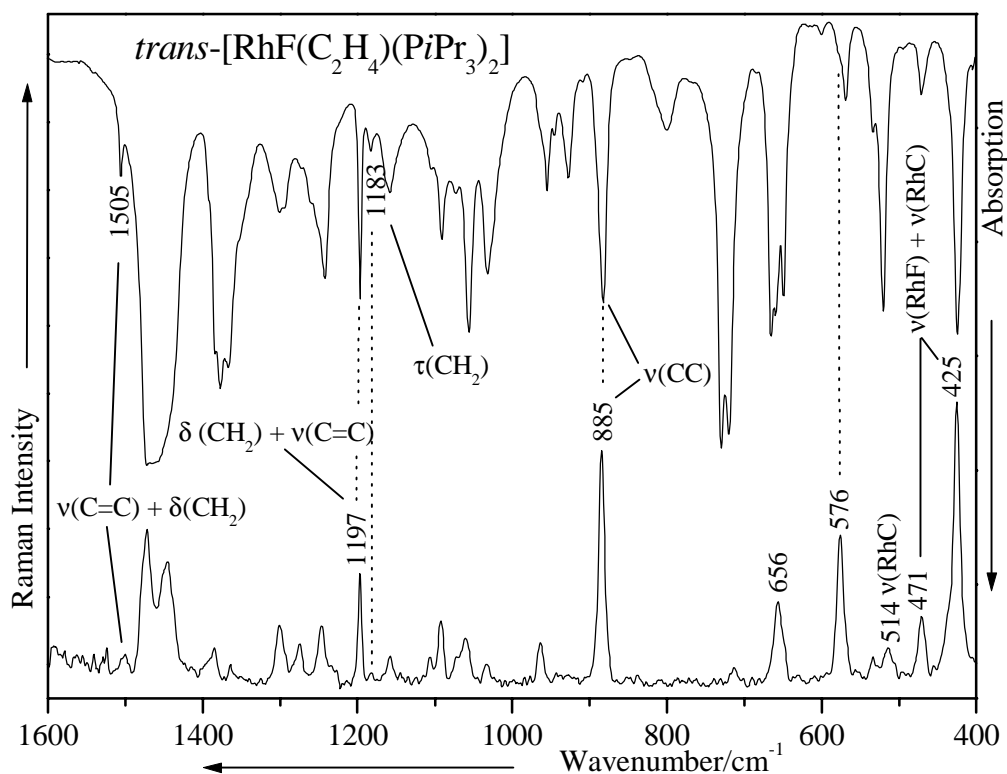


Figure 24. The IR and FT-Raman spectra of *trans*-[RhF(C₂H₄)(PiPr₃)₂] (**17**).

A vibration which is mainly a $\nu(\text{Rh-F})$ stretching in character was calculated at 409 cm^{-1} . The band observed in the FT-IR and FT-Raman spectra of **17** at 514 cm^{-1} (Figure 24) was tentatively assigned to the antisymmetric Rh-C₂H₄ stretching mode. The intense and medium bands at 425 and 471 cm^{-1} , respectively, could be due to the Rh-F and the symmetric Rh-C₂H₄ stretching modes. One may notice that these bands lie in the same region as these of the fluororhodium complexes *trans*-[RhF(C₂H₂)(PCy₃)₂] and *trans*-[RhF(PhC≡CPh)(PCy₃)₂] (421 and 462 cm^{-1} , respectively) which were ascribed to the $\nu(\text{RhF})$ stretching mode^[93].

Some bands are observed as for the vinylidene and carbonyl complexes in the FT-IR and FT-Raman spectrum between 534 and 432 cm^{-1} . These bands could be assigned to (CC₃)-, (CPC)-deformation modes. The $\nu(\text{C}=\text{C})$ vibrational mode for complex **17** was observed at 1505 cm^{-1} in the IR- and FT-Raman spectrum (Figure 24). This value is close to the calculated one (1495 cm^{-1} , DFT1) for the model compound *trans*-[RhF(C₂H₄)(PMe₃)₂]. The $\nu(\text{C}=\text{C})$ wavenumber is 117 cm^{-1} lower than that of gaseous ethylene (1623 cm^{-1})^[94] and also slightly lower than that of the $\nu(\text{C}=\text{C})$ band of [RhCl(C₂H₄)(PiPr₃)₂] (1510 cm^{-1})^[92].

Table 13. Selected calculated and experimental vibrational wavenumbers (cm^{-1}) for *trans*-[RhF(C₂H₄)(PMe₃)₂] and *trans*-[RhF(C₂H₄)(PiPr₃)₂] complexes together with their tentative assignment.

<i>trans</i> -[RhF(C ₂ H ₄)(PiPr ₃) ₂]		<i>trans</i> -[RhF(C ₂ H ₄)(PMe ₃) ₂]				Assignment
R	IR	DFT1	DFT2	DFT3	DFT5	
1501w	1505m	1495	1501	1480	1510	$\nu(\text{C}=\text{C}) + \delta(\text{CH}_2)$
1438sh.m	1438br.sh	1436	1419	1424	1439	$\delta(\text{CH}_2)$
1197s	1197s	1188	1187	1198	1197	$\delta(\text{CH}_2) + \nu(\text{C}=\text{C})$
1183w	1183w	1180	1168	1164	1184	$\tau(\text{CH}_2)$
885vs	882s					$\nu(\text{CCC})_{\text{PiPr}_3}$
	801m	791	782		712	$\rho(\text{CH}_2)$
	665vs					$\nu(\text{PC}_3)$
656m	659vs	620	642	646	642	
648m	650vs	615	636	639	635	
576s	576mw					
514m	514mw	470	477	492	494	$\nu_{\text{as}}(\text{Rh}-\text{C}_2\text{H}_4)$
471m	471m	456	448	466	468	$\nu_{\text{s}}(\text{Rh}-\text{C}_2\text{H}_4) + \nu(\text{RhF})$
425vs	425vs	409	404	419	423	$\nu(\text{RhF}) + \nu_{\text{s}}(\text{Rh}-\text{C}_2\text{H}_4)$
349w		320	330	337	337	$\nu(\text{RhP})$
306m		319	312	311	316	$\nu(\text{RhP})$

It should be noted that the $\nu(\text{C}=\text{C})$ stretching mode which is calculated at 1516 cm^{-1} (DFT5) for the model complex *trans*-[RhCl(C₂H₄)(PMe₃)₂] is in good agreement with this experimental result. This result is consistent with the observed C=C bond distances: 131.9(4) pm for the chloro complex^[92] and 138.0(8) pm for the fluoro analogous one^[91]. Nevertheless, only the decrease in the $\nu(\text{C}=\text{C})$ wavenumber alone can not be used as a measure of the M-C₂H₄ bond strength, since the calculations carried out on [PtCl₃(C₂H₄)]^[85], [PdCl₃(C₂H₄)]^[88] and on our model complex *trans*-[RhF(C₂H₄)(PMe₃)₂] show that the $\nu(\text{C}=\text{C})$ stretching vibration is strongly coupled with the in-plane CH₂ scissoring mode (Figure 25). The band at 1197 cm^{-1} , which did not appear in the FT-Raman spectrum of **1**, was attributed to the $\delta(\text{CH}_2)$ mode of the ethylene ligand. For the model complex *trans*-[RhX(C₂H₄)(PMe₃)₂], this band was calculated at 1188 (X = F) and 1198 cm^{-1} (X = Cl) and is also strongly coupled with the $\nu(\text{C}=\text{C})$ mode (Figure 25).

Finally, it is noteworthy, that the *trans* influence in *trans*-[RhX(C₂H₄)(PCy₃)₂] (X = F, Cl, Br, I) has been already examined by Van Gaal^[93] using the infrared and NMR spectroscopy.

Their assignment was restricted to the $\nu(\text{C}=\text{C})$ and $\delta(\text{CH}_2)$ vibrational modes.

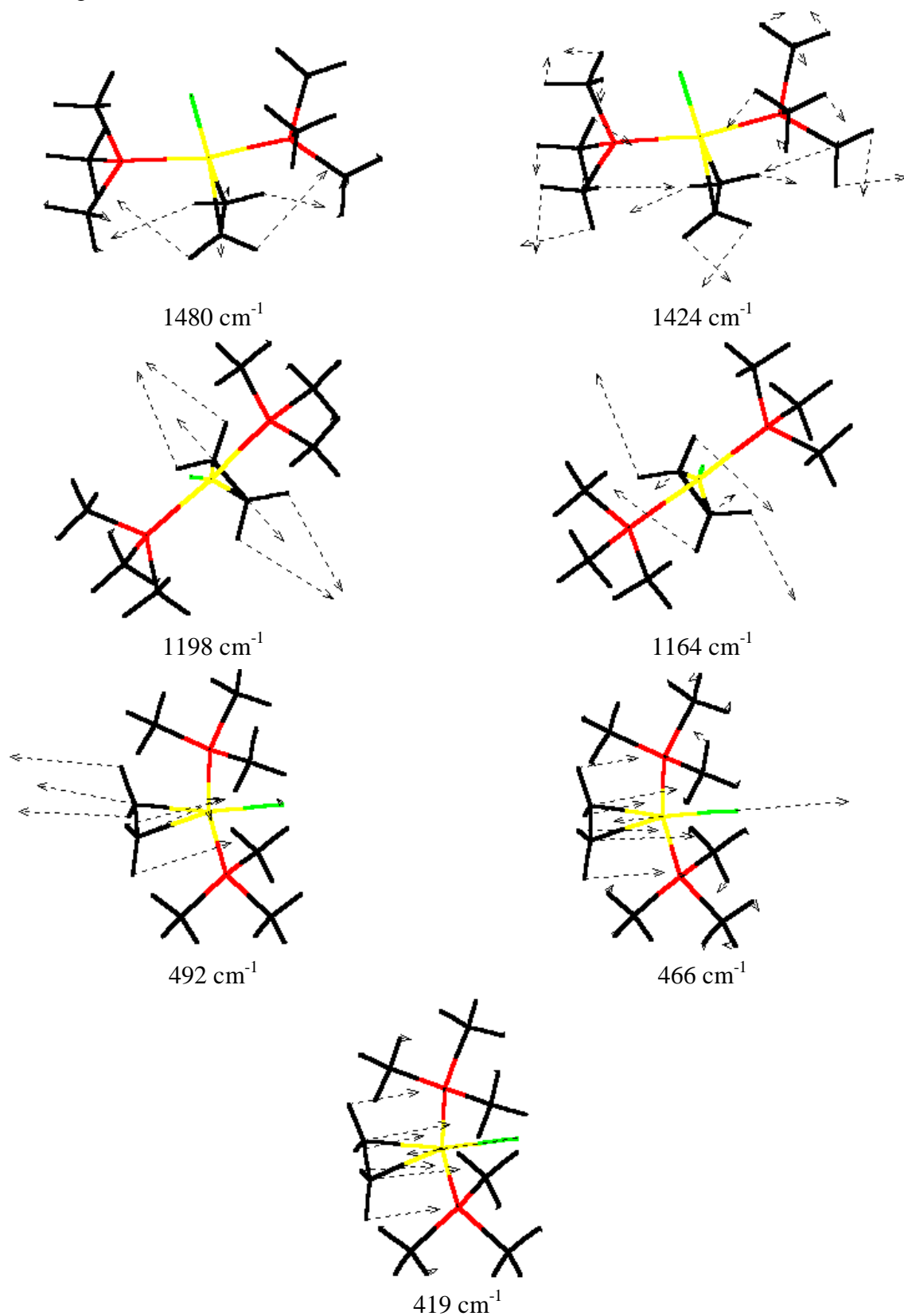


Figure 25. Representation of selected calculated vibrational modes for *trans*- $[\text{RhF}(\text{C}_2\text{H}_4)(\text{PMe}_3)_2]$ using DFT3.

Therefore, the substitution of the fluorine atom by chlorine or iodine in the ethylene complex **17**, should lead as in the vinylidene and carbonyl complexes to a red shift of the $\nu(\text{RhC})$ stretching modes, which will support the assignment of the MC-modes. For the model compound *trans*-[RhCl(C₂H₄)(PMe₃)₂] the $\nu_s(\text{Rh-C}_2\text{H}_4)$ and $\nu_{as}(\text{Rh-C}_2\text{H}_4)$ stretching modes are predicted at 437 and 485 cm⁻¹ using DFT5, respectively, which is in agreement with the previous results. Moreover, the bands observed at 666 and 668 cm⁻¹ in the FT-Raman spectrum of complexes **1** and **12**, respectively, shifts to lower wavenumbers (656 cm⁻¹) in the FT-Raman spectrum of **17** (Figure 24). This band, which has been attributed to the $\nu(\text{PC}_3)$ mode, support the strengthening of the Rh-C bond in the order C₂H₄ > C₂H₂ > CO and is consistent with the previous results.

3.3 Isonitrile rhodium(I) complexes *trans*-[$\{\text{RhX}(\text{PiPr}_3)_2\}_2\{\mu\text{-1,3-}(\text{CN})_2\text{C}_6\text{H}_4\}$] ($X = \text{Cl, I}$)

While the vibrational spectra of metal carbonyls have been extensively studied^[95], there have been only a few reports about the spectra of isoelectronic isocyanide complexes. Moreover, previous spectroscopic studies of these compounds containing M(CNR) or M(CNR)₂ as a molecular unit have been mainly restricted to the assignment of the $\nu(\text{CN})$ mode^[96]. Although this mode is rather unsuitable as a probe for obtaining detailed information about the electronic distribution within the isocyanide group^[97], some information about the metal-ligand bond has been derived by comparing the value of the $\nu(\text{CN})$ mode for an isocyanide-metal complex with that of the free ligand. In principle, the same information should be provided by analyzing the $\nu(\text{MC})$ or $\delta(\text{MCN})$ modes which, unfortunately, have been assigned only in the case of some cobalt(I), cobalt(II)^[44, 98], iron(II), manganese(I)^[99] and platinum(II) isocyanides^[100-101]. For rhodium(I) as the metal center, Jones and Hessel have described the preparation and molecular structure of the square-planar complexes *trans*-[RhCl(CNR)(PiPr₃)₂] with R = neopentyl and 2,6-xylyl and have also assigned the $\nu(\text{CN})$ modes of these compounds^[102].

By taking into consideration the scarce information about the vibrational spectra of transition-metal isocyanides, the aim of the following part is to assign the bands in the low wavenumber region of the FT-Raman spectra of compounds *trans*-[RhX(CNR)(PiPr₃)₂] and, in particular, to identify the $\nu(\text{Rh}=\text{C})$ stretching mode. The wavenumber of this mode should be compared

with the corresponding vibration of isoelectronic carbonyl and vinylidene complexes, thereby taking advantage of the influence of different halide ligands in *trans*-position to the isocyanide on the Rh–CNR bond. In support of the spectroscopic data, DFT calculations were carried out for the model compounds *trans*-[RhX(CNC₆H₅)(PMe₃)₂] (X = F, Cl) and *trans*-[RhF(PR₃)₂]₂{μ-1,3-(CN)₂C₆H₄} (R = H, Me) since they could supply accurate wavenumbers for these molecules.

3.3.1 Experimental and theoretical structures

3.3.1.1 Theoretical structure of *m*-diisocyanobenzene 1,3-(CN)₂C₆H₄

The optimized structure of *m*-diisocyanobenzene, which has been calculated using the BPW91/6-31+G(d) method, is presented in Figure 26.

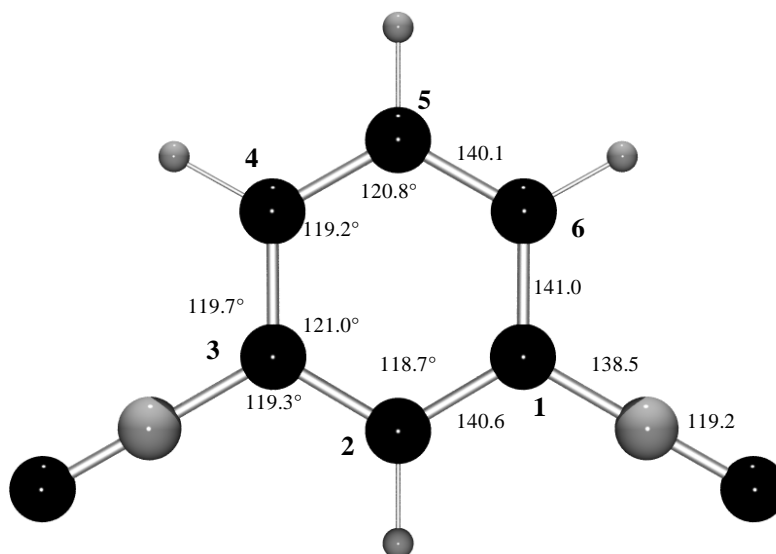


Figure 26. Optimized structure of 1,3-(CN)₂C₆H₄ using BPW91/6-31+G(d) method.

To the best of our knowledge, the molecular structure of 1,3-(CN)₂C₆H₄ in the crystal is unknown and can therefore not be compared with the structural parameters obtained by the calculations. The theoretical bond distances and bond angles of 1,3-(CN)₂C₆H₄ are depicted on Figure 26.

3.3.1.2 Structure of *trans*-[$\{\text{RhCl}(\text{P}i\text{Pr}_3)_2\}_2\{\mu\text{-1,3-(CN)}_2\text{C}_6\text{H}_4\}$] (**18**)

The solid state structure of the dinuclear complex **18** was determined by single-crystal X-ray crystallography and is reported by Berta Callejas-Gaspar in her PhD-Thesis ^[53]. One may notice, that the structure of **18** reveals only a C_2 axis of rotation.

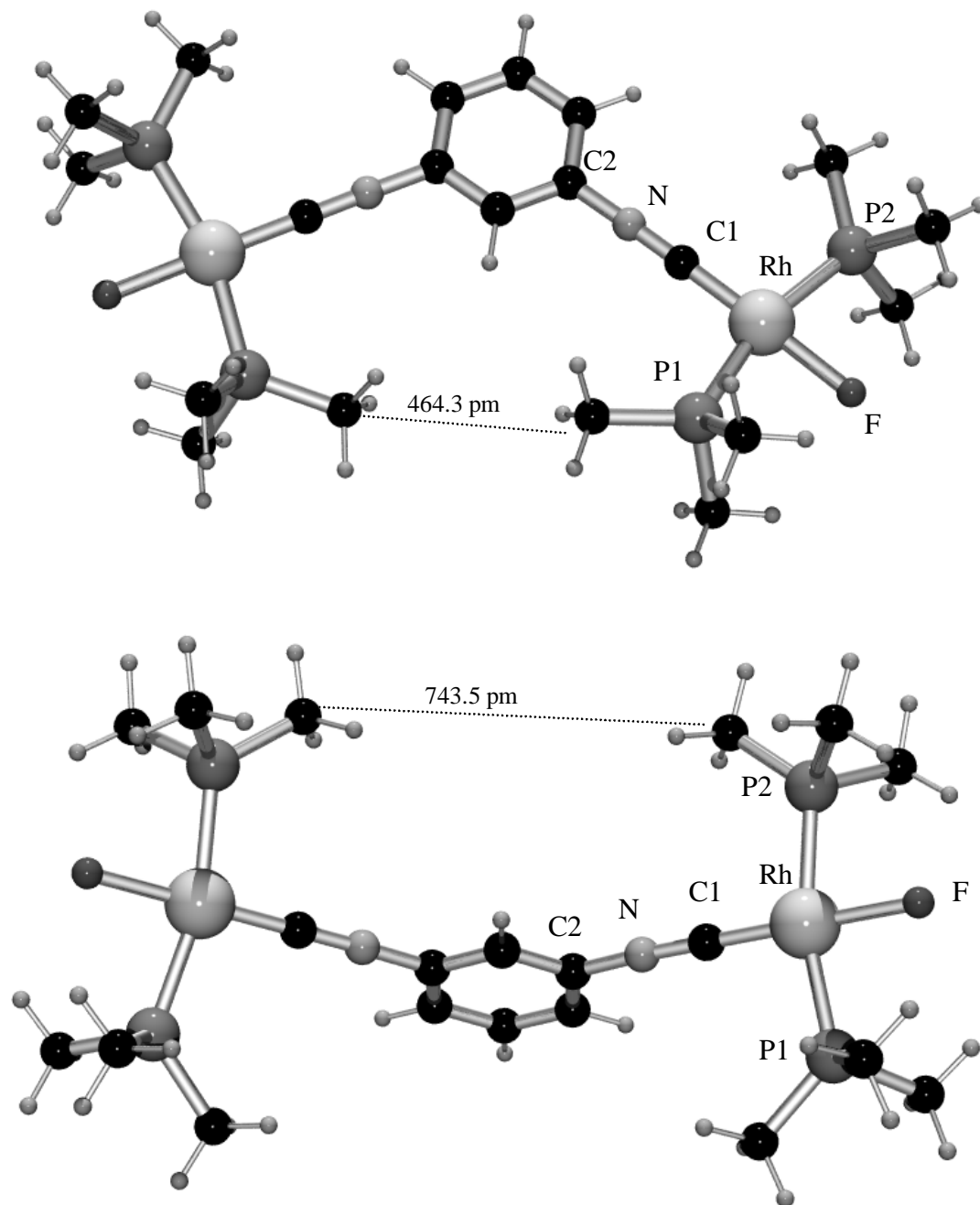


Figure 27. Optimized structures of $\text{trans-}[\{\text{RhF}(\text{PMe}_3)_2\}_2\{\mu\text{-1,3-(CN)}_2\text{C}_6\text{H}_4\}]$ using DFT1. ($E_{\text{BPW91}} = -1340.59054244$ and -1340.589498 hartree, respectively)

Furthermore, the geometry around the two rhodium centers is exactly square-planar (bond angles P1-Rh-P2 178.27(3)° and C1-Rh-Cl 178.42(10)°) with the two phosphines as well as the isocyanide carbon and the chloride in *trans* disposition.

DFT calculations were carried out on the model compounds *trans*-[RhX(L)(PMe₃)₂] (L = CNC₆H₅, X = F, Cl) and *trans*-[RhF(PR₃)₂]₂{μ-1,3-(CN)₂C₆H₄} (R = H, Me) at different level of theory. Except for the model compounds *trans*-[RhF(PR₃)₂]₂{μ-1,3-(CN)₂C₆H₄} (R = H, Me) where H and Me were used, the more realistic methyl group has been employed in the calculations to model the isopropyl groups of the existing complexes in order to reduce the computation time.

The calculations carried out on the model complex *trans*-[RhF(PMe₃)₂]₂{μ-1,3-(CN)₂C₆H₄} using DFT1 led to the two conformations shown in Figure 27. Although the energy difference between both structures is only 2.8 kJ/mol and thus insignificant, the structure shown in the lower part of Figure 27 has a negative eigenvalue and does not present an energy minimum. The fact that the molecular structure of **18** in the crystal nevertheless corresponds to the less favored conformation of the model complex is probably due to the high steric hindrance between the methyl groups of the P*i*Pr₃ ligands. This explanation is consistent with the calculated interatomic distance between the nearest carbon atoms of two neighbored PMe₃ units which is 464.3 pm for one conformation and 743.5 pm for the other (Figure 27).

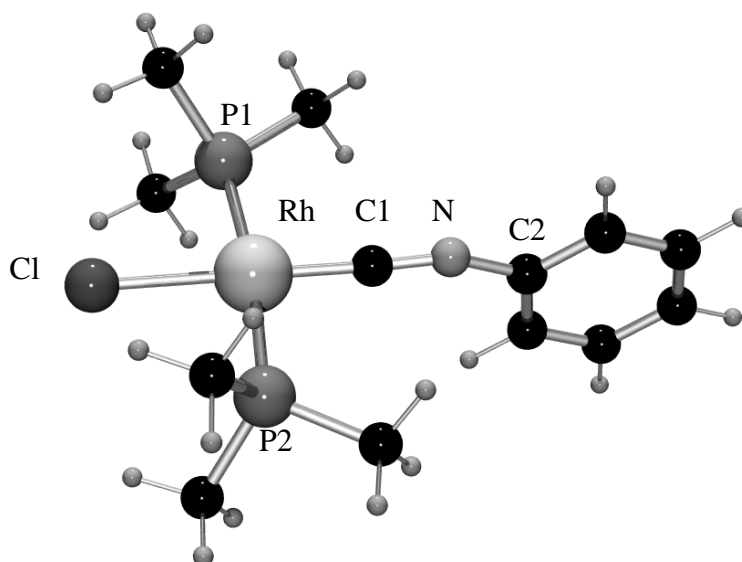


Figure 28. Optimized structure of *trans*-[RhCl(CNC₆H₅)(PMe₃)₂] using DFT2.

In contrast to the dinuclear model compound *trans*-[RhF(PMe₃)₂]₂{μ-1,3-(CN)₂C₆H₄}, where the calculated bond angle C1-N-C2 is 178.8° (see Table 14), the calculations using DFT1 for the mononuclear counterpart *trans*-[RhX(CNPh)(PMe₃)₂] (X = F, Cl) reveal a non

linear C-N-C linkage with a bond angle of 156.2° for X = F and 169.0° for X = Cl. These angles become even smaller (148.4° and 153.5° , respectively) by adding diffuse and polarization functions to the D95 basis set (Figure 28). However, the calculated values match very well with the structural parameters determined for **18** by X-ray diffraction (see Table 14) and this is true not only for the C1-N-C2 and N-C1-Rh bond angles but also for the Rh-C1 and C1-N distances. Except for the Rh-Cl distance, the difference in the bond lengths between the model compound *trans*-[RhCl(CNPh)(PMe₃)₂] and the isolated complex **18** is less than 4 pm. Moreover, we note that both for **18** and the model compound *trans*-[RhCl(CNPh)(PMe₃)₂] the six-membered ring lies nearly perpendicular to the plane formed by the atoms P1, Rh, P2, Cl and C1.

Table 14. Comparison of the calculated bond distances (pm) and angles ($^\circ$) for the model compounds *trans*-[RhX(CNPh)(PMe₃)₂] (X = F, Cl) and *trans*-[RhX(PR₃)₂]₂{ μ -1,3-(CN)₂C₆H₄}] with the experimental values found *trans*-[RhCl(P*i*Pr₃)₂]₂{ μ -1,3-(CN)₂C₆H₄}].

	<i>trans</i> -[RhX(CNC ₆ H ₅)(PMe ₃) ₂]				<i>trans</i> -[RhX(PR ₃) ₂] ₂ { μ -1,3-(CN) ₂ C ₆ H ₄ }]		
	X = F		X = Cl		X = F		X = Cl
	DFT1	DFT2	DFT1	DFT2	R = Me	R = H	R = <i>i</i> Pr
	Bond lengths (pm)						
Rh-X	206.4	206.8	247.4	244.4	206.4	203.0	237.3(1)
Rh-C1	183.9	182.9	184.7	183.9	184.8	185.9	180.3(3)
Rh-P1	237.8	233.6	238.9	234.7	237.6	236.2	234.7(1)
Rh-P2	237.8	233.6	238.9	234.7	237.6	236.2	233.5(1)
C1-N	122.8	122.3	122.0	121.7	122.0	121.6	120.6(4)
N-C2	139.1	138.9	138.5	138.6	137.8	138.0	138.0(4)
	Bond angles ($^\circ$)						
X-Rh-C1	179.3	179.8	179.1	179.8	178.6	179.2	178.4(1)
P1-Rh-P2	165.3	167.4	171.2	172.6	164.5	167.3	178.27(3)
Rh-C1-N	177.2	175.6	178.8	176.1	179.0	179.5	175.0(3)
C1-N-C2	156.2	148.4	169.0	153.5	178.8	177.7	152.4(3)
C1-Rh-P2	97.3	96.3	94.4	93.7	97.8	96.4	88.4(9)
C1-Rh-P1	97.3	96.3	94.4	93.7	97.7	96.2	90.1(1)
P1-Rh-X	82.7	83.7	85.6	86.3	81.4	82.9	89.24(3)
P2-Rh-X	82.7	83.7	85.6	86.3	83.1	84.4	92.29(3)

^aReference 53

In comparison with the free ligand 1,3-(CN)₂C₆H₄, where the C-N bond length was calculated at 119.2 pm using BPW91/6-31+G(d), the corresponding experimental value for complex **18** is 120.6(4) pm and the calculated value for the model compound *trans*-[RhF(PMe₃)₂]₂{μ-1,3-(CN)₂C₆H₄} using DFT1 is 122.0 pm. The N-C(C₆H₄) bond length in the model compound *trans*-[RhF(PMe₃)₂]₂{μ-1,3-(CN)₂C₆H₄} and in complex **18** is slightly shorter than the calculated distance for the free ligand 1,3-(CN)₂C₆H₄ and this is true also for the C-C distances in the phenylene ring. The small increase in the C-N and small decrease in the N-C(C₆H₄) bond lengths following the coordination of 1,3-(CN)₂C₆H₄ to the metal is consistent with the π-acceptor character of the diisocyanide ligand.

An interesting finding concerning the Rh-P bonding has been reported by Landis et al.^[103]. They have shown that the Rh-P bond strength is largely determined by the relative importance of Rh→PR₃ (σ) and Rh→PR₃ (π) bonding, which varies with the nature of the other ligands attached to Rh. In the presence of a good π-acceptor ligand (such as CO), the Rh-P bond strengths increase with phosphorus σ-donor strength. In the opposite situation, the Rh-P bond strengths increase with π-accepting capacity of phosphorus. The *trans*-[RhF(PR₃)₂]₂{μ-1,3-(CN)₂C₆H₄} (R = H, Me) system shows the same trend as observed by Landis et al.^[103]. The Rh-PR₃ and Rh-F interatomic distances become longer as increasingly σ-donating ligands are used on PR₃, whereas the Rh-CN bond shorten (Table 14). Of course, these behaviors are consistent with the expectation that increasing the donor ability of PR₃ will enhance the Rh→CN π-back-bonding. Taking these observations into consideration, the use of Me instead of H to simulate the P*i*Pr₃ leads to more realistic results.

3.3.2 Vibrational Spectroscopy

3.3.2.1 Vibrational spectrum of *m*-diisocyanobenzene 1,3-(CN)₂C₆H₄

Whereas the molecular structures and the vibrational spectra of benzonitrile and dicyanobenzenes have been extensively investigated extensively^[104-106], neither the Raman spectrum of the solid *m*-diisocyanobenzene has been reported in the literature. Moreover, there are only a few studies based on the IR and Raman investigations of substituted and unsubstituted phenylisocyanides^[107-108]. Therefore, the FT-Raman spectrum of *m*-diisocyanobenzene has been here reported and its assignment has been supported using the BPW91/6-31+G(d) method. The Raman intensities for the normal modes of 1,3-(CN)₂C₆H₄ have been also calculated and are listed in Table 15.

In the high wavenumber region of the spectrum of 1,3-(CN)₂C₆H₄, four bands, corresponding to the $\nu(\text{CH})$ modes, have been observed at 3074, 3052, 3043 and 3014 cm⁻¹. The calculated positions of these bands are 3176, 3165, 3162 and 3142 cm⁻¹. It is well known that theoretical $\nu(\text{CH})$ are about 2-6% higher than the experimental values. The very strong band at 3074 cm⁻¹, can be here assigned to the ν_2 mode (Wilson notation ^[109]). The symmetric and antisymmetric $\nu(\text{CN})$ modes for 1,3-(CN)₂C₆H₄ were calculated at 2119 and 2116 cm⁻¹ and observed at 2147, 2130 and 2117 cm⁻¹, respectively. One may notice that in comparison to the isomer 1,3-C₆H₄(CN)₂, the $\nu(\text{CN})$ modes for 1,3-(CN)₂C₆H₄ are about 100 cm⁻¹ red shifted ^[104-106], while for the $\nu(\text{C}=\text{C})$ modes (observed at 1609, 1598 and 1586 cm⁻¹) a small blue shift is observed (Figure 29).

Singh assigned the $\nu(\text{C}-\text{CN})$ modes to the bands at 1248 and 900 cm⁻¹ in the Raman spectrum of *m*-dicyanobenzene ^[106]. For the diisocyanide 1,3-(CN)₂C₆H₄, the $\nu(\text{C}_{\text{ring}}-\text{NC})$ vibrational modes have been calculated at 1235, 1131 and 913 cm⁻¹ and the bands observed at 1227 and 1132 and 911 cm⁻¹ are assigned to these modes. The animation of the calculated symmetric and antisymmetric $\nu(\text{C}_{\text{ring}}-\text{NC})$ mode (1235 and 913 cm⁻¹) confirms that they are mixed with both a ring bending $\delta(\text{CCC})$ and a ring deformation vibration. However, the calculated $\nu(\text{C}_{\text{ring}}-\text{NC})$ mode at 1131 cm⁻¹ shows mainly an antisymmetric character slightly mixed with a $\delta(\text{CH})$ bending of the ring. Several bands of medium or medium-to-weak intensities, observed in the spectrum of 1,3-(CN)₂C₆H₄ at 1179 (calc. 1171), 1132 (calc. 1131) and 1089 (calc. 1090) cm⁻¹, can be tentatively assigned to in-plane CH bending modes. The very strong and weak bands at, respectively, 1000 and 991 cm⁻¹ (the calculated positions being 987 and 955 cm⁻¹), probably correspond to the ring breathing and to an out-of-plane CH deformation mode. In agreement with the DFT calculations, the bands in the low wavenumber region at 594 (calc. 610 cm⁻¹) and 426 cm⁻¹ (calc. 422 cm⁻¹) should be attributed to the out-of-plane and in-plane $\delta(\text{CNC})$ modes, respectively (Figure 30). The out-of-plane bending $\delta(\text{CNC})$ is mixed with an out-of-plane CH and ring deformations.

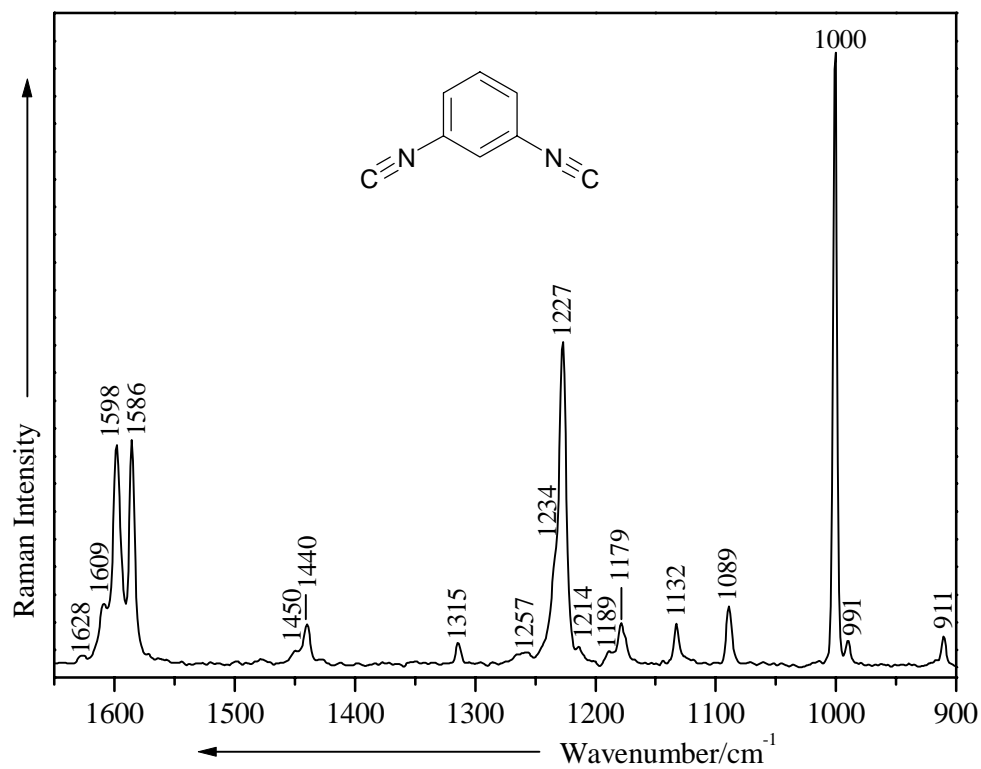


Figure 29. The FT-Raman spectrum of 1,3-(CN)₂C₆H₄ between 1650 and 900 cm⁻¹.

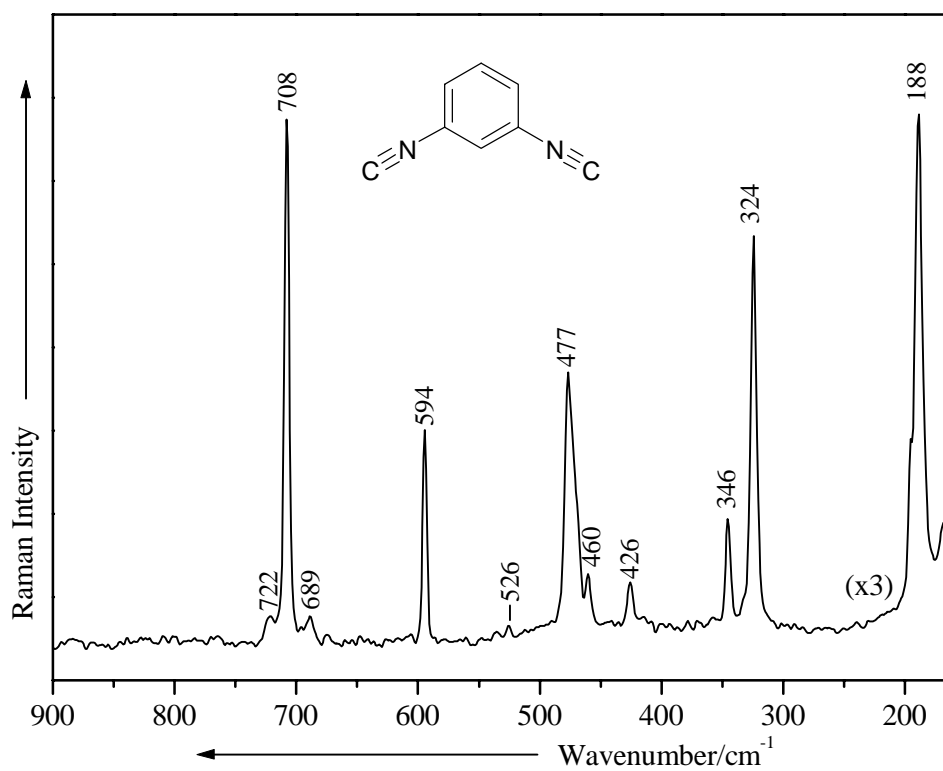


Figure 30. Low wavenumber region of the FT-Raman spectrum of 1,3-(CN)₂C₆H₄.

Table 15. Comparison of the calculated and observed vibrational modes of 1,3-(CN)₂C₆H₄.

1,3-(CN) ₂ C ₆ H ₄				
Exp.	<i>I</i> _{Ra}	BPW91/6-31+G(d)	<i>I</i> _{Ra} (Å ⁴ /amu)	Assignment
3074	vs	3167	182.4	v(CH)
3053	w	3175	62.8	
3043	w	3162	73.0	
3014	w	3142	76.5	
2147	m			v(CN)
2130	vs	2119	904.6	
2117	ms	2116	314.7	
1609	m			v(C=C)
1598	s	1600	111.0	
1586	s	1580	58.5	
1450	w	1478	4.0	δ(CH)
1440	m	1429	12.2	
1315	m	1351	5.0	v(C-C)
1234	shs			
1227	s	1235	126.4	v(N-C _{ring}) _s + δ(CH) + δ(CCC)
1214	w			
1189	w			
1179	m	1171	1.0	δ(CH) i.p.
1132	m	1131	7.3	v(N-C _{ring}) _{as} + i.p. δ(CH)
1089	m	1090	1.6	i.p. δ(CH)
1000	vs	986	53.9	ring breathing
991	mw	955	0.1	o.o.p.δ(CH)
911	mw	913	0.9	v(N-C _{ring}) _{as} + ring def.
708	vs	700	12.2	ring def. δ(CCC)
689	vw	667	0.1	ring. tor.
594	m	610	2.8	o.o.p δ(CNC) + o.o.p ring def.
526	vw	529	0.3	o.o.p δ(CNC) + ring tor.
477	ms	468	9.5	δ(CCC) ring def.
460	m	462	3.3	ω(CNC) + ring tor.
426	m	422	0.9	i.p. δ(CNC)
346	ms	349	0.8	o.o.p δ(CNC) + o.o.p ring def.
324	s	325	4.9	
188	vs	178	3.6	ω(CCN) + ring tor.

3.3.2.2 Vibrational spectrum of *trans*-[$\{\text{RhX}(\text{P}i\text{Pr}_3)_2\}_2\{\mu\text{-1,3-(CN)}_2\text{C}_6\text{H}_4\}$] ($\text{X} = \text{Cl, I}$) (**18-19**)

The comparison between the FT-Raman and FT-IR spectra of the two rhodium compounds **18** and **19** reveal several significant band shifts, which allow a proper assignment of the fundamental vibrational modes (Figures 31-33).

The $\nu(\text{C}\equiv\text{N})$ stretching vibration appearing in the FT-Raman spectrum of **18** as a very broad band with a maximum at 1987 cm^{-1} , is shifted to higher wavenumbers by replacing chloride with iodide and is assigned in the Raman spectrum of **19** to the strong and medium bands at 1998 and 2035 cm^{-1} , respectively. The assignment of the $\nu(\text{C}\equiv\text{N})$ in the FT-IR spectrum of **18** is more complicated since it appears as a very broad band between 1935 and 2033 cm^{-1} . Moreover, several bands of weak and strong intensities are observed at, respectively 2101 , 2041 , 1929 and 1913 cm^{-1} and at 2093 , 2035 , 1924 and 1903 cm^{-1} in the FT-IR spectra of **18** and **19**, and are tentatively attributed to combination vibrations. It is noteworthy that in comparison with **19** all these modes are shifted to higher wavenumbers in the spectrum of **18**. These modes probably result from a combination between the ring and the CN vibrations, since the diisocyanide unit is located between two very significant rigid masses.

Although owing to the broadness of the band at 1987 cm^{-1} it might be questionable to draw a conclusion about the shift by going from **18** to **19**, the calculated value obtained for the model compounds *trans*-[$\{\text{RhF}(\text{PMe}_3)_2\}_2\{\mu\text{-1,3-(CN)}_2\text{C}_6\text{H}_4\}$] (2056 and 2031 cm^{-1} , DFT1), *trans*-[$\text{RhF}(\text{CNPh})(\text{PMe}_3)_2$] (1987 cm^{-1} , DFT1) and *trans*-[$\text{RhCl}(\text{CNPh})(\text{PMe}_3)_2$] (2000 cm^{-1} , DFT2) match well with the experimental results. Moreover, the shift of the $\nu(\text{C}\equiv\text{N})$ stretching vibration for complexes **18** and **19** to lower wavenumbers compared with the Jones compounds *trans*-[$\text{RhCl}(\text{CNCH}_2\text{C}(\text{CH}_3)_3)(\text{P}i\text{Pr}_3)_2$] (2056 and 2032 cm^{-1}) and *trans*-[$\text{RhCl}(\text{CN-2,6-xylyl})(\text{P}i\text{Pr}_3)_2$] (2047 and 2016 cm^{-1})^[102] also agrees with the different C1-N and N-C2 bond lengths found by X-ray structure analyses.

The next significant shifts, which have been observed in the fingerprint region of the FT-Raman spectrum of compounds **18** and **19**, correspond to the $\nu(\text{C}=\text{C})$ and $\nu(\text{N-C}_{\text{ring}})$ stretching modes. The band of high intensity at 1583 (for **18**) and 1577 cm^{-1} (for **19**) is assigned to the $\nu(\text{C}=\text{C})$ vibrational mode and is slightly shifted to lower energy due to the stronger *trans* influence of the iodo ligand. The medium or strong bands at 1149 and 1268 cm^{-1} (for **18**) and at 1144 and 1263 cm^{-1} (for **19**) (see Figure 31), which have been observed at 1132 (calc. 1131) and 1227 (calc. 1235) cm^{-1} in the FT-Raman spectrum of the free ligand $1,3\text{-(CN)}_2\text{C}_6\text{H}_4$, are assigned to the $\nu_{\text{as}}(\text{N-C}_{\text{ring}})$ and $\nu_{\text{s}}(\text{N-C}_{\text{ring}})$ stretching modes, respectively.

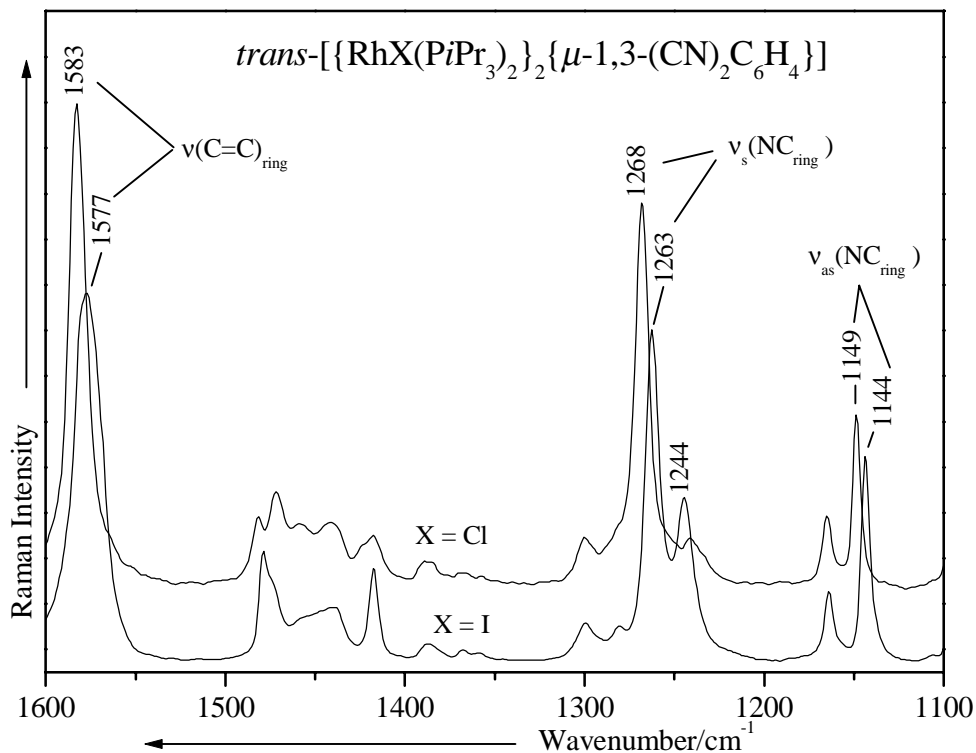


Figure 31. FT-Raman spectrum of $trans-[[RhCl(PiPr_3)_2]_2\{\mu-1,3-(CN)_2C_6H_4\}]$ (**18**) and $trans-[[RhI(PiPr_3)_2]_2\{\mu-1,3-(CN)_2C_6H_4\}]$ (**19**) between 1600 and 1100 cm⁻¹.

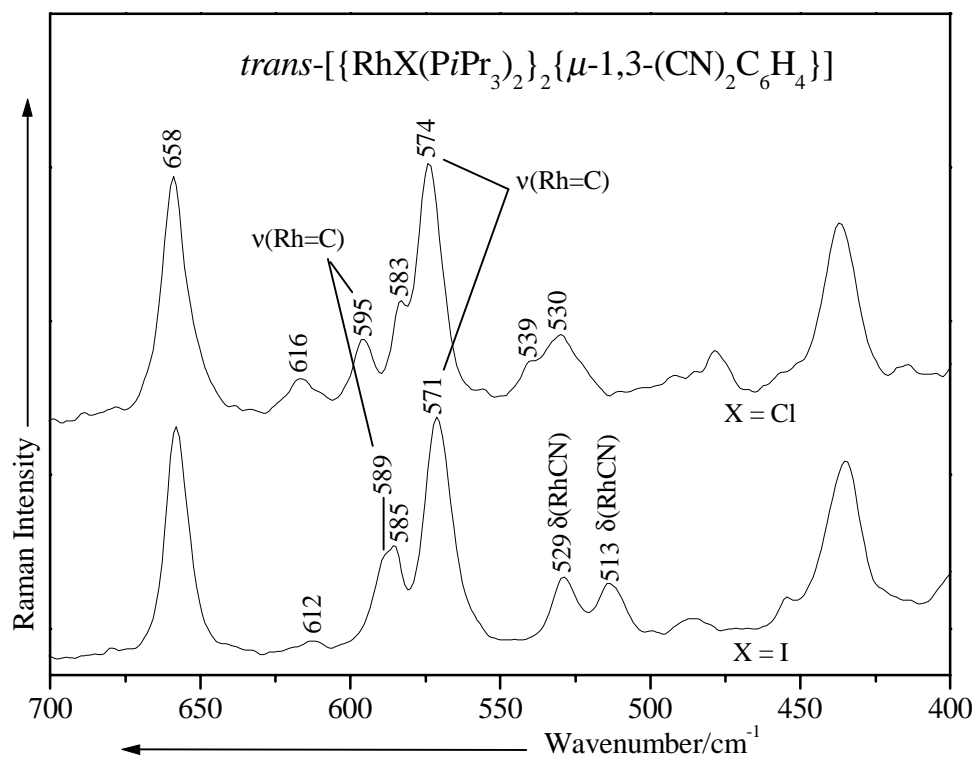


Figure 32. Low wavenumber region of the FT-Raman spectrum of $trans-[[RhCl(PiPr_3)_2]_2\{\mu-1,3-(CN)_2C_6H_4\}]$ (**18**) and $trans-[[RhI(PiPr_3)_2]_2\{\mu-1,3-(CN)_2C_6H_4\}]$ (**19**).

Regarding the $\nu(\text{N-C}_{\text{ring}})$ vibration, there is a remarkable analogy between the rhodium isocyanides **18** and **19** and the corresponding vinylidene complexes **6-9**. For the latter, the $\nu(\text{C-C}_{\text{ring}})$ vibrational mode was assigned on the basis of DFT calculations to the strong band at 1225 and 1220 cm^{-1} in the FT-Raman spectrum of **7** and **9**, respectively. Again, the influence of the ligand *trans*-disposed to the vinylidene unit is quite obvious. In this context it should also be mentioned that the calculated Rh-C bond length for the model compound *trans*-[RhCl(C=CHPh)(PMe₃)₂], using the DFT2 method is 181.1 pm and thus almost identical to that found for the isocyanide complex **18** (180.3(3) pm). Therefore it is not surprising that as illustrated in Figure 34 the FT-Raman spectra of **18** and *trans*-[RhCl(C=CHPh)(PMe₃)₂] are very similar indeed.

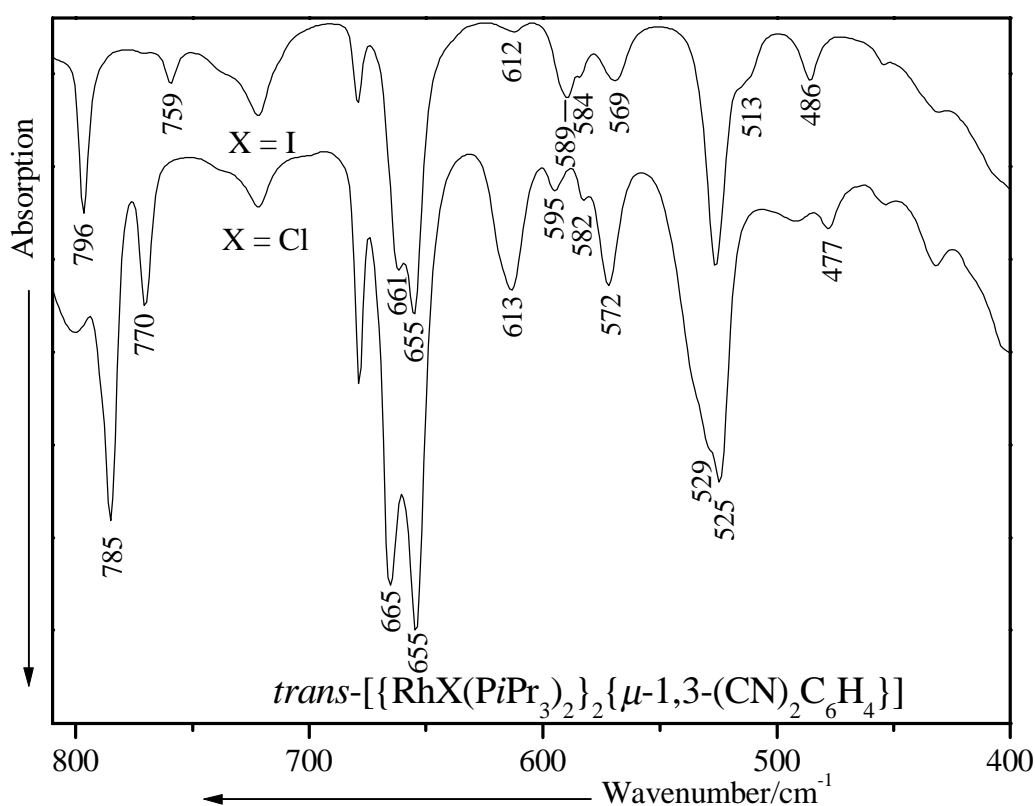


Figure 33. Low wavenumber region of the FT-IR spectrum of *trans*-[[RhCl(PiPr₃)₂]₂{μ-1,3-(CN)₂C₆H₄} (**18**) and *trans*-[[RhI(PiPr₃)₂]₂{μ-1,3-(CN)₂C₆H₄} (**19**).

The four bands at 1461, 1448, 1384 and 1365 cm^{-1} (Figure 10) in the finger print region of the free PiPr₃ ligand which correspond in the FT-Raman spectrum of **18** to the bands at 1481, 1472, 1418 and 1387 cm^{-1} should be ascribed to the $\delta(\text{CH}_3)$ and $\delta(\text{CH})$ vibrational modes. However, the bands of medium intensity observed at 1300, 1244 and 1233 cm^{-1} which did not appear in the FT-Raman spectrum of 1,3-(CN)₂C₆H₄ and which are observed at 1299 and

1241 cm^{-1} in the FT-Raman spectrum of **18**, are also good candidates for the $\delta(\text{CH}_3)$ vibrational modes of the coordinated PiPr_3 groups.

Since for the model compounds $\text{trans}[\text{RhX}(\text{CNPh})(\text{PMe}_3)_2]$ ($\text{X} = \text{F}, \text{Cl}$) some of the calculated modes are higher or lower in wavenumbers compared with the dinuclear complex, and since only one $\nu(\text{RhC})$ stretching mode has been predicted for both molecules whereas two are expected for complex **18**, the vibrational modes for the dinuclear model compounds $\text{trans}[\{\text{RhF}(\text{PR}_3)_2\}_2\{\mu\text{-}1,3\text{-(CN)}_2\text{C}_6\text{H}_4\}]$ ($\text{R} = \text{H}, \text{Me}$) have also been calculated (see Table 16). However, the size of this molecule limits the use of a large basis set and therefore the calculations were performed only for $\text{X} = \text{F}$ using the small basis set LANL2DZ (DFT1).

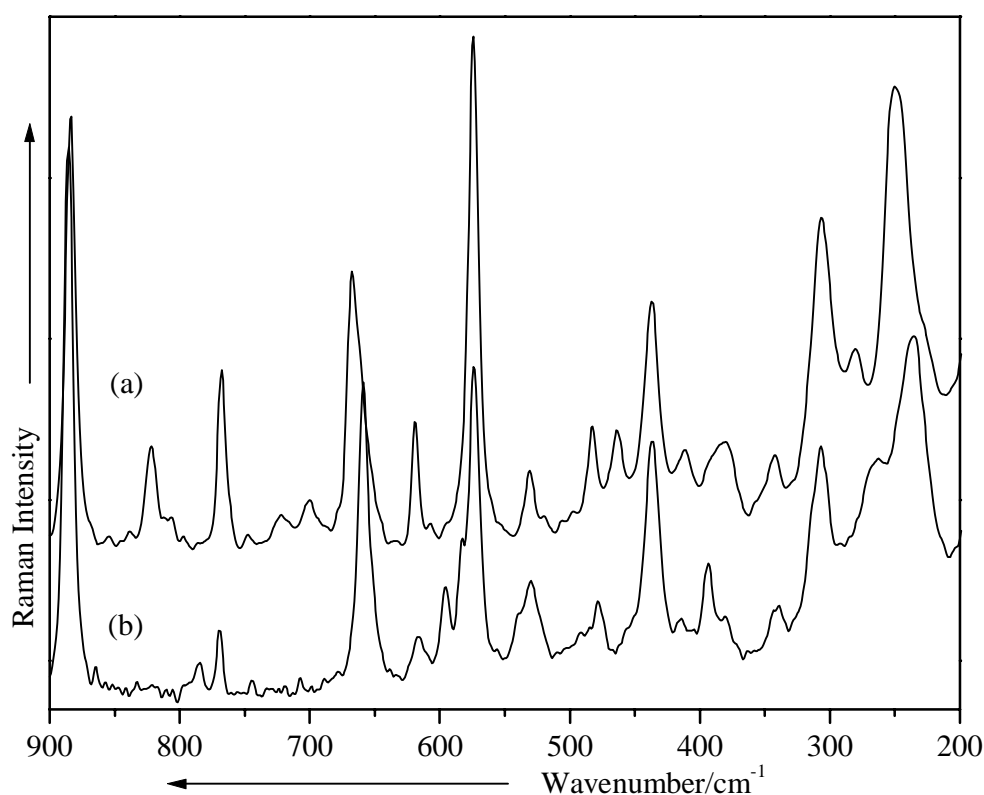


Figure 34. Low wavenumber region of the FT-Raman spectrum of $\text{trans}[\text{RhCl}(\text{C}=\text{CHPh})(\text{PiPr}_3)_2]$ (a) and $\text{trans}[\{\text{RhCl}(\text{PiPr}_3)_2\}_2\{\mu\text{-}1,3\text{-(CN)}_2\text{C}_6\text{H}_4\}]$ (b).

The FT-Raman spectrum of **18** displays two medium to weak bands at 784 and 770 cm^{-1} , which are shifted by 13 and 10 cm^{-1} to higher and lower wavenumbers in the spectrum of compound **19**, respectively. According to the DFT calculations performed on the model compound $\text{trans}[\{\text{RhF}(\text{PMe}_3)_2\}_2\{\mu\text{-}1,3\text{-(CN)}_2\text{C}_6\text{H}_4\}]$, the band at higher wavenumbers (calc. 786 cm^{-1} , DFT1) should be attributed to a $\delta(\text{CH})$ vibration and that at lower wavenumbers (calc. 764 cm^{-1} , DFT1) to a symmetric ring bending mixed with the $\nu(\text{RhC})$ stretching mode.

Table 16. Selected calculated and experimental vibrational wavenumbers (cm^{-1}) for *trans*-[$\{\text{RhF}(\text{PR}_3)_2\}_2\{\mu\text{-1,3-(CN)}_2\text{C}_6\text{H}_4\}$] ($\text{R} = \text{H}, \text{Me}$) and *trans*-[$\{\text{RhCl}(\text{PiPr}_3)_2\}_2\{\mu\text{-1,3-(CN)}_2\text{C}_6\text{H}_4\}$] complexes together with their tentative assignment.

<i>trans</i> -[$\{\text{RhF}(\text{PR}_3)_2\}_2\{\mu\text{-1,3-(CN)}_2\text{C}_6\text{H}_4\}$]		<i>trans</i> -[$\{\text{RhX}(\text{PiPr}_3)_2\}_2\{\mu\text{-1,3-(CN)}_2\text{C}_6\text{H}_4\}$]		assignment
R = H, DFT1	R = Me, DFT1	X = Cl, Exp. ^a	X = I, Exp. ^a	
2074	2056		2035 m	$\nu_{\text{as}}(\text{CN})$
2053	2031	1987 vbr.	1998 s	$\nu_{\text{s}}(\text{CN})$
1591	1589	1583 s	1577 s	$\nu(\text{C}=\text{C})$
1565	1561			$\nu(\text{C}=\text{C})$
1472	1471	1481	1478	i.p. $\delta(\text{CH})_{\text{ring}} + \nu(\text{C}=\text{C})$
1414	1411	1423 shm	1418	ring bending + i.p. $\delta(\text{CH})_{\text{ring}}$
1362	1360	1370vw	1368vw	i.p. $\delta(\text{CH})_{\text{ring}} + \nu(\text{C}=\text{C})$
1294	1290	1300m	1299m	i.p. $\delta(\text{CH})_{\text{ring}}$
1273	1274	1268	1263	$\nu_{\text{s}}(\text{CN}-\text{C}_{\text{ring}}) + \text{ring bending}$
1184	1183	1165m	1164m	i.p. $\delta(\text{CH})_{\text{ring}}$
1162	1161	1149s	1144s	$\nu_{\text{as}}(\text{CN}-\text{C}_{\text{ring}}) + \text{i.p. } \delta(\text{CH})_{\text{ring}}$
791	786	784	797	o.o.p. $\delta(\text{CH})_{\text{ring}}$
761	764	770	759	ring bending + $\nu(\text{RhC})$
606	606	616	613	$\delta(\text{NCC}_{\text{ring}})$
596	598	595	588sh	$\nu_{\text{s}}(\text{RhC}) + \text{ring bending}$
		583	586	
586	587	574	571	$\nu_{\text{as}}(\text{RhC})$
521	513	539	529	i.p. $\delta_{\text{s}}(\text{RhC1NC}_{\text{ring}}) + \text{ring tor.}$
507	502	530	513	$\delta(\text{RhC1NC}_{\text{ring}})$
494	475	492mw	486br	i.p. $\delta_{\text{as}}(\text{RhC1NC}_{\text{ring}}) + \text{ring tor.}$
		485mw		
		479m		
479	463		454m	o.o.p. $\delta_{\text{s}}(\text{C1NC}_{\text{ring}})$
473	453			o.o.p. $\delta_{\text{as}}(\text{C1NC}_{\text{ring}})$
448				
470	447			$\nu_{\text{s}}(\text{RhF})$
469	445			$\nu_{\text{as}}(\text{RhF})$

^aFT-Raman spectrum

As mentioned above, these modes are expected at lower and higher wavenumbers for the mononuclear model compounds *trans*-[RhX(CNPh)(PMe₃)₂] (767 and 821 cm⁻¹ for X = F and 769 (746) and 819 (814) cm⁻¹ for X = Cl using DFT1 (DFT2)), respectively.

The position of the two ν(RhC) modes (symmetric and antisymmetric) anticipated for the model compound *trans*-[₂{RhF(PMe₃)₂}]₂{μ-1,3-(CN)₂C₆H₄} have been calculated at 598 and 587 cm⁻¹, respectively. This allow to assign these modes to the bands observed at 595 and 574 cm⁻¹ for **18** and 589 and 571 cm⁻¹ for **19** (Figures 32 and 33).

Similarity as for the vinylidene complexes, the shift of the ν(RhC) stretching mode reflects the *trans* influence of the halide ligand in the order I > Cl. It should be also noted that the ν(C=C) stretching vibration of the ring is sensitive to the type of the ligand *trans*-disposed to the CNR unit and is shifted to lower wavenumbers for complex **19** compared to **18** (Δν = 6 cm⁻¹). The fact that the ν(Rh=C) stretching mode has been also shifted to lower wavenumbers (Δν = 6 cm⁻¹) by replacing the chloride with iodide indicates that both modes are coupled. Although it is curious that the ν(RhC) appears at the same wavenumber for the analogous isocyanide and the vinylidene compounds, a direct comparison of this mode for both **18** and **7** is unreasonable due to its coupling with a ring vibration.

However, the comparison between **18** and **7** provides some useful informations regarding the assignment of the δ(CNC) modes. Thus, the band at 616 cm⁻¹ in the spectrum of **18** which may correspond to that one observed at 594 cm⁻¹ in the spectrum of 1,3-(CN)₂C₆H₄ is a good candidate for an in-plane δ(CNC) vibrational mode. This mode which appears at higher wavenumbers as the ν(RhC) is shifted to lower wavenumbers in the iodo complex **19**. In addition, it should be noticed that the δ(CNC) mode, which mix with δ(CC) of the six-membered ring, has been calculated at 606 cm⁻¹ for *trans*-[₂{RhF(PMe₃)₂}]₂{μ-1,3-(CN)₂C₆H₄} (DFT1) and at 618 (X = F) or 607 cm⁻¹ (X = Cl) for *trans*-[RhX(CNC₆H₅)(PMe₃)₂] using DFT1 and DFT2, respectively. The two bands at 539 and 513 cm⁻¹ in the spectra of **18** and **19** can be assigned to the δ(RhCNC) modes. Moreover, the calculated modes for the model compound *trans*-[RhCl(CNPh)(PMe₃)₂] using DFT2 at 488 and 510 cm⁻¹ belong to an out-of-plane δ(CNC) vibration which is coupled with an out-of-plane δ(CH) bending mode.

Finally, regarding the region between 400 and 500 cm⁻¹ the medium to strong band in the spectra of *trans*-[RhX(=C=CHPh)(PiPr₃)₂] at 499 (X = F), 482 (X = Cl), 481 (X = Br) and 481 cm⁻¹ (X = I) was tentatively assigned to a Rh-C1(C2)-C_{ring} deformation mode mixed with an out-of-plane ring bending. The weaker band at, respectively, 475, 464, 459 and 458 cm⁻¹

in the spectra of these vinylidene complexes was attributed to a pure out-of-plane RhC1C2 bending vibration. Indeed, this band appears only in the spectra of *trans*-[RhX(=C=CHPh)(PiPr₃)₂] and in analogy to the $\nu(\text{RhC})$ mode is also red shifted following the order $\text{F} > \text{Cl} > \text{Br} > \text{I}$. The strong band at 437 cm^{-1} , which is observed both in the FT-Raman spectra of the isocyanide and the vinylidene complexes, is assigned to deformation modes of the PiPr₃ groups and found between 469 and 421 cm^{-1} in the spectrum of the free phosphine.

3.4 Isonitrile rhodium(I) complexes *trans*-[RhX(CNR)(PiPr₃)₂] ($X = \text{F}, \text{Cl}, \text{Br}, \text{I}, \text{PhC}\equiv\text{C}, \text{R} = 2,6\text{-xylyl}; X = \text{Cl}, \text{R} = t\text{Bu}$)

3.4.1 Experimental and theoretical structures

3.4.1.1 Theoretical structure of 2,6-xylyl isocyanide

The geometry of the 2,6-xylyl isocyanide ligand has been calculated using the BPW91/6-31+G(d) and BPW/6-311+G(d) methods.

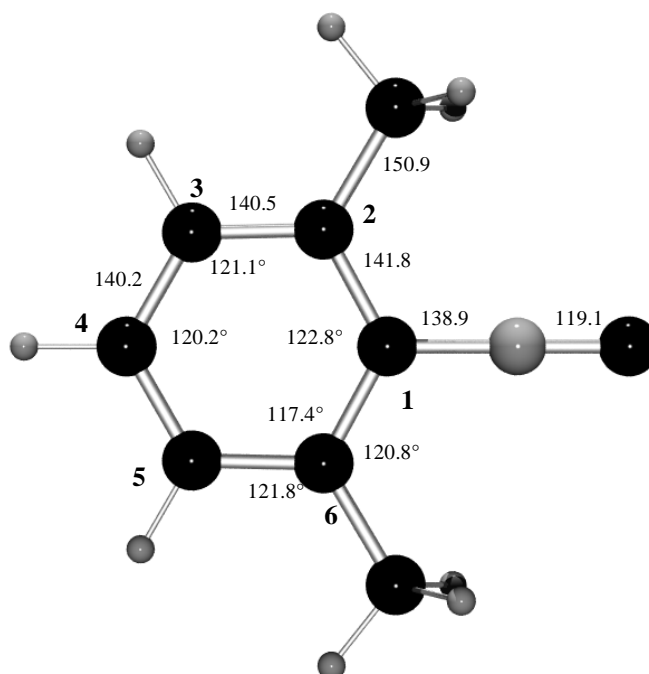


Figure 35. Optimized structure of the 2,6-xylyl isocyanide using BPW91/6-31+G(d) method.

The calculated structure is depicted in Figure 35 with their structural parameters. To the best of our knowledge, the molecular structure of the 2,6-xylyl isocyanide ligand in the crystal is unknown and can therefore not be compared with the structural parameters obtained by the calculations.

3.4.1.2. Structure of *trans*-[RhX(CNR)(PR'₃)₂] (X = F, Cl, Br, I, PhC≡C, R = 2,6-xylyl, *t*Bu; R' = Me, *i*Pr) (20-25)

The structural parameters of the model compounds *trans*-[RhX(CNR)(PMe₃)₂] (R = 2,6-xylyl, *t*Bu; X = F, Cl), which were calculated using the DFT1-2 and -5 methods, are summarized in Table 17 together with the X-ray crystallographic data for the isocyanide complexes *trans*-[RhCl(CN-2,6-xylyl)(PiPr₃)₂] and *trans*-[RhCl(CNCH₂CMe₃)(PiPr₃)₂]^[102].

Figures 36 and 37 show the calculated structures of the model compounds *trans*-[RhCl(CN-2,6-xylyl)(PMe₃)₂] and *trans*-[RhCl(CN-*t*Bu)(PMe₃)₂]. It is noteworthy that the bond angle C-N-C, which is calculated for the model compounds *trans*-[RhF(CN-2,6-xylyl)(PMe₃)₂] and *trans*-[RhCl(CN-2,6-xylyl)(PMe₃)₂] at 180.0° and 175.0° (DFT1), respectively (see Table 17), become even smaller (155.2° and 168.9°, respectively) by using DFT2 and DFT5.

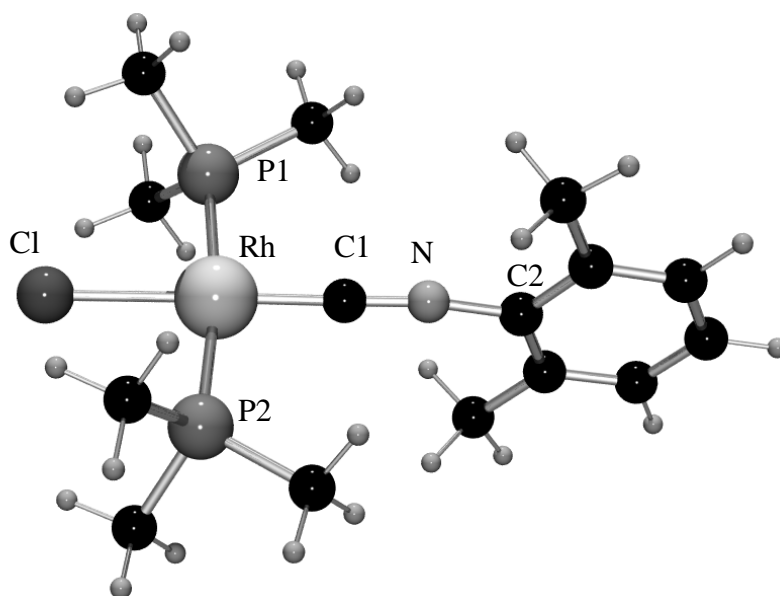


Figure 36. Optimized structure of *trans*-[RhCl(CN-2,6-xylyl)(PMe₃)₂] using DFT2.

Table 17. Comparison of selected bond lengths (pm) and angles ($^{\circ}$) for the complexes *trans*-[RhCl(CNR)(P*i*Pr₃)₂] (R = 2,6-xylyl, neopentyl) with the model compounds *trans*-[RhX(CNR)(PMe₃)₂] (X = F, Cl; R = 2,6-xylyl, *t*Bu).

	<i>trans</i> -[RhF(CNR)(PMe ₃) ₂]					<i>trans</i> -[RhCl(CNR)(PMe ₃) ₂]					<i>trans</i> -[RhCl(CNR)(P <i>i</i> Pr ₃) ₂]				
	R = 2,6-xylyl		R = <i>t</i> Bu			R = 2,6-xylyl		R = 2,6-xylyl			R = 2,6-xylyl		R = CH ₂ CMe ₃		
	DFT1	DFT5	DFT1	DFT2	DFT1	DFT2	DFT1	DFT2	DFT1	DFT2	DFT1	DFT2	DFT1	DFT2	Exp. ^a
Bond lengths (pm)															
Rh-X	206.8	204.8	207.5	207.7	247.5	244.6	239.5	238.9	238.9	238.9	238.9	238.9	239.5	238.9	238.9 (2)
Rh-P1	237.7	232.1	237.2	232.7	238.7	234.4	233.4	232.3	233.4	234.4	233.4	232.3	233.4	234.4	232.3 (1)
Rh-P2	237.7	232.1	237.2	232.7	238.7	234.4	233.4	232.1	233.4	234.4	233.4	232.1	233.4	234.4	232.1 (3)
Rh-Cl	184.8	182.7	185.4	184.6	185.2	184.9	183.0	183.4	185.2	184.9	183.0	183.4	183.0	184.9	183.4 (4)
C1-N	122.0	121.8	122.1	121.4	121.8	121.0	117.7	115.9	121.8	121.0	117.7	115.9	117.7	121.0	115.9 (5)
N-C2	138.4	138.4	146.0	145.2	138.7	137.9	139.5	143.4	138.7	137.9	139.5	143.4	139.5	137.9	143.4 (6)
Bond angles ($^{\circ}$)															
	DFT1	DFT5	DFT1	DFT2	DFT1	DFT2	DFT1	DFT2	DFT1	DFT2	DFT1	DFT2	DFT1	DFT2	Exp. ^a
P1-Rh-P2	164.4	167.4	164.2	166.1	170.9	171.8	178.21	175.88	170.9	171.8	178.21	175.88	170.9	171.8	175.88 (4)
F-Rh-Cl	179.7	179.2	179.9	179.8	178.8	179.0	178.8	179.0	178.8	179.0	178.8	179.0	178.8	179.0	^b
P1-Rh-F	82.2	83.7	82.1	83.3	85.5	86.0	89.11	90.76	85.5	86.0	89.11	90.76	85.5	86.0	90.76 (5)
P1-Rh-Cl	97.7	96.3	97.9	96.8	94.5	94.0	90.89	88.7	94.5	94.0	90.89	88.7	94.5	94.0	88.7 (1)
Rh-Cl-N	180.0	174.7	176.3	175.6	180.0	178.5	180.0	178.4	180.0	178.5	180.0	178.4	180.0	178.5	178.4 (4)
C1-N-C2	179.1	155.2	157.9	152.0	175.2	168.9	180.0	166.8	175.2	168.9	180.0	166.8	175.2	168.9	166.8 (4)

^aReference 102, ^bvalue is not given

The fact that the molecular structure of **21** in the crystal nevertheless shows a linear C-N-C linkage is probably due to the high steric hindrance between the methyl groups of the xylyl and the $PiPr_3$ ligands. However, the calculated values are in good agreement with the structural parameters determined for $trans$ -[RhCl(CN-2,6-xylyl)($PiPr_3$)₂] and $trans$ -[RhCl(CNCH₂CMe₃)($PiPr_3$)₂]^[102] (Table 17).

As expected, the six membered ring lies nearly perpendicular to the plane formed by the atoms P1, P2, Rh, X and C1. In comparison with the free 2,6-xylyl isocyanide ligand, where the C-N bond length was calculated at 119.1 pm using BPW91/6-31+G(d), the corresponding experimental value for complex **21** is 117.7(6) pm and the calculated value for the model compound $trans$ -[RhCl(CN-2,6-xylyl)(PMe₃)₂] using DFT2 is 121.0 pm. The calculated N-C(xylyl) bond length in the model compound $trans$ -[RhCl(CN-2,6-xylyl)(PMe₃)₂] is slightly shorter than for the free 2,6-xylyl isocyanide ligand. It should be noticed that the calculations are carried out on model compounds in the gas phase. Therefore, small deviations are expected between experimental and theoretical bond angles and bond distances.

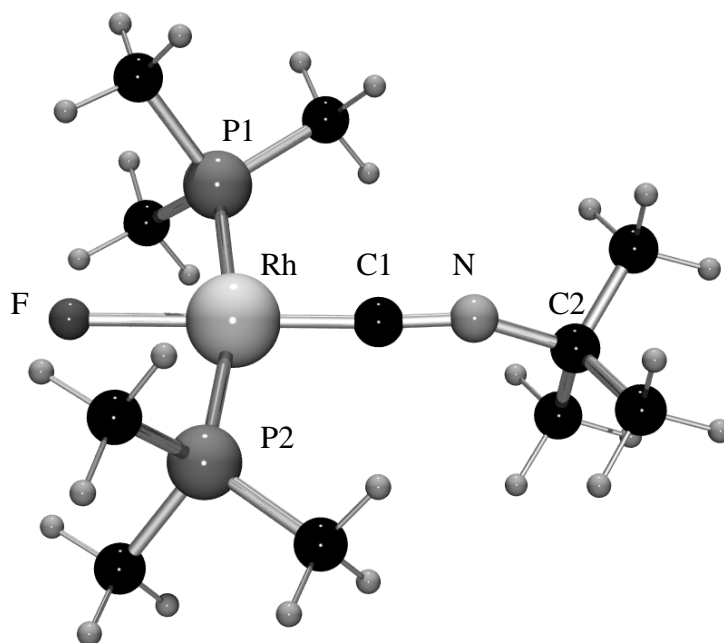


Figure 37. Optimized structure of $trans$ -[RhF(CN-*t*Bu)(PMe₃)₂] using DFT2.

3.4.2 Vibrational Spectroscopy

3.4.2.1 Vibrational spectrum of 2,6-xylyl isocyanide

Although the infrared and Raman spectrum of the liquid C_6H_5NC and C_6D_5NC compounds have been investigated ^[108], we decided to measure the FT-Raman spectrum of the 2,6-xylyl isocyanide ligand. DFT calculations have been used in order to assign the characteristic modes of the 2,6-xylyl isocyanide ligand (Table 18).

In the high wavenumber region of the FT-Raman spectrum of the 2,6-xylyl isocyanide, the very strong band at 2122 cm^{-1} corresponding to the $\nu(C\equiv N)$ stretching mode has been calculated at 2108 cm^{-1} using BPW91/6-31+G(d). The $\nu(C=C)$ vibrational modes can be ascribed in the FT-Raman spectrum of 2,6-xylyl isocyanide to the bands observed at 1603 and 1592 cm^{-1} (Figure 38).

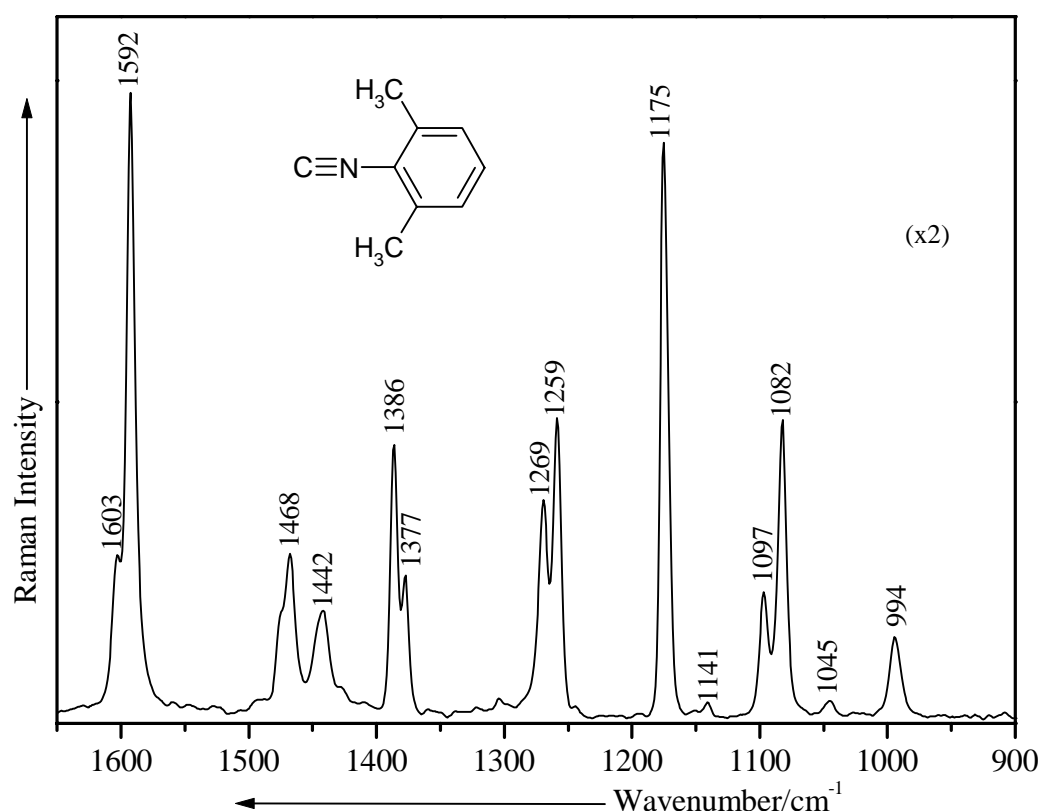


Figure 38. The FT-Raman spectrum of CN-2,6-xylyl between 1650 and 900 cm^{-1} .

The $\delta(\text{CH}_3)$ and $\nu(\text{CH}_3\text{-C}_{\text{ring}})$ vibrational modes can be ascribed to the strong bands observed at 1386 and 1377 cm^{-1} and at 1269 and 1259 cm^{-1} in the FT-Raman spectrum of the 2,6-xylyl isocyanide ligand (Figure 38), since they have been calculated at 1397 and 1393 cm^{-1} and at 1256 and 1254 cm^{-1} , respectively.

Table 18. Selected calculated and experimental fundamental vibrational wavenumbers (cm^{-1}) for 2,6-xylyl isocyanide ligand together with their tentative assignment.

BPW91/6- 311+G(d)	BPW91/6- 31+G(d)	I_{Ra} ($\text{\AA}^4/\text{amu}$)	Exp.	I_{Ra}	Assignment
2096	2108	461.4	2122	vs	$\nu(\text{CN})$
1591	1597	74.1	1603	m	$\nu(\text{C}=\text{C})$ (8a)
1583	1588	7.4	1592	vs	$\nu(\text{C}=\text{C})$ (8b)
1480	1485	6.1	1474	m	$\nu(\text{CCC})$ (19b) + $\delta(\text{CH}_3)$
1476	1482	14.8	1468	m	$\nu(\text{CCC})$ (18a) + $\delta(\text{CH}_3)$
1457	1464	19.9	1474	sh	$\delta(\text{CH}_3)$
1413	1421	14.3	1442	mbr.	$\nu(\text{CCC})$ (19a) + $\nu(\text{CN-C}_{\text{ring}})$
			1428	mw	+ $\delta(\text{CH}_3)$
1386	1398	19.8	1386	s	i. phase $\delta_s(\text{CH}_3)$
1384	1396	16.4			o.o. phase $\delta_s(\text{CH}_3)$
1326	1340	5.4	1377	m	$\nu(\text{CCC})$ (14) + $\delta(\text{CH}_3)$
1255	1259	59.9	1269	s	$\nu(\text{NC}_{\text{ring}})$ + $\nu(\text{C-CH}_3)$
1251	1254	0.1	1259	s	$\delta(\text{CH})$
1171	1174	17.9	1175	vs	$\nu(\text{CN-C}_{\text{ring}})$ + i.p. $\delta(\text{CCC})$
1168	1172	5.6			
1085	1089	27.3	1097	m	$\delta(\text{CH})$
			1082	s	
633	635	30.1	641	vs	ring breathing
563	563	2.2	570	m	$\delta(\text{C-N-ring})$
537	553	0.5	547	mw	$\delta(\text{CCCC})$ (16b)
500	509	0.01	510	mw	$\delta(\text{CCCC})$ (16a)
491	491	3.5	497	ms	$\delta(\text{C-N-ring})$ + $\delta(\text{CCCC})$
452	451	5.0	463	ms	$\delta(\text{CCCC})$ (6a)
357	370	2.5	366	ms	$\delta(\text{CNC})$ (16b)
	358	0.9			$\delta(\text{CNC})$ + $\rho(\text{CH}_3\text{-ring})$
	272	1.1	291		
	222	2.2	245		
	138	5.8	166	vs	$\delta(\text{CNC})$ (10b)

The very strong band appearing at 1175 cm^{-1} in the FT-Raman spectrum of the free ligand corresponds to the $\nu(\text{CN-C}_{\text{ring}})$ mode and has been calculated at 1174 cm^{-1} using the BPW91/6-31+G(d) method. This mode is assigned at 1185 cm^{-1} in the Raman spectrum of phenylisocyanide ^[108]. The strong band observed at 641 cm^{-1} (calc. 635 cm^{-1}) is attributed to the ring breathing. In agreement with the DFT calculations, the bands observed at 570 , 547 , 510 and 497 cm^{-1} (Figure 39) can be attributed to the CNC deformation modes.

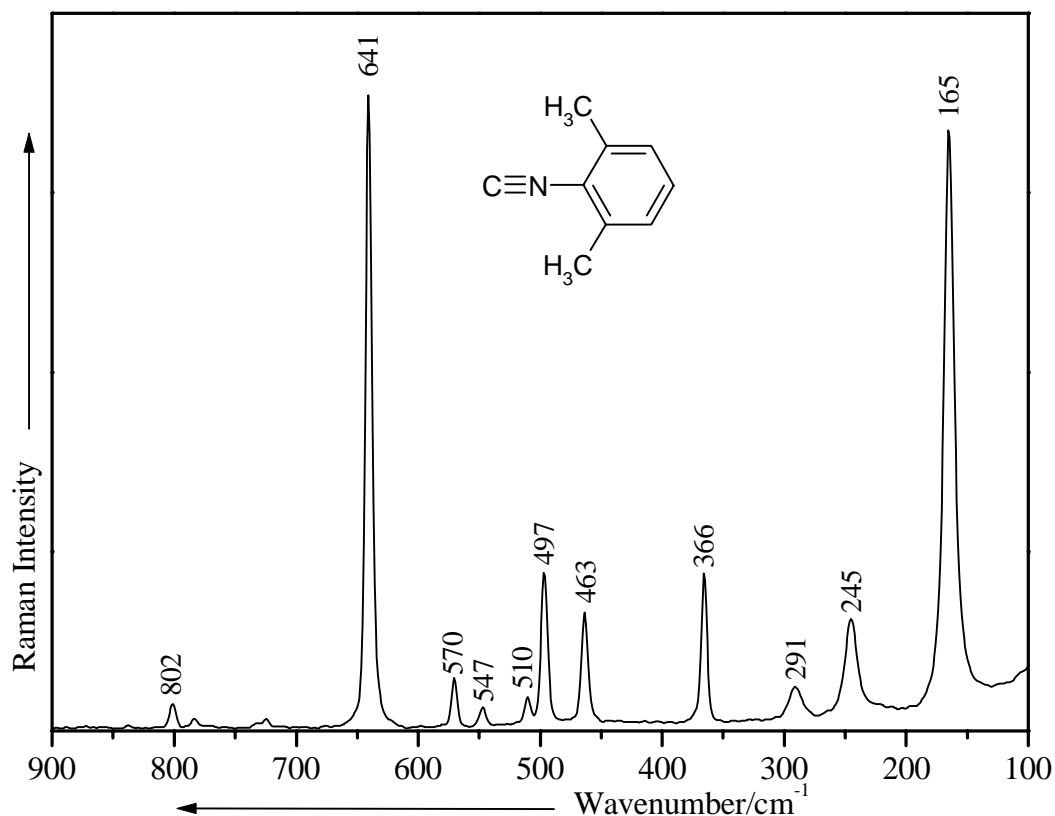


Figure 39. The low-wavenumber region of the FT-Raman spectrum of CN-2,6-xylyl.

3.4.2.2 Vibrational spectrum of *trans*-[RhX(CN-2,6-xylyl)(PiPr₃)₂] (X = F, Cl, Br, I, C≡CPh) (20-24)

Jones and Hessell have described the preparation and molecular structure of **21** and have limited their assignment to the $\nu(\text{C}\equiv\text{N})$ mode ^[102]. As for the vinylidene and carbonyl complexes, we have been interested to characterize the $\nu(\text{Rh}=\text{C})$ mode, using the influence of different halide ligands on the *trans* disposed Rh-CNR bond.

The two bands, which are observed for the $\nu(\text{C}\equiv\text{N})$ mode in the Raman spectrum of the studied complexes **20-23** (Figure 40) are not to be assigned to isomers or to a group effect

such as molecular stacking ^[102]. Multiple splittings of the IR spectra of other isonitrile complexes are documented in the literature ^[110-113]. The calculated $\nu(\text{CN})$ stretching modes for the model compounds *trans*-[RhF(CN-2,6-xylyl)(PMe₃)₂] (2035 cm⁻¹ DFT1; 1991 cm⁻¹ DFT5) and *trans*-[RhCl(CN-2,6-xylyl)(PMe₃)₂] (2039 cm⁻¹ DFT1; 2052 cm⁻¹ DFT2) are consistent with the experimental results (Figure 40).

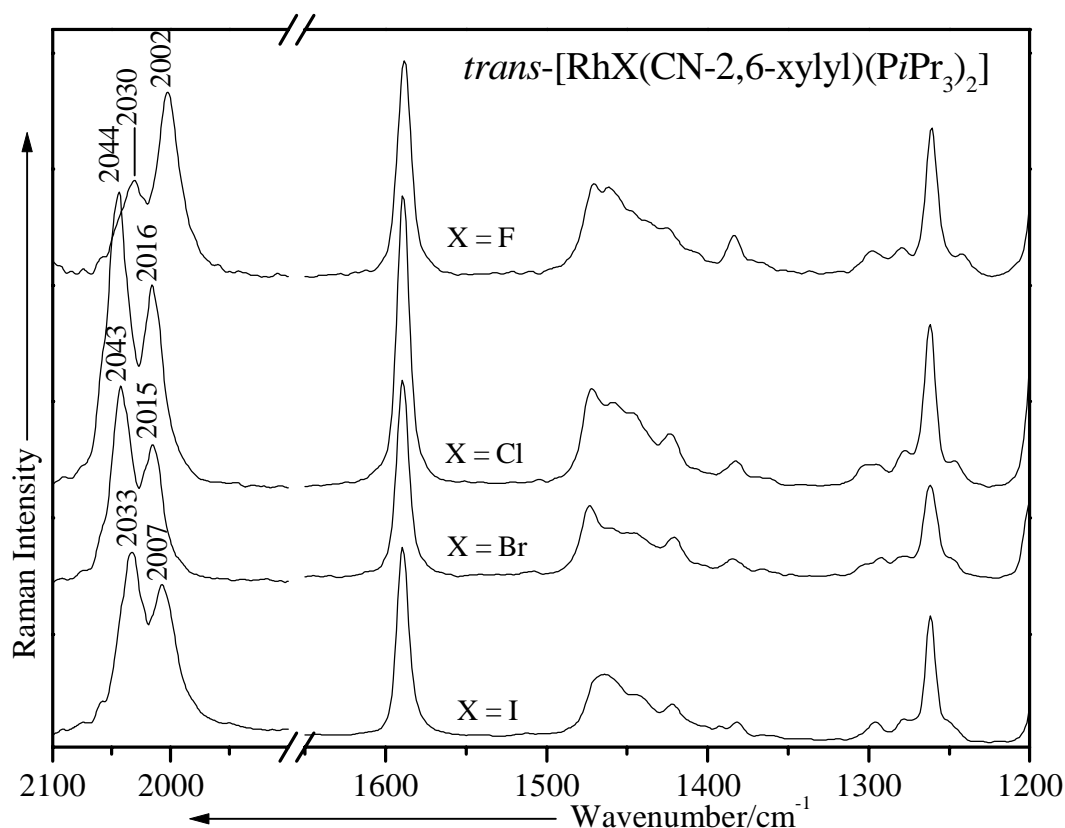


Figure 40. The high-wavenumber region of the FT-Raman spectrum of *trans*-[RhX(CN-2,6-xylyl)(PiPr₃)₂] (X = F, Cl, Br, I).

Surprisingly, the $\nu(\text{C}\equiv\text{N})$ stretching mode in the complexes **20-23** decreases in the order $\text{Cl} \geq \text{Br} > \text{I} > \text{F}$, being slightly different to this obtained for the carbonyl and vinylidene complexes. In contrast to the dinuclear compounds **18** and **19**, where the $\nu(\text{C}=\text{C})$ stretching mode is sensitive to the *trans*-disposed ligand, this mode is observed at 1589 cm⁻¹ (calc. 1580 and 1600 cm⁻¹ for X = F (DFT1); 1581 and 1600 cm⁻¹ for X = Cl (DFT1); 1582 and 1600 cm⁻¹ for X = I (DFT1)) in the FT-Raman spectrum of **20-23** (Figure 40). The comparison between the low wavenumber region of the FT-Raman and FT-IR spectra of the rhodium isocyanides complexes **20-23** reveal several significant band shifts, which allow a proper assignment of the $\nu(\text{Rh}=\text{C})$ stretching mode (Figure 41-42).

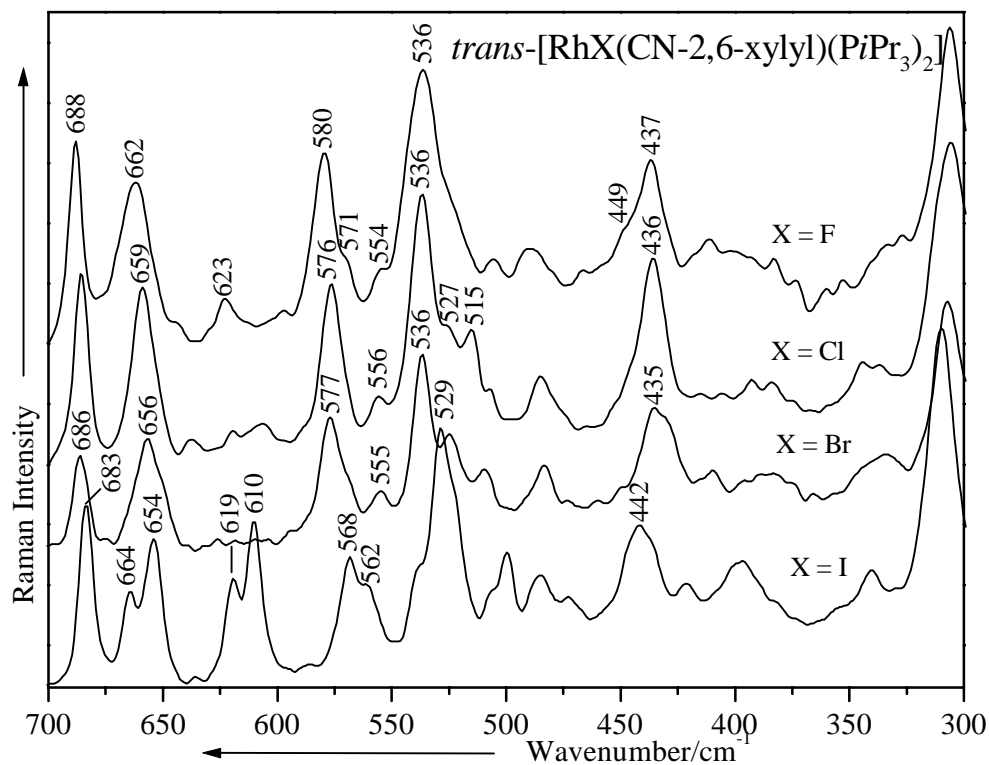


Figure 41. The low-wavenumber region of the FT-Raman spectrum of *trans*-[RhX(CN-2,6-xylyl)(PiPr₃)₂] (X = F, Cl, Br, I).

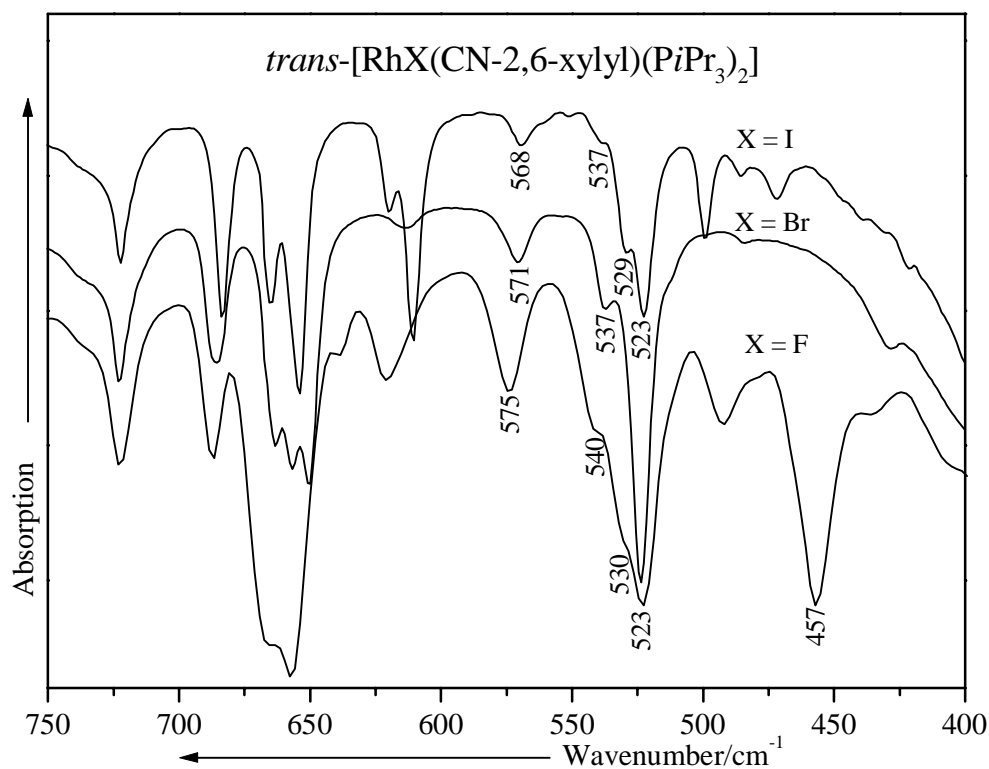


Figure 42. The low-wavenumber region of the FT-IR spectrum of *trans*-[RhX(CN-2,6-xylyl)(PiPr₃)₂] (X = F, Cl, I).

According to the DFT calculations carried out on the model compounds *trans*-[RhX(CN-2,6-xylyl)(PMe₃)₂] (X = F, Cl), two vibrations corresponding to the $\nu(\text{Rh}=\text{C})$ stretching mode have been found at 528 and 683 cm⁻¹ for X = F (DFT1) and at 519 and 680 cm⁻¹ for X = Cl (DFT2) (Figure 43). However, both modes mix strongly with a ring bending vibration.

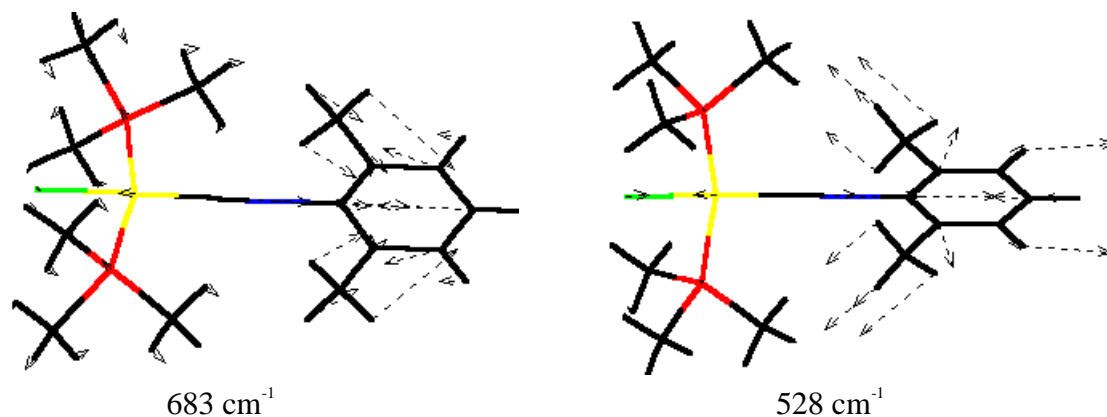


Figure 43. Calculated $\nu(\text{RhC})$ for the model complex *trans*-[RhF(CN-2,6-xylyl)(PMe₃)₂] using DFT1.

Therefore the medium strong band at 688 cm⁻¹ in the FT-Raman spectrum of **20**, being shifted to lower wavenumbers in **21-23**, can be ascribed to the $\delta(\text{CCC})_{\text{ring}}$ and $\nu(\text{Rh}=\text{C})$ stretching modes. Similarly as for the vinylidene and carbonyl complexes, the shift of these modes to lower wavenumbers in the order F > Cl ≥ Br > I reflects the *trans* influence of the halide ligand in the order I > Br > Cl > F (Figure 41).

The assignment of the second $\nu(\text{RhC})$ vibrational mode (see Figure 43) is more complicated due to the presence of several broad bands observed in the 510-540 cm⁻¹ spectral region of the FT-Raman spectrum of compounds **20-23** (Figures 41–42). However, the FT-IR spectrum of compounds **20**, **21** and **23** reveal some useful information for the assignment of this mode. Whereas one broad band can be observed at 536 cm⁻¹ in the FT-Raman spectrum of **20**, two are detected at 530 and 540 cm⁻¹ in its FT-IR spectrum. Moreover, these bands may correspond to that ones observed at 537 and 529 cm⁻¹ in the FT-IR spectrum of **22** and **23**, respectively. Therefore, the assignment of the $\nu(\text{Rh}=\text{C})$ stretching mode (Figure 43) to these bands is consistent with the previous results.

The bands observed in the spectral region between 610-664 cm⁻¹ are ascribed to the $\nu(\text{PC}_3)$ stretching modes and the medium one at 580 cm⁻¹ in the FT-Raman of complex **20** is attributed to the $\delta(\text{CNC})_{\text{ring}}$ bending vibration. This shifts to lower wavenumbers in the FT-Raman spectrum of complex **21-23**. Similarly as for the fluoro vinylidene, carbonyl and ethylene complexes, the $\nu(\text{RhF})$ vibration is slightly mixed with the $\nu(\text{Rh}=\text{C})$ stretching

mode. However, the pure $\nu(\text{RhF})$ mode calculated at 452 cm^{-1} (DFT5) for the model compound $\text{trans}[\text{RhF}(\text{CN-2,6-xylyl})(\text{PMe}_3)_2]$ is assigned to the strong band at 457 cm^{-1} in the FT-IR spectrum of **20** (Figure 43). It should be noticed that this mode appears at the same wavenumber than for the vinylidene complex **1**.

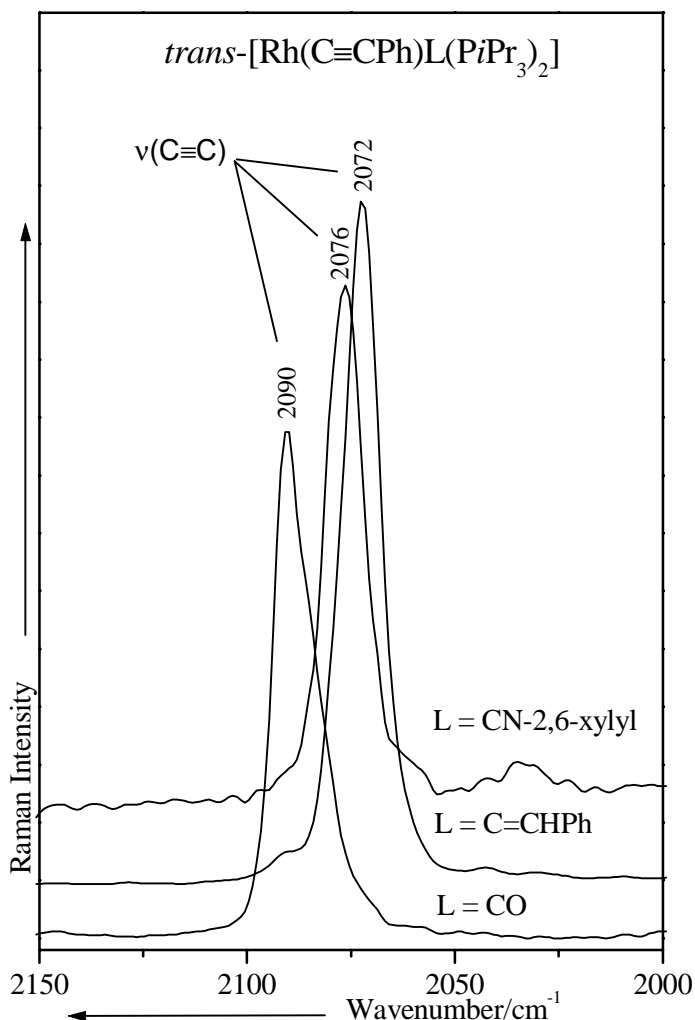


Figure 44. The $\nu(\text{C}\equiv\text{C})$ wavenumber region of the FT-Raman spectrum of $\text{trans}[\text{Rh}(\text{C}\equiv\text{CPh})\text{L}(\text{PiPr}_3)_2]$ ($\text{L} = \text{CO}, \text{C}=\text{CHPh}, \text{CN-2,6-xylyl}$).

Finally, the $\nu(\text{C}\equiv\text{C})$ stretching mode of the $\text{PhC}\equiv\text{C}$ ligand can be assigned in the FT-Raman and FT-IR spectrum of complex **24** to the strong and medium bands at 2076 cm^{-1} (calc. 2076 cm^{-1} , DFT1), respectively. In comparison with the vinylidene complex **11**, this mode is shifted only 4 cm^{-1} to higher wavenumbers (Figure 44). Therefore, the $\nu(\text{Rh-C})$ mode is expected in the same wavenumber region and can be assigned in the FT-Raman spectrum to the medium band at 545 cm^{-1} (calc. 546 cm^{-1} , DFT1). The shifts to higher wavenumbers of the $\nu(\text{C}\equiv\text{C})$ stretching mode in the order $\text{CO} > 2,6\text{-xylyl} \geq \text{C}=\text{CHPh}$ for the complexes $\text{trans}[\text{Rh}(\text{C}\equiv\text{CPh})\text{L}(\text{PiPr}_3)_2]$ ($\text{L} = \text{CO}, \text{C}=\text{CHPh}, 2,6\text{-xylyl}$) indicates the strongest π -acceptor character of the phenylvinylidene ligand.

As for the carbonyl complex **16**, the $\nu(\text{C-C}_{\text{ring}})$ stretching mode of the $\text{PhC}\equiv\text{C}$ ligand is observed at 1209 cm^{-1} (calc. 1214 cm^{-1} , DFT1) in the FT-Raman spectrum of **24** and the $\nu(\text{CN-C}_{\text{xylyl}})$ which has been expected only by **24**, is assigned to the strong band at 1189 cm^{-1} (calc. 1198 cm^{-1} , DFT1). Moreover, the strong and medium-to-weak bands at 1261 and 1291 cm^{-1} (calc. 1262 and 1272 cm^{-1} , DFT1) in the FT-Raman spectrum of **20**, respectively, which did not appear in the spectra of **11** and **16**, should be assigned to the $\nu(\text{CH}_3\text{-C}_{\text{ring}})$ modes. In agreement with the DFT calculations the medium band at 512 cm^{-1} (calc. 513 cm^{-1} , DFT1) observed in the FT-Raman spectrum of *trans*- $[\text{Rh}(\text{C}\equiv\text{CPh})(\text{CN-2,6-xylyl})(\text{PiPr}_3)_2]$ can be assigned to the $\nu(\text{Rh}=\text{C})$.

3.4.2.3 Vibrational spectrum of *trans*- $[\text{RhCl}(\text{CN-}t\text{Bu})(\text{PiPr}_3)_2]$ (**25**)

For the model compound *trans*- $[\text{RhF}(\text{CN-}t\text{Bu})(\text{PMe}_3)_2]$, the $\nu(\text{C}\equiv\text{N})$ stretching mode is calculated at 2007 and 2005 cm^{-1} using DFT1-2, respectively. The FT-Raman spectrum of compound **25** shows two bands of high and medium intensities at 2059 and around 2085 cm^{-1} . The exact position of the second band which is a broad one can not be determined unequivocally. At least, the shift of the $\nu(\text{C}\equiv\text{N})$ stretching mode for complex **25** to higher wavenumbers compared with the Jones compounds *trans*- $[\text{RhCl}(\text{CNCH}_2\text{CMe}_3)(\text{PiPr}_3)_2]$ (2056 and 2032 cm^{-1}) and *trans*- $[\text{RhCl}(\text{CN-2,6-xylyl})(\text{PiPr}_3)_2]$ (2047 and 2016 cm^{-1}) also agrees with the different C1-N and N-C2 bond lengths found by X-ray structure analyses^[102].

By comparing the FT-Raman spectrum of compounds **21** and **25** (Figure 45), one can discern some peaks belonging to the group R of the isocyanide ligand, since the bands at 508 , 515 and 527 cm^{-1} appear only in the FT-Raman spectrum of the complex **21**. Therefore, these bands are good candidates for ring deformations of the 2,6-xylyl isocyanide complexed ligand, whereas the band at 752 cm^{-1} in the FT-Raman spectrum of **25** should be ascribed to the $\nu(\text{CC}_3)$ mode of the *t*Bu group. This mode is calculated at 744 cm^{-1} (DFT2) for the model compound *trans*- $[\text{RhF}(\text{CN-}t\text{Bu})(\text{PMe}_3)_2]$ and is mixed with the $\nu(\text{RhC})$ vibrational mode (Figure 46). Furthermore, a vibrational mode with $\nu(\text{RhC})$ and $\delta(\text{CNC})$ components is found at 520 cm^{-1} (Figure 46) and is assigned to the medium band at 531 cm^{-1} in the FT-Raman spectrum of **25**. A direct comparison of these modes for both **21** and **25** is unreasonable due to its coupling with other vibrations.

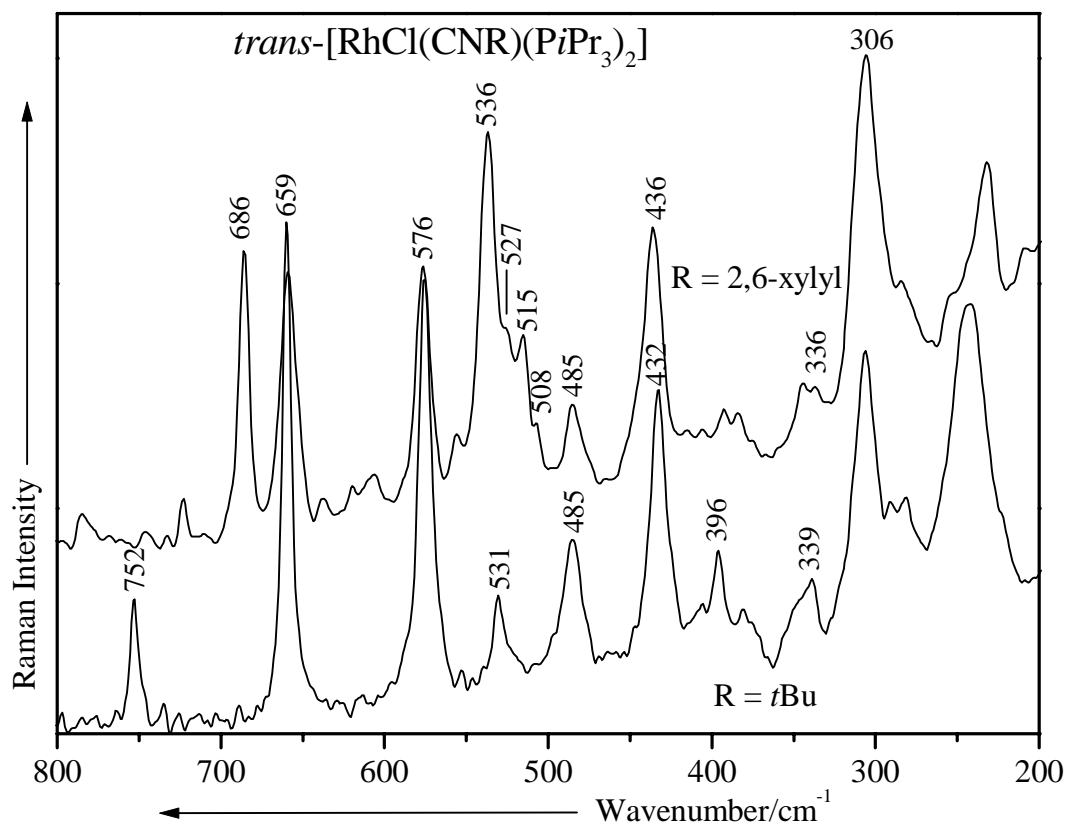


Figure 45. The low-wavenumber region of the FT-Raman spectrum of $trans\text{-}[\text{RhCl}(\text{CNR})(\text{PiPr}_3)_2]$ ($\text{R} = 2,6\text{-xylyl}$, $t\text{Bu}$).

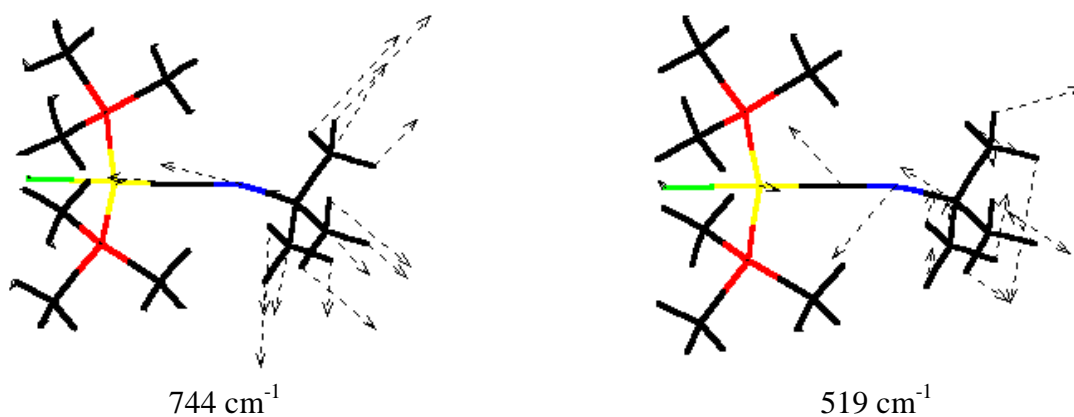


Figure 46. Calculated vibrational modes at 519 and 744 cm^{-1} for the model compound $trans\text{-}[\text{RhF}(\text{CN-}t\text{Bu})(\text{PMe}_3)_2]$ using DFT2.

Chapter 4

Vibrational spectroscopy studies and DFT calculations on tungsten and molybdenum complexes

4.1 Tungsten complexes $mer\text{-}[W(CO)_3(dmpe)(\eta^2\text{-S=CR}_2)]$ ($R = H, D$)

The FT-IR and FT-Raman spectra of the thioaldehyde complexes $mer\text{-}[W(CO)_3(dmpe)(\eta^2\text{-S=CH}_2)]$ (**26**) and $mer\text{-}[W(CO)_3(dmpe)(\eta^2\text{-S=CD}_2)]$ (**27**) are reported for the first time in the following part. The investigated compounds have been synthesized in the work group of Prof. Schenk^[114]. This project was within the framework of the *SFB 347*. One of the most relevant features of the vibrational spectra of this class of compounds are the metal-carbon and metal-sulfur stretching vibrations, since they are directly related to such a substantial property of the molecule as the M-C and M-S bond strength. However, the assignment of the $\nu(\text{MC})$ vibrational modes is very often quite complicated due to the presence of other bands in the same region or of their low intensity. By using isotopic substitution, in conjunction with theoretical calculations, it has been possible to bypass these

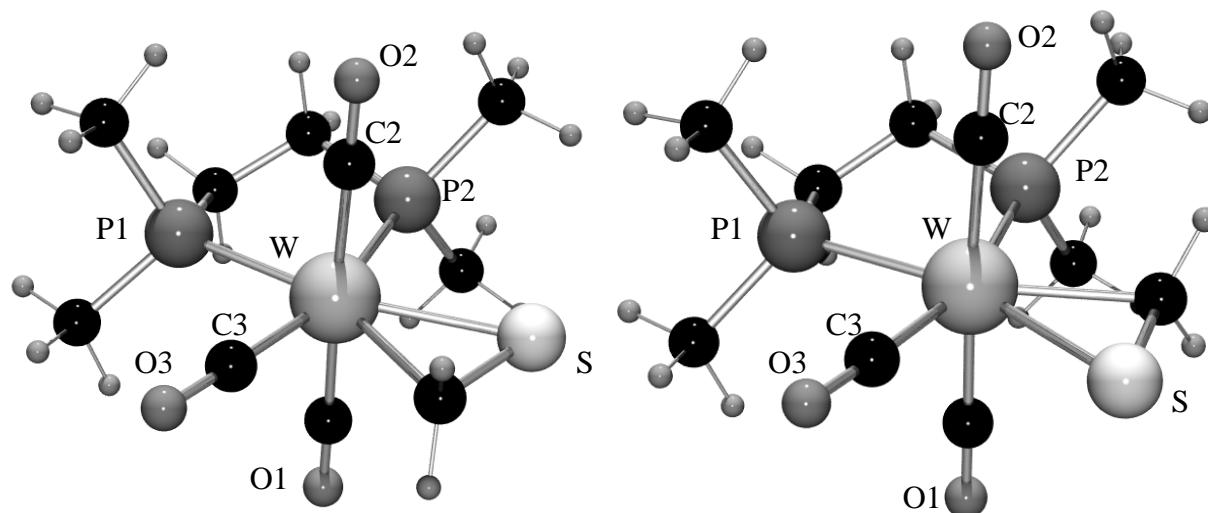
difficulties and to do an exact assignment of the $\nu(\text{WC})$ and $\nu(\text{CS})$ stretching modes. The theoretical energy difference between the different stereo-isomers of compound **26** is also reported.

4.1.1 Experimental and theoretical structures

The DFT calculations were performed using Gaussian 98^[54] and Becke's 1988 exchange functional^[55] in combination with the Perdew-Wang 91 gradient-corrected correlation functional (BPW91)^[56]. The Los Alamos effective core potential plus double zeta (LANL2DZ)^[57-60] was employed for tungsten, whereas the Dunning/Huzinaga full double zeta basis set with polarization and diffuse function was used (D95+(d)) for P, C, H, S and O atoms (DFT2).

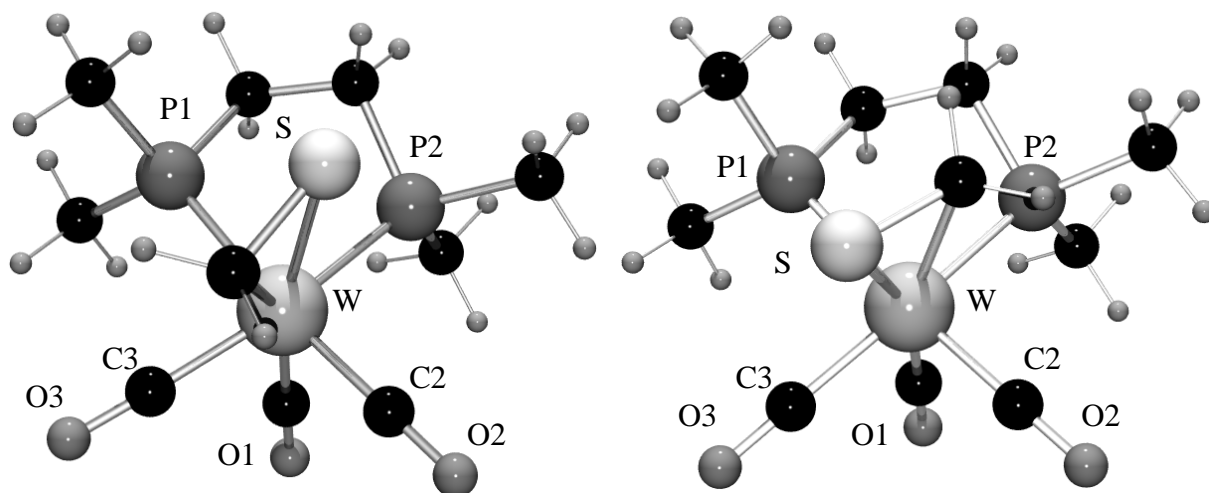
The structural parameters for the calculated compound **26** and their different stereo-isomers **28-30** (Figure 47) are summarized together with the experimental data of **26** in Table 19. Except for the theoretical WS bond length, which is 7 pm overestimated, the computed values are in very good agreement with the experimental ones, so that the difference for the other bond distances is less than 4 pm. It should be noticed, that a C-S single bond is found at 183.4(6) pm for the η_1 -phosphonothiolate complex $(\text{CO})_5\text{W}[\text{SC}(\text{H})\text{Ph}(\text{PMe}_3)]$ and at 181.9(5) pm for thiomethanol^[115], while the value for a C=S double bond is determined at 162.0(1) pm for the pentacarbonyl(thiobenzaldehyde) tungsten complex $(\text{CO})_5\text{W}[\text{SC}(\text{H})\text{Ph}]$ ^[116]. Therefore, the CS bond length, which has been measured at 174.5(3) pm in **26**, presents a partial double bond with more single bond character analog to the ethylene complex first characterized by Dewar^[89], Chatt and Ducanson^[90].

The WS bond distance in complex **26** (249.37(8) pm) is about 2 pm longer and 8 pm shorter than in $(\text{CO})_5\text{W}[\text{SC}(\text{H})\text{Ph}]$ and $(\text{CO})_5\text{W}[\text{SC}(\text{H})\text{Ph}(\text{PMe}_3)]$, respectively^[116]. Furthermore, the WC bond length is measured at 229.0(3) pm (calc. 230.0 pm), being a M-C single bond. Whereas the calculated C4-S-P1-P2 and C4-S-C3-W dihedral angles for **26** have been determined at 0.7° and 2.4°, the theoretical W-S-C4, W-C4-S and P1-W-P2 bond angles were found at 60.8°, 77.4° and 79.0°, respectively.



(26) $E = -1766.532510$ hartree
 $E_0 = -1766.274315$ hartree

(28) $E = -1766.526095$ hartree
 $E_0 = -1766.268366$ hartree



(29) $E = -1766.533814$ hartree
 $E_0 = -1766.275088$ hartree

(30) $E = -1766.525626$ hartree
 $E_0 = -1766.267328$ hartree

Figure 47. Optimized structures of $[\text{W}(\text{CO})_3(\text{dmpe})(\eta^2\text{-S}=\text{CH}_2)]$ using DFT2.

Furthermore, the W-P2 bond length, *trans* to the carbonyl ligand, is about 6 pm longer than the W-P1 interatomic distance (Table 19). This may be due to the good π -acceptor carbonyl ligand which shows a shorter W-C3 bond length. This effect can be also observed in the calculated structures **29** and **30**, where two carbonyls are *trans* to the dmpe ligand. For these complexes, both calculated W-P bond lengths are quite similar so that the W-P1 bond distance is lengthened by about 6 pm in comparison with **26**. The *trans* influence of sulfur on

the W-P1 bond length can be also observed by the comparison between the calculated structures **26** and **28**.

Table 19. Theoretical and experimental selected bond lengths (pm) and angles (degrees) for the thioaldehyde complexes **26** and **28-30**.

	(26)	(26)	(28)	(29)	(30)
	DFT2	Exp.	DFT2	DFT2	DFT2
Bond lengths (pm)					
W-C3	200.4	202.1(3)	201.9	199.7	201.4
C3-O3	117.9	114.2(4)	117.5	118.0	117.5
W-S	256.0	249.37(8)	257.1	256.8	257.4
S-C4	175.9	174.5(3)	175.3	175.2	174.0
W-C4	230.9	229.0(3)	230.0	233.0	233.2
W-C1	202.6	203.1(3)	202.6	199.8	200.0
C1-O1	118.0	115.0(4)	118.0	118.1	118.2
W-C2	202.8	201.1(3)	202.6	199.7	199.4
C2-O2	117.9	116.1(4)	118.0	118.0	118.0
W-P1	248.2	247.16(7)	249.0	254.7	254.0
W-P2	253.8	249.92(8)	252.5	254.1	253.4
Bond angles (°)					
W-S-C4	61.3	62.49(11)	60.8	61.9	61.9
W-C4-S	76.7	74.99(12)	77.4	76.5	76.9
P1-W-P2	79.9	78.82(3)	79.0	79.1	80.0
C1-W-C2	177.6	178.35(12)	177.0	84.1	88.1
P2-W-C3	163.4	157.20(9)	162.6	160.8	162.8
P1-W-C3	83.5	78.39(9)	83.6	87.5	92.1
P1-W-C2	92.4	89.69(9)	92.3	173.9	175.2
C1-W-C3	91.2	91.45(13)	91.5	81.8	83.9

4.1.2 MO calculation

The energies of the molecular orbitals for the compounds **26-30** have been calculated and investigated too. The geometries of the LUMO and HOMO for the complexes **26** and **28** are depicted in Figure 48. The LUMO of **26** is a combination of the $d_{xz}(\text{W})$, $p_y(\text{S})$ and $p_y(\text{C4})$ orbitals, the contribution of the $p_y(\text{S})$ being the most important. The HOMO is mainly

composed of the p_x orbital of S in the complexes. The calculated HOMO is in good agreement with the strong electrophilic activity found experimentally on the sulfur atom for compound **26**.

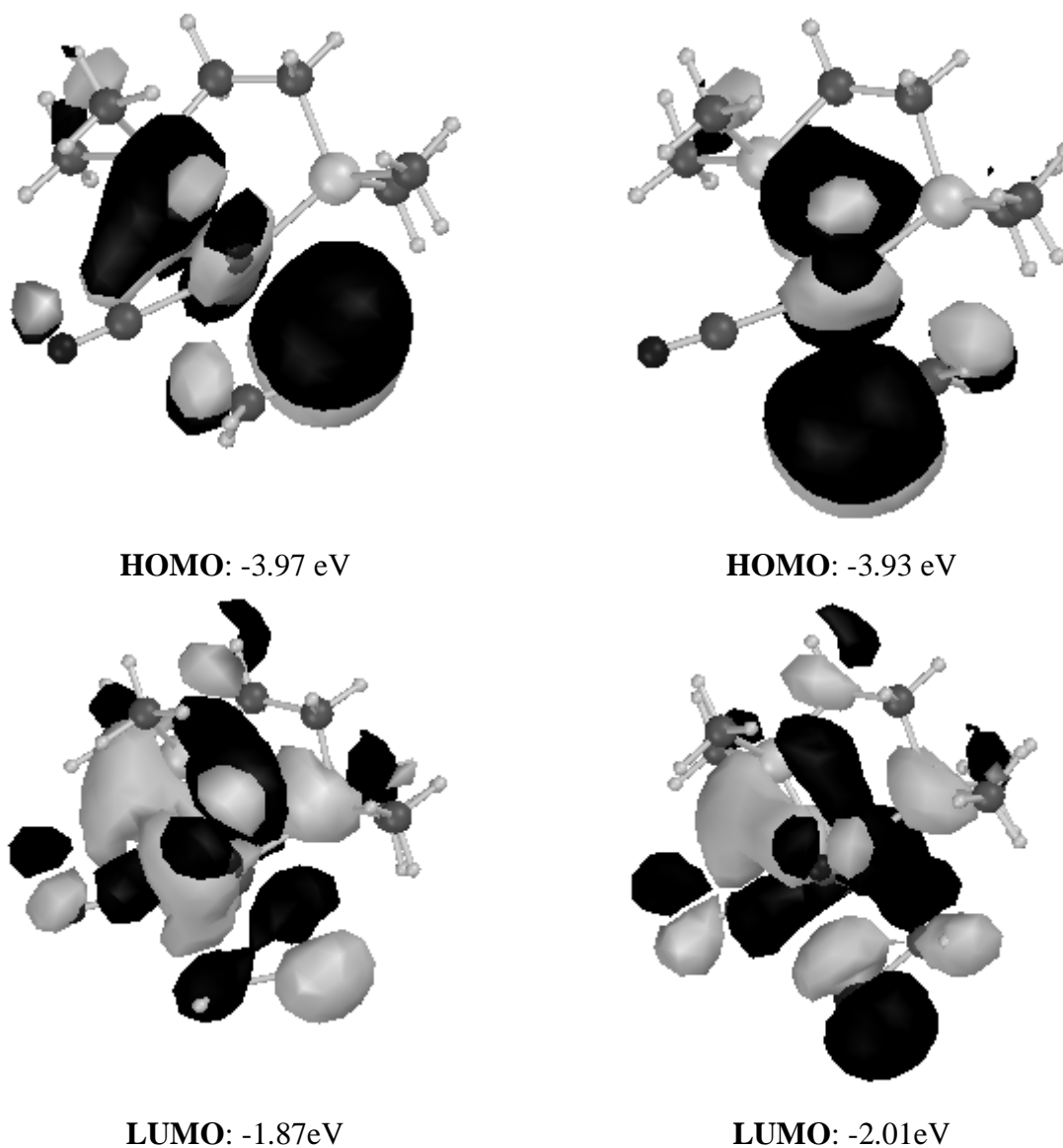


Figure 48. Representation of the calculated HOMO and LUMO of the complexes **26** and **28** using DFT2 (isocontour = 0.02).

According to the DFT2, **26** is 15.5 kJ/mol more stable than its isomeric form **28** (Figure 47). Moreover, the calculated energy of the HOMO and LUMO for the different complexes **26**, **28-30** is represented in Table 20. It is notable that the HOMO-LUMO gap is the highest for **26** and **29**. Although **26** was characterized by X-Ray, compound **29** has been calculated to be the most stable conformer. However, the energy difference between **26** and **29** or **28** and **30** is less than 5 kJ/mol so that **29** is expected in the solution state. One may notice that **28** is more stable than **30** in opposite to **26** and **29**.

Table 20. Calculated energy (in eV) of the HOMO and LUMO of the complexes **26**, **28-30** using DFT2.

	[W(CO) ₃ (dmpe)(η ² -S=CH ₂)]			
	26	28	29	30
E _{LUMO}	-1.87	-2.01	-2.32	-2.56
E _{HOMO}	-3.97	-3.93	-4.35	-4.22
E _{HOMO-LUMO}	-2.10	-1.92	-2.02	-1.66

The investigation of **26** in a solution state should show an equilibrium between **26** and **29**, which can be observed on the basis of the vibrational or NMR spectroscopy. Indeed, the different WP and WC bond lengths characterized within the complex should give different $J(\text{WP})$ coupling constant or different wavenumbers for the corresponding $\nu(\text{W-L})$ modes. Moreover, according to the calculations, the $\nu(\text{CO})$ of the different complexes **26**, **28-30** are expected at different wavenumbers (see following part).

4.1.3 Vibrational spectroscopy

4.1.3.1 Vibrational spectrum of *mer*-[W(CO)₃(dmpe)(η²-S=CR₂)] (R = H, D)

For the assignment of the vibrations of the W(SCH₂) skeleton of complex **26** and its deuterium analog **27**, the calculated fundamental modes for these compounds have been analysed and displayed in Table 21 together with the experimental values from the infrared (FT-IR) and FT-Raman spectroscopic measurements.

The antisymmetric and symmetric $\nu(\text{CD}_2)$ modes observed at 2157 and 2257 cm⁻¹ in the FT-Raman spectrum of **27** have been theoretically determined at 2200 and 2330 cm⁻¹, respectively. The wavenumber differences between theory and experiment are acceptable due to the higher anharmonicity of these modes. Moreover, the difference between the calculated symmetric and antisymmetric $\nu(\text{CD}_2)$ modes is only 30 cm⁻¹ overestimated.

The $\nu(\text{CO})$ vibrational modes were assigned to the strong bands at 1905 and 1991 cm⁻¹ in the FT-Raman spectrum and at 1850, 1915 and 1990 cm⁻¹ in the IR spectrum (Figures 49 and 50). For the complex **26** three $\nu(\text{CO})$ modes are expected and predicted at 1890, 1928 and 1986 cm⁻¹ using the DFT2 method. Whereas, two of these modes are Raman active, all the three are

IR active. The animation of the calculated vibrational modes for **26** shows for the highest Raman active mode a symmetric stretching vibration for all three carbonyls, which looks like a breathing motion. For the second Raman active mode the equatorial carbonyl ligand shows a out of phase stretching vibration to both *trans*-axial carbonyls. And the third $\nu(\text{CO})$ stretching mode which is only IR active, represents an out-of-phase stretching vibration of both CO, lying in the axial position (Figure 50).

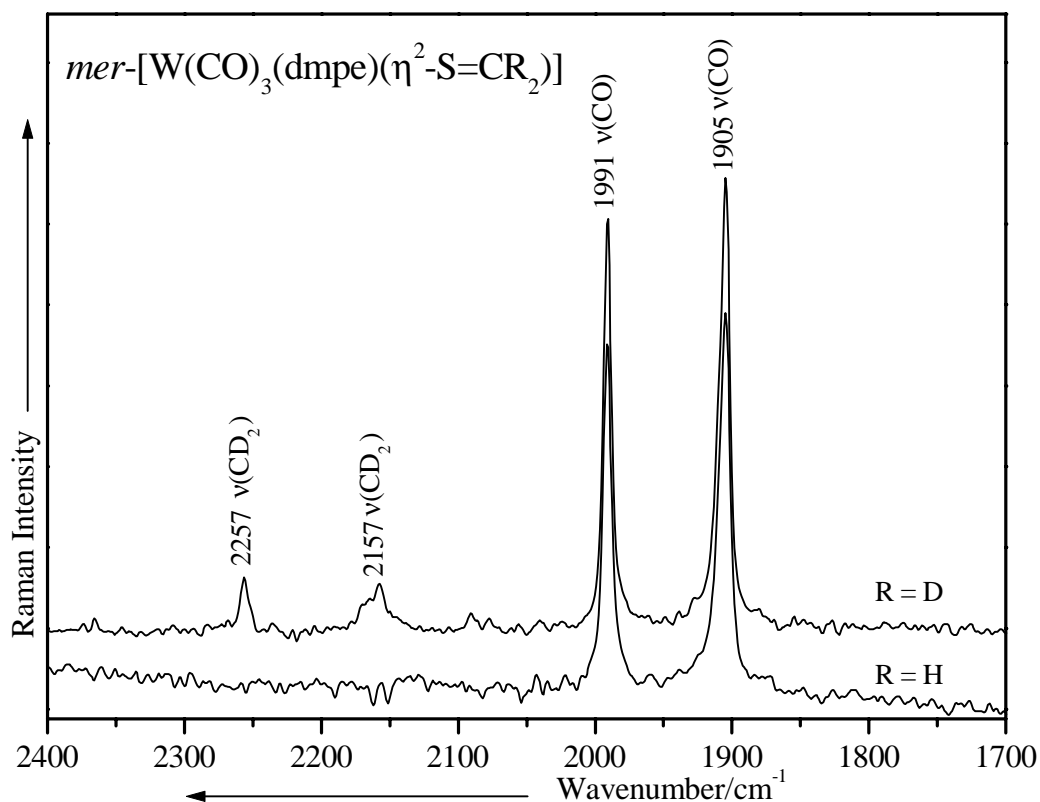


Figure 49. The high-wavenumber region of the FT-Raman spectrum of $mer\text{-}[\text{W}(\text{CO})_3(\text{dmpe})(\eta^2\text{-S=CH}_2)]$ (**26**) and $mer\text{-}[\text{W}(\text{CO})_3(\text{dmpe})(\eta^2\text{-S=CD}_2)]$ (**27**).

The $\nu(\text{CS})$ stretching mode, which is attributed to the medium band at 786 cm^{-1} in the FT-Raman spectrum of **26**, shifts 32 cm^{-1} to lower wavenumbers in the FT-Raman spectrum of **27** owing to the mass effect of the deuterium atoms. This mode was theoretically determined at 800 and 763 cm^{-1} for **26** and **27**, respectively. This represents a shift of 37 cm^{-1} , which is consistent with the previous result.

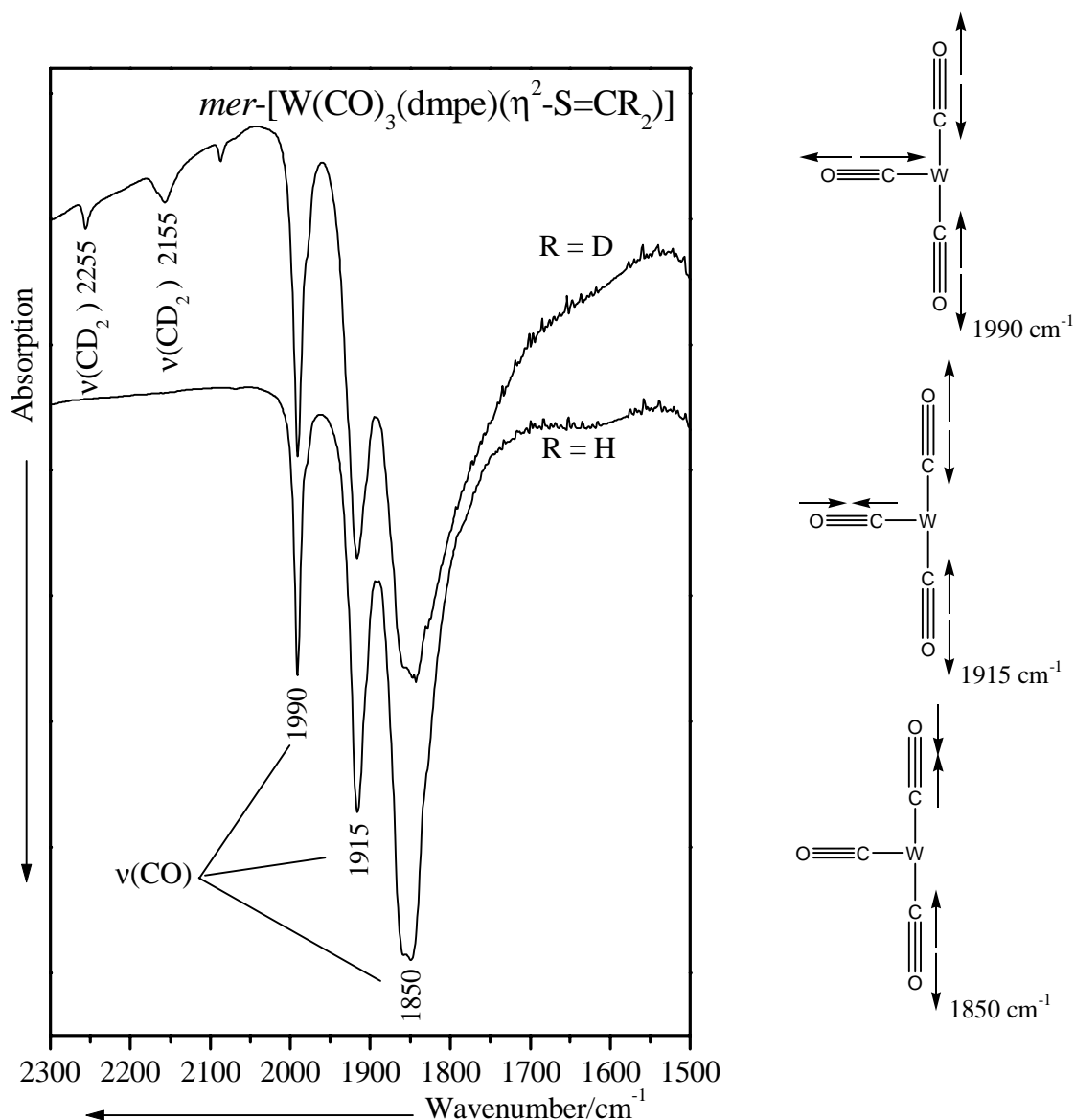


Figure 50. The high-wavenumber region of the FT-IR spectrum of *mer*-[W(CO)₃(dmpe)(η^2 -S=CH₂)] (**26**) and *mer*-[W(CO)₃(dmpe)(η^2 -S=CD₂)] (**27**).

Since the $\nu(\text{C-S})$ and $\nu(\text{C=S})$ modes were experimentally determined to be around 700 and 1100 cm^{-1} , respectively^[9, 94], the CS bond in complex **26** seem to have more single than double bond character as it has been discussed for its molecular structure. The selected calculated $\nu(\text{CS})$, $\nu(\text{WC})$ and $\nu(\text{WS})$ with the DFT2 method are depicted in Figure 51.

Since the $\delta(\text{MCO})$ deformation modes are well-known for their strong IR activity, the strong peaks observed at 605 and 585 cm^{-1} in the FT-IR spectrum of **26** and **27** should be ascribed to the $\delta(\text{W-CO})$ deformation modes. These modes were calculated at 611, 605 and 590 cm^{-1} .

The strong bands observed at 461, 449 and 442 cm^{-1} in the FT-Raman spectrum of **26** and **27** should be attributed to the $\nu(\text{W-CO})$ stretching modes.

Table 21. Selected calculated and experimental fundamental vibrational wavenumbers (cm^{-1}) for the complexes *mer*-[W(CO)₃(dmpe)(η^2 -S=CR₂)] (R = H, D) (**26-27**) together with their tentative assignment.

(26)			(27)			Assignment
R	IR	DFT	R	IR	DFT	
			2257mw	2255	2330	$\nu(\text{CD}_2)$
			2157mw	2155	2200	$\nu(\text{CD}_2)$
1991s	1990s	1986	1991s	1990s	1986	$\nu(\text{CO})$
1905s	1915s	1928	1905s	1915s	1928	$\nu(\text{CO})$
-	1850vs	1890	-	1850vs	1890	$\nu(\text{CO})$
		975				$\omega(\text{CH}_2)$
786m	785ms	800	754m		763	$\nu(\text{CS})$
777w	771vw	777				$\tau(\text{CH}_2)$
				720s	726	$\omega(\text{CD}_2)$
				708s	720	$\tau(\text{CD}_2)$
	605s	611		605s	611	$\delta(\text{WCO})$
	585s	605		585s	605	
		590			590	
				565m	570	$\tau(\text{CD}_2)$
	543m	537		541m	537	$\delta(\text{WCO})$
	534w	521		534w	519	
	522w			522w		
514m	514m		511m	509m		
461s	460 m	471	460m	459s	470	$\nu(\text{W-CO})$
449s	444 m	454	444 m	449s	454	
442s				442		
416shm	416m	440	416m	416m	439	$\delta(\text{WCO})$
		410			410	
421m	422sh	401	403m	406m	385	$\nu(\text{W-C})$
347m		326	346m		326	$\nu(\text{W-P})$
328s		309	328s		309	$\nu(\text{W-P})$
307s		288	306s		288	$\nu(\text{W-S}) + \delta(\text{CPC})$
262s		278	261s		278	$\nu(\text{W-S}) + \text{CH}_2\text{-CH}_2$ torsion
		249			249	$\delta(\text{CPC})$

One may notice, that the lower IR intensity of these bands is characteristic for the $\nu(\text{W-CO})$ stretching modes (Figures 52 and 53).

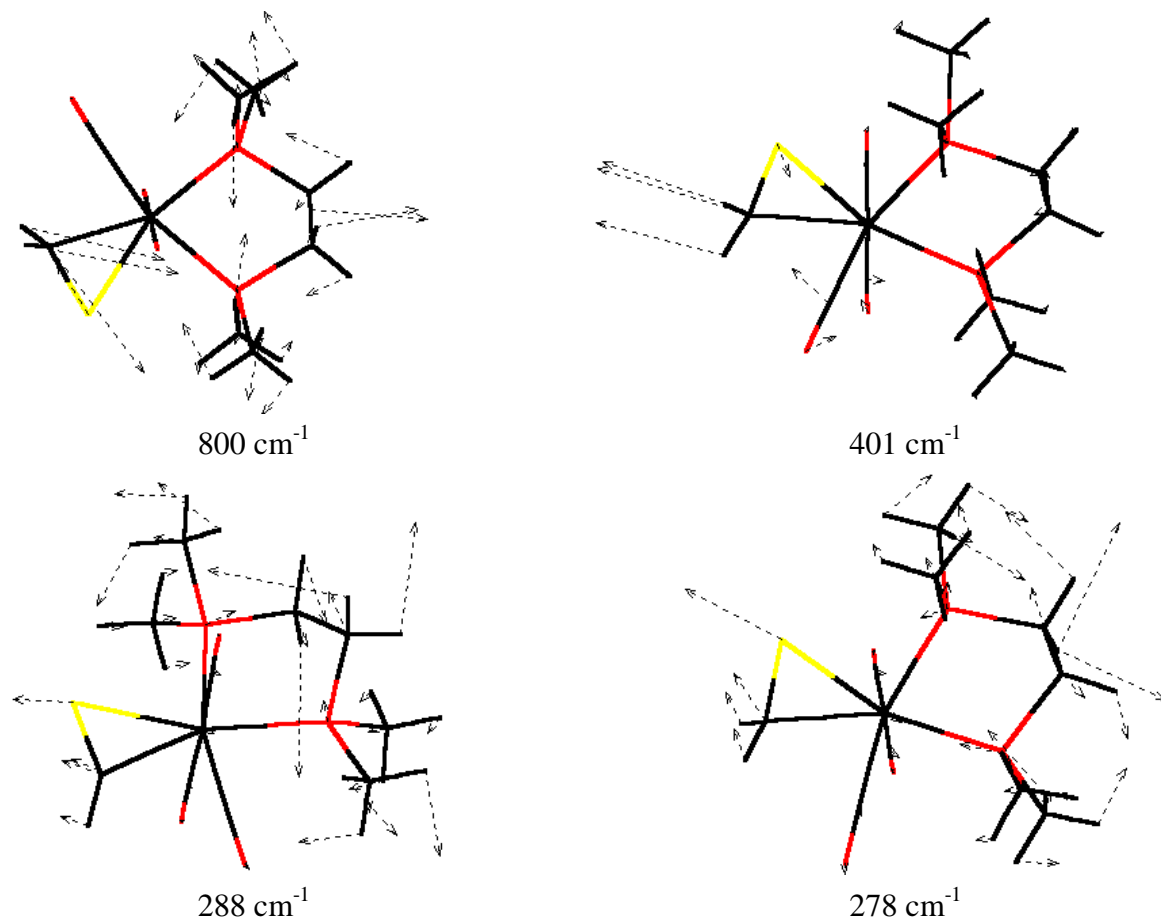


Figure 51. Calculated $\nu(\text{CS})$, $\nu(\text{WC})$ and $\nu(\text{WS})$ using DFT2.

According to the DFT calculations, the CH_2 twisting mode in compound **26** was tentatively assigned to the weak and very weak peaks at 777 and 771 cm^{-1} in the FT-Raman and IR spectrum of **26**, respectively. This mode is shifted to lower wavenumbers in the IR spectrum of the isotopomer **27** and is ascribed to the band at 565 cm^{-1} (cal. $\tau(\text{CD}_2) = 570\text{ cm}^{-1}$). The $\nu(\text{W-C})$ stretching mode between the thioaldehyde ligand and the tungsten is attributed to the medium band at 421 cm^{-1} which shifts 15 cm^{-1} to lower wavenumbers in **27**. The theoretical $\nu(\text{W-C})$ stretching mode is determined at 401 and 385 cm^{-1} in complexes **26** and **27**, respectively. This represents a shift of 16 cm^{-1} , which agrees very well with the experimental one. One may notice that these assignments are consistent with the results reported by Davidson and Davies^[117]. They studied the vibrational behaviour of Bis(ethene)tetracarbonyl molybdenum and tungsten complexes and mentioned that the symmetric (A1) M-C2 stretching mode is normally found in the range $358\text{-}405\text{ cm}^{-1}$ in related systems, whereas other $\text{C}_2\text{H}_4\text{M}$ systems give the antisymmetric (B1) M-C2 mode in the spectral region between 415 and 513 cm^{-1} .

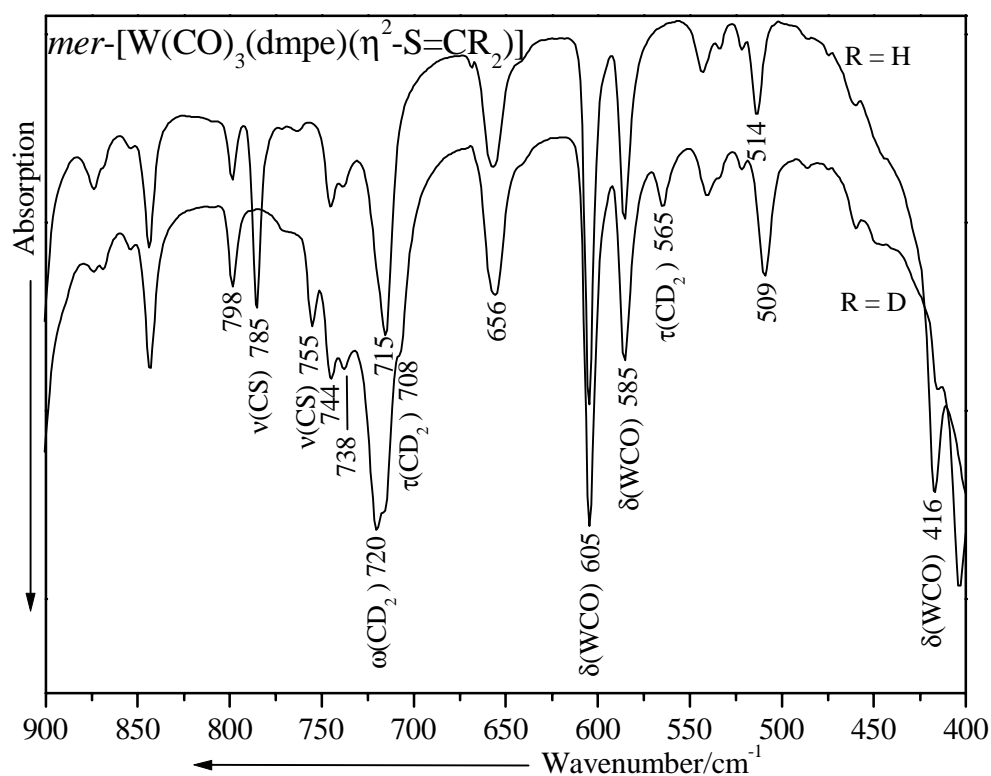


Figure 52. The low-wavenumber region of the FT-IR spectrum of *mer*-[W(CO)₃(dmpe)(η²-S=CH₂)] (**26**) and *mer*-[W(CO)₃(dmpe)(η²-S=CD₂)] (**27**).

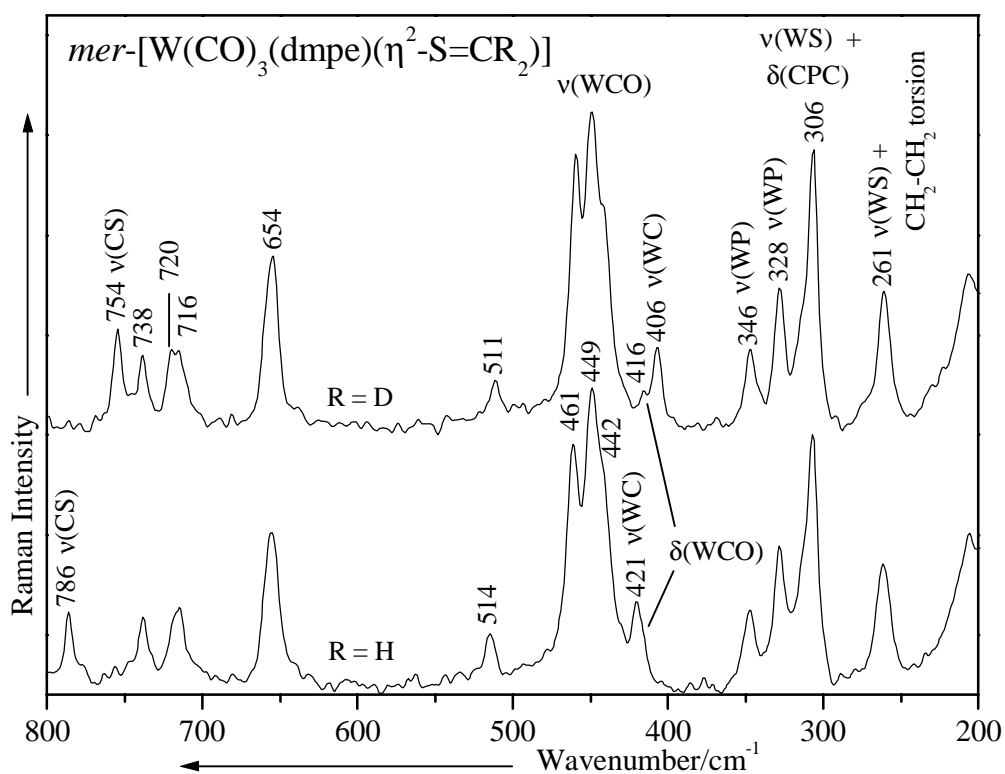


Figure 53. The low-wavenumber region of the FT-Raman spectrum of *mer*-[W(CO)₃(dmpe)(η²-S=CH₂)] (**26**) and *mer*-[W(CO)₃(dmpe)(η²-S=CD₂)] (**27**).

Table 22. Selected calculated fundamental vibrational wavenumbers (in cm^{-1}) for the complexes **26**, **28-30**.

[W(CO) ₃ (dmpe)(η^2 -S=CH ₂)]				Assignment
26	28	29	30	
1986	1991	1981	1988	$\nu(\text{CO})$
1928	1940	1922	1936	$\nu(\text{CO})$
1890	1889	1910	1907	$\nu(\text{CO})$
800	806	810	824	$\nu(\text{CS})$
401	402	390	382	$\nu(\text{W-C})$
326	325	318	326	$\nu(\text{W-P})$
309	307	302	309	$\nu(\text{W-P})$
		291	299	$\delta(\text{CPC})$
288	292			$\nu(\text{W-S}) + \delta(\text{CPC})$
278	286	269	273	$\nu(\text{W-S}) + \text{CH}_2\text{-CH}_2$ torsion
249	252	249	258	$\delta(\text{CPC})$

According to our theoretical results, the medium-to-strong peaks at 328 and 348 cm^{-1} should be ascribed to the $\nu(\text{WP})$ stretching modes and the strong one at 306 cm^{-1} is a combination between the $\nu(\text{W-CH}_2\text{S})$ and the $\delta(\text{CPC})$ vibrational modes.

The medium strong band at 261 cm^{-1} is a good candidate for the $\nu(\text{WS})$ stretching mode, since it has been calculated at 278 cm^{-1} in compounds **26** and **27** using DFT2. All the spectra were recorded in the crystalline state. However, the recording of the IR spectrum of **26** in solution reveals new bands in the $\nu(\text{CO})$ spectral region.

One may notice, that some differences in the structural parameters of compound **26**, **28-30** have been mentioned in the previous part so that different wavenumbers are expected for the fundamental $\nu(\text{M-L})$ vibrational modes as shown in Table 22 where the $\nu(\text{CO})$, $\nu(\text{CS})$, $\nu(\text{WC})$, $\nu(\text{WP})$ and $\nu(\text{WS})$ are reported for the calculated complexes **26**, **28-30**. The presence of new $\nu(\text{CO})$ bands is in agreement with the formation of an equilibrium state between **26** and one of its isomeric form **28**, **29** or **30**. According to our calculations, **29** is the expected isomeric form. This can be also confirmed by the analysis of the IR and NMR data. From these data, one can deduce that the equilibrium ratio between **26** and **29** is about 10:1, where **26** is the main product ^[114].

4.2 $Cp(CO)_2W=PtBu_2$ and $Cp(CO)_2\overline{W-PR_2-X}$ ($M = Mo, W$; $R = Me, tBu, Ph$; $X = S, Se$)

The bonding in hypervalent phosphorus compounds has received much attention in recent years^[118]. From the theoretical point of view^[119], the nature of the phosphoryl bond in phosphine oxides has been characterized by calculating PO bond lengths and bond energies, charge distributions, orbital and overlap populations, and localized orbitals. The bonding situation is best described in terms of a semi polar bond, with σ donation from the phosphine to the oxygen atom reinforced by π back-donation from the oxygen lone pairs through $p\pi-d\pi$ interactions. It has been established that phosphorus d orbitals contribute significantly to the bonding although they should not be regarded as valence orbitals^[118, 119a]; their role is enhanced by electronegative substituents at the phosphorus atom. The thiophosphoryl bond in phosphine sulfides has been studied in an analogous manner^[119d] and found to be quantitatively similar to the phosphoryl bond but much weaker with regard to both σ and π components. Vibrational spectral studies of phosphine oxide, sulfide or selenide ($R_3P=X$; $X = O, S, Se$) ligands have been extensively reported^[120-123] and have been used to probe the bonding in these molecules by determining their force fields^[124]. However, in contrast to ethylene complexes, there is no detailed vibrational analysis of phosphametallacycle complexes. Therefore, the FT-IR and FT-Raman spectra of the title compounds are reported for the first time in the following part.

The investigated compounds were synthesized in the work group of Prof. Malisch. DFT calculations were carried out on the model compounds $Cp(CO)_2W=PMe_2$ and $Cp(CO)_2W-PRR'-X$ ($R = R' = Me, tBu, Ph$; $R = Me, R' = tBu$; $X = S, Se$). The most interesting modes in the present investigation are the $\nu(P=X)$ ($X = Se, S$), $\nu(MX)$ ($M = Mo, W$; $X = Se, S$), $\nu(M-P)$ ($M = Mo, W$) and the $\nu(CO)$, since they are directly related to such a substantial property of the molecule as the M-C, M-P and M-X bond strengths. Taking advantage of the different masses of the tungsten and molybdenum atoms it has been possible to assign the $\nu(ML)$ vibrational modes. In this manner, we avoided the use of isotopic substitution.

4.2.1 Experimental and theoretical structures

4.2.1.1 Structure of $\text{Cp}(\text{CO})_2\text{W}=\text{PtBu}_2$ (**31**)

The model compound $\text{Cp}(\text{CO})_2\text{W}=\text{PMe}_2$ has been calculated using DFT3 and the BP86 functional with the quasi relativistic energy-adjusted effective core potential (ECP) for the 60 core electrons of tungsten in conjunction with the contracted basis (341/321/21) for the valence orbitals^[59] and the 6-31+G(d) Pople basis set for the other atoms H, P, C, O (DFT7). Figure 54 shows the POV-Ray^[62] plot of the model compound $\text{Cp}(\text{CO})_2\text{W}=\text{PMe}_2$ and the theoretical bond lengths and angles are reported in Table 23 together with the values measured for **31**. Except for the calculated W-C1 bond length, which differs with about 10 pm from the experimental value, all of the other structural parameters of the model compound $\text{Cp}(\text{CO})_2\text{W}=\text{PMe}_2$ are very closed to the reported ones (Table 23).

The existence of a metal phosphorus double bond involving a trigonal planar sp^2 -hybridized phosphorus atom is proved by the short WP bond distance and the unusual high coupling constant $J(\text{WP})$ (550-850 Hz)^[125]. The calculated W-P bond length (225.9 pm, DFT3) for the model compound $\text{Cp}(\text{CO})_2\text{W}=\text{PMe}_2$ agrees very well with the experimental value found for **31** and the theoretical evaluated W=P double bond (226 pm; $r_w = 122$ pm in $[\text{Cp}(\text{CO})_2\text{W}]_2$ ^[125-127]; $r_p = 104$ pm in $[2.4.6\text{-tri-tert-butylphenyl}]_2\text{P}_2$ ^[128]).

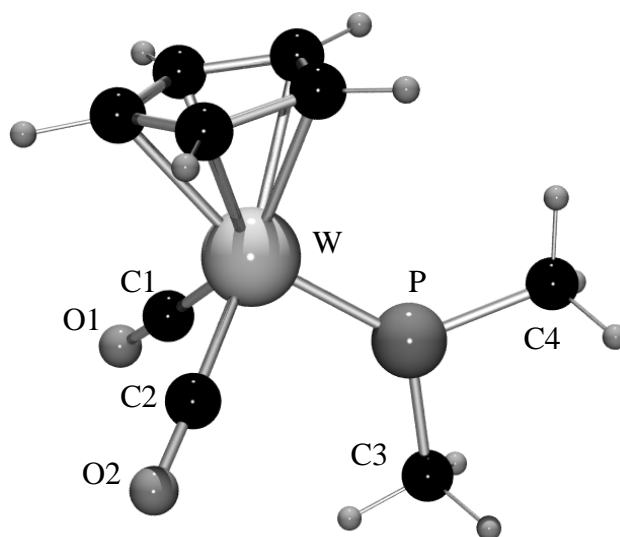


Figure 54. Optimized structure of $\text{Cp}(\text{CO})_2\text{W}=\text{PMe}_2$ using DFT3.

Table 23. Theoretical and experimental selected bond lengths and angles for complex **31**.

	Cp(CO) ₂ W=PMe ₂		Cp(CO) ₂ W=PtBu ₂
	DFT3	DFT7	Exp. ^a
Bond lengths (pm)			
W-P	225.9	226.4	228.4(4)
W-C1	195.9	196.2	186.9(1)
C1-O1	117.7	118.3	120.2(2)
W-C2	195.9	196.2	193.7(2)
C2-O2	117.7	118.3	114.3(2)
P-C3	185.1	186.3	190.2(2)
P-C4	184.4	185.6	190.9(2)
Bond angles (°)			
W-P-C3	130.2	130.2	126.1(6)
W-P-C4	128.7	128.4	124.4(6)
C ₃ -P-C4	101.1	101.3	109.4(8)
C1-W-C2	80.4	81.2	79.8(8)
C1-W-P	91.5	92.4	93.9(6)
C2-W-P	91.5	92.4	92.4(5)

^aReferences 125, 129

DFT7: BP86/ W-ECP 4 60 [341/321/21]; 6-31+G(d) for H, P, C, O

4.2.1.2 Structures of Cp(CO)₂ $\overline{\text{M-PR}_2\text{-X}}$ (M = Mo, W; R =Ph, Me, *t*Bu) (32-35)

The theoretical structures obtained with the BPW91 and BP86 functionals are consistent with the measured X-Ray structure of the complex Cp(CO)₂ $\overline{\text{W-P(Me)(tBu)-Se}}$. The optimized geometry of the complex Cp(CO)₂ $\overline{\text{W-PPh}_2\text{-S}}$ using DFT7 is represented in Figure 55. It is notable that the calculated (203-207 pm) and measured (202.1 pm) PS bond lengths are shorter than the expected P-S single bond (213.2(6) pm^[130a] and 192.6(1)-196.6(2) pm^[130b,c] for a single and double bond, respectively). Experimentally, the P=S donor bond has been determined at 194.0 pm in trimethyl^[131], 188.4 pm in trichloro^[132] and 187.0 pm in trifluorophosphine sulfide^[133], which shows the influence of the substituent on the PS bond length.

The W-S bond distance is much longer (Table 24) than the single W-S bond which has been measured at 230.3 and 227.5 pm for the *cis*- and *trans*-complexes [W{CH(CF₃)=C(CF₃)S}(η²-CF₃C₂CF₃)η⁵-C₅H₅], respectively^[134]. Additionally, it is also

about 10 pm longer than the measured one in the thioaldehyde complex **26**. The calculated bond angles S-W-P, W-S-P and W-P-S agree also very well with the experimental values determined at 47.7°, 61.5° and 70.8°, respectively (Table 24).

Table 24. Theoretical and experimental selected bond lengths (pm) and angles (degrees) for the complexes $\text{Cp}(\text{CO})_2\overline{\text{W-PRR}'\text{-S}}$.

	$\text{Cp}(\text{CO})_2\overline{\text{W-PRR}'\text{-S}}$					
	R = R' = Me		R = R' = <i>t</i> Bu	R = R' = Ph		R = Me, R' = <i>t</i> Bu
	DFT2	DFT8	DFT2	DFT2	DFT9	Exp. ^a
	Bond lengths (pm)					
W-P	242.4	241.4	249.1	243.3	242.8	239.9(1)
W-C1	195.9	195.7	196.1	196.2	196.2	194.8(4)
C1-O1	118.6	118.9	118.6	118.5	118.9	115.9(5)
W-C2	196.3	196.0	195.0	196.2	195.9	194.7(3)
C2-O2	118.2	118.5	118.4	118.3	118.8	115.9(4)
P-S	206.0	203.6	207.4	206.6	204.4	202.1(1)
W-S	264.5	260.9	261.7	263.1	259.9	257.9(1)
P-C3	185.2	184.5	193.9	184.6	183.8	184.2(3)
P-C4	185.8	185.2	194.9	184.8	184.0	181.9(3)
	Bond angles (°)					
C1-W-C2	78.6	79.8	79.4	78.9	80.1	78.2(1)
W-P-C3	124.6	124.5	122.9	127.7	126.4	128.3(1)
W-P-C4	125.7	125.5	120.6	120.8	121.5	121.5(1)
C3-P-S	112.5	113.4	108.9	111.5	112.9	112.1(1)
C4-P-S	112.6	113.5	113.2	113.7	113.6	111.9(1)
W-S-P	60.5	61.2	62.9	61.0	61.7	61.5(1)
S-P-W	71.8	71.2	69.3	71.0	70.5	70.8(1)
S-W-P	47.7	47.6	47.8	48.0	47.8	47.7(1)
C3-P-C4	104.1	103.9	112.2	106.0	106.1	105.5(2)

^aReference 125

DFT8: BPW91/W-ECP 4 60 [341/321/21]; 6-31G for H, C; 6-31+G(d) for P, O; 6-311+(3df) for S.

DFT9: BP86/W-ECP 4 60 [341/321/21]; 6-31G for H, C; 6-31+G(d) for P, O; 6-311+(3df) for S.

The SPR_2 unit act as a three electrons donor ligand in the complex. Formally, the phosphorus and the sulfur atoms could give one or two electrons, respectively.

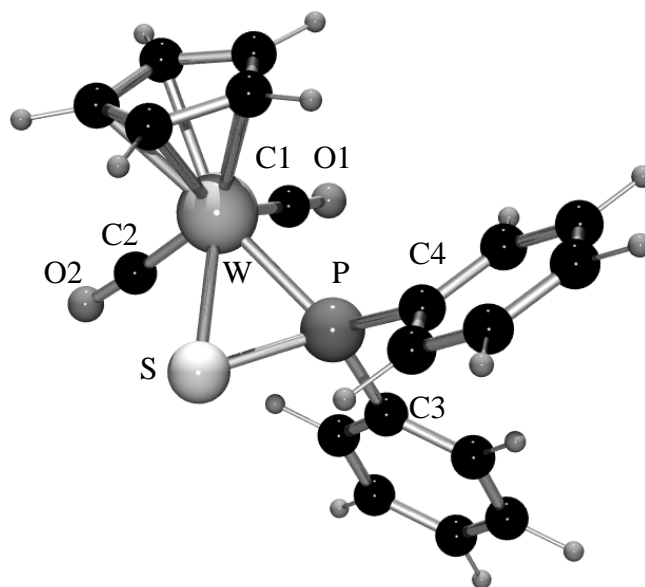


Figure 55. Optimized structure of $\text{Cp}(\text{CO})_2\text{W-PPh}_2\text{-S}$ using DFT7.

4.2.1.3 Structures of $\text{Cp}(\text{CO})_2\text{M-PR}_2\text{-Se}$ ($\text{M} = \text{Mo}, \text{W}$; $\text{R} = \text{Ph}, \text{Me}, t\text{Bu}$) (36-39)

The coordination of R_2PSe could be interpreted as a square pyramidal one. The optimized geometry of $\text{Cp}(\text{CO})_2\text{W-PPh}_2\text{-Se}$ with DFT7 is represented in Figure 56. Selected X-Ray data for the complexes $\text{Cp}(\text{CO})_2\text{W-P}t\text{Bu}_2\text{-Se}$ and $\text{Cp}(\text{CO})_2\text{W-P}(\text{Me})(t\text{Bu})\text{-Se}$ are reported in Table 25 together with the corresponding theoretical values found in a series of model compounds.

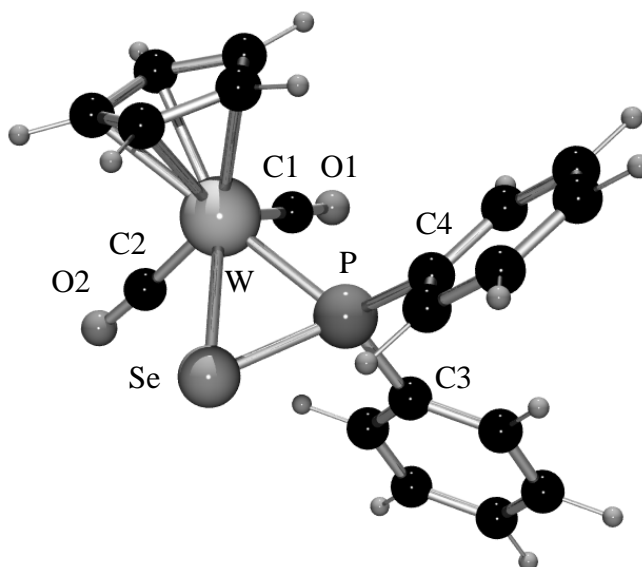


Figure 56. Optimized structure of $\text{Cp}(\text{CO})_2\text{W-PPh}_2\text{-Se}$ using DFT9.

As for the sulfur complexes, theoretical and experimental results are in very close to each other. It is noteworthy that the measured P-W and W-Se bond lengths (Table 25) are longer than the expected theoretical W-P and W-Se single bonds (240.4 pm and 247.7 pm as the sum of the covalent radii)^[135]. As a consequence of the different W-P and W-Se distances, the W-P-Se angle (71.2°) is much larger than the W-Se-P (58.9°) one. Furthermore, the P-Se bond length which has been measured at 217.1(2) pm, situates this bond between a single (221-230 pm) and a double bond (212 pm)^[136].

Table 25. Theoretical and experimental selected bond lengths (pm) and angles (degrees) for the complexes Cp(CO)₂W-PRR'-Se.

Cp(CO) ₂ W-PRR'-Se							
	R = R' = Me		R = R' = <i>t</i> Bu		R = <i>t</i> -Bu, R' = Me		R = Ph
	DFT10	Exp. ^a	DFT9 ^c	DFT9 ^d	Exp. ^b	DFT9	
Bond lengths (pm)							
W-P	243.1	243.1(1)	245.2	243.8	241.1(6)	243.2	
W-C1	195.9	191.1(7)	196.2	195.7	196.1(2)	196.0	
C1-O1	118.6	117.8(7)	119.0	119.2	115.4(3)	118.9	
W-C2	196.3	193.2(7)	195.3	195.9	195.7(3)	196.0	
C2-O2	118.2	115.4(7)	118.8	118.7	115.8(3)	118.7	
P-Se	220.2	217.1(2)	219.7	219.5	216.6(7)	219.7	
W-Se	276.4	268.9(1)	274.0	274.1	270.6(3)	273.7	
P-C3	185.4	187.5(6)	185.5	190.7	185.7(2)	187.7	
P-C4	186.0	189.4(6)	191.1	186.0	182.2(3)	184.1	
Bond angles (°)							
C1-W-C2	78.8	80.2(3)	80.1	80.2	78.7(1)	80.4	
W-P-C3	124.4	122.4(2)	118.0	128.1	127.6(8)	126.3	
W-P-C4	124.9	120.1(2)	131.2	120.2	120.8(9)	120.9	
C3-P-Se	112.9	109.7(2)	111.1	113.4	112.5(8)	113.0	
C4-P-Se	113.3	114.6(2)	114.1	111.7	112.6(9)	113.9	
W-Se-P	57.3	58.9(4)	58.3	57.9	58.0(2)	57.8	
Se-P-W	73.1	71.2(5)	72.0	73.3	72.2(2)	72.3	
Se-W-P	49.6	49.9(4)	49.7	49.7	49.7(2)	49.9	
C3-P-C4	103.9	111.3(3)	104.9	105.6	105.6(1)	105.8	

^aReference 125, ^bReference 137, ^cE_{BP86} = -3429.056852 hartree. ^dE_{BP86} = -3429.058947 hartree; DFT10: BPW91/ LANL2DZ for W, D95+(d) for H, P, C, O, 6-311+G(d) for Se; DFT9: BP86/W-ECP 4 60 [341/321/21]; 6-31G for H, C; 6-31+G(d) for P, O; 6-311+(3df) for Se.

4.2.2 NBO and MO calculations

Figure 57 shows the geometries of the three highest occupied molecular orbitals calculated for the model complex $\text{Cp}(\text{CO})_2\text{W-PMe}_2\text{-S}$. The HOMO and HOMO-1, which indicate mainly $\text{M}(\pi) \rightarrow \text{CO}(\pi^*)$ interactions, are essentially composed of the d_{xy} and d_z^2 metal-orbitals, respectively. However, the HOMO presents a π -bonding character between the phosphorus and the sulfur atoms. The HOMO-2 is built from a p_π - d_π overlap between the sulfur and the tungsten atoms and is mainly localized on the chalcogenide. Moreover, the HOMO-LUMO gap for the model compounds $\text{Cp}(\text{CO})_2\text{W-PMe}_2\text{-X}$ has been calculated at 2.22 eV (X = S) and 2.12 eV (X = Se).

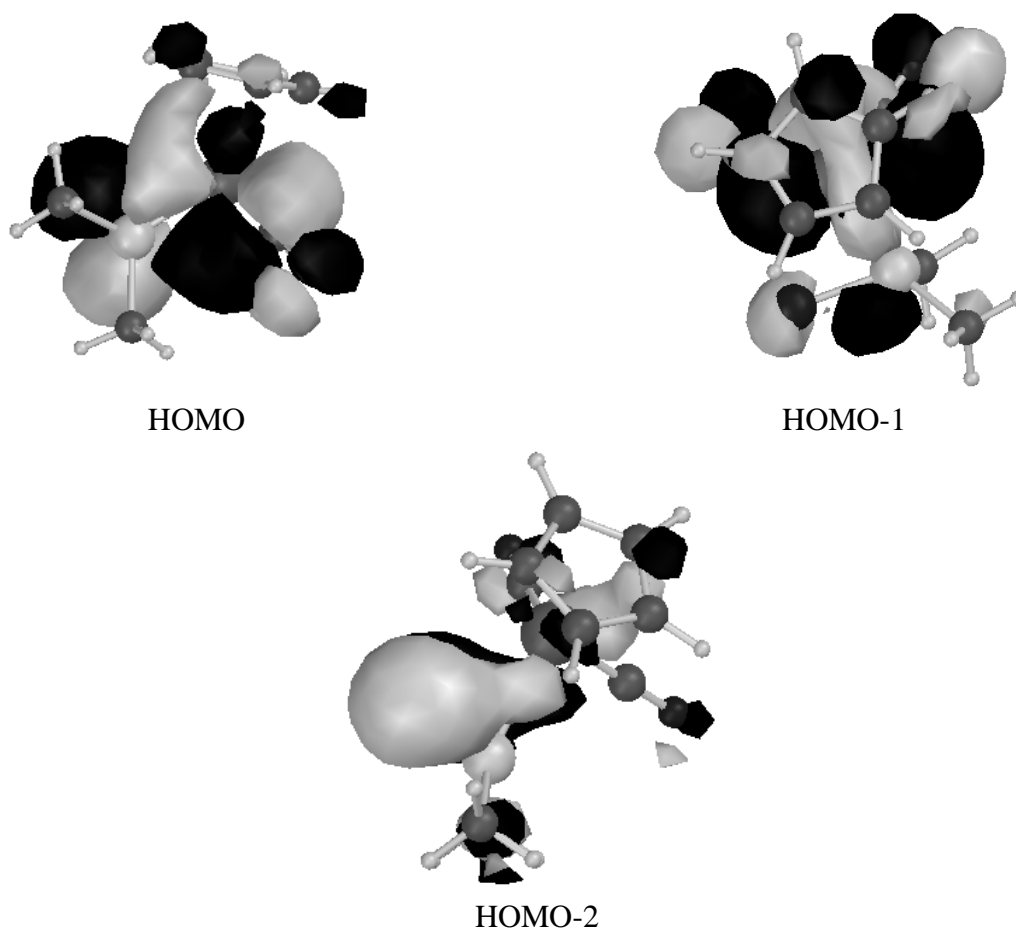


Figure 57. Representation of the calculated HOMO, HOMO-1 and HOMO-2 for the model compound $\text{Cp}(\text{CO})_2\text{W-PMe}_2\text{-S}$ (isocontour = 0.02).

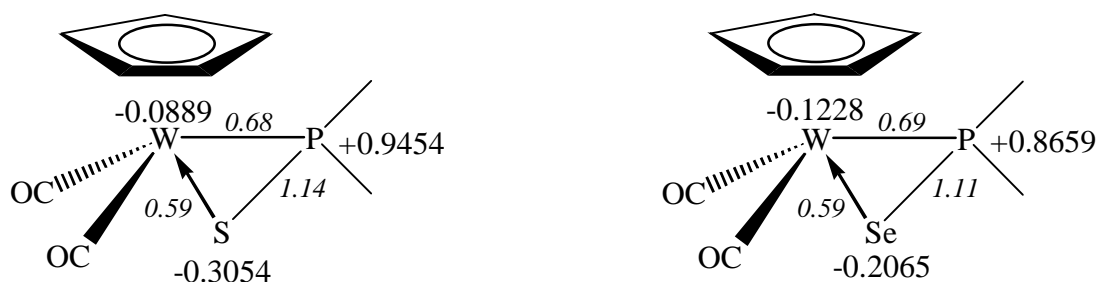


Figure 58. Calculated natural charges (in e) and Wiberg Bond indices (italic value) for the model compounds $\text{Cp}(\text{CO})_2\text{W-PMe}_2\text{-X}$ ($\text{X} = \text{S}, \text{Se}$), determined by the NBO Analysis.

A slightly higher charge concentration can be observed at the sulfur atom of the model compound $\text{Cp}(\text{CO})_2\text{W-PMe}_2\text{-S}$ using the NBO analysis (Figure 58). This is also true for the tungsten atom of the model compound $\text{Cp}(\text{CO})_2\text{W-PMe}_2\text{-Se}$. The obtained Wiberg bond indices, for the W-P and W-X distances, from the model compounds $\text{Cp}(\text{CO})_2\text{W-PMe}_2\text{-X}$ ($\text{X} = \text{S}, \text{Se}$) are quite similar (Figure 58). However, the PS bond seem to be slightly stronger than the PSe one.

4.2.3 Vibrational spectroscopy

4.2.3.1 Vibrational spectrum of $\text{Cp}(\text{CO})_2\text{W=PtBu}_2$ (**31**)

The FT-Raman spectrum of the complex $\text{Cp}(\text{CO})_2\text{W=PtBu}_2$ (**31**) has been already reported in the PhD-Thesis of Claudia Fickert^[138]. The aim of this part is to support or to complete her assignment using DFT calculations.

The symmetric and antisymmetric $\nu(\text{CO})$ stretching modes are calculated at 1946 and 1888 cm^{-1} , respectively, for the model compound $\text{Cp}(\text{CO})_2\text{W=PMe}_2$ using DFT3. The deformation modes of the *tert*-butyl group are assigned to the bands at 1468 until 1422 cm^{-1} whereas the $\nu(\text{C}=\text{C})$ stretching modes of the cyclopentadienyl ring are attributed to the peaks at 1356 (calc. 1361 cm^{-1}) and 1365 cm^{-1} (calc. 1367 cm^{-1}).

As expected, the characteristic cyclopentadienyl ring breathing was ascribed to the very intense band at 1110 cm^{-1} (calc. 1103 cm^{-1}). The $\nu_{\text{as}}(\text{PC}_2)$ and $\nu_{\text{s}}(\text{PC}_2)$ stretching modes were assigned by Fickert to the medium weak bands at 607 and 586 cm^{-1} , respectively. For the model compound $\text{Cp}(\text{CO})_2\text{W=PMe}_2$, the two bands calculated at 688 and 698 cm^{-1} correspond to the $\nu(\text{PC})$ stretching modes and mix with a rocking vibration $\rho(\text{CH}_3)$. This difference in

wavenumbers can be due to a mass effect, since the methyl groups are less heavy than the *tert*-butyl ones.

Fickert assigned the $\nu_s(\text{WC})$ stretching mode for compound **31** to the medium-to-strong band at 501 cm^{-1} . Strikingly, the calculated wavenumber for this mode is found at 501 cm^{-1} too. Furthermore, the $\delta(\text{WCO})$ deformation modes, which were theoretically determined at 529, 508, 483 and 473 cm^{-1} for the model compound $\text{Cp}(\text{CO})_2\text{W}=\text{PMe}_2$, should be attributed to the weak bands emerging in the same region. The $\nu(\text{W}=\text{P})$ stretching mode, which gave rise to the band at 468 cm^{-1} in the IR spectrum was predicted at 372 cm^{-1} using DFT3. One may notice that several bands below 400 cm^{-1} have been not considered. Namely, the medium one at 390 cm^{-1} is a good candidate for the $\nu(\text{W}=\text{P})$ stretching mode. The $\nu_{\text{as}}(\text{Cp}-\text{W})$ are calculated to be at 324 and 340 cm^{-1} whereas the symmetric one was found at 304 cm^{-1} . Thus, the bands at 320 and 300 cm^{-1} can be assigned to these modes. The other one at 233 cm^{-1} is owed to the $\delta(\text{PC})$ mode.

4.2.3.2 Vibrational spectrum of $\text{Cp}(\text{CO})_2\overline{\text{M}-\text{PPh}_2-\text{X}}$ ($\text{M} = \text{W}, \text{Mo}$; $\text{X} = \text{S}, \text{Se}$) (**32-33**, **36-37**)

In the $\nu(\text{CO})$ region of complexes **32-33** and **36-37** several bands of medium-to-low intensity are observed as for the phosphonium complex **31**. Such splittings are well-known^[138] and maybe due to a group effect such as molecular stacking. Therefore, the two most intensive $\nu(\text{CO})$ bands, used in the comparison of the different complexes are observed at 1922 and 1851 cm^{-1} for $\text{Cp}(\text{CO})_2\overline{\text{W}-\text{PPh}_2-\text{S}}$ (**32**), 1929 and 1856 cm^{-1} for $\text{Cp}(\text{CO})_2\overline{\text{W}-\text{PPh}_2-\text{Se}}$ (**36**), 1934 and 1864 cm^{-1} for $\text{Cp}(\text{CO})_2\overline{\text{Mo}-\text{PPh}_2-\text{S}}$ (**33**) and 1939 and 1871 cm^{-1} for $\text{Cp}(\text{CO})_2\overline{\text{Mo}-\text{PPh}_2-\text{Se}}$ (**37**). They have been assigned to the symmetrical and asymmetrical $\nu(\text{CO})$ stretching mode, respectively. Although tungsten and molybdenum have the same covalent radius, the red line shifts of the $\nu(\text{CO})$ mode in **32** and **36**, in relation to the corresponding molybdenum complexes **33** and **37**, indicate a stronger π -back bonding in the tungsten compounds. Such effects are well known for heavy-atoms of the fourth-row, as result of their relativistic effects. The comparison between the compounds **32** and **36** reveals a small blue shift (5 and 7 cm^{-1}) of the $\nu(\text{CO})$ mode in the selenium complexes. Besides drawing a parallel between **31** or **32** and **36**, one may notice that the $\nu(\text{CO})$ stretching modes in **31** are shifted to lower wavenumbers.

The $\nu(\text{C}=\text{C})$ stretching modes of the phenyl rings are here insensitive, so they have been assigned for all the complexes to the two bands of medium and strong relative intensity at 1571 and 1584 cm^{-1} , respectively. The $\nu(\text{C}=\text{C})$ stretching modes of the cyclopentadienyl

ligand were found at 1434, 1420 and 1352 cm^{-1} , in accordance with the theoretically determined values at 1419, 1413 and 1346 cm^{-1} .

In the 1200 - 950 cm^{-1} spectral region several bands belonging to the phenyl substituents or to the cyclopentadienyl ligand as the $\delta(\text{CC})$, $\delta(\text{CH})$ or ring deformation modes are expected. In good agreement with the DFT calculations, the two peaks at 1106 (calc. 1098 cm^{-1}) and 1062 cm^{-1} (calc. 1073 cm^{-1}) are characteristic for the cyclopentadienyl ligand, whereas the ones at 1027 and 999 cm^{-1} have been assigned to ring vibrations of the phenyl unit. As expected^[94], in the FT-Raman spectra of **34-35** and **38-39**, the $\nu(\text{PC}_{\text{ring}})$ vibrational modes give rise to two bands of strong and medium intensity at 1092 (calc. 1097 cm^{-1}) and 1070 cm^{-1} (calc. 1085 cm^{-1}), respectively.

The position of the $\nu(\text{P}=\text{X})$ stretching mode may indicate the relative amount of $\text{X}(\text{p}_\pi)\text{-P}(\text{d}_\pi)$ bonding. Any such multiple bonding will tend to delocalize sulfur electrons causing a decrease of the basicity of the sulfur while increasing the wavenumber of $\nu(\text{P}=\text{X})$. Vibrational spectra of some phosphine sulfides, as well as their Cu(I) complexes, have been already assigned in the literature^[120-122]. One may notice that the $\nu(\text{P}-\text{S})$ and the $\nu(\text{P}=\text{S})$ stretching modes have been expected around 480 and 650 cm^{-1} , respectively^[9]. For example, the $\nu(\text{P}=\text{S})$ in the $\text{R}_3\text{P}=\text{S}$ compounds with $\text{R} = \text{Ph}$, Me and Et , has been ascribed at 639, 565 and 536 cm^{-1} , respectively. But, there are some controversies in the literature concerning the explanation of the band shift of the $\nu(\text{P}=\text{S})$ stretching mode in these complexes. On one hand, the high wavenumber of $\nu(\text{P}=\text{S})$ in $\text{Ph}_3\text{P}=\text{S}$ has been explained with the increasing of the electron withdrawing power of the phenyl group relative to alkyl groups, which facilitates $\text{p}_\pi\text{-d}_\pi$ backbonding from sulfur to phosphorus. On the other hand, Colthup et al.^[139] found, that the $\text{P}=\text{S}$ band varies in intensity, and the wavenumber shifts do not correlate with the substituent electronegativity because the $\text{P}=\text{S}$ stretching mode is expected to interact mechanically (to varying degrees) with the symmetrical PX_3 stretching vibration, giving rise to two bands. The basic $\text{P}=\text{S}$ stretching vibration is roughly estimated to have a wavenumber of about 675 cm^{-1} ^[139], and this may be near the symmetrical PX_3 stretching mode for various types of X group substituents. It should be noticed that Cowley and Mills assigned the $\nu(\text{P}=\text{S})$ at 701 cm^{-1} in $(i\text{-C}_3\text{H}_7)_3\text{PS}$ and at 596 or 583 cm^{-1} in $(n\text{-C}_3\text{H}_7)_3\text{PS}$ ^[140].

The FT-Raman spectra of **33** in CH_2Cl_2 solution with isotropic and anisotropic scattering allowed us to assign some of the fundamental vibrational modes (Figure 60). The $\nu(\text{PS})$ stretching mode, calculated at 589 cm^{-1} for $\text{Cp}(\text{CO})_2\overline{\text{W}}\text{-PPh}_2\text{-S}$ (**32**) (Figure 59), was tentatively ascribed to the strong polarized band at 598 cm^{-1} in the FT-Raman spectrum of the complex $\text{Cp}(\text{CO})_2\overline{\text{Mo}}\text{-PPh}_2\text{-S}$ (**33**). In the FT-Raman spectrum of the crystals **32** and **33** this band was observed at 591 and 594 cm^{-1} , respectively (Figure 61).

As against the $\text{Ph}_3\text{P}=\text{S}$ ^[120], the $\nu(\text{PS})$ stretching mode in the FT-Raman spectrum of **32** and **33** shifts to lower wavenumbers, which is consistent with the partial PS double bond postulated in these complexes. It should be noticed that the band observed at 620 cm^{-1} appears in the FT-Raman spectrum of the selenium complexes too (Figure 62). Therefore this band can not be attributed to the $\nu(\text{PS})$ mode.

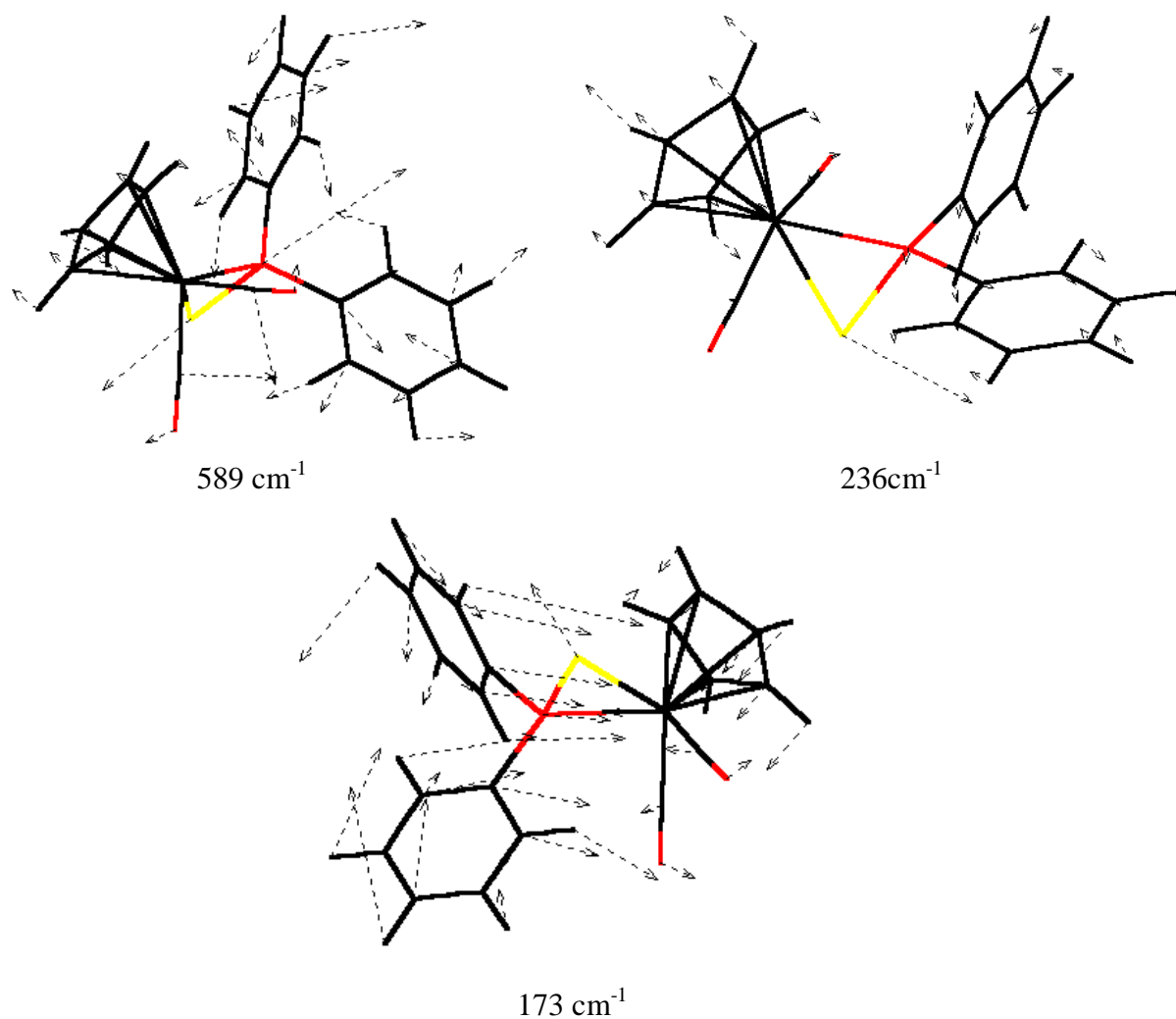


Figure 59. Calculated $\nu(\text{PS})$, $\nu(\text{WS})$ and $\nu(\text{WP})$ modes using DFT9.

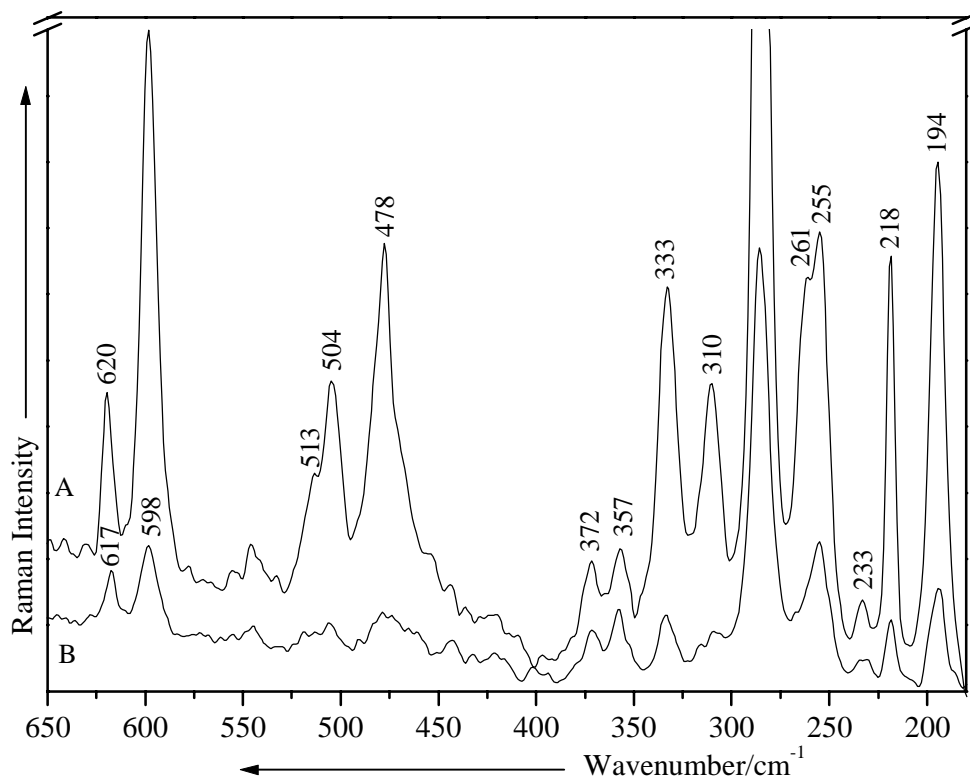


Figure 60. FT-Raman spectrum of $\text{Cp}(\text{CO})_2\text{Mo-PPh}_2\text{-S}$ in CH_2Cl_2 solution. (A) parallel polarized. (B) perpendicular polarized.

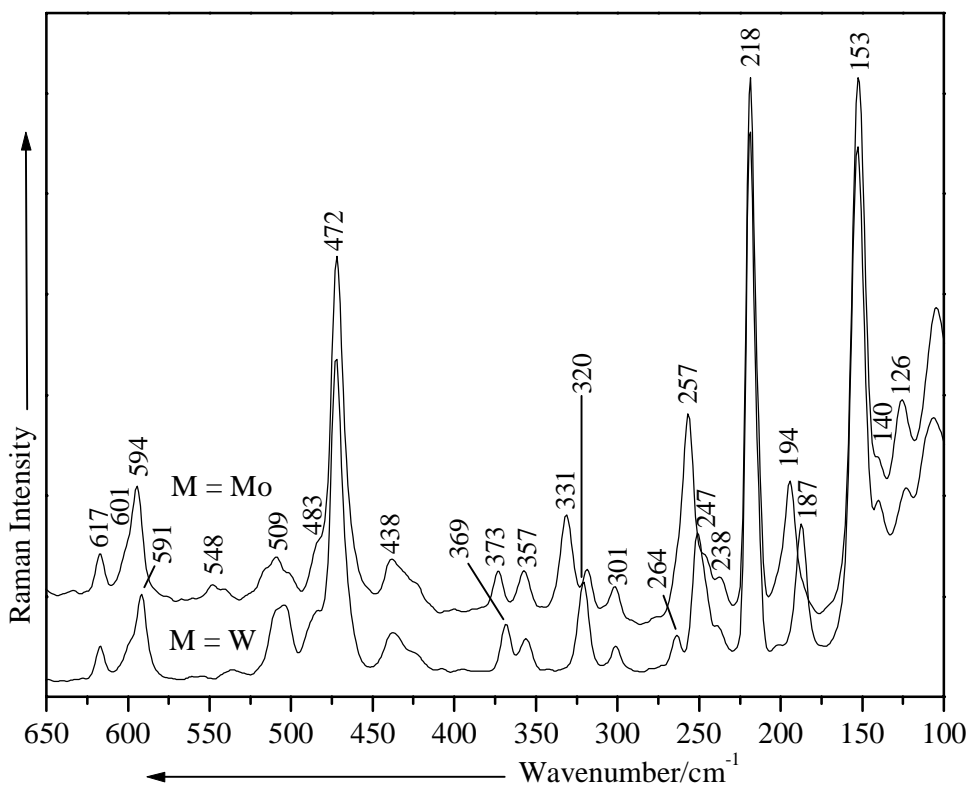


Figure 61. The low-wavenumber region of the FT-Raman spectrum of $\text{Cp}(\text{CO})_2\text{W-PPh}_2\text{-S}$ and $\text{Cp}(\text{CO})_2\text{Mo-PPh}_2\text{-S}$.

The spectroscopic studies which have been undertaken on molecules containing a phosphorus-selenium linkage are very limited. Austad *et al.* ^[120] relate their work to further studies, where some authors characterized the $\nu(\text{P}=\text{Se})$ stretching modes. More exactly, Chittenden and Thomas ^[141] reported the 473-535 and 517-577 cm^{-1} spectral ranges for the $\text{P}=\text{Se}$ valence vibration. Since the $\nu(\text{P}=\text{Se})$ stretching mode was theoretically determined at 538 cm^{-1} for **36**, it can be ascribed to one of the two bands observed at 532 and 544 cm^{-1} in its FT-Raman spectrum. The corresponding wavenumbers for the molybdenum complex **37** were observed at 532 and 552 cm^{-1} . It should be mentioned, that these bands which are not present in the FT-Raman spectrum of **32** and **33**, are characteristic for the selenium complexes **36-37**.

Although both peaks have a relative strong intensity, the strongest one is observed at 532 cm^{-1} . This band appears at the same wavenumbers in the tungsten and molybdenum complexes, which shows the insensitivity of this mode to the presence of the metal. The red shift of the band at 544 cm^{-1} in the molybdenum complex may be due to the metal mass effect. The PSe stretching mode is expected as a strong Raman signal, since the relative intensity of the PX stretch increases dramatically in going from the oxide to the sulfide and selenide, which is consistent with the reduced polarity and greater polarizability of the PS and PSe bonds ^[121]. Therefore, the $\nu(\text{PSe})$ has been tentatively assigned to the band at 532 cm^{-1} , being in good agreement with our DFT calculations and the experimental results reported by Thomas and Chittenden ^[141]. As for the sulfur compounds, the comparison of our selenides complexes with $\text{Ph}_3\text{P}=\text{Se}$ point out a shift to lower wavenumbers of the $\nu(\text{PSe})$ stretching mode ^[120], which confirms the partial PSe double bond postulated in the complexes $\text{Cp}(\text{CO})_2\text{Mo}-\overline{\text{PPh}_2}\text{-Se}$ and $\text{Cp}(\text{CO})_2\text{W}-\overline{\text{PPh}_2}\text{-Se}$.

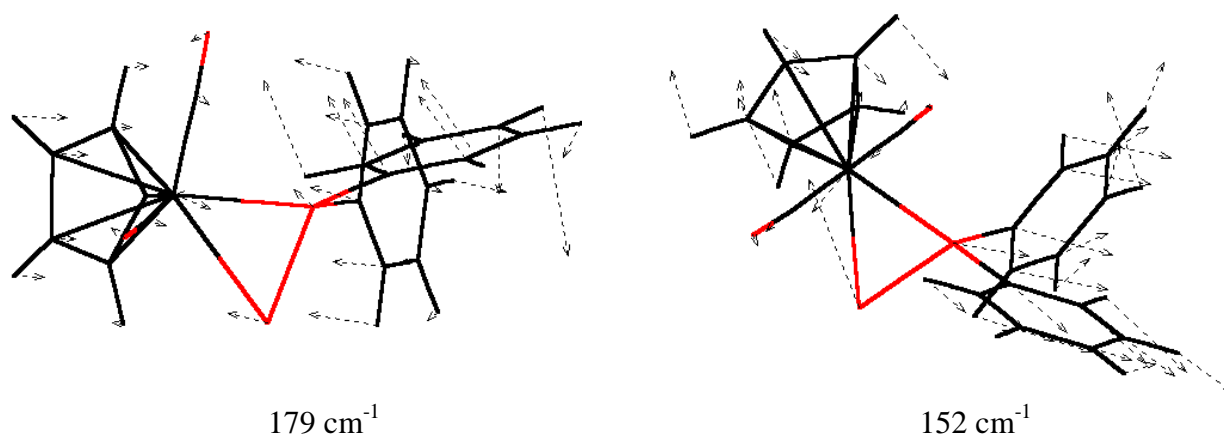


Figure 62. Calculated $\nu(\text{W-Se})$ and $\nu(\text{W-P})$ stretching modes using DFT9.

According to the DFT calculations carried out on the complexes $\text{Cp}(\text{CO})_2\text{W-PPh}_2\text{-S}$ and $\text{Cp}(\text{CO})_2\text{W-PPh}_2\text{-Se}$, the $\nu(\text{W-CO})$ and $\delta(\text{W-CO})$ vibrations, should occur in the same wavenumber region and should be therefore coupled. Thus, the bands observed at 513, 504 and 478 cm^{-1} in the FT-Raman spectrum of $\text{Cp}(\text{CO})_2\text{Mo-PPh}_2\text{-S}$ (Figure 59) and at 512, 499, 477 and 466 cm^{-1} in the FT-Raman spectrum of $\text{Cp}(\text{CO})_2\text{W-PPh}_2\text{-Se}$ (Figure 63) are good candidates for these modes.

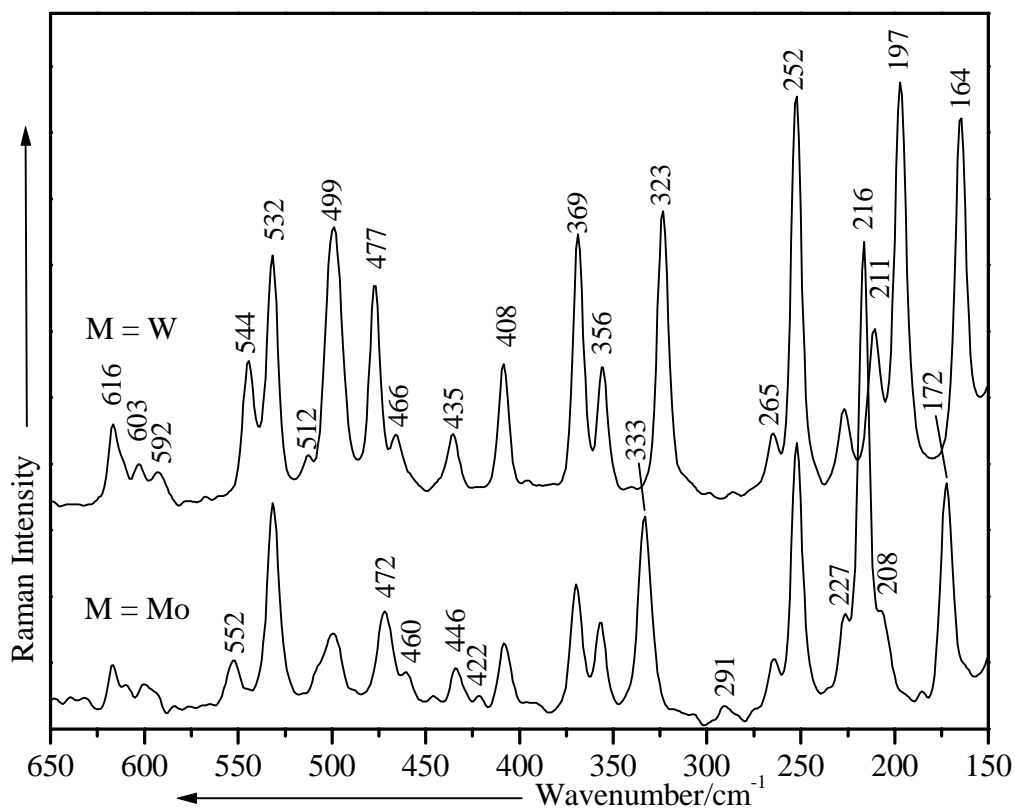


Figure 63. The low-wavenumber region of the FT-Raman spectrum of $\text{Cp}(\text{CO})_2\text{W-PPh}_2\text{-Se}$ and $\text{Cp}(\text{CO})_2\text{Mo-PPh}_2\text{-Se}$.

Whereas the $\nu(\text{WS})$ stretching mode was assigned at 261 cm^{-1} in the FT-Raman spectrum of **26**, it shifts to lower wavenumbers, namely at 247 cm^{-1} (calc. 236 cm^{-1}) in the FT-Raman spectrum of the complex **32** (Figure 60). This is consistent with the shortest W-S bond lengths measured in the thioaldehyde complex **26**. Furthermore, in the FT-Raman spectrum of the molybdenum complex **33** this mode was observed at higher wavenumbers (257 cm^{-1}), probably due to the mass effect occurring by replacing tungsten with molybdenum. This band shifts to 261 cm^{-1} in CH_2Cl_2 solution and is strongly polarized (Figure 60).

The $\nu(\text{M-Cp})$ stretching modes can be attributed to the bands at 320 and 301 cm^{-1} (calc. 335 and 312 cm^{-1}) and 331 and 310 cm^{-1} in the FT-Raman spectrum of $\text{Cp}(\text{CO})_2\text{W-PPH}_2\text{-S}$ and $\text{Cp}(\text{CO})_2\text{Mo-PPH}_2\text{-S}$, respectively.

Finally, the $\nu(\text{MP})$ stretching modes were quoted by Adams in the range 180-460 cm^{-1} for various phosphine complexes ^[142], and are assigned at 171 and 164 cm^{-1} in the complexes $\text{Mo}(\text{CO})_5\text{PPh}_3$ and $\text{W}(\text{CO})_5\text{PPh}_3$ ^[143], respectively. A closer examination of the FT-Raman spectrum of **32** and **33** (Figure 61) indicates the presence of a band of medium-to-strong intensity at 187 (calc. 173 cm^{-1}) and 194 cm^{-1} , respectively. The animation of the calculated modes at 152 and 179 cm^{-1} revealed a coupling between the $\nu(\text{M-Se})$ and the $\nu(\text{M-P})$ stretching modes (Figure 62). So that, these modes were ascribed to the peaks at 164 and 197 cm^{-1} and at 172 and 216 cm^{-1} in the FT-Raman spectrum of **36** and **37**, respectively.

Chapter 5

Photodissociation of carbonyl iron silyl complexes $Cp(CO)_2FeSiH_2CH_3$ and $Cp(CO)_2FeCH_2SiH_3$: A theoretical study

5.1 Introduction

Silyl iron complexes of the type $Cp(CO)_2Fe-SiH_2R$ (Cp =cyclopentadienyl); ($R=H$ (**40**), Me (**41**)) offer a large synthetic potential in inorganic and organometallic chemistry^[144]. Base-free transition-metal silylene complexes represent unusual organometallic species insofar as they possess a Lewis acidic center directly bound to the transition metal^[145-147]. Several examples of base free silylene complexes of iron^[146], ruthenium^[148], tungsten^[149] and osmium^[150] have been synthesized.

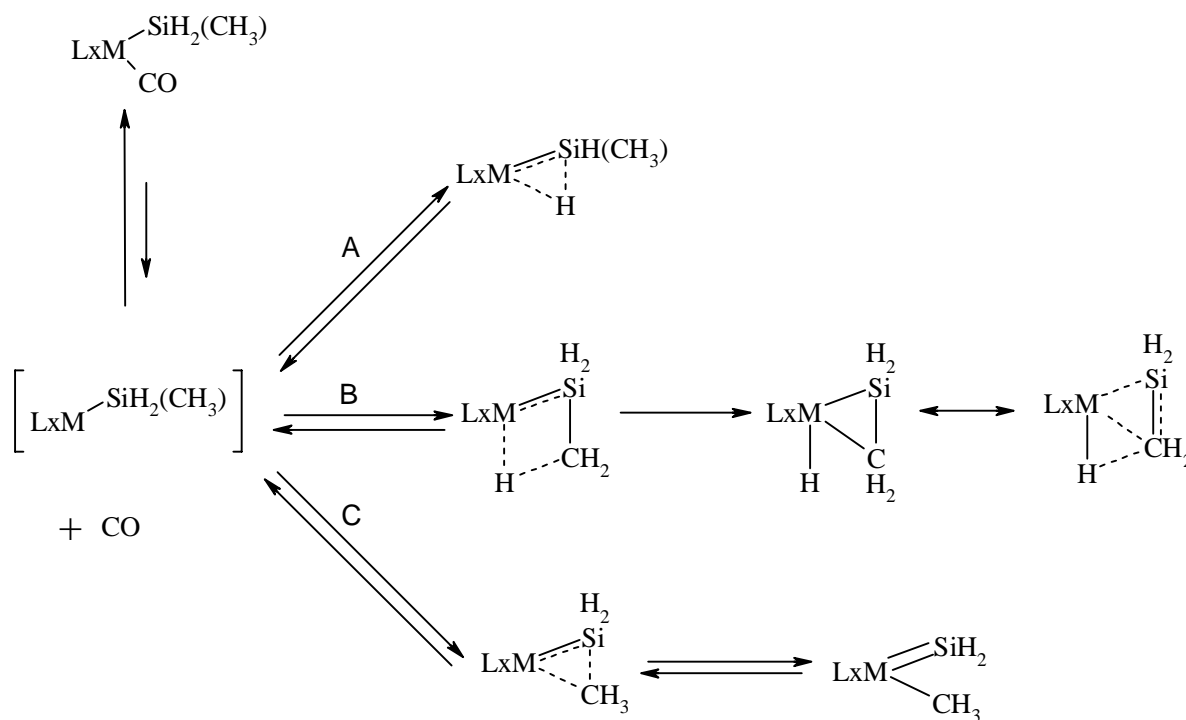
For complexes with $Fe=SiR_2$ units, heteroatom substitution on the silicon guarantees the isolation of these complexes. With the matrix isolation technique it should be possible to identify silylene complexes with the silicon bearing organic groups, hydrogen or halogen, respectively^[151-152]. In previous works^[153-155], some of us reported on FT-IR and Raman

studies by means of the matrix isolation technique in order to obtain information on the photodecomposition of **40** and **41**. The Raman spectrum of **40**, whose assignment was supported by DFT calculations, clearly shows that UV irradiation leads to a CO loss followed by an intramolecular rearrangement to generate primarily a 16-electrons and secondarily a stabilized 18-electrons species^[153]. Besides the α -H-transfer in analogy to **40** (pathway A) in the methyl substituted silyl complex **41**, two further mechanisms for the photochemical conversion are plausible as depicted in Scheme 1. The reaction pathway B involves a β -H abstraction, whereas an oxidative addition of the Si-C bond to the metal is characteristic for pathway C. From the various possible photoproducts of **41a**, Fickert et al.^[154-155] have proposed the α -H rearrangement as the most probable one (pathway A, Scheme 1) by comparing the Raman spectra of irradiated complexes **40** and **41a**. It has been shown that under normal condition, UV irradiation of **41a** leads after elimination of silylene (via pathway A, see Scheme 1) or silaethene (via pathway B, see Scheme 1), and CO addition, to the final photoproduct $\text{Cp}(\text{CO})_2\text{FeH}$ (**42**), which is thermolabile and transforms to $[\text{Cp}(\text{CO})_2\text{Fe}]_2$ ^[156]. Earlier, Gerhartz et al.^[157] have shown that the photoexcitation of the complex $\text{Cp}(\text{CO})_2\text{Fe}(\text{C}_2\text{H}_5)$ yields $\text{Cp}(\text{CO})_2\text{FeH}$ (**42**) even at 10 K in an Ar matrix and that **42** shows two characteristic $\nu(\text{CO})$ vibrational modes at 2024 and 1967 cm^{-1} .

One may notice, that $\text{Cp}(\text{CO})_2\text{FeH}$ (**42**) could a priori be generated via pathway A from **43a** (Figure 64) or via pathway B from **43b-c** (Scheme 1), where two bonds have to be simultaneously broken with a CO coordination.

The characterization of the isolated photoproduct(s) by spectroscopical methods is still a subject of discussion. Therefore, DFT calculations have been performed in order to explore the theoretical reaction pathways of $\text{Cp}(\text{CO})_2\text{Fe-SiH}_2\text{Me}$ in the electronic ground state and to bring additional information to the experimental results. Since the irradiation of $\text{Cp}(\text{CO})_2\text{Fe-CH}_2\text{SiH}_3$ (**43b**) should lead to **43d**, an isomeric form of **43c**, its molecular properties and photolysis products have also been determined theoretically. In addition, energy and vibrational modes were calculated. Particularly, transition states and intermediate species along the reaction pathways were determined and characterized to further elucidate the decay dynamics of **41a-b**.

It has been shown, that new generation of gradient-corrected DFT methods are efficient and accurate methods in studies of transition-metal reactions, especially for treating much larger systems and complexes containing first row transition metals^[158].



Thus, the geometries were fully optimized at the BPW91/6-311G* level and then used to compute the vibrational harmonic wavenumbers and zero-point corrections. The transition states TS were determined with the STQN method (QST2) in Gaussian. The Synchronous Transit-Guided Quasi-Newton (STQN) method, developed by Schlegel *et al.* ^[159], uses a linear synchronous transit or quadratic synchronous transit approach to get closer to the quadratic region around the transition state and then uses a quasi-Newton or eigenvector-following algorithm to complete the optimization.

5.2 Results and discussion

Figure 64 displays the different rearranged 18 electron complexes **43a-e**, mentioned in Scheme 1. The expected 16 electron transition-states **44a-44c** (TS) were calculated with the STQN method of the Gaussian program ^[54]. One imaginary vibrational mode was determined for **44a-c** at -411 , -70 and -154 cm^{-1} , respectively.

It is well-known that a minimum with all positive eigenvalues in Hessian matrix corresponds to an equilibrium structure, while a saddle point with one negative eigenvalue to a transition-state structure usually connecting two stationary structures. The normal mode corresponding to the imaginary wavenumber of a saddle point must be determined, so that the nature of the TS structure can be analysed. The eigenvectors of the imaginary wavenumber of the TS

structure indicate which geometrical parameters are involved in the reaction coordinate (RC). In this respect, the corresponding vibrational mode was animated and studied with the help of the MOLDEN chemical package.

The calculated energy of **43c** with the BPW91/6-311G* method is predicted to be 37.2 kJ/mol lower than **43e**, 22.2 kJ/mol lower than **43b** and 28.9 kJ/mol higher than **43a**. Using the same method, the **44a** and **44b** transition structures were found to be 45.6 and 69.4 kJ/mol energetically higher than **43a**. Additionally, the Cp(CO)(SiH₂Me)Fe-CO bond dissociation energy of **41a** was theoretically determined on the BPW91/6-311G* level. As expected, the $D_0 = 186.2$ kJ/mol calculated value was very similar to that of the corresponding M-CO cleavages in Fe(CO)₅ [160]. Comparing the calculated structures of **43a** and **43c**, we notice interesting discrepancies in the metal-silicon bonding. While the Fe-Si bond length in **43a** is about 20 pm shorter in comparison to **41a**, the calculations indicate a shortage of 10 pm for **43c**. At the same time, the calculated Fe-H bond length in **43a** and **43c** is 161.0 and 176.1 pm, respectively. The much shorter iron-hydrogen interatomic distance in Cp(CO)₂FeH (**42**) of 149.9 pm could represent a good bond order reference in this case. As shown in Figure 64, the complexes **43a**, **43c** and **43d** are stabilized with agostic interactions [161]. The modification of the Z-Matrix for **43c** and reoptimization of the geometry have led to the compound **43b**, that represents a local minimum of the potential energy surface with a higher energy difference of 15.1 kJ/mol with respect to **43c**. For **43a**, no such compound was found and the optimization conducted systematically back to the more stable compound **43a**. Compound **43b** is the result of the H-β-shift addition on iron. The calculated Fe-H bond length of 148.5 pm corresponds well to the iron hydride bond length calculated for **42**. Compared to **43c**, the Fe-Si and the Fe-C bonds are in this case about 9 pm longer and 14 pm shorter, respectively.

Compound **43c** is stabilized by the β-H-agostic C-H-Fe-interaction, depicted in Figure 64. In this context it should be mentioned that the Si=C bond distance has been determined in H₂Si=CH₂ [162] and (CH₃)₂Si=CH₂ [163] to be 170.4 and 169.2 pm, respectively. Moreover, silaethene coordinated to ruthenium [164] and tungsten [165] is found to have a value for the Si-C bond length of 179.0 and 180.0 pm, respectively. The Si-C interatomic distance in **43b** was calculated in this study to be 180.7 pm, which is in good agreement with these cited experimental results. The Si-C bond length in **43c** is calculated to be 191.0 pm, which indicates a considerable Si-C single-bond character, so that **43c** can be described as a pseudo metallasilacyclopropane compound similarly to the model proposed by Dewar [89], Chatt and Duncanson [90] for the ethylene complexes. Compound **43e** represents the photoproduct expected in the reaction pathway C. The Fe-Si bond length of 211.4 pm, which shows a d_π-p_π character, is only 1 pm shorter than in **43a**. The Fe-C_{Me} interatomic distance is calculated to be 206.8 pm. Further relevant parameters of the compounds **41a-44c**, calculated with the BPW91 functional and the 6-311G* basis set, are listed in Table 25.

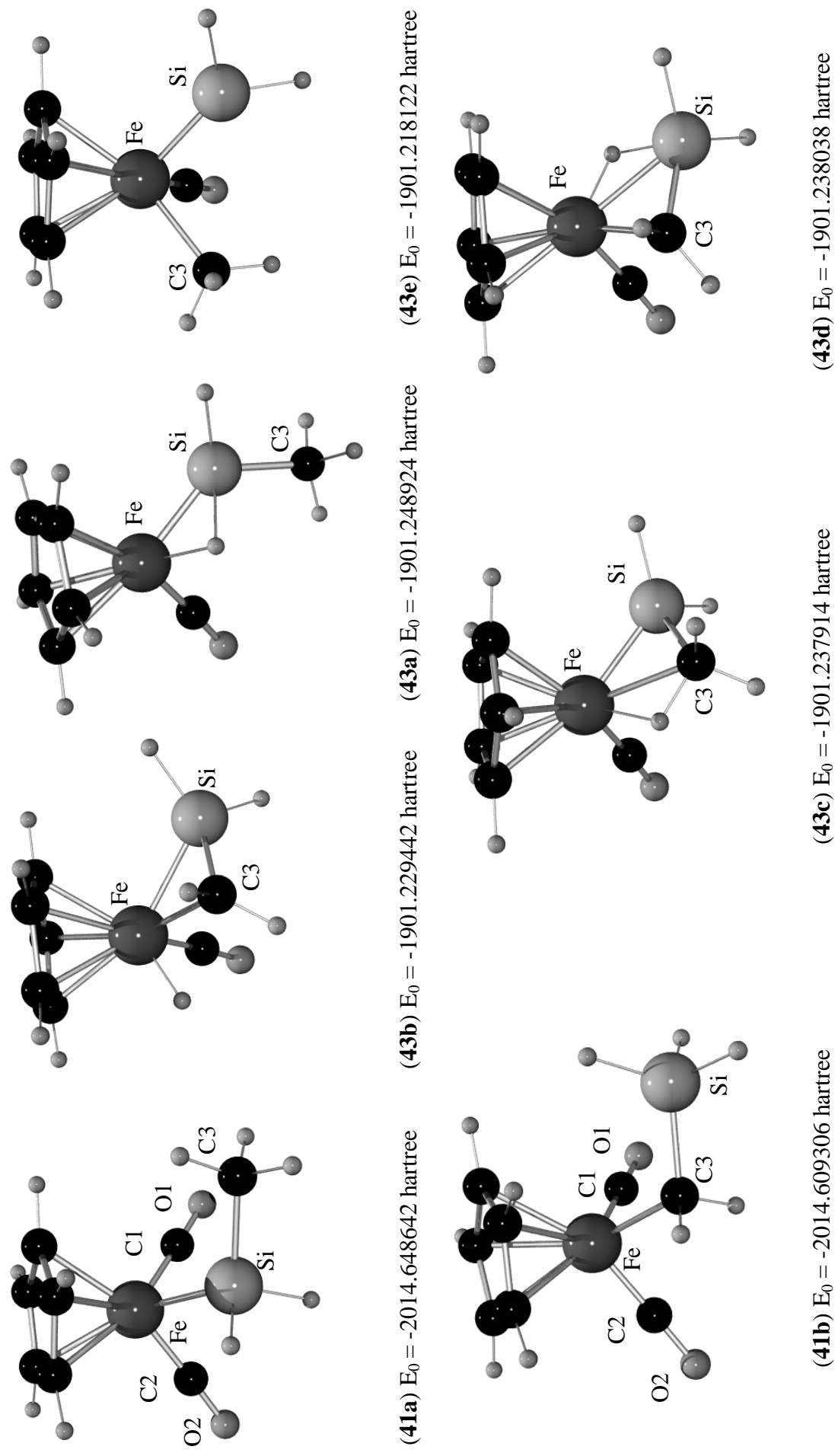
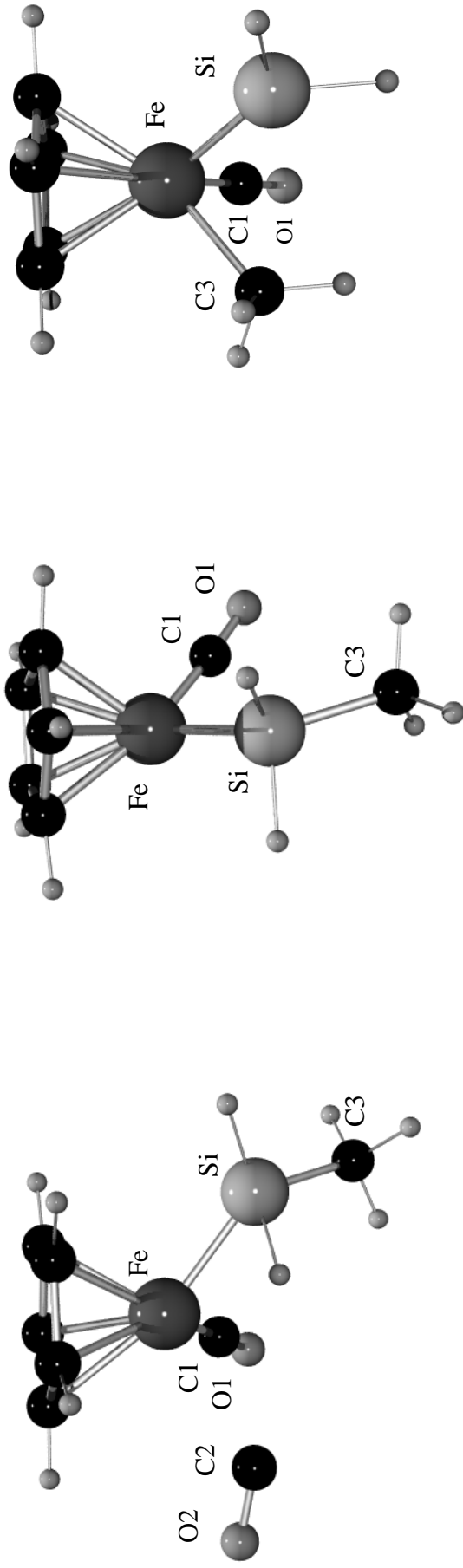


Figure 64. Calculated structures and energies (in hartree) for the rearranged 18 electron complexes mentioned in Scheme 1.



Free CO $E_0 = -113.328855$ hartree

*1 Hartree = 627.51 kcal/mol = 27.2116 eV

Figure 64. To be continued. Calculated structures and energies (in hartree) for the rearranged 18 electron complexes mentioned in Scheme 1.

The calculations have shown that compound **43a** is thermodynamically the most stable one, therefore it should be the favored compound in the matrix layer. But, by the photolysis carried out using wavelengths in the range between 333 and 364 nm, an energy of 359.5 to 330.2 kJ/mol was deposited on the parent molecule. According to the theoretical results, there is sufficient energy to overcome the transition states **44a-c**. Consequently, the previously discussed reaction pathways could be valid.

Fickert et al. ^[154-155] showed that the photochemical conversion was not complete and an increase of the irradiation time will produce no further changes. Therefore, they suggested an equilibrium between the silyl complex **41a** and the intermediate form **44a** during photochemical conversion, a phenomenon that has already been observed. For example, the ultraviolet photolysis of Fe(CO)₅ in an argon matrix leads to Fe(CO)₄ and CO. Subsequent exposure of the matrix to the light from the Nernst glower of the infrared spectrometer rapidly destroys all the Fe(CO)₄ and regenerates the parent Fe(CO)₅ ^[156]. If the UV photolysis is continued for several hours, it is found that the reaction can be only partially reversed. Prolonged photolysis allows the CO to diffuse away through the matrix layer until a definite concentration is reached, preventing subsequent recombination. The UV light used for the photolysis contains far more energy than is required to break the M-CO bond. Since no visible fluorescence is observed in these reactions, the excess of energy is presumably distributed as vibrational energy in the photoproducts. One of the least understood features of matrix isolation is the detailed nature of photochemical processes therein, including, for example, the cage effect. Some aspects have been discussed elsewhere ^[166-167]. The use of photolysis and spectroscopy with plane polarized light has demonstrated that some species can be rotated during the photochemical act.

Thus, it seems clear now that all proposed photoproducts **43a-e** could be present in the matrix layer studied by Fickert et al. ^[154-155]. The significant structural differences in the [FeSiH₂Me] unit for the mentioned photoproducts should lead to the appearance of new signals in the Raman and IR spectra corresponding to the (FeH) or the (FeC) vibrational modes, or to a shift of (FeSi) and the (SiC) modes. In this way, one could distinguish between the forms **43a-e**. For the compounds **43a**, **43c** and **43e**, the calculations revealed a higher [FeSi] bond order. This leads to a similar shift of the $\nu(\text{FeSi})$ mode to higher wavenumbers, as for the iron-carbon single and double bond (HFe-CH_3 : 522 cm⁻¹; Fe=CH_2 : 624 cm⁻¹) ^[168]. Table 26 presents the most important theoretically predicted characteristic normal modes of **43a-e** and **44a-c**, which might help to identify the isolated compound(s) in the matrix experiments performed by Fickert et al. A close examination of the high and low spectral wavenumber region in Table 26 indicates, as expected, different calculated wavenumbers for the before mentioned vibrational modes in **43a-e**.

Table 26. Calculated Vibrational wavenumbers (in cm^{-1}) at BPW91/6-311G* for the iron complexes

(41a)	(41b)	(TS-44a)	(43a)	(43b)	(43c)	(43d)	(43e)	(42)
2089 [SiH ₂]	2154 [SiH ₂]	2111 [SiH]	2065 [SiH]	2173 [SiH ₂]	2319 [CH ₂ -H]	2178 [SiH]	2106 [SiH]	
2118 [SiH ₂]	2129 [SiH ₂]			2143 [SiH ₂]		2163 [SiH]	2073 [SiH]	
	2117 [SiH ₂]							
		2014 [CO]free		2059 [FeH]	2145 [SiH]			2030 [CO] _s
2010 [CO] _s	2018 [CO] _s	1954 [CO]	1960 [CO]	1976 [CO] + [FeH]	1961 [CO]	1974 [CO]	1970 [CO]	1980 [CO] _{as}
1970 [CO] _{as}	1976 [CO] _{as}	1913 [SiH]	1692 [FeH]		1564 [FeH]	1736 [FeH]		1978 [FeH]
1269 [δCH ₃] _s	1400 [δCH ₂]	1272 [δCH ₃] _s	1264 [δCH ₃] _s	1397 [δCH ₂] _s	1363 [δCH ₃] _s	1403 [δCH ₂] _s	1231 [δCH ₃] _s	
1115	1117	1111	1111	1116	1110	1113	1115	1114
[breathing] _{cp}	[breathing] _{cp}	[breathing] _{cp}	[breathing] _{cp}	[breathing] _{cp}	[breathing] _{cp}	[breathing] _{cp}	[breathing] _{cp}	[breathing] _{cp}
927 [δSiH ₂]	931 [δSiH ₃] _{as}	910 [δSiH] + [ρCH ₃]	952 [δSiH ₂]	930 [δSiH ₂]	952 [δSiH ₂]	932 [δSiH ₂]	978 [δSiH ₂]	
			925 [δSiH] + [ρCH ₃]					
879 [ρCH ₃]	926 [δSiH ₃] _{as}	829 [δSiH ₂]	852 [δFeH _s]	840 [ρFeH _{CH₃]}	864 [ρCH ₃] + [ωSiH ₂]	885 [ρCH ₂]		773 [δCpFeH] + [δCH] _{cp} o.o.p.
						o.o.p.		
876 [ρCH ₃]	913 [δSiH ₃] _s	821 [ρCH ₃]		809 [ρCH ₃]		870 [ωCH] _{CH₂}	807 [ρCH ₃]	
						865 [ωCH] _{CH₂} + [δCH] _{cp} o.o.p.	803 [ρCH ₃] + [δCH] _{cp} o.o.p.	
						822 [δCCC] _{cp}	770 [ωCH ₃]	648 [FeCO] _s
713 [ωSiH ₂] + [ωCH ₃]	738 [ρCH ₂]	702 [SiCH ₃]	718 [SiCH ₃]	798 [SiCH ₃]	659 [SiC]		623 [FeCO]	
				765 [δFeH]			+ [ωSiH ₂]	
663 [SiCH ₃] + [δFeCO]				659 [ωFeH] + [δFeCO]				
656 [SiCH ₃]	723 [SiC]	671 [SiCH ₃]	671 [SiCH ₃]	616 [ωSiH ₂]	626 [ωSiH ₂]	797 [SiCH ₂]	605 [FeCO] + [ωSiH ₂]	598 [FeCO]
608 [δFeCO]	649 [FeCH ₂] + [ωSiH ₂]	587 [FeCO]	589 [FeCO]	598 [FeCO] + [ωSiH ₂]	602 [FeCO] + [ωSiH ₂ CH ₃]	776 [ωCH ₂]	532 [ρSiH ₂] + [δFeCO]	554 [δFeCO]
600 [δFeCO]	645 [δFeCO]	584 [FeCO] + [δCC] _{cp}	577 [δFeCO]	580 [δFeCO]	594 [δFeCO]	755 [δFeH]	523 [ρSiH ₂] + [δFeCO]	531 [δFeCO]

Table 26. To be continued

532 [FeCO] _s	597 [δFeCO]	575 [δFeCO]	571 [δFeCO]	574 [δFeCO] + [δCC] _{cp}	577 [δFeCO] + [δCC] _{cp}	672 [ωSiH ₂]	495 [FeCH ₃]	498 [δFeCO]
515 [FeCO] _{as}	522 [FeCO] _s	551 [ωSiH ₂] + [δCC] _{cp} o. p.		544 [ρSiH ₂]	543 [ρSiH ₂] 536 [τCH ₃]	613 [ρSiH ₂] + [FeCO]	458 [FeSi]	400 [FeCp] _{as}
	516 [FeCO] _{as}	416 [FeSi]	521 [ρSiH ₂] 434 [FeSi]	485 [τSiH ₂] 444 [FeSiH ₂ CH ₂]	507 [τSiH ₂] 435 [FeSiH ₂ CH ₃]	587 [δFeCO] 562 [δFeCO] + [ρSiH ₂]	391 [FeCp] _{as} 371 [FeCp] _{as}	368 [FeCp] _{as} 362 [FeCp] _s
392 [FeCp] _{as}		413 [FeCp] _{as}	392 [FeCp] _{as}		407 [FeCp] _{as}	496 [τSiH ₂] + [τCH ₂]	338 [FeCp] _s	357 [FeCp] _s
383 [FeCp] _{as}	382 [FeCp] _{as}	376 [FeCp] _{as}	377 [FeCp] _{as}	395 [FeCp]	375 [FeCp] _{as}	448 [FeCH ₂]		
366 [FeCp] _s	350 [FeCp] _s	323 [FeCpSi]	343 [FeCp] _s	375 [FeCp]	346 [FeCH ₂ Cp] _{as}	398 [FeCpCH ₂]		
310 [FeSi]	341 [FeCp] _s			370 [FeCpCH ₂] _s	311 [FeCH ₂ SiH ₂] _s	376 [FeCp] _s		
				314 [FeCpSiH ₂] _s		363 [FeCp] _{as} 288 [FeSi]		

The $\nu(\text{FeSi})$ and $\nu_s(\text{FeCp})$ modes of **41a**, which have been calculated at 310 and 366 cm^{-1} , were earlier assigned to the strong bands at 318 and 375 cm^{-1} , respectively [154-155]. Whereas these two bands decrease in intensity during the UV irradiation of the sample, a few new bands can be observed in the spectral region between 280-450 and 570-840 cm^{-1} . Consequently the new band at 348 cm^{-1} could be attributed, according to our calculation, to the $\nu_s(\text{FeCp})$ mode of **41a** (calc. 343 cm^{-1}) or to the $\nu_{\text{as}}(\text{CpFeCH}_2)$ of **43c** (calc. 346 cm^{-1}). It is also possible that the calculated mode at 314 cm^{-1} for **43b** or 311 cm^{-1} for **43c** (see Table 26), which appears in the same region as the $\nu(\text{FeSi})$ mode in **41a**, can be overlapped from the mentioned mode and can not be clearly observed in the Raman spectra. According to our calculations, the strong doublet from 429 and 439 cm^{-1} can be assigned to the $\nu(\text{FeCp})$ (calc. 407 cm^{-1}) and $\nu(\text{Fe}-\begin{array}{c} \text{CH}_3 \\ | \\ \text{SiH}_2 \end{array})$ (calc. 435 cm^{-1}) modes for **43c** or to the $\nu(\text{FeCp})$ (calc. 392 cm^{-1}) and $\nu(\text{FeSi})$ (calc. 434 cm^{-1}) vibrational modes for **43a**. Using the $\lambda_0 = 514.5$ nm excitation line for photodissociation, these modes and a few new bands in the 500 and 650 cm^{-1} spectral region have been enhanced. This is in good agreement with the orange-red color of the photoproduct, which has been observed in the matrix layer [154-155].

The calculated HOMO-LUMO gaps of the discussed compounds **43a-e**, **44a** and **41a**, respectively, are listed in Table 27. The complex **41a** presents an absorption maximum at 363 nm. This band is comparable to the HOMO-LUMO transition of **41a**, which has been calculated at 357 nm (see Table 27).

Table 27. Energy differences in eV and nm between the HOMO and LUMO of the iron complexes

HOMO-LUMO gap	41a	41b	44a	43a	43b	43c	43d	43e
In eV	3.47	3.18	1.20	2.13	3.47	2.15	2.67	2.10
In nm	357	389	1032	581	357	575	465	591

Furthermore, the calculated HOMO-LUMO gaps for the photoproducts **43a** and **43c** are shifted to higher wavelength; this may corresponds to the orange-red colour of the matrix layer and the resonance or preresonance effects observed in the Raman spectrum excited with $\lambda_0 = 514.5$ nm. Surprisingly, the HOMO-LUMO gap of **43b** is much greater than that for **43c** and corresponds to an absorption in the UV spectral region.

A close analysis of the $\nu(\text{Si-C})$ wavenumber region could also help to distinguish between the compounds **43a-d**. In the Raman spectrum of **41a**, the polarised band at 680 cm^{-1} can be

assigned to the $\nu(\text{Si-C})$ mode according to the calculated value at 656 cm^{-1} . For the compounds **43b**, **43a**, **44a**, **43c** and **41a**, these values were determined at 798, 718, 702, 659 and 656 cm^{-1} , respectively. The assignment of the $\nu(\text{Si-C})$ vibrational mode is quite complicated due to its low intensity and the presence of other bands in the same region. Two new bands of weak intensity could be observed in the Raman spectrum at 702 and 621 cm^{-1} and attributed to this mode. According to the DFT calculations (see Table 26), the new strong bands at 597 cm^{-1} and 567 cm^{-1} could be ascribed to the $\nu(\text{Fe-CO})$ and $\delta(\text{FeCO})$ vibrational modes, respectively. On the basis of the DFT-calculations the new strong band at 839 cm^{-1} in the Raman spectra of **41a** can be tentatively assigned to the $\text{FeH}_{\text{Si, CH}_3}$ rocking modes of **43a** (852 cm^{-1}) or **43b** (840 cm^{-1}). The detailed analysis of the low-wavenumber region does not offer a determinant factor in distinguishing between the possible isolated photoproduct(s), so that a look on the high wavenumber region, where some changes are also expected, might be decisive. The Cp ring modes are relatively insensitive to the remaining complex fragment, and therefore, the Cp ring breathing can be used as internal standard. Indeed, the calculations revealed a deviation of less than 5 cm^{-1} from the experimental value in the title compounds.

For the compound **41a**, Fickert et al. ^[154-155], assigned the weak signal at 1249 cm^{-1} (calc. at 1269 cm^{-1}) to the $\delta(\text{CH}_3)$ vibrational mode, as it was expected to occur in the 1200 and 1350 cm^{-1} spectral region. The two new bands, which were not considered by the authors, in fact show up as medium and weak bands at 1302 and 1341 cm^{-1} ^[154-155] and seem to play an important role in our characterization. The $\delta_s(\text{CH}_3)$ modes for **43a-e** were calculated to be at 1264, 1397, 1363 1403 and at 1231 cm^{-1} , respectively.

The characteristic SiH_2 modes, as well as the symmetric and antisymmetric CO vibrations in **41a**, which were located at 2090 (br) (calc. 2118, 2090), 2001 (calc. 2010) and 1942 cm^{-1} (calc. 1970), respectively, present a decrease of the intensity during the UV irradiation. The appearance of a new signal at 2136 cm^{-1} in the IR spectrum demonstrates a CO loss, so that the $[\text{CpFe}(\text{CO})\text{SiH}_2\text{Me}]$ equilibrium structures **43a-e** were suggested. The broad band at 1942 cm^{-1} splits clearly into two bands after the UV irradiation of **41a**. The new band at 1953 cm^{-1} is increasing, whereas the two $\nu(\text{CO})$ bands of **41a** are decreasing. Thus, this band could be assigned to the $\nu(\text{CO})$ mode of the photoproducts **43a** and/or **43c**, where both calculated wavenumbers have been found at 1960 cm^{-1} . Furthermore, the new band at 2149 cm^{-1} in the FT-IR spectrum agrees very well with the calculated $\nu(\text{SiH})$ modes for **43c** (2145 and 2120 cm^{-1}). The theoretical $\nu(\text{SiH})$ mode for **43a**, which has been determined to be 2065 cm^{-1} could not be observed in the reported spectra. One may notice, that the characteristic Fe-H spectral region can certainly help to elucidate the problem in question. According to Tursi and Nixon ^[169], the medium bands at 1591 and 1600 cm^{-1} observed in the FT-IR spectrum indicate the water's presence in the matrix layer studied by Nagel et al. ^[153]. But the IR spectrum of **41a**

presents two broad bands at 1622 and 1712 cm^{-1} before and after the UV irradiation. The weak band for water, usually expected at around 1630 cm^{-1} , should not be attributed to these strong broad signals. On one hand, during the sample heating in order to bring it in the gas phase, some structural changes, which could explain these two new signals, can occur. On the other hand, the comparison between those values and the calculated wavenumbers shows a good agreement with the compounds **43a** (1692 cm^{-1}), **43c** (1564 cm^{-1}) and **43d** (1736 cm^{-1}). But one should take into account that the two broad bands could also overlap the $\nu(\text{FeH})$, $\nu(\text{FeHSi})$ or $\nu(\text{FeHCH}_2)$ modes. Thus, the assignment in this region is still under question.

5.2.2 Conclusion

The best agreement between the theoretical and experimental data was observed for the $\nu(\text{CC})$ modes of the cyclopentadienyl ligand, as well as for the $\nu(\text{FeSi})$ and $\nu(\text{FeCp})$ low wavenumber vibrational modes. In these cases the discrepancy was only -8 cm^{-1} between experimentally observed and calculated values for **41a**. One may notice that the $\nu(\text{CO})$ modes have been also predicted with high accuracy. The present study has shown that the characteristic vibrational modes of the metal ligand unit for the various photoproducts are significantly different in constitution, but very similar in wavenumbers. That complicates the differentiation between **43a**, **43b** and **43d** in the experimental results. Whereas, the new band observed at 839 cm^{-1} , which is attributed to the FeH rocking mode of **43a**, supports the reaction pathway A, the two new bands at 1302 and 1341 cm^{-1} favour the reaction pathway B, whose final product presents a change of the CH_3 unit during the photolysis. It seems to reveal the presence of compounds **43a** and **43c** or **43d**. The band which appears at 281 cm^{-1} has not been explained previously ^[154-155] but with the help of DFT-calculations, it could be tentatively assigned to the $\nu(\text{FeSi})$ vibrational mode calculated to be 288 cm^{-1} for **43d**. The compound **43d**, for which the theoretical calculations led to the same energy as for the isomeric form **43c**, should be also generated after the photoexcitation of the complex $\text{Cp}(\text{CO})_2\text{Fe}-\text{CH}_2\text{SiH}_3$ (**41b**). Further IR and Raman matrix investigations are recommended for a more certain and correct elucidation of the reaction pathways involved by the irradiation of the title complexes. In this way, matrix investigations of **41b** can prove the presence of **43d** and help to decide if it rearranges to compound(s) **43c** and/or **43a**.

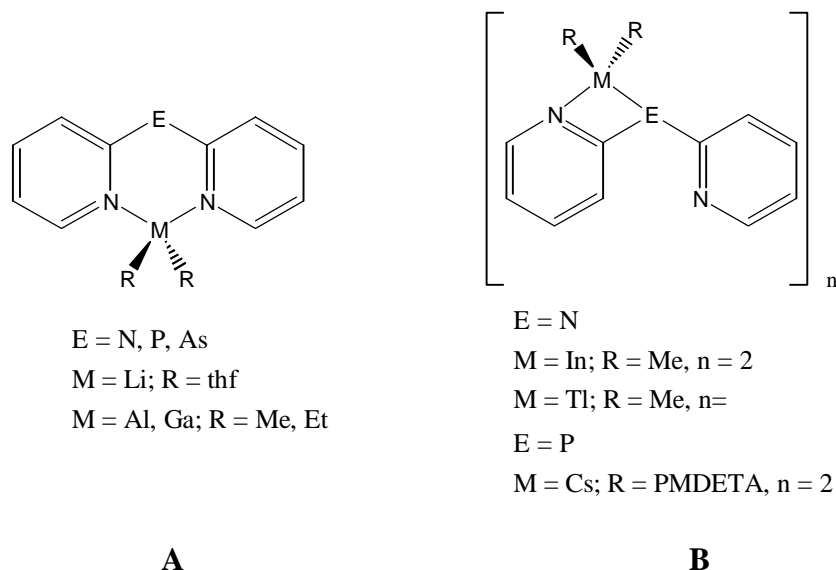
Chapter 6

A theoretical and vibrational analysis of the coordination behaviour of the $(2\text{-Py})_2\text{P}^-$ and $(2\text{-Py})_2\text{N}^-$ anions

6.1 Introduction

N-Heteroaryl ring systems are well-known as bridging functions between transition metal centers^[170]. Recently Stalke et al. described related complexes of di(2-pyridyl)amides, -phosphides and -arsenides $(2\text{-Py})_2\text{E}^-$ (E = N, P, As) with main group metal fragments, mainly group 13 metal organics^[171-173]. The resulting low molecular aggregates contain group 13 and 15 elements and are of interest as volatile precursors for III/V semiconducting films^[174].

The main feature of the ligands is the flexible chelating coordination behavior towards the various metal centers. They either coordinate exclusively by both pyridyl nitrogen atoms leaving the bridging E atom two coordinated without any metal contact (**A** in Scheme 2)^[171-173, 175] or in a mixed bridging-N/ring-N fashion in some di(2-pyridyl)amides and di(2-pyridyl)phosphides (**B** in Scheme 2)^[172, 176-177].

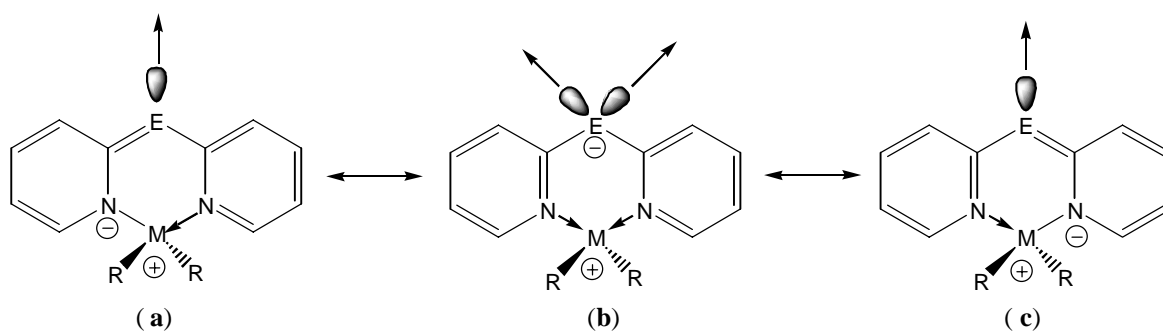


E = N, P, As
 M = Li; R = thf
 M = Al, Ga; R = Me, Et

E = N
 M = In; R = Me, n = 2
 M = Tl; R = Me, n =
 E = P
 M = Cs; R = PMDETA, n = 2

Scheme 2

The two coordinated bridging atom (N, P, As) in complexes described in **A** should in principle be able to coordinate either one or even two further Lewis acidic metals. According to the mesomeric structures it can act as a $2e^-$ or even a $4e^-$ donor (Scheme 3).



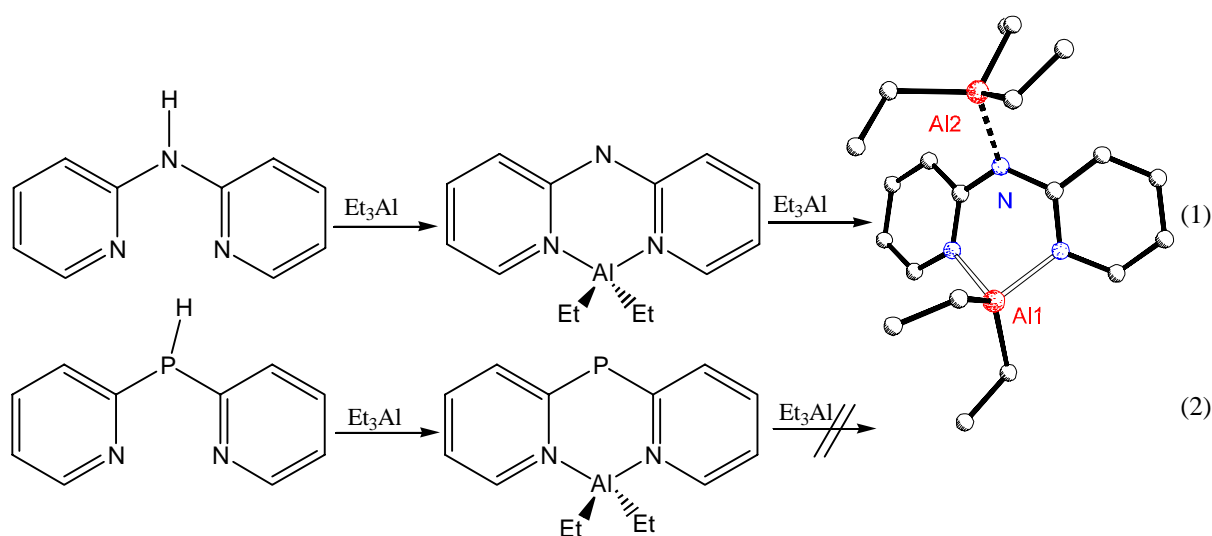
Scheme 3

The essential differences of these compounds concerning a further coordination of the bridging nitrogen or phosphorus atom have been described from a synthetic, analytical (Raman spectroscopy) and theoretical (DFT calculations) point of view. In the previous parts, it has been shown that Raman spectroscopy is an important additional tool in the determination of structural parameters of new compounds.

The present class of compounds have not yet been studied conclusively by this method. Therefore the vibrational behavior of the known compounds (2-Py)₂NH (**45**)^[178], (2-Py)₂PH (**46**)^[171], Me₂Al(2-Py)₂N (**47**)^[172] and Me₂Al(2-Py)₂P (**48**)^[171] have been investigated and the vibrational modes were assigned using density functional theory (DFT) calculations. Additionally, the theoretical donor-acceptor bond energy for the model complexes Me₂Al(2-Py)₂N→AlMe₃ (**52**) and Me₂Al(2-Py)₂P→AlMe₃ (**53**) has been evaluated and compared with the well-known systems Me₃N→AlMe₃ and Me₃P→AlMe₃ reported in the literature^[179] in order to explain the reactivity of Et₂Al(2-Py)₂N (**49**) and Et₂Al(2-Py)₂P (**50**) toward a further equivalent of Et₃Al.

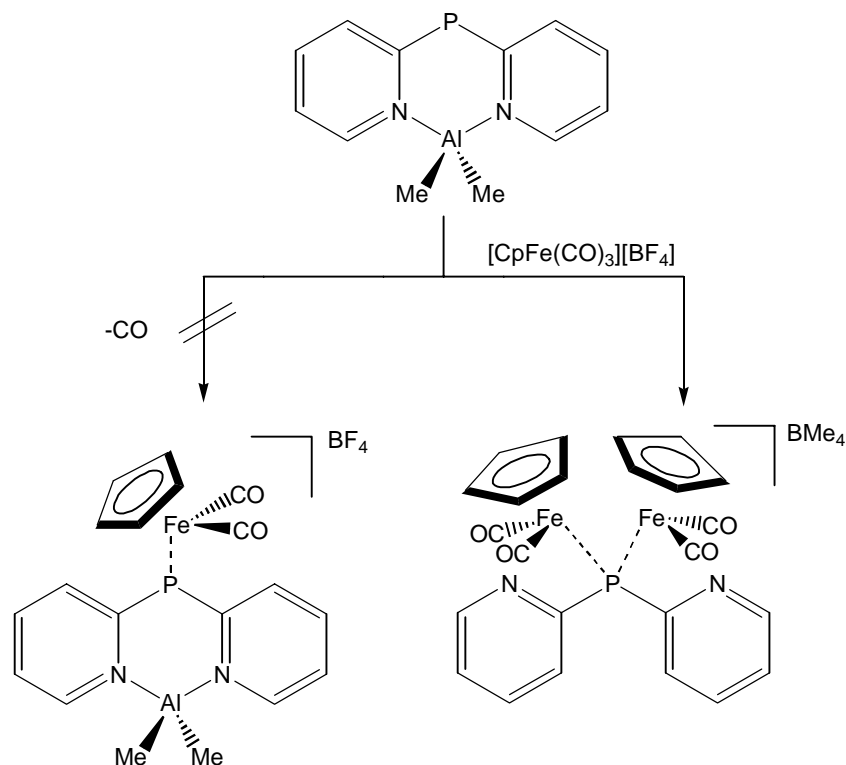
6.2 Reactivity

Di(2-pyridyl)amine **45**^[178] and di(2-pyridyl)phosphane **46**^[171] are reacted with an equimolar amount of triethyl aluminum in Et₂O at -78°C leading to ethane and diethyl aluminum amide **49** and -phosphide **50**, respectively. The diethyl aluminum fragment is coordinated via both pyridyl N-atoms and the bridging atom N or P is left two coordinated. Adding a second equivalent of triethyl aluminum to Et₂Al(2-Py)₂N (**49**) the adduct Et₂Al(2-Py)₂NAlEt₃ (**51**) is formed where the bridging N-atom coordinates to the Lewis acid Et₃Al (Eq. (1) Scheme 4). Similar coordination features for the (2-Py)₂N⁻ ligand have been reported in the literature^[180]. However, Et₂Al(2-Py)₂P (**50**) does not form an adduct with a second equivalent of Et₃Al. Monitoring the reaction by ³¹P-NMR there is no other signal raising than this from **50** at 23.7 ppm. In contrast to Et₂Al(2-Py)₂N (**49**), the P atom in Et₂Al(2-Py)₂P (**50**) is not Lewis basic enough to coordinate to the hard Lewis acid Et₃Al (Eq. (2)).



Scheme 4

In an attempt to prepare heterobimetallic compounds the aluminium derivative $\text{Me}_2\text{Al}(2\text{-Py})_2\text{P}$ was reacted with $[\text{Cp}(\text{CO})_3\text{Fe}][\text{BF}_4]$ where in general a carbonyl group can be easily replaced by a phosphane ^[181].



Scheme 5

The vacant phosphorus site was expected to coordinate with Fe(II) while retaining the Al-N bonds. However, the Al-N bonds in the complex were cleaved presumably by the formation of the thermodynamically favourable AlF_3 accompanied by the alkylation of the tetrafluoroborate anion. This leads to the formation of $[\{\text{Cp}(\text{CO})_2\text{Fe}\}_2\{\mu\text{-P}(\text{Py})_2\}][\text{BMe}_4]$ which confirms the anticipated ability of the phosphorus centre in the $(2\text{-Py})_2\text{P}^-$ anion to coordinate soft metals (Scheme 5) ^[177].

6.3 Experimental and theoretical structures

The structural features of the title complexes are here shortly described. More details are available in the PhD-Thesis of Mathias Pfeiffer ^[182].

In the monomeric complex $\text{Et}_2\text{Al}(2\text{-Py})_2\text{P}$ (**50**) the aluminum and phosphorus atoms are μ_2 -bridged by two pyridyl ring systems. The phosphorus atom is two coordinated and the two crystallographically independent P-C bonds are identical within estimated standard deviations

(P1-C1 177.7(3); P1-C6 177.8(3) pm), indicating a delocalization of the negative charge throughout the anion. A P-C single bond is about 185 pm long while the values for P=C double bonds in phosphalkenes range from 161 to 171 pm^[183].

All shows a distorted tetrahedral coordination sphere. Both Al-N bonds are of the same length (192.4(2) and 192.3(2) pm) and correspond well to the related value in Me₂Al(2-Py)₂N (**47**)^[172] (av. 192.4(2) pm). While the Al-N bond in the three-coordinated aluminum triamide Al[N(SiMe₃)₂]₃^[184] is 14 pm shorter than in **50**, the Al-N donor bond in P(2-Py)₃AlMe₃^[171] is about 13 pm longer. Consequently, the Al-N bond in **50** ranges between a single bond and a donor bond. As in **48** and **50** the P atom in Me₂Al(μ-NMe_s*)₂P^[185] is only two coordinated. The Al-N distance in the AlN₂P ring system is 6 pm longer than in **48** and **50**. The Al-C bond lengths (av 196.5 pm) are in accordance with those in related systems^[186].

In complex **50** both pyridyl ring planes intersect at an angle of 163°. The related angle in Me₂Al(2-Py)P (**48**) is 155° in contrast to (thf)₂Li(2-Py)P^[171], where the deviation from planarity is only marginal (173°). Therefore the ethyl groups are nonequivalent in the solid state. Nevertheless, ¹H and ¹³C spectra from solution show only one signal for the C atoms of the ethyl groups even at low temperature. The “bite“ of the ligand (N···N distance) in such compounds ranges from 292.2 pm in **48**, 294.8 pm in **50** up to 306.4 pm in the nearly planar (thf)₂Li(2-Py)P, respectively. Hence the ligand shows coordination flexibility towards different metal fragments, while not giving up the full conjugation. In Et₂Al(2-Py)₂N→AlEt₃ (**51**) the coordination mode of the Et₂Al⁺-fragment is similar to complex **50**. All is coordinated by two pyridyl rings. The bridging N atom in contrast to the P atom in **50** is no longer two coordinated. It forms a third bond to a second equivalent of the Lewis acid Et₃Al. Both N-C bond lengths are identical within estimated standard deviations (N2-C1 139.2(5) pm; N2-C6 138.3(4) pm), indicating a delocalization of the negative charge like in **50**, but the central N-C bonds in the adduct are considerably longer than in the parent Me₂Al(2-Py)₂N (**47**) (av. 134.3(2) pm). A N-C single bond is about 147 pm long while the bond length for a N=C double bond is about 129 pm^[187]. All as well as Al2 show a distorted tetrahedral coordination sphere. Both Al1-N bonds (193.3(3) and 191.1(4) pm) are nearly of the same length and similar to those in **47** (av. 191.5(2) pm), **48** (192.1(2) pm), and **50** 192.4(2) pm). Consequently, the Al1-N bonds in **51** range between a single bond and a donor bond. Because of the formation of a donor bond to the Et₃Al-fragment in the adduct **51**, the bridging N atom is three coordinated. The N-Al2 bond of 201.0(3) pm is a typical Al-N donor bond^[171]. Due to the Lewis acid base adduct formation the N-C_{ipso} bonds are lengthened considerably to 138.8(4) pm in comparison to 134.3(2) pm in Me₂Al(2-Py)₂N (**47**). While the Al1-C distances are marginally shorter (av. 195.2(4) pm) than the Al2-C distances (av. 198.8(4) pm) both values fit the range covered by organo aluminum compounds^[188].

It is noteworthy that both aluminum atoms in **51** are not located in the plane of the amide anion. Like the phosphide anion in **50** and different to the planar complex $\text{Me}_2\text{Al}(\text{2-Py})_2\text{N}$ (**47**) it adopts a butterfly conformation. Both planes of the pyridyl rings intersect at an angle of 155.7° . Interestingly, the Al atom of the Et_3Al Lewis acid is located at the same side as the Et_2Al^+ aluminum atom. While the Al1 atom of the Et_2Al^+ moiety is 86.2 pm above the best plane of the three nitrogen atoms, the Al2 of the Et_3Al Lewis acid is 96.2 pm above that plane. Although the ethyl groups are magnetically nonequivalent in the solid state they equilibrate in the ^1H and ^{13}C spectra from solution at room temperature.

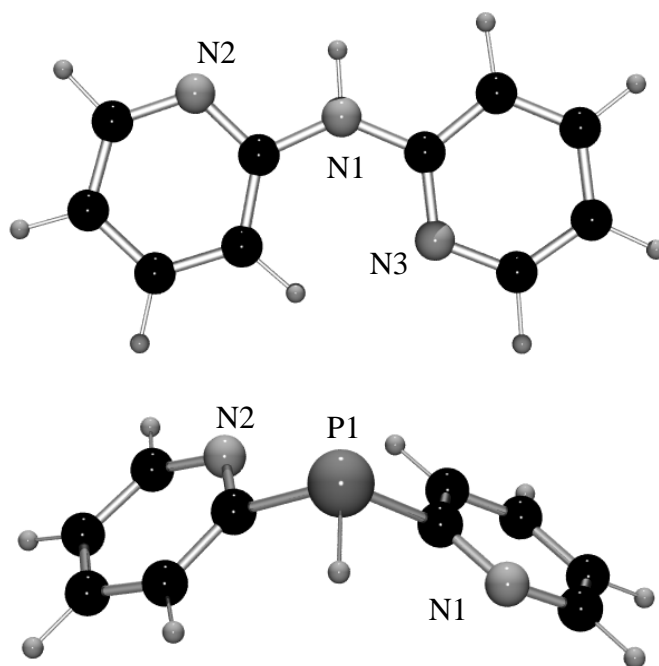


Figure 65. Optimized structures of $(2\text{-Py})_2\text{NH}$ (**45**) and $(2\text{-Py})_2\text{PH}$ (**46**) using BPW91/6-31+G(d)

Even at low temperature it is not possible to verify the asymmetry and to freeze out different signals. It is obvious from the experimental and theoretical data of all $(2\text{-Py})_2\text{N}^-$ and $(2\text{-Py})_2\text{P}^-$ anions that significant shortening of the central N-C and P-C bonds occurs, while proceeding from the parent neutral amine $(2\text{-Py})_2\text{NH}$ (**45**) to the amide and from the neutral phosphane $(2\text{-Py})_2\text{PH}$ (**46**) to the phosphides (Tables 28-29). The pyridyl rings in the charged ligands exhibit alternating bond lengths, i.e. short bonds in the 3- and 5-positions, different to the delocalized rings in **45** and **46**. The structures of the amides can be compared to experimental solid state crystal structure data of the amine $(2\text{-Py})_2\text{NH}$ (**45**)^[189], while such data are not available for the phosphane $(2\text{-Py})_2\text{PH}$ (**46**). Therefore, DFT calculations have been carried out on these compounds using different level of theory and are depicted in Figure 65.

Table 28. Selected calculated and experimental structural parameters for Py₂NH (**45**).

	B3LYP/6-31+G*	BPW91/6-31+G*	Explt. ^a
Bond lengths (pm)			
N1-H1	101.3	102.1	92.0(20)
N1-C1	139.6	139.9	138.8(2)
N1-C6	138.6	139.0	139.1(2)
C1-N2	134.6	135.5	134.3(2)
N2-C5	133.6	134.3	134.5(2)
C1-C2	140.8	141.4	140.0(2)
C2-C3	139.2	139.8	137.8(2)
C3-C4	139.8	140.4	138.4(2)
C4-C5	139.5	140.2	137.4(2)
N3-C6	133.9	134.9	133.5(2)
C6-C7	141.6	142.2	140.1(2)
C7-C8	138.5	139.2	137.5(2)
C8-C9	140.3	140.8	138.5(2)
C9-C10	139.1	139.8	137.7(2)
C10-N3	134.2	134.9	134.1(2)
H1----N2	228.8	228.9	210.0(20)
Bond and dihedral angles (°)			
C1-N1-C6	132.6	132.7	127.5(1)
C6-N1-H1	116.2	116.3	
C1-N1-H1	111.2	111.0	
N3-C6-N1-H1	-180.0	-180.0	
N2-C1-N1-H1	0.0	0.0	

^aValues from ^[189c]; av. of four crystallographically independent pyridyl rings in the asymmetric unit; structure determination at 150 K.

The DFT calculations of harmonic wavenumbers were performed by using fully optimized molecular geometry as the reference geometry. The DFT geometry optimization was carried out for (2-Py)₂NH (**45**), (2-Py)₂PH (**46**), Me₂Al(2-Py)₂N (**47**) and Me₂Al(2-Py)₂P (**48**), with the Becke-Lee-Yang-Paar (BLYP) ^[190], the Becke-Perdew-Wang (BPW91) ^[56] gradient corrected density functional methods and the hybrid functional B3LYP ^[191] method. The 6-31G, 6-31G(d), 6-31+G(d) basis sets were employed in the geometry optimization and the vibrations calculations. The two B3LYP and BPW91 functionals gave the best results with the 6-31+G(d) basis set for all structures. In general the structural features of the experiments

could be mimicked by both methods. The vibrational assignment in the experimental spectra was feasible with the help of the BPW91 calculations.

Table 29. Selected calculated structural parameters for Py₂PH (**46**).

	BPW91			BLYP		B3LYP
	6-31+G(d)	6-31G(d)	6-31G	6-31+G(d)	6-31G	6-31+G(d)
Bond lengths (pm)						
P1-H1	142.7	142.7	145.3	142.9	145.6	141.7
P1-C1	186.6	186.6	190.4	187.9	191.9	186.1
P1-C6	186.0	185.8	190.0	187.3	191.4	185.6
N1-C1	135.1	135.1	136.0	135.6	136.4	134.3
C1-C2	141.1	140.9	141.0	141.5	141.4	140.4
C2-C3	140.0	140.0	140.6	140.4	140.9	139.4
C3-C4	140.3	140.2	140.8	140.7	141.1	139.6
C4-C5	140.3	140.2	140.5	140.6	140.8	139.6
N1-C5	134.8	134.7	136.2	135.3	136.7	134.0
N2-C6	135.4	135.4	136.3	135.9	136.8	134.6
C6-C7	141.2	141.1	141.2	141.6	141.5	140.5
C7-C8	140.1	140.0	140.5	140.5	140.8	139.5
C8-C9	140.2	140.1	140.7	140.6	141.1	139.6
C9-C10	140.3	140.2	140.4	140.7	140.7	139.6
C10-N2	134.7	134.6	136.1	135.2	136.6	133.9
N1----H1	266.7	269.5	274.1	268.8	276.6	267.6
Bond and dihedral angles (°)						
C1-P1-C6	102.6	103.3	102.5	102.7	102.6	102.6
C6-P1-H1	97.2	97.3	97.3	97.0	97.2	97.2
C1-P1-H1	95.4	95.9	95.9	95.5	96.0	95.7
N2-C6-P1-H1	-166.5	-165.0	-161.0	-167.7	-160.7	-168.0
N1-C1-P1-H1	-28.4	-33.8	-33.1	-29.0	-34.3	-31.1
N2-C6-C1-N1	-161.1	-166.0	-161.5	-162.2	-162.3	-164.4

While the vibrations calculated using B3LYP have to be scaled by $k=0.97$ the wavenumbers obtained with the BPW91 functional were directly in good agreement with the experimental values ^[192]. Therefore the geometrical features derived from that method have been compared to the experiments. The calculations represent the solid state experimental parameters very well.

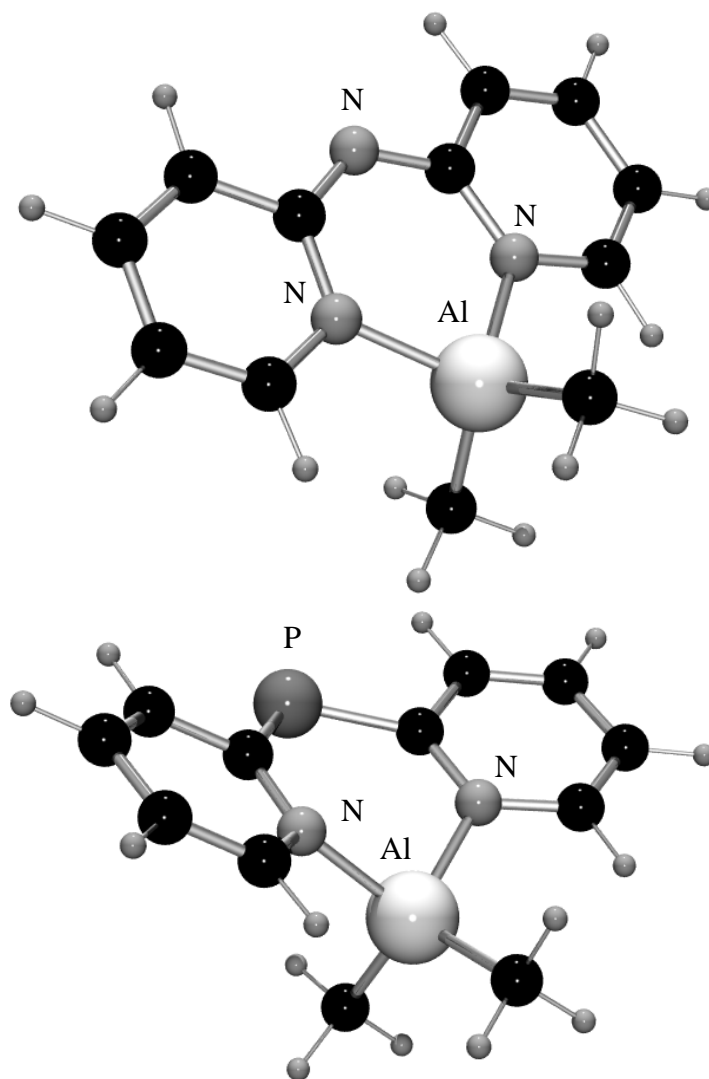


Figure 66. Optimized geometry of $\text{Me}_2\text{Al}(2\text{-Py})_2\text{N}$ (**47**) and $\text{Me}_2\text{Al}(2\text{-Py})_2\text{P}$ (**48**) using BPW91/6-31+G(d).

The ring nitrogen atoms in the amine $(2\text{-Py})_2\text{NH}$ (**45**) are oriented *trans* with respect to the central nitrogen atom ^[189]. The central N1 and the three neighboring atoms are in a plane, indicating sp^2 hybridization of N1 (Figure 65). The average central (H)N-C distance (139.4 (calc.) and 138.7(2) pm (exp.) ^[189c]) is of the length of a standard $\text{N}(\text{sp}^2)\text{-C}(\text{sp}^2)$ bond distance of 140 pm ^[187]. In general the calculated distances in the rings are marginally longer than in the solid state crystal structure, nevertheless it is obvious from both data that the N-C and C-C bond length do not differ, indicating full conjugation. Selected calculated geometrical parameters of $(2\text{-Py})_2\text{NH}$ are compared with experimental data in Table 28. The same is valid for the rings in the calculated di(2-pyridyl)phosphane **46**. The N-C and C-C bonds, respectively, are of the same lengths (Table 29). Different to the central nitrogen atom in **45** the central phosphorous atom in **46** clearly shows pyramidal environment (Figure 65). The C1-P1-C6 angle of 102.6° is much more acute than the C1-N1-C6 angle in **45** (132.7°).

Like in **45** the two ring nitrogen atoms are arranged in the *trans* conformation relative to the P atom. The BPW91/6-31+G(d) calculated P-C_{ipso} distance of 186.6 pm almost exactly matches the standard value of a P-C single bond of 185 pm^[187].

Deprotonation of **45** and **46** and subsequent ring coordination to a R₂Al⁺ moiety in Me₂Al(2-Py)₂N (**47**) and Me₂Al(2-Py)₂P (**48**) has a considerable impact to the structures of the related complexes in comparison to the parent amine and phosphane (Figure 66; Table 30):

- Both ring nitrogen atoms are arranged *cisoid* with respect to the central N- and P atom and coordinated to the aluminum atom.
- The central N-C bond is shortened by 4.4 pm and the central P-C bond by 8.2 pm, indicating partial double bond character.
- Full conjugation of the pyridyl rings is precluded and partial double bond character is found in the 3- and 5-positions.

Predominantly the last two features indicate that the resonance forms **a** and **c** in Scheme 3 contribute most to the bond description in the complexes **47** and **48**. However, while the *a priori* 4e⁻ donor capacity of the ligand can be ruled out by these findings, the question of to what extent it is a 2e⁻ donor remains open.

6.4 The (2-Py)₂P⁻ and (2-Py)₂N⁻ anions

Structure of **48** reveals that in order to avoid repulsion the pyridyl ligands are twisted along the P-C bond and the aluminum atom is displaced from the ligand plane. As shown, this non planarity of the P-ligand give rise to a butterfly arrangement in **48**. Similar coordination mode has been observed in the case of dipyridyl arsenide. It is noteworthy that the pyridyl phosphid and amid exhibit different reactivity and structural features depending on the nature of the metal^[172, 177]. However, coordination with the *cis-cis*, *cis-trans* and *trans-trans* conformers are documented for both (2-Py)₂E⁻ anions (E = N, P)^[182]. On the one hand, the di(2-pyridyl)phosphide ligand shows a metal-dependant coordination response and is involved in a highly unusual σ/π interaction with caesium ion. On the other hand, the phosphorus atom is Lewis basic enough to bridge two soft iron metal centres. In opposite to the *transoid* and *cisoid* 2,2'-bipyridydine ligand, the (2-Py)₂E⁻ anion offer due to its bridging heteroatom more flexibility toward metal fragment for complexation. In this context, the different conformers of (2-Py)₂N⁻ and (2-Py)₂P⁻ have been analysed by DFT calculations.

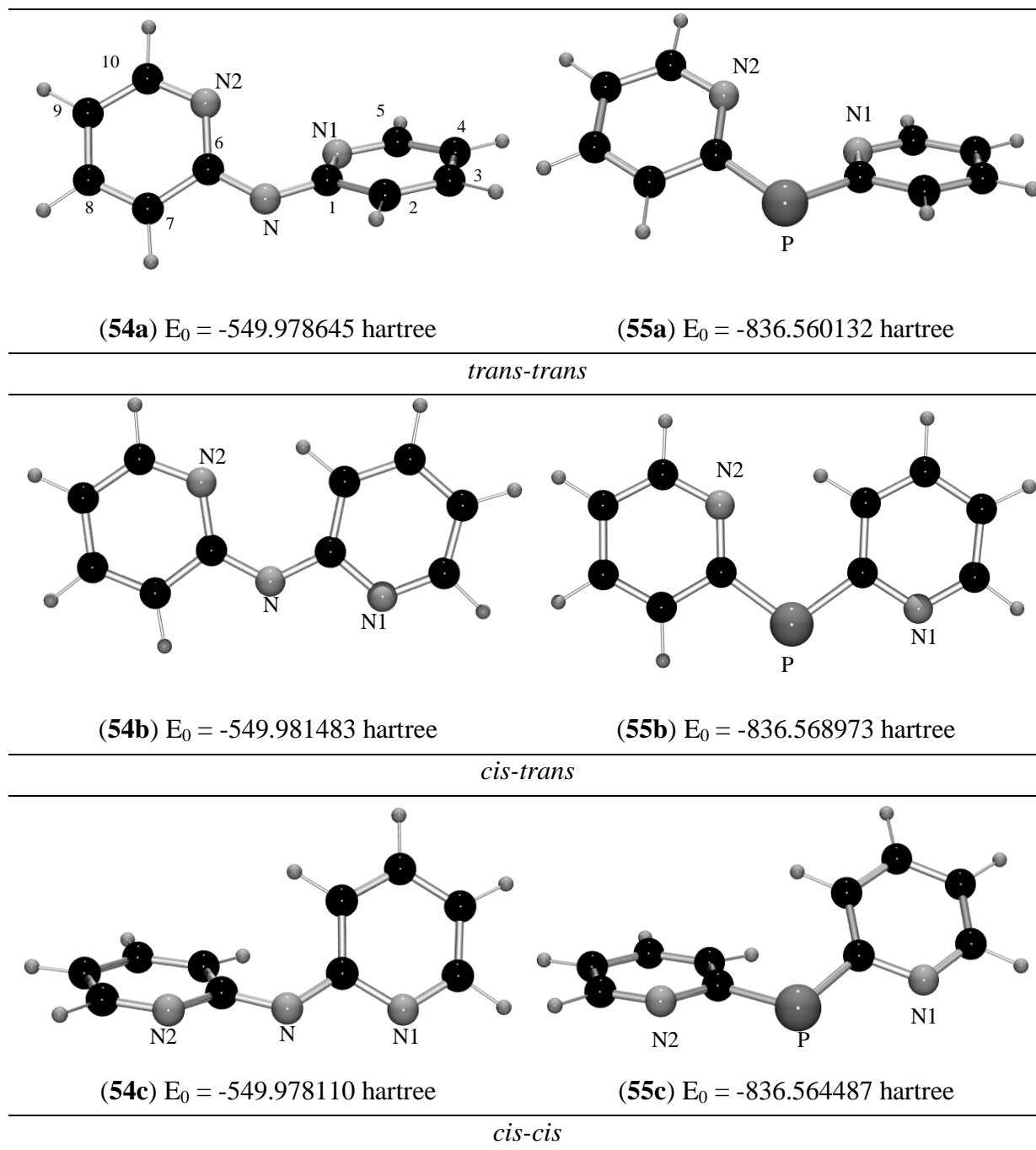


Figure 67. Optimized geometries for the different conformers of the $(2\text{-Py})_2\text{N}^-$ and $(2\text{-Py})_2\text{P}^-$ ligands using the BPW91/6-31+G(d) method.

As expected, the *cis-trans* configuration of $(2\text{-Py})_2\text{E}^-$ is more stable than the *trans-trans* one. The energy differences between the conformers **54a/54c** and **55a/55c** are 7.44 and 23.19 kJ/mol, respectively. The *trans-trans* configuration of $(2\text{-Py})_2\text{N}^-$ is only 1.4 kJ/mol more stable than the *cis-cis* one, while in case of the Py_2P^- anion the *cis-cis* form is with 11.42 kJ/mol significantly more stable than the *trans-trans* one (Figure 67).

Table 31. Selected calculated parameters for the (2-Py)₂N⁻ and (2-Py)₂P⁻ anions, at the BPW91/6-31+G(d) level of theory.

	Py ₂ N ⁻		Py ₂ P ⁻	
	<i>trans-trans</i>	<i>cis-trans</i>	<i>trans-trans</i>	<i>cis-trans</i>
	Bond lengths (pm)			
E-C1	135.4	136.2	182.1	182.0
C1-C2	144.2	144.3	143.5	143.1
C2-C3	138.9	139.4	139.2	139.5
C3-C4	141.4	140.9	141.3	141.1
C4-C5	140.6	140.7	140.6	140.7
C5-N1	134.1	133.8	134.2	134.0
N1-C1	138.1	138.7	137.2	138.0
N1---N2	301.6		308.2	
E-C6	135.4	135.3	182.1	181.8
C6-C7	144.2	144.7	143.5	144.0
C7-C8	138.9	138.6	139.2	138.8
C8-C9	141.4	141.8	141.3	141.8
C9-C10	140.6	140.1	140.6	140.1
C10-N2	134.1	134.5	134.2	134.6
N2-C6	138.1	138.8	137.2	137.9
	Bond and dihedral angles (°)			
C1-E-C6	124.5	126.5	107.0	108.4
N1-C1-C6-N2	-51.0	-180.0	-39.8	180.0
				<i>cis-cis</i>
				182.2
				143.4
				139.2
				141.2
				140.6
				134.1
				138.2
				182.2
				143.4
				139.2
				141.2
				140.6
				134.1
				138.2

Moreover, the *cis-trans* anions are planar, whereas the N-C-C-N dihedral angle in **54a** and **55a** has been calculated to be -51.0° and -39.8° , respectively (Table 31). Since the interatomic distance between the two ring nitrogen atoms has been evaluated at 301.6 and 308.2 pm for the anions **54a** and **55a**, respectively, the observed deformation from planarity may be due to the electrostatic repulsion of the lone pair present on the nitrogen atoms. Hence, the N-C-C-N dihedral angle is about 10° smaller than in the amide anion. The C-N-C angle in the bridge position has been calculated to be 124.5° , 126.5° and 123.9° for the *trans-trans*, *cis-trans* and *cis-cis* (2-Py)₂N⁻ anion, respectively (Table 31). Despite the electronic competition between the deprotonated central nitrogen atom and the ring ones in **54a-c**, the metal center is chelated by the two ring nitrogen atoms in **49**, which means that the anion should have the depicted *trans-trans* conformation (Figure 67). However, the energy difference between the three conformers is less than 9 kJ/mol. This is not the case for the phosphide anions where the *trans-trans* form has been expected to be 23.19 kJ/mol less stable than the *cis-trans* one. One may notice that the C-P-C angle in the bridging position, which has been calculated to be 107.0° , 108.4° and 105.0° for the *trans-trans*, *cis-trans* and *cis-cis* (2-Py)₂P⁻ anion, respectively, is significantly smaller than the corresponding C-N-C angle (Table 31). A closer examination of the calculated structures reveal partially localized double bonds in the pyridyl rings at the -3 and -5 positions. However, the calculated C5-N1 bond length is about 5 pm shorter than the N1-C1 one (Table 31).

6.5 Study of the donor-acceptor bond

One difference between the Lewis-type donor-acceptor bond and the normal covalent bonds is that the dissociation of the former yields two closed-shell fragments with an electron lone-pair donor and an electron-pair acceptor, while the latter gives two open-shell fragments. Haaland^[179] defines dative bonds as a new type on the basis of their bond rupture behaviour, which is different from covalent bonds. Another difference is that the bond length of a normal covalent bond did not usually change in different aggregation states, while donor-acceptor bonds have frequently larger interatomic distances in the gas phase than in the solid state^[179].

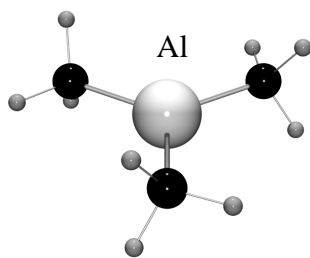
The goal of this part has been to characterize the E-Al donor-acceptor bond energy in the complex Et₂Al(2-Py)₂NAlEt₃ (**51**) and the model compounds **52** and **53**, since Et₂Al(2-Py)₂P (**50**) does not form the adduct Et₂Al(2-Py)₂PAlEt₃ with a second equivalent of AlEt₃. We were able to evaluate the theoretical methods used for the di(2-pyridyl)amides and -phosphides

complexes, with a simple well-known system. Thus, the molecular structures and the donor-acceptor bond dissociation energy of the complexes $\text{Me}_3\text{N}\rightarrow\text{AlMe}_3$ and $\text{Me}_3\text{P}\rightarrow\text{AlMe}_3$, which have been already determined in the gas phase ^[193-194], constitute an ideal starting point. Consequently, the theoretical parameters calculated at the CBS-4M, MP2/6-31+G(d) and BPW91/6-31+G(d) level of theory are reported in Table 32 together with the experimental values obtained by Haaland.

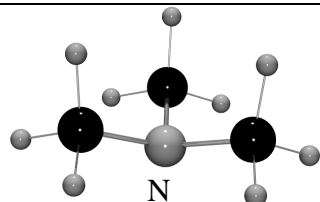
Table 32. Experimental and calculated structural parameters for AlMe_3 , Me_3N , Me_3P , $\text{Me}_3\text{N}\rightarrow\text{AlMe}_3$ and $\text{Me}_3\text{P}\rightarrow\text{AlMe}_3$.

		CBS4M/MP2/BPW91	Exptl. ^b
Bond lengths (pm)			
AlMe_3	Al-C	198.1/197.3/198.5	195.7(3)
Me_3P	P-C	184.7/185.0/187.4	184.6(3)
Me_3N	N-C	146.4/145.6/146.1	147.4(3)
$\text{Me}_3\text{P}\rightarrow\text{AlMe}_3$	P-C	182.8/183.3/185.4	182.2(3)
	P-Al	254.2/250.7/255.0	253.0(40)
	Al-C	200.5/199.8/201.0	197.3(3)
$\text{Me}_3\text{N}\rightarrow\text{AlMe}_3$	N-C	149.7/148.1/148.7	147.4(3)
	N-Al	206.4/211.1/216.4	209.9(10)
	Al-C	200.9/199.8/200.9	198.7(5)
Bond angles (°)			
AlMe_3	C-Al-C	120.0/120.0/120.0	120.0(assumed)
Me_3P	C-P-C	99.5/99.2/99.4	98.6(3)
Me_3N	C-N-C	113.0/110.7/110.7	110.6(6)
$\text{Me}_3\text{P}\rightarrow\text{AlMe}_3$	C-P-C	103.3/103.2/103.0	103.4(8)
	C-P-Al	115.1/115.1/115.3	115.0(7)
	P-Al-C	100.4/99.8/101.1	100.0(13)
$\text{Me}_3\text{N}\rightarrow\text{AlMe}_3$	C-Al-C	116.8/117.1/116.6	117.1(8)
	C-N-C	109.5/109.1/109.5	- ^c
	C-N-Al	109.4/109.8/109.4	109.3(4)
	N-Al-C	103.6/102.0/102.8	102.3(3)
	C-Al-C	114.6/115.8/115.2	114.8(2)

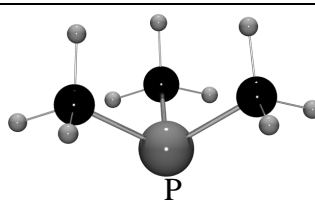
^aCBS-4M, MP2/6-31+G(d), BPW91/6-31+G(d) ^bStructure of free Me_3P ^[195], Me_3N ^[196], AlMe_3 ^[197]. Structure of the adduct $\text{Me}_3\text{P}\rightarrow\text{AlMe}_3$ ^[193] and $\text{Me}_3\text{N}\rightarrow\text{AlMe}_3$ ^[194]. ^cnot available.



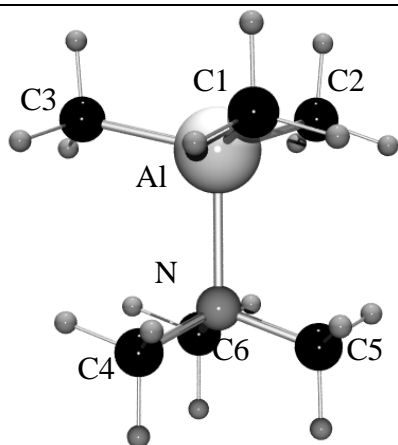
CBS-4(0°K) = -361.526041, CBS-4(Enthalpy) = -361.516530, CBS-4(Energy) = -361.517474,
 E(MP2) = -361.213268, E₀(MP2) = -361.104634,
 E(BPW91) = -362.144817, E₀(BPW91) = -362.040536



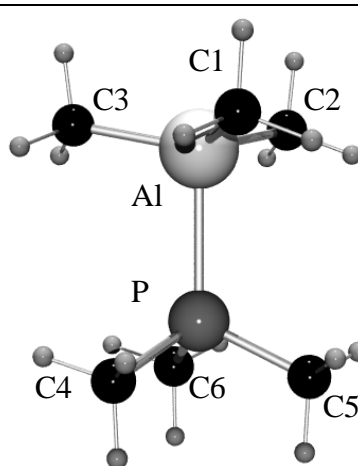
CBS-4(0°K) = -174.158570,
 CBS-4(Enthalpy) = -174.152022,
 CBS-4(Energy) = -174.152967,
 E(MP2) = -173.839502, E₀(MP2) = -173.716132,
 E(BPW91) = -174.445246, E₀(BPW91) = -174.327450



CBS-4(0°K) = -460.420457,
 CBS-4(Enthalpy) = -460.412889,
 CBS-4(Energy) = -460.413833,
 E(MP2) = -460.076783, E₀(MP2) = -459.961305,
 E(BPW91) = -461.067222, E₀(BPW91) = -460.956690



CBS-4(0°K) = -535.729422,
 CBS-4(Enthalpy) = -535.668552,
 CBS-4(Energy) = -535.715216,
 E(MP2) = -534.061109336, E₀(MP2) = -534.866728
 E(BPW91) = -536.618044, E₀(BPW91) = -536.392024



CBS-4(0°K) = -821.981449,
 CBS-4(Enthalpy) = -821.964109,
 CBS-4(Energy) = -821.965053,
 E(MP2) = -821.325940, E₀(MP2) = -821.099858
 E(BPW91) = -823.236116, E₀(BPW91) = -823.018798

Δ CBS-4(0°K) = 117.4 kJ/mol

Δ CBS-4(Enthalpy) = 120.0 kJ/mol

Δ CBS-4(Energy) = 117.4 kJ/mol

Δ E(MP2) = 130.4 kJ/mol Δ E₀(MP2) = 120.4 kJ/mol

Δ E(BPW91) = 73.4 kJ/mol Δ E₀(BPW91) = 63.0 kJ/mol

Exptl. Δ H_{dis}⁰ = 129.6 kJ/mol

Δ CBS-4(0°K) = 91.5 kJ/mol

Δ CBS-4(Enthalpy) = 91.1 kJ/mol

Δ CBS-4(Energy) = 88.6 kJ/mol

Δ E(MP2) = 94.0 kJ/mol Δ E₀(MP2) = 89.0 kJ/mol

Δ E(BPW91) = 63.1 kJ/mol Δ E₀(BPW91) = 56.6 kJ/mol

Exptl. Δ H_{dis}⁰ = 96.1 kJ/mol

Figure 68. Optimized geometries and calculated energies (in hartree) E and E₀ (with ZPE correction) at CBS4M, MP2/6-31+G(d) and BPW91/6-31+G(d) level of theory.

As observed experimentally, the Al-C bond distance in these complexes is significantly longer and the C-Al-C valence angle significantly smaller than in the free monomeric AlMe₃. Furthermore, the comparison of the adducts with the free PMe₃ and NMe₃, shows that on formation of these complexes, the length of the P-C and N-C bonds considerable decrease, while the C-P-C and C-N-C valence angles increase importantly. These modifications observed for both, theoretical and experimental values, are in good agreement with the valence shell electron pair repulsion model (VSEPR) ^[198].

Table 33. Experimental and calculated structural parameters for MeCH₂N, MeCH₂P, MeCH₂N→AlMe₃ and MeCH₂P→AlMe₃.

		BPW91/6-31+G(d)	MP2/6-31+G(d)
Bond lengths (pm)			
MeCH ₂ P	P-CH ₂	168.2	167.5
	P-CH ₃	187.7	185.6
MeCH ₂ N	N-CH ₂	127.7	128.0
	N-CH ₃	145.7	145.8
MeCH ₂ P→AlMe ₃	P-CH ₂	167.4	166.6
	P-CH ₃	185.7	183.7
	P-Al	260.0	261.1
	Al-C	200.2	198.8
MeCH ₂ N→AlMe ₃	N-CH ₂	128.4	128.4
	N-CH ₃	146.6	146.5
	N-Al	211.2	209.9
	Al-C	200.7	199.5
Bond angles (°)			
MeCH ₂ P	C-P-C	103.2	102.2
MeCH ₂ N	C-N-C	117.7	116.5
MeCH ₂ P→AlMe ₃	C-P-C	107.6	107.3
	CH ₃ -P-Al	124.5	123.9
	CH ₂ -P-Al	127.9	128.8
	P-Al-C	99.0	97.8
	C-Al-C	117.9	118.6
MeCH ₂ N→AlMe ₃	C-N-C	119.3	118.8
	CH ₃ -N-Al	117.8	123.6
	CH ₂ -N-Al	122.8	117.6
	N-Al-C	102.2	99.5
	C-Al-C	116.2	116.7

As expected, the high costly computational methods CBS-4M and MP2/6-31+G(d) gave the best structural and energetical results. Although the BPW91/6-31+G(d) method overestimated slightly the N-Al and P-Al donor-acceptor bond lengths, the resulting bond dissociation energies were extremely low (Figure 68).

Likewise, DFT and MP2 calculations were carried out on the model compounds MeCH₂N, MeCH₂P, MeCH₂N→AlMe₃ and MeCH₂P→AlMe₃, since these models should be more consistent with compounds **52** and **53**. Similar to the complexes Me₃N→AlMe₃ and Me₃P→AlMe₃, the AlMe₃ fragment presents no significant structural difference through the coordination with the phosphorus or the nitrogen atoms. In contrast with the Al-N bond, which has been shortened only by about 1 and 5 pm, the P-Al interatomic distance has been surprisingly lengthened by 5 and 10 pm with the MP2 and BPW91/6-31+G(d) methods, respectively (Table 33). Furthermore, the calculated bond dissociation energy at the MP2 level of theory, which was the most reliable one for the Haaland complexes, has been determined in this case at 106.6 and 50.3 kJ/mol for MeCH₂N→AlMe₃ and MeCH₂P→AlMe₃, respectively (Table 34). Consequently, the sp²-hybridisation of the heteroatom has a strong effect upon the dissociation enthalpy of the E-Al bond and particularly, for the phosphorus adducts.

Table 34. Calculated bond energies of MeCH₂N→AlMe₃ and MeCH₂P→AlMe₃ (kJ/mol)

Methods	MeCH ₂ N→AlMe ₃	MeCH ₂ P→AlMe ₃
BPW91/6-31+G(d)	D _e = 76.9	D _e = 34.3
	D ₀ = 68.1	D ₀ = 28.8
MP2/6-31+G(d)	D _e = 106.6	D _e = 50.3
	D ₀ = 95.7	D ₀ = 44.9
	^a Me ₃ N→AlMe ₃ (Exptl. ΔH _{dis} ⁰ = 129.6 kJ/mol)	Me ₃ P→AlMe ₃ (Exptl. ΔH _{dis} ⁰ = 96.1 kJ/mol)

^aReference 179

Whereas the calculated E-Al bond energy has a quite similar value for Me₃N→AlMe₃ (63.0 kJ/mol) and MeCH₂N→AlMe₃ (68.1 kJ/mol) with the BPW91 method, it differs significantly for Me₃P→AlMe₃ (56.6 kJ/mol) and MeCH₂P→AlMe₃ (28.8 kJ/mol). It is noteworthy that such a trend was observed also with the MP2 method. However, the predicted E-Al bond energies for the MeCH₂E→AlMe₃ (E = N, P) are lower than those for Me₃E→AlMe₃ (E = N, P). These interesting results suggest that in case of the phosphorus adduct the electron density is more delocalized via the neighboring carbon atoms than shared with aluminum. Furthermore, the donor-acceptor bond energy seems to be strongly dependent on the

hybridization of the heteroatom. In addition, the “hard” aluminum atom prefers the “hard” nitrogen donor rather than the “soft” phosphane function.

Population analysis schemes, like the Natural Population Analysis ^[68], assign strong partial charges to the nitrogen atoms of the bipyridyl complexes **47** and **48** (see Figure 69).

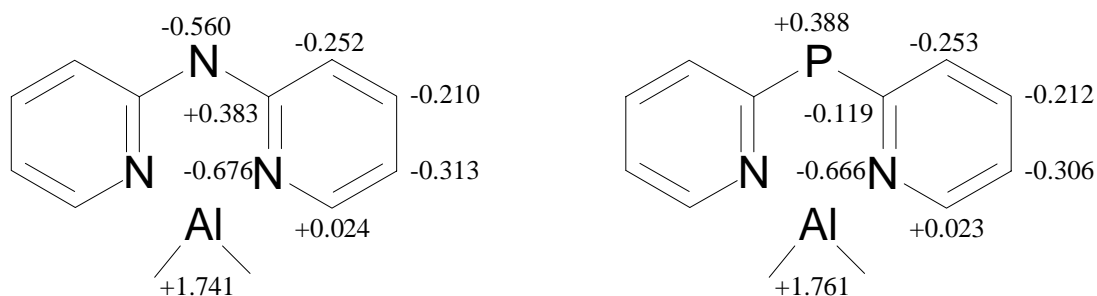


Figure 69. Calculated natural charges in (e) for the complexes $\text{Me}_2\text{Al}(\text{2-Py})_2\text{N}$ (**47**) and $\text{Me}_2\text{Al}(\text{2-Py})_2\text{P}$ (**48**) which were determined with the Natural Population Analysis.

The polarity of the E-C bond for the calculated compounds **47** and **48** shows a different orientation, since the nitrogen and the phosphorus atoms in the bridging position are negatively and positively charged, respectively (Figure 69). In this sense, the natural atomic orbital occupancies for the selected heteroatoms N and P in complexes **47** and **48** are summarized in Table 35. It shows that the s and p_π populations of the AO for the bridging phosphorus and nitrogen atoms are significantly different, which is in agreement with the calculated charges and total electron density (Figures 69 and 70). Thus, the 3s orbital of the phosphorus atom is more populated than the 2s orbital of the nitrogen atom. Unlike the p orbitals of the phosphorus atom present a reverse behaviour (Table 35).

Table 35. Natural atomic orbital occupancies for the heteroatoms N and P in complexes **47** and **48**.

E = N	N ₁	N ₂	E = P	N ₁	N ₂
Type (AO)/Occupancy (in e)					
2s/1.327	2s/1.337	2s/1.337	3s/1.563	2s/1.329	2s/1.329
2p _x /1.199	2p _x /1.478	2p _x /1.478	3p _x /0.591	2p _x /1.517	2p _x /1.517
2p _y /1.666	2p _y /1.420	2p _y /1.420	3p _y /1.173	2p _y /1.395	2p _y /1.395
2p _z /1.348	2p _z /1.420	2p _z /1.420	3p _z /1.254	2p _z /1.400	2p _z /1.400

The calculated electron density for **47** and **48**, depicted in Figure 70, shows a clear difference in the total density distribution. While the charge density in the amide ligand of $\text{Me}_2\text{Al}(\text{2-}$

$\text{Py})_2\text{N}$ (**47**) indicates considerable electron density at the central bridging nitrogen atom (Figure 70, left), there is less density remaining at the central bridging phosphorus atom in $\text{Me}_2\text{Al}(2\text{-Py})_2\text{P}$ (**48**) (Figure 70, right). Hence, the Lewis basicity of this atom is quite low compared to the nitrogen atoms.

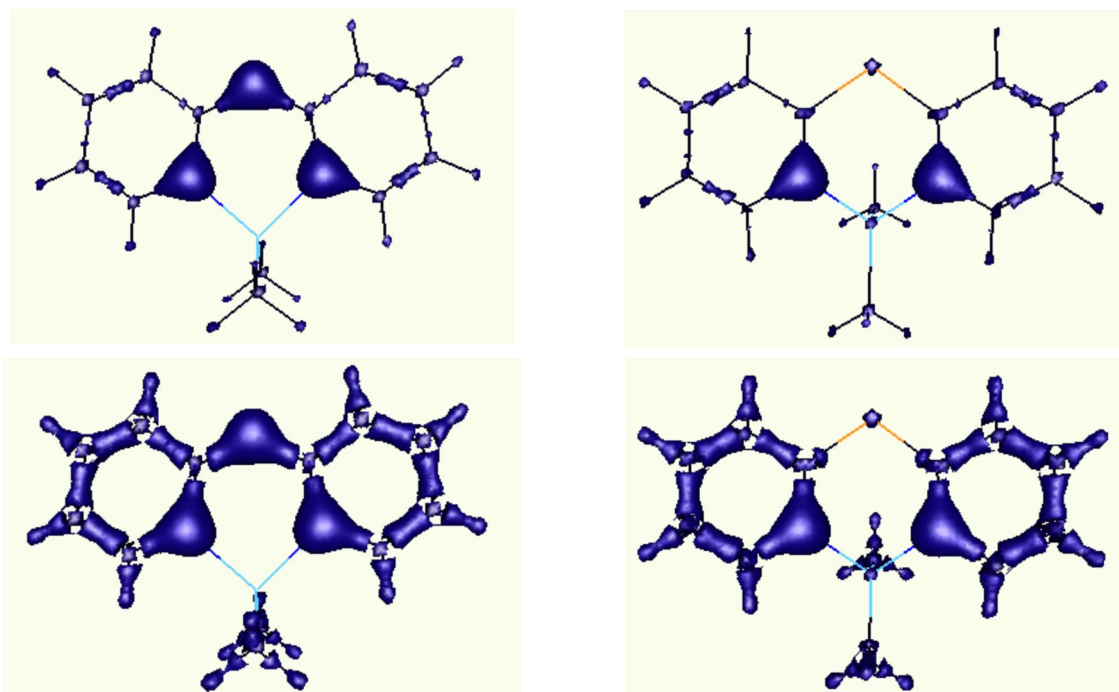
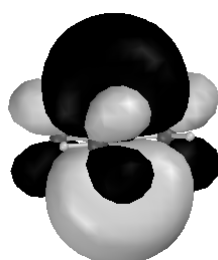


Figure 70. Total electron density of $\text{Me}_2\text{Al}(2\text{-Py})_2\text{N}$ (**47**) (left) and $\text{Me}_2\text{Al}(2\text{-Py})_2\text{P}$ (**48**) (right); (upside isocontour = 0.30, downside isocontour = 0.25).

Plots were obtained by using the gOpenMol package (Laaksonen, L., Espoo, Finland, <http://laaksonen.csc.fi/gopenmol/gopenmol.html>).

Furthermore, the two representations on the top show clearly concentration of charge density at the -3 and -5 positions of the pyridyl rings, which is in good agreement with the partial double bond localisation on these positions, as previously discussed for the experimentally and theoretically determined molecular structures.



LUMO, $E = -1.12$ eV, (isocontour = 0.01)

Figure 71. Representation of the calculated LUMO for AlMe_3 using BPW91/6-31+G(d)

Besides, the HOMO and HOMO-2 for the complexes **47** and **48**, as well as the LUMO of the free AlMe_3 fragment are also depicted in Figures 71 and 72. While the HOMO of the phosphide and amide ligand are essentially composed of the p_z orbital of the heteroatoms N or P, the HOMO-2 are constituted of the p_y AO of the heteroatom N or P.

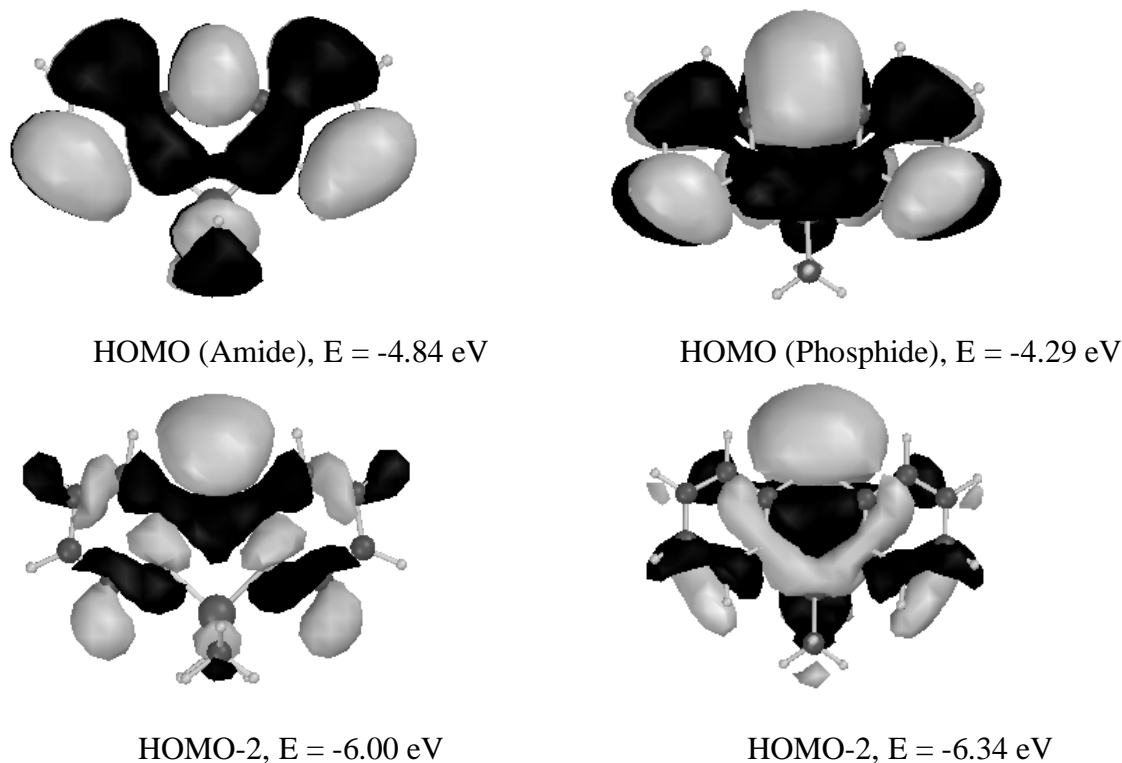


Figure 72. Representation of the calculated HOMO and HOMO-2 for **47** and **48** using BPW91/6-31+G(d).

As suggested by the geometry of the model compounds **52** and **53** depicted in the figure 73, the overlapping between the LUMO of the AlMe_3 fragment and the HOMO-2 of **47** or **48** should be taken into consideration. Moreover, the HOMO-2 of the phosphide complex is energetically higher than that of the amide. Additionally, the NBO analysis indicates a higher p_π population on the p_y AO of the nitrogen bridging atom than for the phosphorus one. Since all these results suggest the formation of a metal nitrogen bond rather than a metal phosphorus one, we were interested to evaluate quantitatively the E-Al bond energy in the model compounds **52** and **53**. In this case, selected bond lengths and bond angles for these compounds are reported in Table 36 together with the experimental values measured in the complex **51**.

Through the coordination of the AlMe_3 fragment with the bridging nitrogen atom the bipyridyl rings take an accentuated butterfly conformation analogous to $\text{Me}_2\text{Al}(\text{2-Py})_2\text{P}$.

Furthermore, the heteroatom in the bridging position seems to become a pseudo sp^3 -hybridization, leading to a deviation of the $AlMe_3$ fragment from the plane containing the N1, E and N2 atoms. Surprisingly, the comparison between the model compounds $Me_2Al(2-Py)_2N \rightarrow AlMe_3$ and $Me_2Al(2-Py)_2P \rightarrow AlMe_3$ reveals a different position of the $AlMe_3$ fragment regarding the butterfly geometry of the bipyridyl rings (Figure 73).

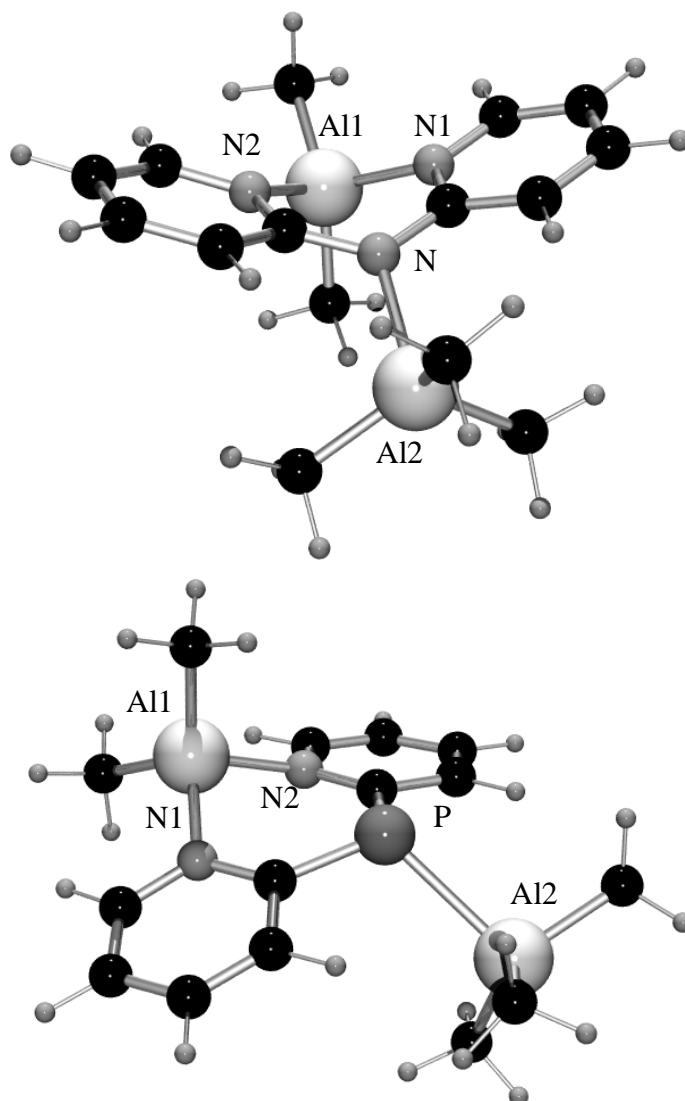
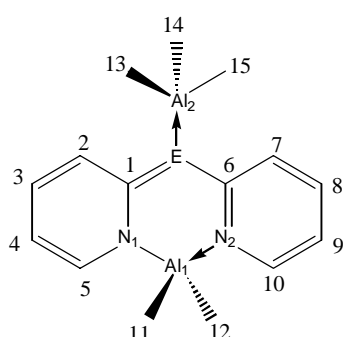
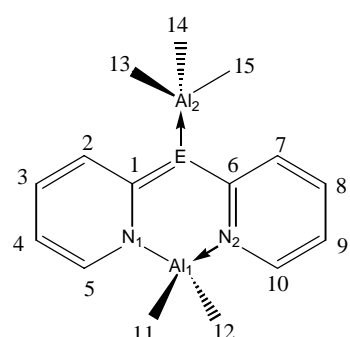


Figure 73. BPW91/6-31+G* optimized geometry of $Me_2Al(2-Py)_2N \rightarrow AlMe_3$ (**52**) and of $Me_2Al(2-Py)_2P \rightarrow AlMe_3$ (**53**).

Moreover, the calculated Al1-E-Al2 bond angle has been found to be 139.1 and 151.3° for $Me_2Al(2-Py)_2N \rightarrow AlMe_3$ and $Me_2Al(2-Py)_2P \rightarrow AlMe_3$, respectively. As mentioned by *Pfeiffer*, the Al2-N bond length in **51** is significantly longer than a covalent bond but is about 5 pm shorter than a pure dative one^[182]. However, donor-acceptor bonds have frequently larger interatomic distances in the gas phase than in the solid state^[179]. Hence, the Al2-N bond, which has been calculated to be 212.9 pm, is much longer than the measured one.

Table 36. Selected calculated structural parameters compared to crystal structure data of $\text{Me}_2\text{Al}(\text{2-Py})_2\text{N} \rightarrow \text{AlMe}_3$ (**52**) and $\text{Me}_2\text{Al}(\text{2-Py})_2\text{P} \rightarrow \text{AlMe}_3$ (**53**)

	E = N		E = P
			
	BPW91/6-31+G(d)	Exptl.	BPW91/6-31+G(d)
Bond lengths (pm)			
E-C1/E-C6	137.8	138.3(4)/139.2(5)	180.4
E-Al2	212.9	201.0(3)	266.0
C1-C2/C6-C7	142.5	137.2(6)/140.7(5)	143.0
C2-C3/C7-C8	138.6	137.0(5)/135.5(5)	138.6
C3-C4/C8-C9	141.3	139.5(5)	141.7
C4-C5/C9-C10	138.4	134.0(5)/136.7(5)	138.5
C5-N1/C10-N2	136.7	138.0(5)/135.4(4)	136.8
N1-C1/N2-C6	137.7	138.0(5)/136.2(5)	138.5
N1-Al1/N2-Al1	197.8	191.1(1)/193.3(3)	197.4
Bond angles (°)			
C1-E-Al2	118.0	117.4(2)	112.0
C1-E-C6	123.3	122.4(3)	102.2
E-Al2-C13	106.6	109.04(14)	106.2
E-Al2-C15	103.8	105.24(14)	102.8
Al1-E-Al2	139.1	-	151.3
C11-Al1-C12	121.6	122.7(2)	120.2
N1-Al1-N2	90.1	91.57(14)	97.1
C15-Al2-C13	115.2	113.7	117.3
C14-Al2-C15	110.8	111.0	112.0

The calculated bond energy at the MP2/6-31+G(d) level for the complexes $\text{Me}_3\text{E} \rightarrow \text{AlMe}_3$ (E = N, P) differs from the experimental values with less than 10 kJ/mol. However, the theoretically predicted dissociation energies at the BPW91 level are too low. Owing to the good performance of the MP2 method, a single point calculation at this level of theory has been carried out on **52** and **53**. For this, the fully optimized geometry at BPW91/6-31+G(d)

has been used. The energies obtained with the BPW91/6-31+G(d) and BPW91/6-31+G(d)//MP2/6-31+G(d) methods are reported in Table 37.

Table 37. Calculated bond energies of **52** and **53** (kJ/mol)

Methods	$\text{Me}_2\text{Al}(\text{2-Py})_2\text{N} \rightarrow \text{AlMe}_3$	$\text{Me}_2\text{Al}(\text{2-Py})_2\text{P} \rightarrow \text{AlMe}_3$
BPW91/6-31+G(d)	$D_e = 50.2$ $D_0 = 43.2$	$D_e = 37.6$ $D_0 = 31.2$
BPW91/6-31+G(d)//MP2/6-31+G(d)	$D_e = 133.6$ $D_0 = 125.4$	$D_e = 81.4$ $D_0 = 75.4$
	${}^a\text{Me}_3\text{N} \rightarrow \text{AlMe}_3$ (Exptl. $\Delta H_{\text{dis}}^0 = 129.6$ kJ/mol)	$\text{Me}_3\text{P} \rightarrow \text{AlMe}_3$ (Exptl. $\Delta H_{\text{dis}}^0 = 96.1$ kJ/mol)

^aReference 179

Quite remarkable is the improvement of the dissociation energy by using the single point calculation at the MP2 level of theory. One may notice that the theoretical bond dissociation energy for complex **52** (125.4 kJ/mol) is in this case very closed to the experimental value determined for $\text{Me}_3\text{N} \rightarrow \text{AlMe}_3$ (129.6 kJ/mol). Unlike the same theoretical method led to a donor-acceptor bond in **53** with 20.7 kJ/mol lower than the measured one in $\text{Me}_3\text{P} \rightarrow \text{AlMe}_3$.

It should be noticed, that all di(2-pyridyl) amides and -phosphides coordinate the R_2Al^+ fragment via both ring nitrogen atoms. This already suggests that the charge density in the anions is coupled into the rings and accumulated at the ring nitrogen atoms, but the Lewis basicity of the central nitrogen atom in **49** is still high enough to coordinate a second equivalent AlEt_3 and to form the Lewis acid base adduct $\text{Et}_2\text{Al}(\text{2-Py})_2\text{NAlEt}_3$ **51**. All these findings confirm the formation of metal nitrogen rather than metal phosphorus bonds even in reaction pathways, like the one established by Budzelaar in the reaction of (2-pyridyl)phophanes with methyl lithium^[199]. Our theoretical results, which are supported by experiments, show that while in the amides (E = N) the amido nitrogen does function as a typical Lewis base, the situation in the corresponding phosphides (E = P) is different. In the latter case, nearly all the charge density couples into the pyridyl rings leaving the central phosphorus atom attractive only for soft metals in the form of a π -acid type of coordinating centre.

6.6 Vibrational spectroscopy

The partial localization of the ring double bonds in **47** versus **45** and **48** versus **46** is clearly verified by Raman spectroscopical experiments. Especially the wavenumbers shifts in the $\nu(\text{C}=\text{C})$ and $\nu(\text{C}=\text{N})$ region indicate this feature. The Raman spectrum of **47** (partially shown in Figure 74) is dominated by intense bands in the wavenumber region between 1200 and 1300 cm^{-1} . The band at 1255 cm^{-1} is assigned to the deformation vibration $\delta(\text{CH}_3)$. Both methyl groups in **47** are equivalent and give only rise to one single signal. The other bands are assigned to $\delta(\text{CN})$ at 1302 and 1290 cm^{-1} . In this region the $\delta(\text{CH})_{\text{ar}}$ are also observed and combined with the previous bands. The $\delta(\text{CNH})$ deformation for secondary amines with aromatic groups occurs between 1550 and 1650 cm^{-1} [94] and is assigned to the strong signal in **45** at 1594 cm^{-1} . Figure 74 shows several band shifts which indicates localization of double bonds in the 3- and 5- position in the pyridyl rings.

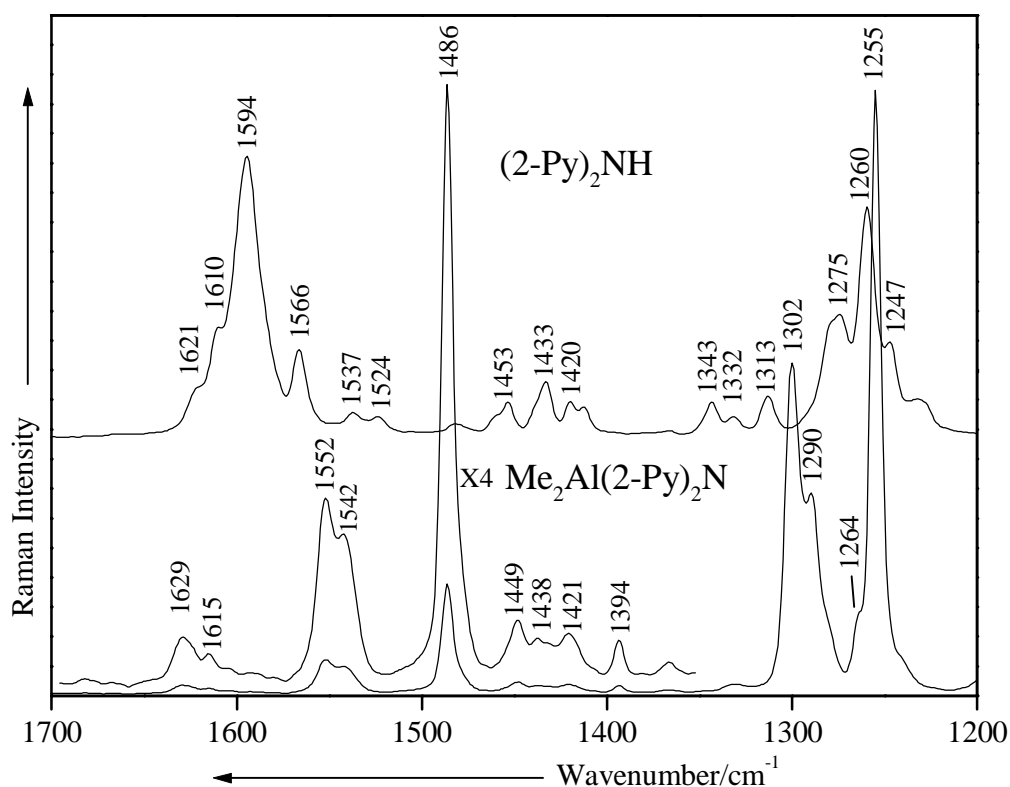


Figure 74. The FT-Raman spectra of (2-Py)₂NH (**1**) and Me₂Al(2-Py)₂N (**3**) between 1200 and 1700 cm^{-1} .

The signals which occur at 1552 and 1486 cm^{-1} are assigned to a partial $\nu(\text{C}=\text{N})$ stretching vibration indicating the partial $\text{C}=\text{N}$ double bond at the bridging position (Figure 75). In general the $\nu(\text{C}=\text{N})$ and $\nu(\text{C}-\text{N})$ stretching vibrations occur at about 1630-1650 cm^{-1} and 1280-1360 cm^{-1} [94]. The $\nu(\text{Al}-\text{CH}_3)$ stretching and $\rho(\text{CH}_3)$ rocking vibrations are assigned at

672 and 578 cm^{-1} (not shown in Figure 74). The pure $\nu_s(\text{Al-CH}_3)$ stretching vibration is found at 556 cm^{-1} (calc. 557 cm^{-1}). The $\nu_s(\text{Al-N})$ and $\nu_{as}(\text{Al-N})$ stretching modes are found at 377 and 393 cm^{-1} (calc. 363 and 377 cm^{-1}). They are combined with the middle ring breathing.

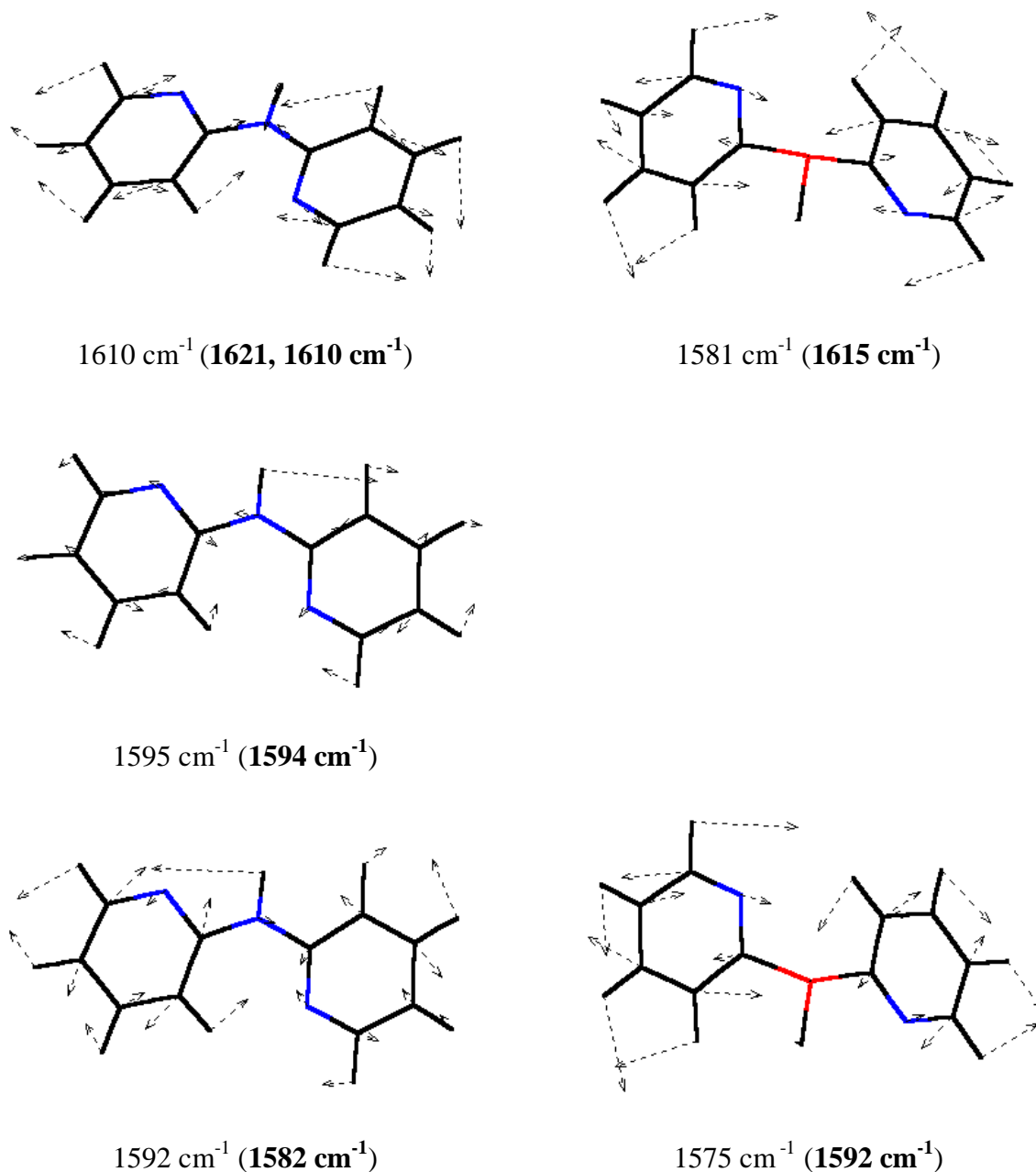


Figure 75. Calculated (BPW91/6-31+G(d)) $\nu(\text{C=C})$ and $\nu(\text{C=N})$ stretching vibrations in (2-Py)₂NH (**45**) (left column) and (2-Py)₂PH (**46**) (right column). **Experimental** values for the wavenumbers are also given in brackets for comparison.

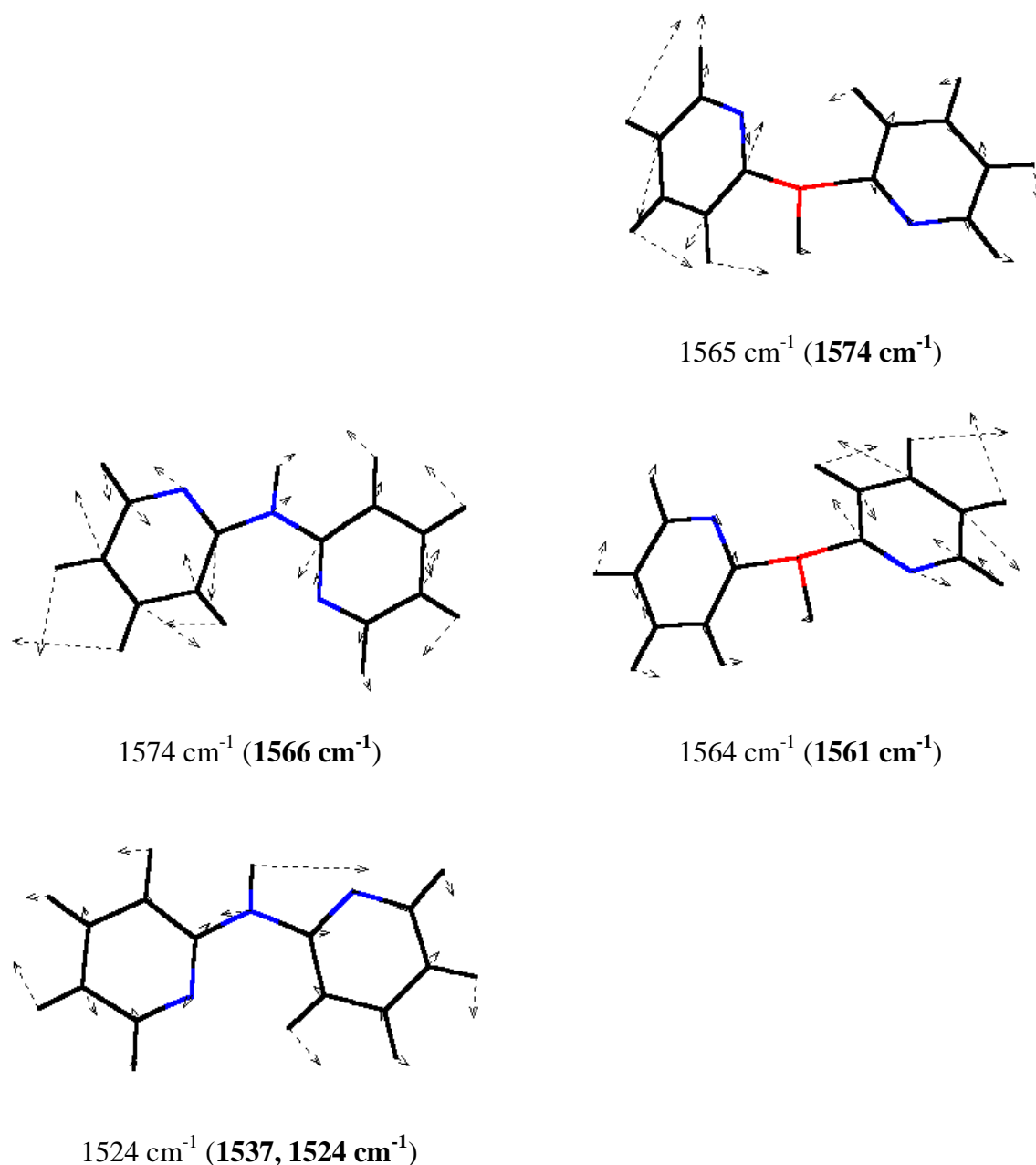


Figure 75. (to be continued) Calculated (BPW91/6-31+G(d)) $\nu(\text{C}=\text{C})$ and $\nu(\text{C}=\text{N})$ stretching vibrations in $(2\text{-Py})_2\text{NH}$ (**45**) (left column) and $(2\text{-Py})_2\text{PH}$ (**46**) (right column). **Experimental** values for the wavenumbers are also given in brackets for comparison.

The $\nu(\text{PH})$ stretching vibration of **46** occurs at 2306 cm^{-1} and disappears after the reaction with trimethyl aluminum due to the evolution of methane (Figure 76). Because of the anharmonicity, the calculated wavenumbers of the $\nu(\text{CH})$ and the $\nu(\text{PH})$ stretching vibrations are shifted compared to the experimentally observed ones. Like in **47** the characteristic stretching vibrations $\nu(\text{C}=\text{C})$ and $\nu(\text{C}=\text{N})$ from the pyridyl rings show a significant shift in the region between 1650 and 1500 cm^{-1} (Figure 77). Unfortunately, the $\nu(\text{PC})$ vibrational modes

in **46** and **48** are combined with the pyridyl ring vibrations ($1080\text{--}1200\text{ cm}^{-1}$) so that direct comparison of their bond strength is precluded. The calculation predicts only one signal for the $\delta(\text{CH}_3)$ in the planar molecule of **47** whereas two signals are calculated for the butterfly conformation in **48**. The difference between the two calculated signals is 11 cm^{-1} and has been verified in the experiment. The $\nu(\text{Al-CH}_3)$ stretching and $\rho(\text{CH}_3)$ rocking vibrations are assigned to 666 and 574 cm^{-1} , respectively the pure $\nu(\text{Al-CH}_3)$ stretching vibration is found at 521 or 554 cm^{-1} (cal. 554 cm^{-1}). In the region of $500\text{--}400\text{ cm}^{-1}$ in the spectra several PC deformation vibrations occur. The $\nu(\text{Al-N})$ stretching modes are combined with the middle ring breathing which is localized at 350 and 370 cm^{-1} (calculated 335 and 338 cm^{-1}).

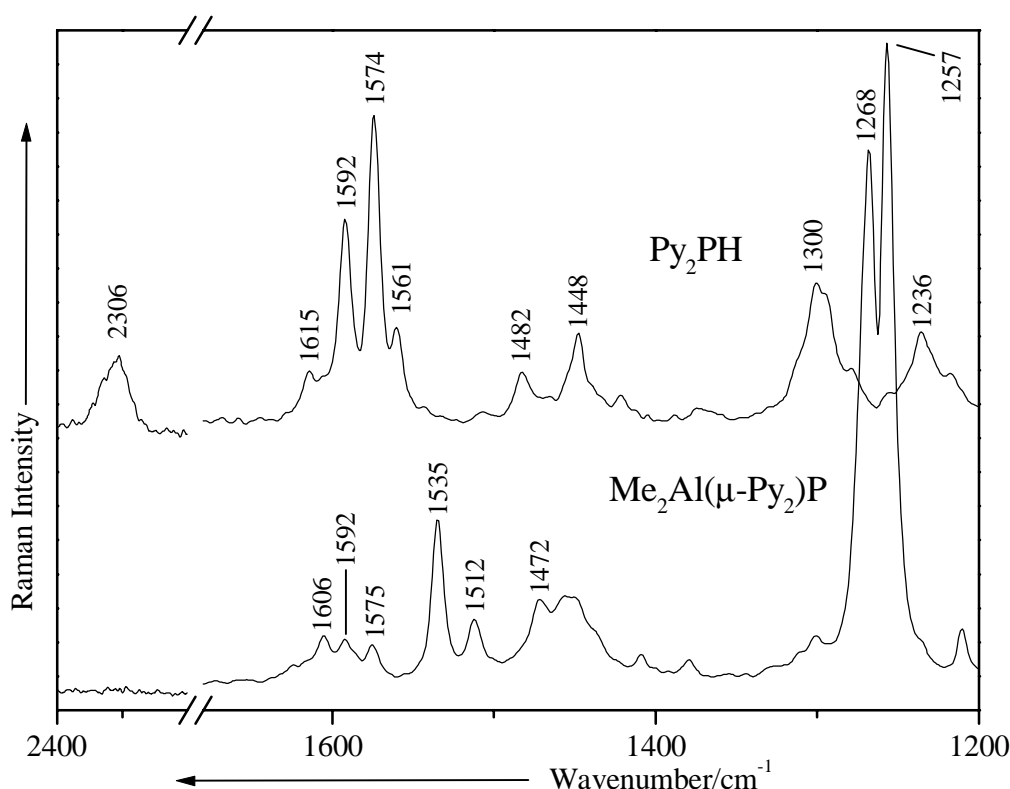


Figure 76. Part of the FT-Raman spectra of Py_2PH (**46**) and $\text{Me}_2\text{Al}(\mu\text{-Py}_2)\text{P}$ (**48**)

The calculated vibrations of **47** and **48** using BPW91/6-31+G(d) are in good agreement with the experiments. The difference in the first two $\nu(\text{C}=\text{C})$ modes of **47** and **48** is 14 cm^{-1} , in both, the experiment and theory. Comparison of the wavenumbers for these vibrations in **47** and **48** reveals a shift of 23 cm^{-1} to higher wavenumbers in **47** relative to **48**. This shift indicates higher partial double bond localization in the 3- and 5-position in **48**. The vibrations at 1542 in **47** and 1535 cm^{-1} in **48** indicate stronger bonds in the 4- and 7-ring positions of **47** relative to **48**. Hence, all bonds in **47** are strengthened while partial double bond localization is emphasized in **48**. Furthermore the vibrations at 1551 and 1486 cm^{-1} in **47** show partial

$\nu(\text{N}=\text{C})$ stretching of the $\text{N}-\text{C}_{\text{ipso}}$ bond combined to the $\nu(\text{C}=\text{C})$ stretching wavenumber of the 3- and 5-positions.

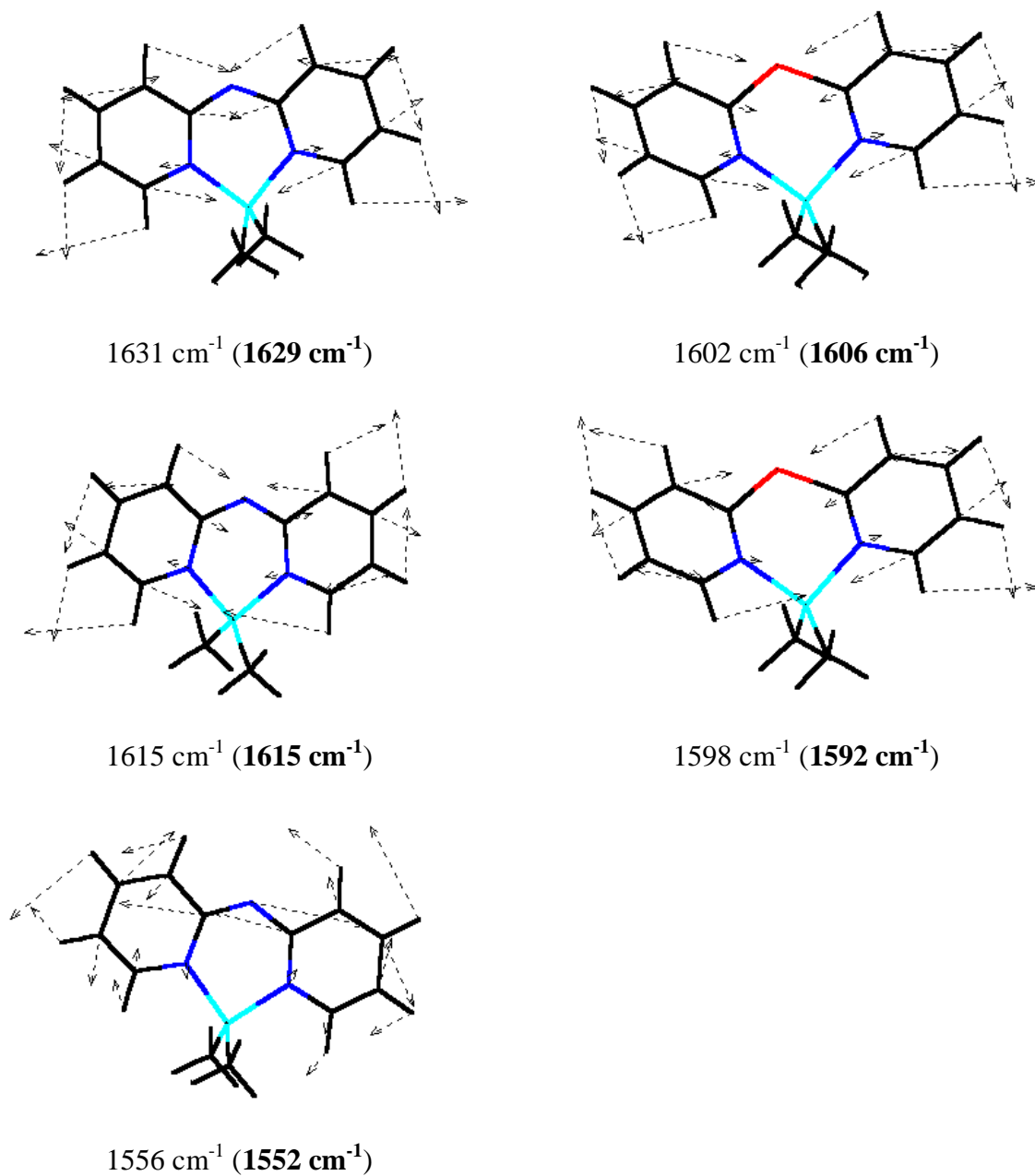


Figure 77. Calculated (BPW91/6-31+G(d)) $\nu(\text{C}=\text{C})$ and $\nu(\text{C}=\text{N})$ stretching vibrations in $\text{Me}_2\text{Al}(\text{2-Py})_2\text{N}$ (47) (left column) and $\text{Me}_2\text{Al}(\text{2-Py})_2\text{P}$ (48) (right column). **Experimental** values for the wavenumbers are also given in brackets for comparison.

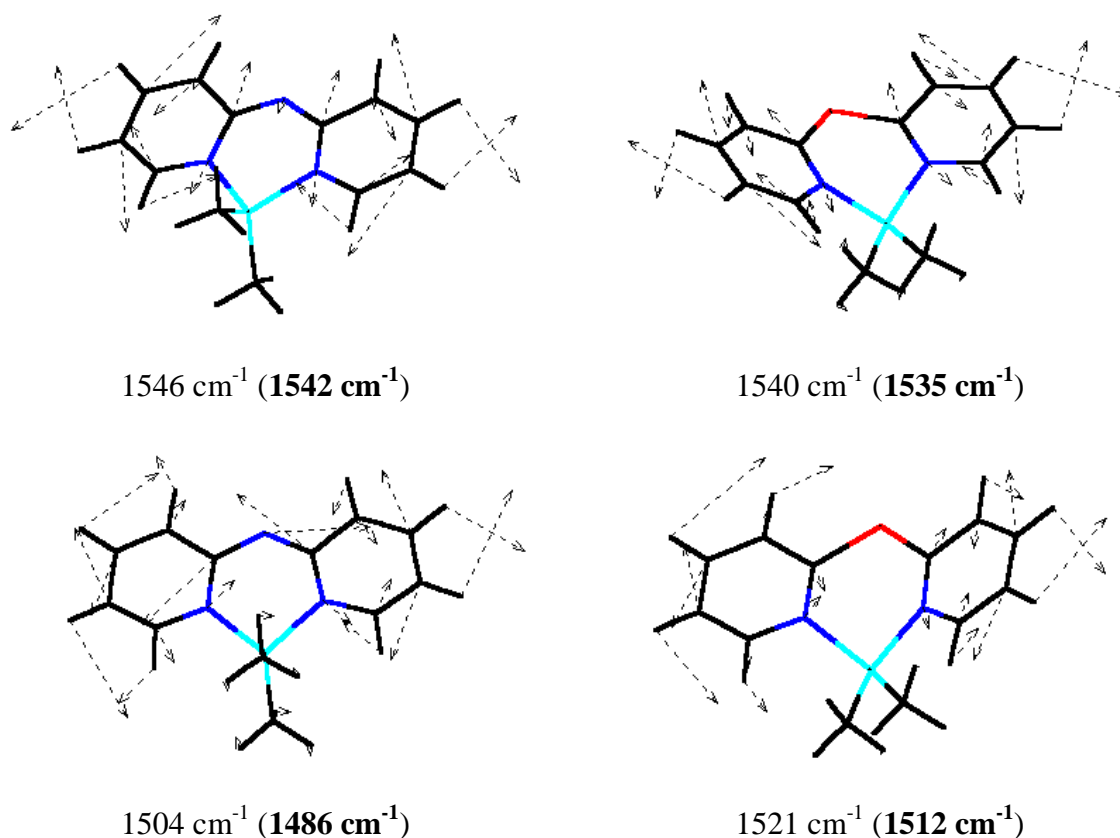


Figure 77. (to be continued) Calculated (BPW91/6-31+G(d)) $\nu(\text{C}=\text{C})$ and $\nu(\text{C}=\text{N})$ stretching vibrations in $\text{Me}_2\text{Al}(\text{2-Py})_2\text{N}$ (**47**) (left column) and $\text{Me}_2\text{Al}(\text{2-Py})_2\text{P}$ (**48**) (right column). **Experimental** values for the wavenumbers are also given in brackets for comparison.

Comparison of the vibrations of 1486 and 1512 cm^{-1} is humped because E-C_{ipso} contribution occurs only in **47** but not in **48**. The shift of 27 cm^{-1} for the $\nu_{\text{as}}(\text{Al-N})$ and 23 cm^{-1} for the $\nu_{\text{s}}(\text{Al-N})$ stretching vibration of **47** versus **48** to higher wavenumbers indicates different Al-N bonding, possibly due to different coordination geometries in the complexes. The discussed computational tools facilitate the unambiguous assignment of the Raman ring vibrational wavenumbers. The shift to higher wavenumbers proceeding from the parent amine **45** and phosphane **46** to the metal complexes **47** and **48** indicates partial double bond localization in the ring positions 3 and 5. This effect is more pronounced in the di(2-pyridyl)amide complex than in the phosphide. Due to the higher electronegativity of the central nitrogen atom in **47**, **49** and **51** compared to the bridging two coordinated phosphorus atom in **48** and **50** the di(2-pyridyl)amide is the hardest Lewis base. In the phosphides merely all charge density couples into the rings leaving the central phosphorus atom only attractive for soft metals.

6.7 [Me₂Al{Py(Bth)P}]

6.7.1 Experimental and theoretical structures

The synthesis and X-Ray structure of [Me₂Al{Py(Bth)P}] are available in the PhD-Thesis of Mathias Pfeiffer ^[182].

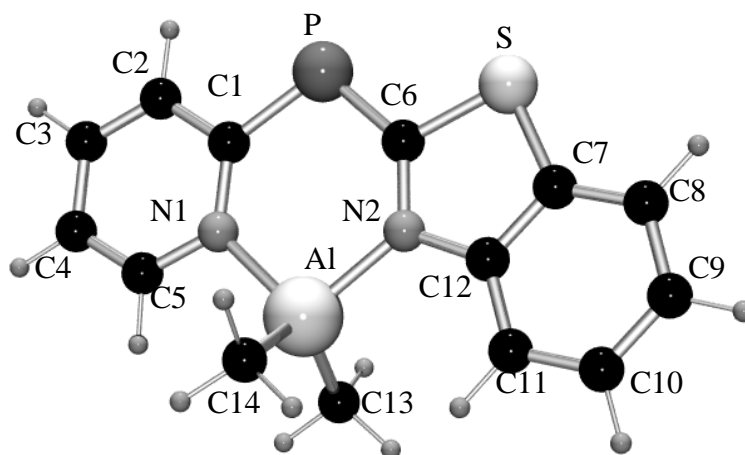


Figure 78. Calculated structure of [Me₂Al{Py(Bth)P}] (**56**) using BPW91/6-311+G(d). (Bth = 2-Benzothiazolyl)

DFT calculations have been carried out on the complex [Me₂Al{Py(Bth)P}] (**56**) at different levels of theory and the selected theoretical parameters are reported in Table 37 together with the corresponding experimental values. As expected, the agreement between theory and experiment is better for the 6-311+G(d) basis set. One may notice that both [Me₂Al{Py(Bth)P}] (**56**) and Me₂Al(2-Py)₂P (**48**) present similar coordination state (Figures 66 and 78). However, the theoretical structure of [Me₂Al{Py(Bth)P}] is almost planar and totally different from the observed butterfly conformation in **48**.

In Me₂Al(2-Py)₂P the P-C(ipso) and Al-N interatomic distances are on both sides quite similar, which shows an even delocalisation of the electron density over both pyridyl rings. This is not the case for [Me₂Al{Py(Bth)P}], where both experimental and theoretical Al-N and P-C(ipso) bond distances are significantly different (Table 38). Thus, the P-C6 bond length, which has been calculated at 175.4 pm and measured at 175.6(7) pm, has a double bond character (P=C-double bond: 167 pm ^[197]), whereas the P-C1 bond length, calculated at 180.2 pm and measured at 179.2(7) pm, has more a P-C single bond character (P-C-single bond: 185 pm). This is in good agreement with the mesomeric structure depicted on the right in Scheme 6.

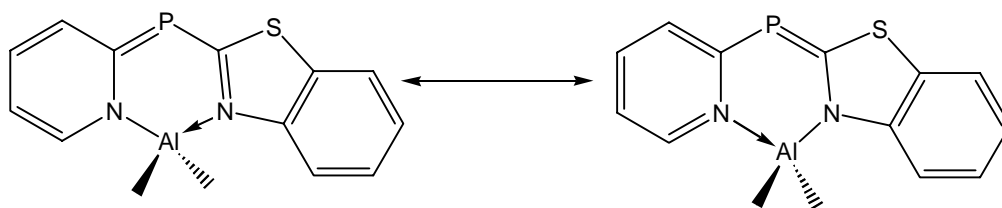
Table 38. Selected calculated and experimental structural parameters for [Me₂Al{Py(Bth)P}] (**56**).

	BPW91/6-311+G(d)	BPW91/6-31+G(d)	BPW91/6-31G(d)	Exptl. ^a
Bond distances (pm)				
P-C1	180.2	180.5	180.6	179.2(7)
C1-C2	142.6	142.9	142.8	140.6(9)
C2-C3	138.1	138.6	138.5	137.2(9)
C3-C4	141.2	141.5	141.4	139.7(9)
C4-C5	138.1	138.5	138.4	136.0(9)
C5-N1	136.5	136.8	136.7	136.4(8)
N1-C1	137.8	140.0	137.9	136.8(8)
N1-Al	199.3	199.5	199.7	194.6(6)
P-C6	175.4	177.9	177.9	175.6(7)
C6-S	178.4	178.6	178.7	175.1(6)
S-C7	175.4	175.4	175.6	174.0(6)
C12-N2	140.1	140.3	140.2	141.5(8)
N2-C6	135.3	135.6	135.5	135.5(8)
N2-Al	197.0	197.2	197.5	190.8(6)
Al-C13	198.6	198.9	198.7	197.2(9)
Al-C14	198.6	198.9	198.7	197.2(9)
C7-C12	141.5	141.9	141.8	
Bond Angles (°)				
N1-Al-N2	99.4	99.3	99.2	99.6(3)
C13-Al-C14	120.9	121.0	121.2	118.6(7)
C1-P-C6	105.4	105.4	105.4	104.7(4)
C6-S-C7	90.7	90.7	90.7	91.3
C1-N1-Al	128.3	128.4	128.5	128.7
C6-N2-Al	124.9	125.0	125.0	125.3
P-C1-N1	128.1	128.0	128.0	
P-C6-N2	133.9	133.8	133.9	

^aReference 182.

Although the electronic charge is delocalized in **56** over the benzthiazolyl ring, the aromaticity of the pyridyl ring is disturbed, since the -1, -3 and -5 positions of the pyridyl ring in **56** are shorter than in **46**. Furthermore, the calculated geometries correspond to individual molecules in gas phase, whereas X-ray data were obtained from molecules

positioned on a crystal lattice. In this context, the theoretical values for the Al-N bonds are much longer than the measured ones, but follow the trend observed experimentally.



Scheme 6

6.7.2 NBO analysis and total electron density calculation

The NBO Analysis^[68] ascribed a strong partial charge to the nitrogen atoms of the benzothiazolyl complexes **56**, but slightly lower for N1 (Figure 79). Consequently, the mesomeric structure (b) depicted on Scheme 5 should be preferred, which is also consistent with the calculated and measured shorter Al-N2 and P-C6 bond lengths in [Me₂Al{Py(Bth)P}] (**56**) (Table 38).

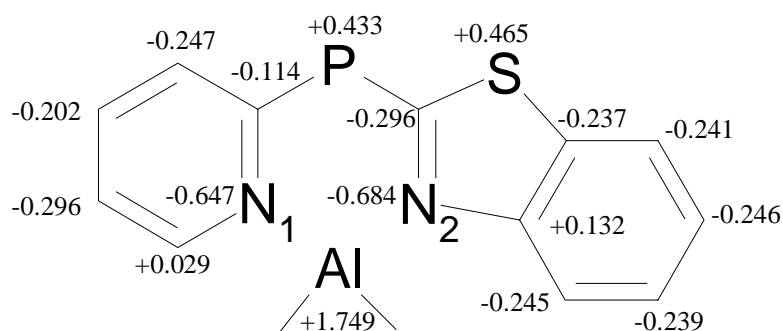


Figure 79. Calculated natural charge (in e) for the complex [Me₂Al{Py(Bth)P}] (**56**).

Due to the positively charged phosphorus and sulfur atoms, a higher concentration of negative charge can be observed on the C6 atoms (Figure 79). Furthermore, the plot of the calculated electron density for **56** (Figure 80) indicates a similar distribution to the one for Me₂Al(2-Py)₂P. In comparison with the nitrogen atoms of the rings, there is almost no density remaining at the central bridging phosphorus and sulfur atoms in [Me₂Al{Py(Bth)P}] (**56**) (Figure 80). Hence, the Lewis basicity of these atoms is quite low and a coordination behaviour such in Me₂Al(2-Py)₂P has been expected for this compound.

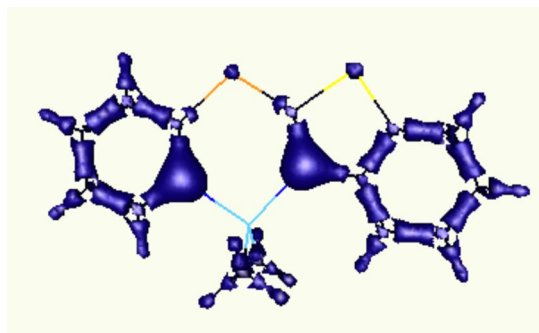


Figure 80. Total electron density of $[\text{Me}_2\text{Al}\{\text{Py}(\text{Bth})\text{P}\}]$ (**56**). (isocontour = 0.25). Plot was obtained by using the gOpenMol package (Laaksonen, L., Espoo, Finland, <http://laaksonen.csc.fi/gopenmol/gopenmol.html>).

6.7.3 Vibrational spectroscopy

Figure 81 presents the high wavenumber region of the FT-Raman spectrum of $[\text{Me}_2\text{Al}\{\text{Py}(\text{Bth})\text{P}\}]$ (**56**) recorded in diethylether containing some trace of toluene.

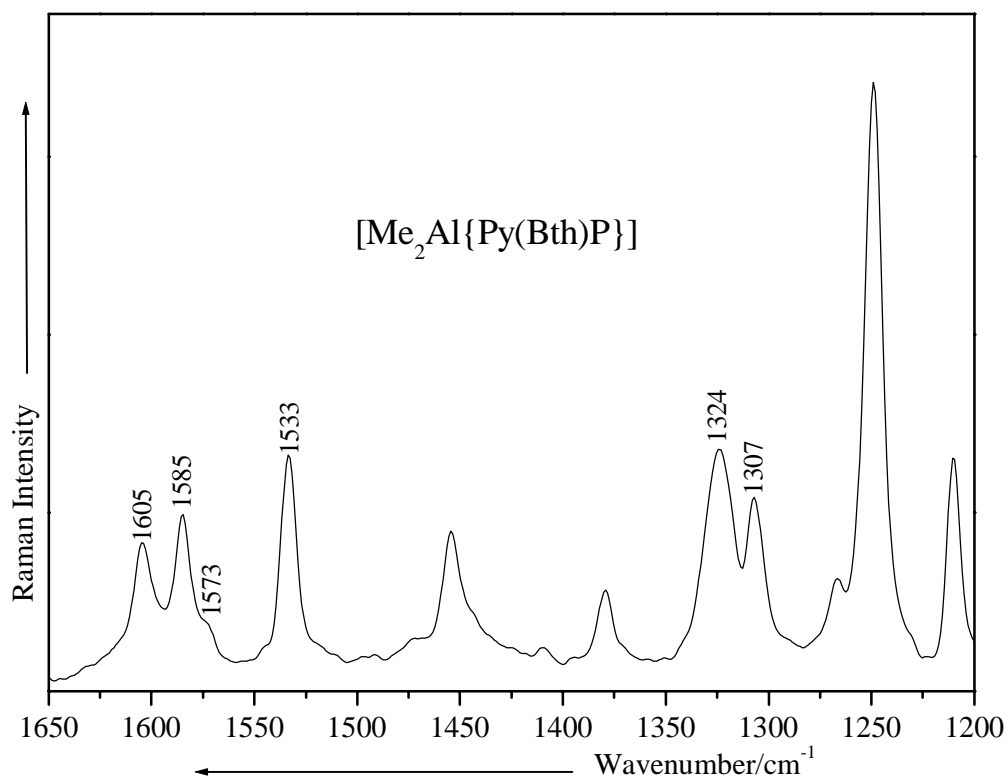


Figure 81. The FT-Raman spectra of $[\text{Me}_2\text{Al}\{\text{Py}(\text{Bth})\text{P}\}]$ (**56**) in the 1200-1650 cm^{-1} spectral region.

The presence of the $\nu(\text{PH})$ stretching mode (2312 cm^{-1}) of the educt in the FT-Raman spectrum of $[\text{Me}_2\text{Al}\{\text{Py}(\text{Bth})\text{P}\}]$ indicates that the reaction was not completely finished. Therefore, further investigations are necessary for a proper assignment of the Raman spectrum of $[\text{Me}_2\text{Al}\{\text{Py}(\text{Bth})\text{P}\}]$ (**56**).

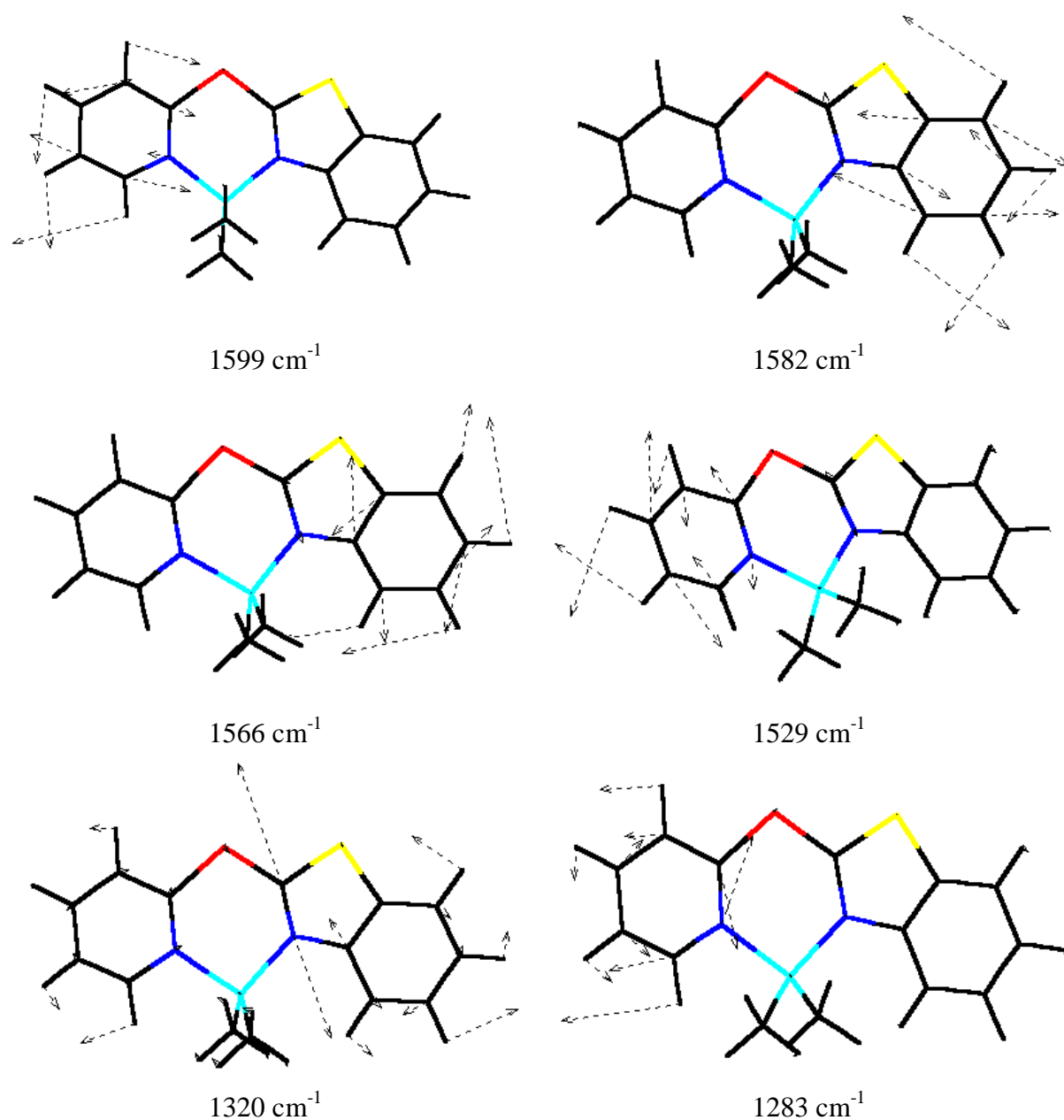


Figure 82. Calculated (BPW91/6-311+G(d)) $\nu(\text{C}=\text{C})$ and $\nu(\text{C}=\text{N})$ stretching vibrations in $[\text{Me}_2\text{Al}\{\text{Py}(\text{Bth})\text{P}\}]$ (**56**).

However, the selected fundamental modes for complex **56**, depicted in Figure 82, are very closed to the experimental values. Indeed, the $\nu(\text{C}=\text{C})$ and $\nu(\text{C}=\text{N})$ stretching modes of the rings, calculated at 1599, 1582, 1566 and 1529 cm^{-1} with the BPW91/6-311+G(d) method,

can be attributed to the bands observed at 1605, 1585, 1573 and 1533 cm^{-1} in the FT-Raman spectrum of $[\text{Me}_2\text{Al}\{\text{Py}(\text{Bth})\text{P}\}]$ (**56**) (Figures 81 and 82). The calculated $\nu(\text{C6-N2})$ stretching mode at 1320 cm^{-1} , which occurred at 1324 cm^{-1} in the FT-Raman spectrum of **56**, did not appear in the spectra of **47** and **48** (Figures 74 and 76). Its presence in a lower wavenumber region supports the single character of this bond and the mesomeric structure (b) depicted in Scheme 6.

Since, the predicted $\nu(\text{CN})$ stretching mode at 1283 cm^{-1} is strongly coupled with the $\nu(\text{CC})$ of the ring, it should be shifted to lower wavenumbers. Therefore, the medium strong band at 1307 cm^{-1} can be a good candidate.

Chapter 7

SUMMARY

The present studies which have been performed in the work-group **C-2** (Prof. W. Kiefer) within the program of the Sonderforschungsbereichs **347**, deal with the FT-Raman and –IR spectroscopy on new organometallic complexes, synthesized in the work-groups **B-2** (Prof. W. Malisch), **B-3** (Prof. W. A. Schenk), **D-1** (Prof. H. Werner) and **D-4** (Prof. D. Stalke). The FT-Raman spectra recorded at 1064 nm led to very useful and interesting information. Furthermore, the DFT calculations which are known to offer promise of obtaining accurate vibrational wavenumbers, were successfully used for the assignment of the vibrational spectra.

For the first time it has been possible to ascribe exactly the $\nu(\text{RhC})$ stretching mode in the vinylidene rhodium(I) complex $\textit{trans}\text{-}[\text{RhF}(=\text{C}=\text{CH}_2)(\text{PiPr}_3)_2]$ by using isotopic substitution, in conjunction with theoretical calculations. This is also true for the complexes $\textit{trans}\text{-}[\text{RhF}(\text{CO})(\text{PiPr}_3)_2]$, $\textit{trans}\text{-}[\text{RhF}(\text{C}_2\text{H}_4)(\text{PiPr}_3)_2]$, $\textit{trans}\text{-}[\text{RhX}(=\text{C}=\text{CHPh})(\text{PiPr}_3)_2]$ ($\text{X} = \text{F}, \text{Cl}, \text{Br}, \text{I}, \text{Me}, \text{PhC}\equiv\text{C}$) and $\textit{trans}\text{-}[\text{RhX}(\text{CN-2,6-xylyl})(\text{PiPr}_3)_2]$ ($\text{X} = \text{F}, \text{Cl}, \text{Br}, \text{I}, \text{C}\equiv\text{CPh}$). In addition, the comparison between the $\nu(\text{RhC})$ wavenumbers of the complexes $\textit{trans}\text{-}[\text{RhF}(=\text{C}=\text{CH}_2)(\text{PiPr}_3)_2]$ and $\textit{trans}\text{-}[\text{RhF}(\text{CO})(\text{PiPr}_3)_2]$, containing the isoelectronic ligands $\text{C}=\text{CH}_2$ and CO , which have the same reduced mass, indicated that the Rh-C bond is stronger in the carbonyl than in the vinylidene complex. Besides, the $\nu(\text{RhF})$ stretching mode,

which has been observed at higher wavenumbers in the FT-Raman and -IR spectra of *trans*-[RhF(CO)(PiPr₃)₂], showed that the carbonyl ligand is a better π -acceptor and a less effective σ -donor than the vinylidene one. Moreover, the comparison of the $\nu(\text{C}\equiv\text{C})$ and $\nu(\text{Rh}-\text{C})$ modes from the FT-Raman spectrum of the complexes *trans*-[Rh(C \equiv CPh)(L)(PiPr₃)₂] (L = C=CHPh, CO, CN-2,6-xylyl) point out that the π -acceptor ability of the ligand *trans* to C \equiv CPh should rise in the order C=CH₂ < CO < CN-2,6-xylyl \leq C=CHPh.

The investigated sensitivity of the $\nu(\text{RhC})$, $\nu(\text{CC})$, $\nu(\text{CO})$ and $\nu(\text{CN})$ vibrational modes to the electronic modifications occurring in the vinylidene, carbonyl, ethylene and isonitrile complexes, should allow in the future the examination of the π -acceptor or π -donor properties of further ligands. Likewise, we were able to characterize the influence of various X ligands on the RhC bond by using the $\nu(\text{RhC})$ stretching mode as a probe for the weakening of this. The calculated wavenumbers of the $\nu(\text{RhC})$ for the vinylidene complexes *trans*-[RhX(=C=CHR)(PiPr₃)₂], where R = H or Ph, suggested that the strength of the Rh=C bond increases along the sequence X = C \equiv CPh < CH₃ < I < Br < Cl < F. For the series of carbonyl compounds *trans*-[RhX(CO)(PiPr₃)₂], where X = F, Cl, Br and I, analogous results have been obtained and confirmed from the model compounds *trans*-[RhX(CO)(PMe₃)₂].

Since, the calculated vibrational modes for the ethylene complex *trans*-[RhF(C₂H₄)(PiPr₃)₂] were in good agreement with the experimental results and supported the description of this complex as a metallacyclopropane, we were interested in getting more information upon this class of compounds. In this context, we have recorded the FT-Raman and -IR spectra of the thioaldehyde complexes *mer*-[W(CO)₃(dmpe)(η^2 -S=CH₂)] and *mer*-[W(CO)₃(dmpe)(η^2 -S=CD₂)] which have been synthesized by **B-3**. The positions of the different WL vibrational modes anticipated by the DFT calculations, were consistent with the experimental results. Indeed, the analysis of the band shifts in the FT-Raman and -IR spectra of the isotopomer *mer*-[W(CO)₃(dmpe)(η^2 -S=CD₂)] confirmed our assignment. The different stereoisomers of complex *mer*-[W(CO)₃(dmpe)(η^2 -S=CH₂)] were investigated too, since RMN and IR-data have shown that complex *mer*-[W(CO)₃(dmpe)(η^2 -S=CH₂)] lead in solution to an equilibrium.

Since the information on the vibrational spectra of the molybdenum and tungsten complexes Cp(CO)₂M-PR₂-X (M = Mo, W; R = Me, *t*Bu, Ph; X = S, Se) is very scarce, we extended our research work to this class of compounds. We have tried to elucidate the bonding properties in these chalcogenoheterocycle complexes by taking advantage of the mass effect on the different metal atoms (W vs. Mo). Thus, the observed band shifts allowed to assign most of the ML fundamental modes of these complexes. This project and the following one were a cooperation within the work-group **B-2**.

The Raman and IR spectra of the matrix isolated photoproducts expected by the UV irradiation of the iron silyl complex $\text{Cp}(\text{CO})_2\text{FeSiH}_2\text{CH}_3$ have been already reported by Claudia Fickert and Volker Nagel in their PhD-thesis. Since no exact assignment was feasible for these spectra, we were interested in the study of the reaction products created by irradiation of the carbonyl iron silyl complex $\text{Cp}(\text{CO})_2\text{FeCH}_2\text{SiH}_3$. Although the calculated characteristic vibrational modes of the metal ligand unit for the various photoproducts are significantly different in constitution, they are very similar in wavenumbers, which did not simplify their identification. However, the theoretical results have been found to be consistent with the earlier experimental results.

Finally, the last part of this thesis has been devoted to the $(2\text{-Py})_2\text{E}^-$ anions which exhibit a high selectivity toward metal-coordination. All di(2-pyridyl) amides and -phosphides which were synthesized by **D-4**, coordinate the R_2Al^+ fragment via both ring nitrogen atoms. This already suggests that the charge density in the anions is coupled into the rings and accumulated at the ring nitrogen atoms, but the Lewis basicity of the central nitrogen atom in $\text{Et}_2\text{Al}(2\text{-Py})_2\text{N}$ is still high enough to coordinate a second equivalent AlEt_3 to form the Lewis acid base adduct $\text{Et}_2\text{Al}(2\text{-Py})_2\text{NAlEt}_3$. Due to the higher electronegativity of the central nitrogen atom in $\text{Me}_2\text{Al}(2\text{-Py})_2\text{N}$, $\text{Et}_2\text{Al}(2\text{-Py})_2\text{N}$ and $\text{Et}_2\text{Al}(2\text{-Py})_2\text{NAlEt}_3$, compared to the bridging two coordinated phosphorus atom in $\text{Me}_2\text{Al}(2\text{-Py})_2\text{P}$ and $\text{Et}_2\text{Al}(2\text{-Py})_2\text{P}$, the di(2-pyridyl)amide is the hardest Lewis base. In the phosphides merely all charge density couples into the rings leaving the central phosphorus atom only attractive for soft metals. These results were confirmed by using DFT and MP2 calculations. Moreover, a similar behaviour has been observed and described for the benzothiazolyl complex $[\text{Me}_2\text{Al}\{\text{Py}(\text{Bth})\text{P}\}]$, where complementary investigations are to be continued.

The DFT calculations carried out on the model compounds analysed in these studies supply very accurate wavenumbers and molecular geometries, these being in excellent agreement with the experimental results obtained from the corresponding isolated complexes.

Zusammenfassung

Die vorliegende Arbeit wurde im Rahmen des Sonderforschungsbereichs **347** „Selektive Reaktionen Metall-aktivierter Moleküle“ im Teilprojekt **C-2** (Prof. W. Kiefer) „Laserspektroskopie zur Charakterisierung der Struktur und Dynamik Metall-gebundener Moleküle“ durchgeführt. Diese befaßt sich mit den Infrarot- und Raman-spektroskopischen Untersuchungen an Übergangsmetallverbindungen, die in den Teilprojekten **B-2** (Prof. W. Malisch), **B-3** (Prof. W. A. Schenk), **D-1** (Prof. H. Werner), **D-4** (Prof. D. Stalke) synthetisiert wurden. Durch den Einsatz der FT-Raman-Spektroskopie mit langwelliger Laseranregung im NIR-Bereich und zum Teil von isotopenmarkierten Molekülen konnten aussagekräftige Spektren erhalten werden. Die Dichtefunktionaltheorie stellte sich als geeignetes Mittel zur Vorhersage und Interpretation der Schwingungsspektren heraus. Abhängig von der Größe der betrachteten Komplexe waren jeweils Rechnungen nötig, die auf sehr unterschiedlichen theoretischen Niveaus basierten.

Zum ersten Mal wurde mit Hilfe der Isotopenmarkierung und der Dichtefunktionaltheorie die Valenzschwingung $\nu(\text{Rh}=\text{C})$ in *trans*- $[\text{RhF}(\text{L})(\text{PiPr}_3)_2]$ ($\text{L} = \text{C}=\text{CH}_2$, $^{13}\text{C} = ^{13}\text{CH}_2$) charakterisiert. Diese zeigte sich als eine starke Raman-Bande und konnte ebenfalls im *trans*- $[\text{RhF}(\text{CO})(\text{PiPr}_3)_2]$ identifiziert werden. Darüber hinaus erkannte man beim Vergleich von *trans*- $[\text{RhF}(^{13}\text{C} = ^{13}\text{CH}_2)(\text{PiPr}_3)_2]$ und *trans*- $[\text{RhF}(\text{CO})(\text{PiPr}_3)_2]$ eine Verschiebung nach höheren Wellenzahlen der Valenzschwingung $\nu(\text{RhC})$ für den Carbonyl-Komplex. Einerseits haben beide Liganden $^{13}\text{C} = ^{13}\text{CH}_2$ und CO die gleiche reduzierte Masse, was die elektronische Natur der $\nu(\text{RhC})$ -Verschiebung zeigt, welche eine Verstärkung der RhC-Valenzkraftkonstanten im Fall des Carbonyls belegt. Andererseits weist die Verschiebung der $\nu(\text{RhF})$ -Streckschwingung nach höheren Wellenzahlen im Carbonyl-Komplex für deren Ligand bessere π -Akzeptor- und schlechtere σ -Donor-Eigenschaften gegenüber dem Vinyliden auf. Durch die aus solchen Untersuchungen gewonnenen $\nu(\text{RhC})$ - und $\nu(\text{C}\equiv\text{C})$ -Verschiebungen in den verschiedenen untersuchten Komplexen ergibt sich die folgende Reihe abnehmender π -Akzeptorstärke: $\text{C}=\text{CHPh} \geq \text{CN-2,6-xylyl} > \text{CO} > \text{C}=\text{CH}_2$.

Die Empfindlichkeit der Valenzschwingungen $\nu(\text{RhC})$, $\nu(\text{CC})$, $\nu(\text{CO})$ und $\nu(\text{CN})$ gegenüber Veränderungen der elektronischen Verhältnisse in Vinylidene-, Carbonyl-, Ethylene- und Isonitrile-Komplexen läßt sich ihrerseits als „Sonde“ zur Untersuchung der π -Akzeptor- bzw. π -Donor-Eigenschaften anderer Liganden nutzen.

Die Beeinflussung, vor allem die Schwächung der RhC-Bindung durch einen *trans*-ständigen Liganden konnte dadurch an den Komplexen *trans*- $[\text{RhX}(^{13}\text{C} = ^{13}\text{CH}_2)(\text{PiPr}_3)_2]$ ($\text{X} = \text{F}, \text{Cl}, \text{Br}$,

I), *trans*-[RhX(C=CHPh)(PiPr₃)₂] (X = F, Cl, Br, I, Me, PhC≡C), *trans*-[RhX(CO)(PiPr₃)₂] (X = F, Cl, Br, I, PhC≡C) und *trans*-[RhX(CN-2,6-xylyl)(PiPr₃)₂] (X = F, Cl, Br, I, PhC≡C) untersucht werden. Die FT-Raman Spektroskopie zeigte sich als eine nützliche Methode zur Untersuchung des Trans-Einflusses. MO- und NBO-Berechnungen waren dabei sehr hilfreich, um diesen Effekt zu charakterisieren.

Eine weitere Substanzklasse der hier untersuchten Übergangsmetallverbindungen stellen die verschiedenen Molybden- und Wolframkomplexe dar, die in den Teilprojekten **B-3** und **B-2** synthetisiert wurden. In diesem Zusammenhang wurden die FT-Raman- und -IR-Spektren von den polykristallinen Thioaldehyd-Komplexen *mer*-[W(CO)₃(dmpe)(η²-S=CR₂)] (R = H, D) aufgenommen und mit Dichtefunktionalrechnungen verglichen. Die Isotopenmarkierung lieferte eine klare Zuordnung der ν(WC) und ν(CS) Valenzstretschwingungen, welche den partialen CS-Doppelbindungscharakter in diesen Verbindungen zeigte. Zudem konnte eine vollständige Analyse dieser Komplexe mit Hilfe der DFT-Rechnungen erlangt werden. NMR- und IR-Daten zeigten, daß bei einer Lösung von *mer*-[W(CO)₃(dmpe)(η²-S=CH₂)] ein Gleichgewicht stattfindet. Infolgedessen wurden die Energien der unterschiedlichen Stereo-Isomere von *mer*-[W(CO)₃(dmpe)(η²-S=CH₂)] untersucht, welche in sehr guter Übereinstimmung mit dem experimentellen Befund standen.

Die Umsetzung der Phosphenium-Komplexe Cp(CO)₂M=PR₂ (M = W, Mo; R = *t*Bu, Ph) mit Schwefel oder Selen lieferte entsprechende stabile [2+1]-Cycloaddukte in guten bis sehr guten Ausbeuten. FT-Ramanspektren von solchen Verbindungen wurden auf der Basis von Dichtefunktionalrechnungen aufgenommen und diskutiert. Diese Untersuchungen fanden in Zusammenarbeit mit Teilprojekt B-2 statt und hatten die Aufklärung der Bindungseigenschaften des Dreirings in diesen Komplexen zum Ziel. Die wichtigsten ν(M-L) Valenzschwingungen konnten ebenso charakterisiert werden.

Bei der UV-Bestrahlung von Cp(CO)₂FeSiH₂Me und Cp(CO)₂FeCH₂SiH₃ sind verschiedene Photoprodukte bzw. Intermediate zu erwarten. In den Dissertationen von Claudia Fickert und Volker Nagel sind Veränderungen an den Raman- bzw. IR-Spektren der UV-Bestrahlungsexperimente der matrixisolierten Substanzen vorgestellt und diskutiert worden. Dabei wurde die α-H-Umlagerung nach photochemischer Decarbonylierung als stabilstes Intermediat postuliert. Jedoch konnten keine eindeutigen Aussagen getroffen werden. Aufgrund dessen wurde die theoretische photochemisch induzierte Decarbonylierung und anschließenden Umlagerungen von Cp(CO)₂FeSiH₂Me und Cp(CO)₂FeCH₂SiH₃ mit Hilfe der Dichtefunktionaltheorie behandelt und in einem Kapitel der vorliegenden Dissertation dargestellt.

Im letzten Teil dieser Arbeit wurden Raman-Spektren und quantenchemische Rechnungen an Di(2-Pyridyl)systemen durchgeführt, die im Teilprojekt D-4 synthetisiert wurden. Die Py_2E^- -Anionen weisen eine außergewöhnliche Selektivität bezüglich der Metallkoordination auf. Um geeignete Vorläufermoleküle zur Darstellung dünner III/V-Schichten mittels MOCVD-Experimente darzustellen, wurde Py_2NH und Py_2PH mit Et_3Al bzw. Me_3Al umgesetzt. Ein deutlicher Unterschied zwischen Amid und Phosphid ist in der Reaktivität gegenüber einem weiteren Lewis-säuren Äquivalent Et_3Al bzw. Me_3Al zu erkennen. Das bivalente amidische Stickstoffatom ist im Gegensatz zum Phosphoratom zu einer weiteren Koordination befähigt, was mittels DFT- und MP2-Rechnungen belegt wurde. Der $\text{Py}(\text{Bth})\text{P}$ -Ligand in $[\text{Me}_2\text{Al}\{\text{Py}(\text{Bth})\text{P}\}]$ kann als doppelter Hart/Weich-Chelatligand bezeichnet werden. Das Me_2Al^+ -Fragment koordiniert über die „harte Seite“ des Liganden (den Pyridylstickstoffatomen), während die „weiche Seite“ als P-S-Chelatligand weiterhin in der Lage sein sollte, weiche Übergangsmetallkomplexfragmente $[\text{M}]$ zu stabilisieren. Diese Verbindung wurde zum Teil mit den obengenannten Methoden charakterisiert und sollte in weiter untersucht werden.

Die durchgeführten DFT-Rechnungen lieferten nicht nur eine Möglichkeit der Interpretation von Schwingungsspektren, sondern erlaubten auch den Vergleich berechneter Molekülgeometrien mit Daten von Kristallstrukturanalysen und lieferten wichtige Antworten zu verschiedenen Problemstellungen.

References

- [1] M. S. Gordon, T. R. Cundari, *Coord. Chem. Rev.*, **1996**, 147, 87.
- [2] Z. Lin, H. B. Hall, *Coord. Chem. Rev.*, **1993**, 123, 149.
- [3] T.V. Russo, R. L. Martin, P. J. Hay, *J. Phys. Chem.*, 1995, 99, 17085.
- [4] C. Van Wüllen, *Int. J. Quantum Chem.*, **1996**, 58, 147.
- [5] I. Bytheway, G. B. Bacskay, N. S. Hush, *J. Phys. Chem.*, **1996**, 100, 6023.
- [6] G. Frenking, I. Antes, M. Böhme, S. Dapprich, A. W. Ehlers, V. Jonas, A. Neuhaus, M. Otto, R. Stegmann, A. Veldkamp and S. F. Vyboishchikov, in *Reviews in Computational Chemistry*, eds. K. B. Lipkowitz and D. B. Boyd, VCH, New York, 1996, vol. 8.
- [7] I. Antes and G. Frenking, *Organometallics*, **1995**, 14, 4263.
- [8] B. Schrader, (Editor) *Infrared and Raman Spectroscopy*, VCH-Verlagsgesellschaft, Weinheim 1995.
- [9] J. Weidlein, U. Müller, K. Dehnicke, *Schwingungsspektroskopie*, 2. überarbeitete Auflage, Georg Thieme Verlag Stuttgart, New-York, 1988.
- [10] T. Hirschfeld and B. Chase, *Appl. Spectrosc.* **1986**, 40, 133.
- [11] S. F. Parker, K. P. J. Williams, P. J. Hendra and A. J. Turner, *Appl. Spectrosc.*, **1988**, 42, 796.
- [12] P. B. Fellgett, *Infrared Phys.*, **1984**, 24, 95.
- [13] P. Jacquinot, *J. Opt. Soc. Am.* **1954**, 44, 761; P. Jacquinot, *Infrared Phys.*, **1984**, 24, 99.
- [14] D. C. Champeney, *Fourier Transforms and their Physical Applications*, Academic Press, London, 1973.
- [15] A. G. Marshall and F. R. Verdun, *Fourier Transforms in NMR, Optical and Mass Spectroscopy*, Elsevier, Amsterdam, 1990.
- [16] L. H. Thomas, *Proc. Camb. Phil. Soc.*, **1927**, 23, 542.
- [17] E. Fermi, *Rend. Accad., Lincei*, **1927**, 6, 602.
- [18] E. Fermi, *Z. Phys.*, **1928**, 48, 73.
- [19] P. A. M. Dirac, *Cambridge Philos. Soc.*, **1930**, 26, 376.
- [20] E. P. Wigner, *Phys. Rev.*, **1934**, 46, 1002.
- [21] J. C. Slater, *Phys. Rev.*, **1951**, 81, 385.
- [22] P. Hohenberg and W. Kohn, *Phys. Rev. A*, **1964**, 136, 864.
- [23] M. Levy, *Proc. Natl. Acad. Sci. U.S.A.*, **1979**, 76, 6062.
- [24] W. Kohn, L. Sham, *J. Phys. Rev. A*, **1965**, 140, 1133.
- [25] F. Jensen, *Introduction to computational Chemistry*, Eds. John Wiley & Sons, New York, 1999.
- [26] P. M. W. Gill, *Density Functional Theory (DFT), Hartree-Fock (HF), and the Self-consistent Field*, in *The Encyclopedia of Computational Chemistry*, P. v. R. Schleyer, N. L.

Allinger; T. Clark, J. Gasteiger, P. A. Kollman, H. F. Schaefer III, P. R. Schreiner, Eds. John Wiley & Sons, Chichester, 1998.

[27] K. Balasubramanian, *Relativistic Effective Core Potential Techniques for Molecules Containing Very Heavy Atoms*, in The Encyclopedia of Computational Chemistry, P. v. R. Schleyer, N. L. Allinger; T. Clark, J. Gasteiger, P. A. Kollman, H. F. Schaefer III, P. R. Schreiner, Eds. John Wiley & Sons, Chichester, 1998.

[28] P. Schwerdtfeger, M. Seth, *Relativistic Effects of the Superheavy Elements*, in The Encyclopedia of Computational Chemistry, P. v. R. Schleyer, N. L. Allinger; T. Clark, J. Gasteiger, P. A. Kollman, H. F. Schaefer III, P. R. Schreiner, Eds. John Wiley & Sons, Chichester, 1998.

[29] M. I. Bruce and A. G. Swincer, *Adv. Organomet. Chem.*, **1983**, 22, 59. H. Werner, *Angew. Chem.*, **1990**, 102, 1109.

[30] V. Jonas, W. Thiel, *J. Chem. Phys.*, **1995**, 102, 8474;

[31] V. Jonas, W. Thiel, *J. Chem. Phys.*, **1996**, 105, 3636.

[32] K. Nakamoto, *Infrared and Raman Spectra of Inorganic and Coordination Compounds*, John Wiley & Sons, 1986.

[33] S.-C. Chang, R. H. Hauge, Z. H. Kafafi, J. L. Margrave, W. E. Billups, *J. Am. Chem. Soc.*, **1988**, 110, 7975.

[34] E. Diana, O. Gambino, R. Rossetti, P. L. Stanghellini, T. Albiez, W. Bernhardt, H. Vahrenkamp, *Spectrochim. Acta*, **1993**, 49A, 1247.

[35] C. E. Anson, N. Sheppard, D. B. Powell, J. R. Norton, W. Fischer, R. L. Keiter, B. F. G. Johnson, J. Lewis, A. K. Bhattacharya, S. A. R. Knox, M. L. Turner, *J. Am. Chem. Soc.*, **1994**, 116, 3058.

[36] E. O. Fischer, Nguyen Quy Dao, W. R. Wagner, *Angew. Chem.*, **1978**, 90, 51. *Angew. Chem. Int. Ed. Engl.*, **1978**, 17, 50.

[37] G. R. Clark, K. Marsden, W. R. Roper, L. J. Wright, *J. Am. Chem. Soc.*, **1980**, 102, 6570.

[38] Nguyen Quy Dao, E. O. Fischer, T. L. Lindner, *J. Organomet. Chem.*, **1981**, 209, 323.

[39] Nguyen Quy Dao, H. Fevrier, M. Jouan, E. O. Fischer, W. Röhl, *J. Organomet. Chem.*, **1984**, 275, 191.

[40] J. K. Manna, R. J. Kuk, R. F. Dallinger, M. D. Hopkins, *J. Am. Chem. Soc.*, **1994**, 116, 9793.

[41] M. Barnes, D. A. Gillet, A. J. Merer, G. F. Metha, *J. Chem. Phys.*, **1996**, 105, 6168.

[42] R. M. Sosa, P. Gardiol, G. Beltrame, *Int. J. Quantum. Chem.*, **1998**, 69, 371.

[43] W. D. Jones and E. T. Hessell, *Organometallics*, **1990**, 9, 719.

[44] P. M. Boorman, P. J. Craig, T. W. Swaddle, *Can. J. Chem.*, **1970**, 48, 838.

[45] D. Steinborn, M. Ludwig, *J. Organomet. Chem.*, **1993**, 463, 65.

[46] T. G. Appleton, H. C. Park and L. E. Manzer, *Coord. Chem. Rev.*, **1973**, 10, 335.

[47] W. A. Nugent and J. M. Mayer, *Metal Ligand Multiple Bonds*, Wiley-Interscience, New York, 1988.

-
- [48] H. L. M. Van Gaal and F. L. A. Van Den Bekerom, *J. Organomet. Chem.*, **1977**, *134*, 237.
- [49] J. K. Burdett and T. A. Albright, *Inorg. Chem.*, **1979**, *18*, 2112.
- [50] E. M. Shustorovich, M. A. Porai-Koshits and Y. A. Busalev, *Coord. Chem. Rev.*, **1975**, *17*, 1.
- [51] P. D. Lyne and D. M. P. Mingos, *J. Organomet. Chem.*, **1994**, *478*, 141; *J. Chem. Soc., Dalton Trans.*, **1995**, 1635.
- [52] N. Kaltsoyannis and P. Mountford, *J. Chem. Soc., Dalton Trans.*, **1999**, 781.
- [53] B. Callejas-Gaspar, PhD-Thesis, Universität Würzburg, 2002
- [54] Gaussian 98, Revision A7, M. J. Frisch, G. W. Trucks, H. B. Schlegel, P. M. W. Gill, B. G. Johnson, M. A. Robb, J. R. Cheeseman, T. Keith, G. A. Petersson, J. A. Montgomery, K. Rhaghavachari, M. A. Al-Laham, V. G. Zakrzewski, J. V. Ortiz, J. B. Foresman, J. Ciolowski, B. B. Stefanov, A. Nanayakkara, M. Challacombe, C. Y. Peng, P. Y. Ayala, W. Chen, M. W. Wong, J. L. Andres, E. S. Replogle, R. Gomberts, R. L. Martin, D. J. Fox, J. S. Binkley, D. J. Defrees, J. Baker, J. P. Stewart, M. Head-Gordon, C. Gonzalez & J. A. Pople; Gaussian inc., Pittsburg PA, 1998.
- [55] A. D. Becke, *Phys. Rev.*, **1988**, *A38*, 3098.
- [56] J. P. Perdew, Y. Wang, *Phys. Rev.*, **1992**, *B45*, 13244.
- [57] P. J. Hay, W. R. Wadt, *J. Chem. Phys.*, **1985**, *82*, 270.
- [58] W. R. Wadt, P. J. Hay, *J. Chem. Phys.*, **1985**, *82*, 284.
- [59] P. J. Hay, W. R. Wadt, *J. Chem. Phys.*, **1985**, *82*, 299.
- [60] T. H. Jr. Dunning, P. J. Hay, in *Modern Theoretical Chemistry*, Ed. H.F. Schaefer III, Plenum: New York, 1976.
- [61] D. Andrae, U. Haeussermann, M. Dolg, H. Stoll, H. Preuss, *Theor. Chim. Acta*, **1990**, *77*, 123.
- [62] The calculated structures are represented with POV-Ray (www.povray.org) using the ORTEP program as input files. C. K. Johnson, ORTEP, Report ORNL-5138, Oak Ridge National Laboratory, Oak Ridge, TN, 1976.
- [63] H. Werner, F. J. Garcia Alonso, H. Otto, J. Wolf, *Z. Naturforsch.*, **1988**, *B43*, 722
- [64] A. Wierzbicki, E. A. Salter, N. W. Hoffman, E. D. Stevens, L. Van Do, M. S. VanLoock, F. D. Madura, *J. Phys. Chem.*, **1996**, *100*, 11250.
- [65] J-C. Choi, K. Osakada, T. Yamamoto, *Organometallics*, **1998**, *17*, 3044.
- [66] J. van Slageren, A. L. Vermeer, D. J. Stufkens, M. Lutz, A. L. Spek, *J. Organomet. Chem.*, **2001**, *626*, 118.
- [67] R. S. Mulliken, *J. Chem. Phys.*, **1955**, *23*, 1833.
- [68] A. E. Reed, R. B. Weinstock and F. Weinhold, *J. Chem. Phys.*, **1985**, *82*(2), 735.
- [69] C. Cauletti, F. Grandinetti, G. Granozzi, M. Casarin, H. Werner, J. Wolf, A. Höhn and F. J. García Alonso, *J. Organomet. Chem.*, **1990**, *382*, 445.

-
- [70] (a) R. Brady, B. R. Flynn, G. L. Geoffroy, H. B. Gray, J. Peone and L. Vaska, *Inorg. Chem.*, **1976**, *15*, 1485; (b) G. L. Geoffroy, H. Isci, J. Litrenti and W. R. Mason, *Inorg. Chem.*, **1977**, *16*, 1950.
- [71] H. Kunkely and A. Vogler, *J. Organomet. Chem.*, **1999**, *577*, 358.
- [72] P. Klaboe, *Spectrochim. Acta.*, **1970**, *26A*, 87.
- [73] R. R. Holmes, G. T. Fey, R. H. Larkin, *Spectrochim. Acta.*, **1973**, *29A*, 665.
- [74] <http://www.aist.go.jp/RIODB/SDBS/menu-e.html>; IR of phenylacetylene SDBS No: 1444; CAS-Registry No: 536-74-3.
- [75] J. Browning, P. L. Goggin, R. J. Goodfellow, M. G. Norton, J. M. A. Rattray, B. F. Taylor, J. Mink, *J. Chem. Soc. Dalton*, **1977**, 2061.
- [76] (a) L. Vaska and J. Peone, *J. Chem. Soc., Chem. Commun.*, **1971**, 418. (b) Yu. S. Varshavskii, M. M. Singh, N. A. Buzina, *Zh. Neorg. Khim.*, **1971**, *16*, 1372.
- [77] Half wave reduction potentials: G. Schiavon, S. Zecch, G. Pilloni, M. Martelli, *J. Inorg. Nucl. Chem.*, **1977**, *39*, 115. Equilibrium constants for halide exchange: (a) F. Araghizadeh, D. M. Branan, N. W. Hoffman, J. H. Jones, E. A. McElroy, N. C. Miller, D. L. Ramage, A. Battaglia Salazar, S. H. Young, *Inorg. Chem.*, **1988**, *27*, 3752. (b) D. M. Branan, N. W. Hoffman, E. A. McElroy, N. C. Miller, D. L. Ramage, A. F. Schott, S. H. Young, *Inorg. Chem.*, **1987**, *26*, 2915.
- [78] M. Tilst, J.-R. Hamon and P. Hamon, *Chem. Commun.*, **1998**, 765.
- [79] J. T. Poulton, M. P. Sigalas, K. Folting, W. E. Streib, O. Eisenstein and K. G. Caulton, *Inorg. Chem.*, **1994**, *33*, 1476.
- [80] F. Abu-Hasanayn, A. S. Goldman and K. Krogh-Jespersen, *Inorg. Chem.*, **1994**, *33*, 5122.
- [81] J. P. Flemming, M. C. Pilon, O. Ya. Borbulevitch, M. Yu. Antipin and V. V. Grushin, *Inorg. Chim. Acta*, **1998**, *280*, 87.
- [82] K. G. Caulton, *New. J. Chem.*, **1994**, *18*, 25.
- [83] G. Frenking and N. Fröhlich, *Chem. Rev.*, **2000**, *100*, 717.
- [84] H. Werner, R. Wiedemann, P. Steinert, J. Wolf, *Chem. Eur. J.*, **1997**, *1*, 127.
- [85] M. J. Grogan and K. Nakamoto, *J. Am. Chem. Soc.*, **1966**, *88*, 5454.
- [86] J. P. Sorzano and J. P. Fackler, *J. Mol. Spectrosc.*, **1967**, *22*, 80.
- [87] J. Hiraishi, *Spectrochim. Acta*, **1969**, *25A*, 749.
- [88] É. Bencze, I. Pápai, J. Mink, P. L. Goggin, *J. Organomet. Chem.*, **1999**, *584*, 118.
- [89] M. J. S. Dewar, *Bull. Soc. Chim. Fr.*, **1951**, *18*, C79.
- [90] J. Chatt, L. A. Duncanson, *J. Chem. Soc.*, **1953**, 2929.
- [91] J. Gil-Rubio, B. Weberndörfer, H. Werner, *J. Chem. Soc., Dalton Trans.*, **1999**, 1437.
- [92] C. Bussetto, A. D'Alfonso, F. Maspero, G. Perego, A. Zazzetta, *J. Chem. Soc., Dalton Trans.*, **1977**, 1828.
- [93] H. L. M. Van Gaal and F. L. A. Van Den Bekerom, *J. Organomet. Chem.*, **1977**, *134*, 237.

-
- [94] (a) F. R. Dollish, W. G. Fateley, F. F. Bentley, *Characteristic Raman Frequencies of Organic Compounds*, John Wiley & Sons, New York, 1974, (b) D. Lin-Vien, N. B. Colthup, W. G. Fateley, J. G. Grasselli, *The Handbook of Infrared and Raman Characteristic Frequencies of Organic Molecules*, Academic Press, Inc., New York, 1991, (c) N. B. Colthup, L. H. Daly, S. E. Wiberley, *Introduction to Infrared and Raman Spectroscopy*, 3rd Ed., Academic Press, New York, 1990.
- [95] D. M. Adams, *Metal-ligand and related vibrations*, Edward Arnold and Co., London, 1967.
- [96] R. W. Stephany, Thesis, Utrecht, 1973.
- [97] F. A. Cotton, F. Zingales, *J. Am. Chem. Soc.*, **1961**, 83, 351.
- [98] W. P. Griffith, A. J. Wickam, *J. Chem. Soc.*, **1969**, A, 834.
- [99] P. Fantucci, V. Valenti, F. Cariati, *Inorg. Chim. Acta*, **1971**, 5, 425.
- [100] W. J. Cherwinski, H. C. Clark, L. E. Manzer, *Inorg. Chem.*, **1972**, 11, 1511.
- [101] H. C. Clark, L. E. Manzer, *Inorg. Chem.*, **1972**, 11, 503.
- [102] W. D. Jones, E. T. Hessell, *Organometallics*, **1990**, 9, 718.
- [103] C. R. Landis, S. Feldgus, J. Uddin, C. E. Wozniak, K. G. Moloy, *Organometallics*, **2000**, 23, 4878.
- [104] Ma. C. Castro-Pedrozo and G. W. King, *J. Mol. Spectrosc.*, **1978**, 73, 386.
- [105] D. N. Shingh, J. S. Singh and R. A. Yadav, *J. of Raman Spect.*, **1997**, 28, 355.
- [106] J. Higgins, X. Zhou, R. Liu, *Spectrochim. Acta Part A*, **1997**, 53, 721.
- [107] I. N Juchnovski, J. A. Tsenov, *Spectrosc. Lett.*, **1995**, 28(2), 211.
- [108] R. A. Nalepa, J. D. Laposa, *J. Mol. Spectrosc.*, **1974**, 50, 10 6.
- [109] E. B. Wilson, *Phys. Rev.*, **1934**, 45, 706.
- [110] S.T. Belt, S. B. Duckett, D. M. Haddleton, R. N. Perutz, *Organometallics*, **1989**, 8, 748.
- [111] J. C. A. Boeyens, N. J. Coville, K. S. Soldenhoff, *Afr. J. Chem.*, **1984**, 37, 153.
- [112] G. W. Harris, M. O. Albers, J. C. A. Boeyens, N. J. Coville, *Organometallics*, **1983**, 2,609.
- [113] G. W. Harris, J. C. A. Boeyens, N. J. Coville, *J. Organomet. Chem.*, **1983**, 255, 87.
- [114] B. Wolfsberger, PhD Thesis, Würzburg 2001-2002.
- [115] T. Kojima, *J. Phys. Soc. Jpn.*, **1960**, 15, 1284.
- [116] H. Fischer, K. H. Fluck, C. Troll, *Chem. Ber.*, **1992**, 125, 2675.
- [117] G. Davidson, C. L. Davies, *Inorg. Chim. Acta*, **1989**, 165, 231.
- [118] W. Kutzelnigg, *Angew. Chem.*, **1984**, 96, 262.
- [119] (a) H. Wallmeier, W. Kutzelnigg, *J. Am. Chem. Soc.*, **1979**, 101, 2804; (b) M. W. Schmidt, S. Yabushita, M. S. Gordon, *J. Phys. Chem.*, **1984**, 88, 382; (c) M. S. Gordon, J. A. Boatz, M. W. Schmidt, *J. Phys. Chem.*, **1984**, 88, 2998; (d) M. W. Schmidt, M. S. Gordon, *J. Am. Chem. Soc.*, **1985**, 107, 1922; (e) M. W. Schmidt, M. S. Gordon, *Can. J. Chem.*, 1985, 63, 1609.

-
- [120] T. Austad, T. Rød, K. Åse, J. Songstad, A. H. Norbury, *Acta Chem. Scand.*, **1973**, 27, 1939.
- [121] H. Rojhtalab, J. W. Nibler, C. J. Wilkins, *Spectrochim. Acta*, **1976**, 32A, 519.
- [122] J. Kincaid, K. Nakamoto, J. A. Tiethof, D. W. Meek, *Spectrochim. Acta*, **1974**, 30A, 2091.
- [123] J. Wan, C-G. Zhan, *Spectrochim. Acta*, **1995**, A51, 1665; J. R. Durig, K. K. Chatterjee, *Inorg. Chem.*, **1989**, 28, 298.
- [124] W. Schneider, W. Thiel, A. Komornicki, *J. Phys. Chem.*, **1988**, 92, 5611.
- [125] K. Jörg, PhD Thesis, Universität Würzburg, 1985.
- [126] R. D. Adams, D. M. Collins, F. A. Cotton, *Inorg. Chem.*, **1975**, 13, 1086.
- [127] R. J. Klinger, W. M. Butler, M. D. Curtis, *J. Am. Chem. Soc.*, **1978**, 100, 5034.
- [128] A. H. Cowley, N.C. Norman, S. Quashie, *J. Am. Chem. Soc.*, **1984**, 106, 5007.
- [129] K. Jörg, W. Malisch, W. Reich, A. Meyer, H. Schubert, *Angew. Chem.*, **1986**, 98, 103.
- [130] (a) S. Amann, PhD Thesis, universität Würzburg, 1989, (b) E. Fluck, G. Gonzalez, K. Peters, H.-G. von Schnering, *Z. Anorg. Allg. Chem.*, **1980**, 473, 51, (c) K. A. Kerr, P. M. Boormann, B. S. Misener, J. G. H. van Roode, *Can. J. Chem.*, **1977**, 55, 3081.
- [131] C. J. Wilkins, K. Hagen, L. Hedberg, Q. Shen, K. Hedberg, *J. Am. Chem. Soc.*, **1975**, 97, 6352.
- [132] T. Moritani, K. Kuchitsu, Y. Morino, *Inorg. Chem.*, **1971**, 10, 344.
- [133] Q. Williams, J. Sheridan, W. Gordy, *J. Chem. Phys.*, **1952**, 20, 164.
- [134] N. M. Agh-Atabay, J. L. Davidon, G. douglas, K. W. Muir, *J. Chem. Soc., Chem. Commun.*, **1987**, 1526.
- [135] L. Pauling, *Die Natur der chemischen Bindung*, Verlag Chemie, Weinheim, 1964.
- [136] G. J. Penny, G. M. Sheldrick, *J. Chem. Soc. A*, **1971**, 245.
- [137] unpublished results
- [138] C. Fickert, PhD Thesis, Universität Würzburg, 1998.
- [139] D. Lin-Vien, N. B. Colthup, W. G. Fateley, J. G. Grasselli, *The Handbook of Infrared and Raman characteristic Frequencies of organic molecules*, Academic Press, Inc. Hartcourt Brace Jovanovich, New York, 1991.
- [140] A. H. Cowley, J. L. Mills, *J. Am. Chem. Soc.*, **1969**, 91, 2911.
- [141] R. A. Chittenden, L. C. Thomas, *Spectrochim. Acta*, **1964**, 20, 1679.
- [142] D. M. Adams, *Metal-Ligand and related Vibrations*, Arnold, London 1967.
- [143] M. F. Guns, E. G. Claeys, G. P. Van der Kelen, *J. Mol. Struct.*, **1980**, 65, 3.
- [144] W. Malisch, K. Hindahl, H. Käß, J. Reising, W. Adam, F. Prechtel, *Chem. Ber.*, **1995**, 128, 963.
- [145] (a) D. A. Straus, S. D. Grumbine, T. D. Tilley, *J. Am. Chem. Soc.*, **1990**, 112, 7801. (b) S. D. Grumbine, T. D. Tilley, A. L. Rheingold, *J. Am. Chem. Soc.*, **1993**, 115, 358. (c) S. D. Grumbine, T. D. Tilley, F. P. Arnold, A. L. Rheingold, *J. Am. Chem. Soc.*, **1993**, 115, 7884. (d) S. K. Grumbine, T. D. Tilley, F. P. Arnold, A. L. Rheingold, *J. Am. Chem. Soc.*, **1994**,

116, 5495. (e) S. K Grumbine, T. D. Tilley, *J. Am. Chem. Soc.*, **1994**, *116*, 6951. (f) G. P. Mitchell, T. D. Tilley, *J. Am. Chem. Soc.*, **1997**, *119*, 11236. (g) J. D. Feldman, G. P. Mitchell, J.-O. Nolte, T. D. Tilley, *J. Am. Chem. Soc.*, **1998**, *120*, 11184. (h) G. P. Mitchell, T. D. Tilley, *J. Am. Chem. Soc.*, **1998**, *120*, 7635. (i) G. P. Mitchell, T. D. Tilley, *Angew. Chem., Int. Ed.*, **1998**, *37*, 2524. (j) S. K. Grumbine, G. P. Mitchell, D. A. Straus, T. D. Tilley, *Organometallics*, **1998**, *17*, 5607. (k) J. C. Peters, J. D. Feldman, T. D. Tilley, *J. Am. Chem. Soc.*, **1999**, *121*, 9871.

[146] (a) M. Denk, R. K. Hayashi, R. West, *J. Chem. Soc., Chem. Commun.*, **1994**, 33. (b) M. Denk, R. West, *Pure Appl. Chem.*, **1996**, *68*, 785.

[147] B. Gehrhus, P. B. Hitchcock, M. F. Lappert, H. Maciejewski, *Organometallics*, **1998**, *17*, 5599.

[148] J. M. Dysard, T. D. Tilley, *Organometallics*, **2000**, *23*, 4726.

[149] B. V. Mork, T. D. Tilley, *Abstr. Pap.-Am. Chem. Soc.*, **2001**, 221st INOR-628.

[150] P. W. Wanandi, P. B. Glaser, and T. D. Tilley, *J. Am. Chem. Soc.*, **2000**, *122*, 972.

[151] A. Haynes, M. W. George, M. T. Harward, M. Poliakoff, J. J. Turner, N. M. Boag, M. Green, *J. Am. Chem. Soc.*, **1991**, *113*, 2011.

[152] K. H. Pannell, T. Kobayashi, F. Cervantes-Lee, Y. Zhang, *Organometallics*, **2000**, *19*, 351.

[153] V. Nagel, C. Fickert, M. Hofmann, M. Vögler, W. Malisch, W. Kiefer, *J. Mol. Struct.*, **1999**, *480-481*, 511.

[154] C. Fickert, V. Nagel, W. Kiefer, S. Möller, H. Jehle, W. Malisch, R. Stowasser, G. Bringmann, *J. of Organomet. Chem.*, **1998**, *566*, 225.

[155] C. Fickert, R. Pıkl, D. Gernet, S. Möller, W. Malisch, W. Kiefer, *Fresenius J. Anal. Chem.*, **1996**, *355*, 340.

[156] R. J. Kazlauskas and M. S. Wrighton, *Organometallics*, **1982**, *1*, 602.

[157] W. Gerhartz, G. Ellerhorst, P. Dahler, P. Eilbracht, *Liebigs Ann. Chem.*, **1980**, 1296.

[158] S. Niu, M. Hall, *Chem. Rev.*, **2000**, *100*, 353.

[159] C. Peng and H. B. Schlegel, *Israel J. of Chem.*, **1993**, *33*, 449.

[160] Y. Chen, W. Petz, G. Frenking, *Organometallics*, **2000**, *19*, 2698.

[161] (a) R. S. Simons, C. A. Tessier, *Organometallics*, **1996**, *15*, 2610; (b) A. R. Howells, M. C. Milletti, *Inorg. Chim. Acta.*, **1993**, *203*, 43; (c) D. Braga, F. Grepioni, K. Biradha, G. R. Desiraju, *J. Chem. Soc., Dalton Trans.*, **1996**, *20*, 3925; (d) N. J. Fitzpatrick, M. A. McGinn, *J. Chem. Soc., Dalton Trans.*, **1985**, *8*, 1637; (e) J. C. Vites, G. Jacobsen, T. K. Dutta, T. P. Fehlner, *J. Am. Chem. Soc.*, **1985**, *107*, 5563; (f) B. E. Bursten, R. H. Cayton, *Organometallics*, **1986**, *5*, 1051.

[162] H. S. Gutowsky, J. Chen, P. J. Hajduk, J. D. Keen, C. Chuang, T. Emilsson, *J. Am. Chem. Soc.*, **1991**, *113*, 4747.

[163] H. S. Gutowsky, J. Chen, P. J. Hajduk, J. D. Keen, T. Emilsson, *J. Am. Chem. Soc.*, **1989**, *111*, 1901.

-
- [164] (a) B. K. Campion, R. H. Heyn, T. D. Tilley, *J. Am. Chem. Soc.*, **1988**, *110*, 7558. (b) B. K. Campion, R. H. Heyn, T. D. Tilley, A. L. Rheingol, *J. Am. Chem. Soc.*, **1993**, *115*, 5527.
- [165] T. S. Koloski, P. J. Carroll, D. H. Berry, *J. Am. Chem. Soc.*, **1990**, *112*, 6405.
- [166] M. Poliakoff, J. J. Turner, *J. Chem. Soc. Dalton*, **1973**, 1351; **1974**, 2276.
- [167] J. K. Burdett, J. J. Turner, in *Cryogenic Chemistry* (G. A. Ozin and M. Moskovits, Eds.), Wiley, London 1976.
- [168] S. C. Chang, Z. H. Kafafi, R. H. Hauge, W. E. Billups, J. L. Margrave, *J. Am. Chem. Soc.*, **1985**, *107*, 1447.
- [169] A. J. Tursi, E. R. Nixon, *J. Chem. Phys.*, **1970**, *52*, 1521.
- [170] for review see: a) P. J. Steel, *Coord. Chem. Rev.*, **1990**, *106*, 227, b) S. Trofimenko, *Prog. Inorg. Chem.*, **1986**, *34*, 115, c) E. C. Constable, P. J. Steel, *Coord. Chem. Rev.* **1989**, *93*, 205, d) P. J. Steel, *Coord. Chem. Rev.*, **1990**, *106*, 227, d) G. R. Newkome, *Chem. Rev.*, **1993**, *93*, 2067.
- [171] a) A. Steiner, D. Stalke, *J. Chem. Soc., Chem. Commun.*, **1993**, 444, b) A. Steiner, D. Stalke, *Organometallics*, **1995**, *14*, 2423.
- [172] H. Gornitzka, D. Stalke, *Eur. J. Inorg. Chem.*, **1998**, 311.
- [173] for review see: T. Kottke, D. Stalke, *Chem. Ber. / Rec.*, **1997**, *130*, 1365.
- [174] a) A. H. Cowley, R. A. Jones, *Angew. Chem.*, **1989**, *101*, 1235; *Angew. Chem., Int. Ed. Engl.*, **1989**, *28*, 1208, b) D. E. Heaton, R. A. Jones, K. B. Kidd, A. H. Cowley, C. M. Nunn, *Polyhedron*, **1988**, *7*, 1901, c) A. H. Cowley, R. A. Jones, *Polyhedron*, **1994**, *13*, 1149, d) W. E. Buhro, *Polyhedron*, **1994**, *13*, 1131.
- [175] a) R. A. Howie, G. Izquierdo, G. P. McQuillan, *Inorg. Chim. Acta*, **1983**, *72*, 165, b) A. J. Blake, S. Parsons, J. M. Rawson, R. E. P. Winpenny, *Polyhedron*, **1995**, *14*, 1895, c) X. M. Wang, H. S. Sun, X. Z. Yu, *Polyhedron*, **1996**, *15*, 3543, d) F. A. Cotton, L. M. Daniels, G. T. Jordan IV, C. A. Murillo, *Polyhedron*, **1998**, *17*, 589.
- [176] a) A. J. Deeming, M. B. Smith, *J. Chem. Soc. Dalton Trans.*, **1993**, 2041, b) L. M. Engelhardt, M. G. Gardiner, C. Jones, P. J. Junk, C. L. Raston, A. J. White, *J. Chem. Soc., Dalton Trans.*, **1996**, 3053, c) W. Liu, A. Hassan, S. Wang, *Organometallics*, **1997**, *16*, 4257, d) G. B. Deacon, S. J. Faulks, B. M. Gatehouse, A. J. Jozsa, *Inorg. Chim. Acta*, **1997**, *21*, L1.
- [177] M. Pfeiffer, T. Stey, H. Jehle, B. Klüpfel, W. Malisch, V. Chandrasekhar, D. Stalke, *Chem. Commun.*, **2001**, 337.
- [178] S. Wagaw, S. L. Buchwald, *J. Org. Chem.* **1996**, *61*, 7240.
- [179] A. Haaland, *Angew. Chem.*, **1989**, *101*, 1017; V. Jonas, G. Frenking, M. T. Reetz, *J. Am. Chem. Soc.*, **1994**, *116*, 8741.
- [180] a) T. J. Hurley, M. A. Robinson, *Inorg. Chem.*, **1968**, *7*, 33, b) L. A. Oro, M. A. Ciriano, F. Viguri, *Inorg. Chim. Acta*, **1986**, *115*, 65, c) S. Aduldecha, B. Hathaway, *J. Chem. Soc., Dalton Trans.*, **1991**, *4*, 993.
- [181] W. Malisch, K. Thirase, J. Reising, *Z. Naturforsch.*, **1998**, *B 53*, 1084.

-
- [182] M. Pfeiffer, "Reaktivität und Koordinationsverhalten ambidenter Ligandensysteme", *PhD Thesis*, Universität Würzburg, **2000**.
- [183] a) R. Appel, F. Knoll, I. Ruppert, *Angew. Chem.*, **1981**, 93, 771; *Angew. Chem., Int. Ed. Engl.*, **1981**, 20, 731, b) R. Appel, F. Knoll, *Adv. Inorg. Chem.*, **1989**, 33, 259.
- [184] G. M. Sheldrick, W. S. Sheldrick, *J. Chem. Soc. A*, **1969**, 2279.
- [185] P. B. Hitchcock, H. A. Jasim, M. F. Lappert, H. D. Williams, *J. Chem. Soc., Chem. Commun.*, **1986**, 1634.
- [186] R. Kumar, S. J. de Mel, J. P. Oliver, *Organometallics*, **1989**, 8, 2488.
- [187] P. Rademacher in *Strukturen organischer Moleküle*, VCH, Weinheim, **1987**.
- [188] a) R. G. Vranka, E. L. Amma, *J. Am. Chem. Soc.*, **1967**, 89, 3121, b) S. K. Byram, J. K. Fawcett, S. C. Nyburg, R. J. O'Brian, *J. Chem. Soc., Chem. Commun.*, **1970**, 16, c) J. C. Huffman, W. E. Streib, *J. Chem. Soc., Chem. Commun.*, **1971**, 911.
- [189] a) J. E. Johnson, R. A. Jacobson, *Acta Crystallogr., Sect. B*, **1973**, 29, 1669, b) G. J. Pyrka, A. A. Pinkerton, *Acta Crystallogr., Sect. C*, **1992**, 48, 91, c) H. Schödel, C. Näther, H. Bock, F. Butenschön, *Acta Crystallogr., Sect. B*, **1996**, 52, 842.
- [190] a) A. D. Becke, *Phys. Rev.*, **1988**, A38, 3098, b) C. Lee, W. Yang, R. G. Paar, *Phys. Rev.*, **1988**, B37, 785.
- [191] A. D. Becke, *J. Chem. Phys.*, **1993**, 98, 5648.26.
- [192] R. Fleischer, B. Walfort, A. Gburek, P. Scholz, W. Kiefer, D. Stalke, *Chem. Eur. J.*, **1998**, 4, 2266.
- [193] A. Almenningen, L. Fernholt, A. Haaland, J. Weidlein, *J. Organomet. Chem.*, **1978**, 145, 109.
- [194] G. A. Andersen, F. R. Forgaard, A. Haaland, *Acta. Chem. Scand.*, **1972**, 26, 1947.
- [195] L. S. Bartell, L. O. Brockway, *J. chem. Phys.*, **1960**, 32, 512.
- [196] B. Beagley, T. G. Hewitt, *Trans. Faraday Soc.*, **1968**, 64, 2561.
- [197] A. Almenningen, S. Halvorsen, A. Haaland, *Acta Chem. Scand.*, **1971**, 25, 1937.
- [198] R. J. Gillespie, *J. Chem. Ed.*, **1970**, 47, 18.
- [199] P. H. M. Budzelaar, *J. Org. Chem.*, **1998**, 63, 1131.

Dank

Mein besonderer Dank gilt meinem Doktorvater Prof. Dr. W. Kiefer, unter dessen Anleitung und mit dessen vielseitiger Unterstützung diese Arbeit entstand.

Für die gute Zusammenarbeit im SFB möchte ich mich an erster Stelle bei Herrn Prof. Dr. H. Werner, Prof. Dr. D. Stalke, Prof. Dr. W. Malisch und Prof. Dr. W. A. Schenk bedanken. Desweiteren möchte ich Prof. Dr. B. Engels und Prof. Dr. M. Kaupp für Ihre Diskussionsbereitschaft bezüglich der Rechnungen danken.

Ganz besonders danken möchte ich Juan Gil-Rubio, Berta Callejas-Gaspar und Ioana Pavel für die sehr gute und angenehme Zusammenarbeit.

AK Werner, AK Stalke, AK Malisch und AK Schenk sei auch natürlich sehr gedankt für die gute Atmosphäre und die Bereitstellung von Material für die experimentellen Untersuchungen.

Inbesondere möchte ich meinen Dank der Feinmechanik- und Elektronikwerkstatt aussprechen, die für ein nettes Arbeitsklima und erfolgreiches Arbeiten gesorgt haben.

Letztendlich möchte ich mich bei allen Freunden, Bekannten und Kollegen bedanken, die dafür gesorgt haben, dass meine gesamte Studien- und Promotionszeit interessant und abwechslungsreich verlief.

Die vorliegende Arbeit wurde dankenswerterweise von der Deutschen Forschungsgemeinschaft (Sonderforschungsbereich 347) durch Sachmittel und Chemikalienspenden unterstützt.

Ein besonders lieber Dank gilt meiner Frau Barbara, mit der ich mein Leben genieße.

Lebenslauf

Persönliche Daten

Damien Moigno
Geboren am 02.02.1972 in Redon (Frankreich)
Französische Nationalität

Schulausbildung

1987-1991 Lycée de Beaumont in Redon
Abschluß: Baccalauréat D (Mathematisch-wissenschaftlicher Schwerpunkt)

Studium

Sept. 1991-Juni 1993 Beginn des Chemie-Studiums am Institut Universitaire de Technologie (IUT) in Rennes (Schwerpunkte: Verfahrenstechnik, Organische Chemie und Analytik)
Abschluß: DUT (Diplôme Universitaire de Technologie)

Okt. 1993-Dez.1996 Anerkennung dieses als **Vordiplom** in Deutschland
Fortsetzung des Chemie-Studiums an der Universität

Würzburg

März 1996-Dez.1996

Diplomarbeit am Institut für Organische Chemie der Universität Würzburg bei Prof. Dr. M. Christl
Thema: "1-Phenyl-1,2-cyclononadien: Synthese und Dimerisierung"

Abschluß: Diplom-Chemiker

Promotion

Seit Juli 1998 Doktorarbeit am Institut für Physikalische Chemie der Universität Würzburg bei Prof. Dr. W. Kiefer

Tätigkeiten

Mai 1993-Juli 1993 Praktikum bei der Hoechst AG, Frankfurt, Fachrichtung Polymerforschung (Analytik)

Aug. 1994 Praktikum bei der BASF Lacke + Farben AG, Würzburg (Farbmetrikmessungen, Beurteilung der Ergebnisse und Dokumentation, Produktionsbegleitung und Prozeßbeschreibung der Passagenfahrweise)

1996 Studentische Hilfskraft an der Universität Würzburg (Betreuung und Anleitung von Versuchen im Chemie-Praktikum für Medizinstudenten)

Feb. 1997-Juni 1998 Service National en Entreprise au titre de la Coopération (Militärsersatzdienst) geleistet als Außendienst im Klinikbereich Infektiologie / Gastroenterologie bei der Firma Hoechst-Marion-Roussel, Bad-Soden

Seit Juli 1998 Wissenschaftlicher Mitarbeiter an der Universität Würzburg im Sonderforschungsbereich 347 der Deutschen Forschungsgemeinschaft; zuständig für die Instandhaltung eines Laserlabors und von EDV-Rechnern

Erklärung

Hiermit erkläre ich ehrenwörtlich, dass ich die Dissertation

„Study of the ligand effects on the metal-ligand bond in some new Organometallic complexes using FT-Raman and -IR spectroscopy, isotopic substitution and density functional theory techniques.“

selbständig angefertigt und keine anderen als die von mir angegebenen Quellen und Hilfsmittel benutzt habe.

Ich erkläre außerdem, dass diese Dissertation weder in gleicher oder anderer Form bereits in einem anderen Prüfungsverfahren vorgelegen hat.

Ich habe früher außer den mit dem Zulassungsgesuch urkundlich vorgelegten Graden keine weiteren akademischen Grade erworben oder zu erwerben versucht.

Würzburg, den 02. November 2001

.....
(Damien Moigno)